

Calculation, simulation, and experimental analysis of  
distorted and enhanced spectra from attenuated total  
reflection (ATR)

Dem Fachbereich Produktionstechnik

der

UNIVERSITÄT BREMEN

zur Erlangung des Grades  
Doktor der Ingenieurwissenschaften (Dr.-Ing.)  
genehmigte

Dissertation

von

Rui Cheng; M.Eng.

Gutachter: Prof. Dr.-Ing. Johannes Kiefer  
Prof. Dr. rer. nat. Arnulf Materny

Tag der mündlichen Prüfung: 10.01.2025



Für den Prüfungsausschuss schlage:

1. **Prof. Dr.-Ing. Johannes Kiefer**      FB 4, Universität Bremen  
**Prof. Dr. rer. nat. Arnulf Materny**      Chemical Physics, School of Science,  
Constructor University
  
2. **PD Dr. Michael Maas**                      FB 4, Universität Bremen  
**Prof. Lutz Mädler**                              FB 4, Universität Bremen
  
3. **Prof. Ella Schmidt**                          FB 5, Universität Bremen  
**Ms. Caroline Drünert**                        FB 4, Universität Bremen

Das Kolloquium fand am 10. Januar 2025 um 11:00 Uhr im FZB Raum 1250 an der Universität Bremen statt.



## **Abstract:**

This doctoral thesis extensively investigates the principles, calculations, experiments, and simulations related to the distortion spectrum and surface-enhanced spectroscopy within the framework of attenuated total reflection Fourier transform infrared spectroscopy (ATR-FTIR). The research encompasses four main aspects:

1. Based on Maxwell's equations, an in-depth exploration is conducted into the origins of spectral distortion with computations utilizing Snell's law. The combination of the established model with Fresnel's equation yields simulation outcomes that align with the experimental spectral data. Correction of the distortion spectrum is realized through the application of the Kramers-Kronig (KK) transform and an algorithm resembling the Fourier transform (FT). The subsequent analysis challenges conventional understanding by revealing the blue shift associated with the degree of spectral distortion.

2. The study systematically introduces the transition from Fourier Transform (FT) methodologies to contemporary deep learning algorithms, particularly neural networks. Recognizing the intrinsic complexity of conventional correction methods, the investigation performs the classification and correction of distorted spectra using artificial neural network algorithms. Comparative assessments with traditional methods indicate that long short-term memory (LSTM) and Transformer models exhibit accelerated processing speeds and heightened batch correction capabilities.

3. Theoretical calculations for surface plasmon generation, accounting for the thickness of the thin layer, were conducted. The surface enhancement spectrum of Pd nanoparticles is demonstrated through the integration of theoretical calculations with experiments.

4. The thesis expounds on the principles of two-dimensional Fourier transform (2D FT) and provides an in-depth analysis of the classification and fundamental principles of two-dimensional infrared spectroscopy (2D IR). As a technique rooted in third-order nonlinear optical phenomena, 2D IR spectroscopy exhibits distortion and surface-enhanced spectroscopy characteristics similar to those observed in one-dimensional (1D) spectroscopy, particularly near the critical angle. Furthermore, due to the unique principles of 2D IR, it also demonstrates enhanced specificity at the Brewster angle.

This thesis offers a comprehensive discussion and comparison of the similarities and differences between 1D and 2D surface-enhanced spectroscopy.

## **Zusammenfassung:**

Diese Doktorarbeit untersucht umfassend die Prinzipien, Berechnungen, Experimente und Simulationen im Zusammenhang mit dem Verzerrungsspektrum und der oberflächenverstärkten Spektroskopie im Rahmen der abgeschwächten Totalreflexions-Fourier-Transformations-Infrarotspektroskopie (ATR-FTIR). Die Forschung umfasst vier Hauptaspekte:

1. Basierend auf den Maxwell'schen Gleichungen wird eine tiefgehende Untersuchung der Ursprünge der spektralen Verzerrung durchgeführt, wobei Berechnungen mit dem Snell'schen Gesetz genutzt werden. Die Kombination des etablierten Modells mit der Fresnel-Gleichung liefert Simulationsergebnisse, die mit den experimentellen Spektraldaten übereinstimmen. Die Korrektur des Verzerrungsspektrums wird durch die Anwendung der Kramers-Kronig (KK) Transformation und eines Algorithmus, der der Fourier-Transformation (FT) ähnelt, realisiert. Die anschließende Analyse stellt das konventionelle Verständnis in Frage, indem sie die Blauverschiebung im Zusammenhang mit dem Grad der spektralen Verzerrung aufzeigt.

2. Die Studie führt systematisch den Übergang von Fourier-Transformations-Methoden (FT) zu Deep-Learning-Algorithmen, insbesondere neuronalen Netzwerken, ein. Angesichts der intrinsischen Komplexität herkömmlicher Korrekturmethode wird die Klassifizierung und Korrektur verzerrter Spektren mit Hilfe von Algorithmen künstlicher neuronaler Netzwerke durchgeführt. Vergleichende Bewertungen mit traditionellen Methoden zeigen, dass Long Short-Term Memory (LSTM) und Transformer-Modelle eine schnellere Verarbeitungsgeschwindigkeit und gesteigerte Batch-Korrekturfähigkeiten aufweisen.

3. Theoretische Berechnungen zur Erzeugung von Oberflächenplasmonen, die die Dicke der dünnen Schicht berücksichtigen, wurden durchgeführt. Das oberflächenverstärkte Spektrum von Pd-Nanopartikeln wird durch die Integration theoretischer Berechnungen mit Experimenten demonstriert.

4. Die Arbeit erläutert die Prinzipien der zweidimensionalen Fourier-Transformation (2D FT) und bietet eine ausführliche Analyse der Klassifikation und grundlegenden Prinzipien der zweidimensionalen Infrarotspektroskopie (2D IR). Als eine auf dritter

Ordnung nichtlinearer optischer Phänomene basierende Technik zeigt die 2D IR-Spektroskopie Verzerrungen und Merkmale der oberflächenverstärkten Spektroskopie, die denen der eindimensionalen (1D) Spektroskopie ähneln, insbesondere in der Nähe des kritischen Winkels. Darüber hinaus demonstriert die 2D IR aufgrund ihrer einzigartigen Prinzipien auch eine erhöhte Spezifität am Brewster-Winkel. Diese Dissertation bietet eine umfassende Diskussion und einen Vergleich der Gemeinsamkeiten und Unterschiede zwischen der 1D- und der 2D-oberflächenverstärkten Spektroskopie.



# Content

Introduction: .....	1
1. Theoretical calculation .....	5
1.1 Maxwell's Equations .....	5
1.2 Wave Equation .....	7
1.3 Boundary Conditions .....	9
1.4 Fresnel's Law .....	12
1.5 Total Internal Reflection and Evanescent Wave .....	14
1.6 Simulation of Distorted Spectrum .....	16
2. Introduction to Various Transforms .....	27
2.1 Phase-Sensitive Detection (PSD) .....	27
2.2 Fourier Transform (FT) .....	37
2.3 Hilbert Transform .....	40
2.4 Lorentz-Drude Model .....	46
2.5 Simulation and Correction .....	50
3. From Fourier Transform to Deep Learning .....	58
3.1 Extension of Fourier Transform .....	58
3.2 Convolutional Neural Network (CNN) .....	61
3.3 The Recurrent Neural Network (RNN) .....	65
3.4 Transformer .....	71
3.5. Simulation, Classification, and Correction with Deep Learning .....	77
4. Surface - Enhanced Spectrum .....	83
4.1 Calculation .....	83
4.2 Simulation .....	92
4.3 Experiment .....	98
5. Introduction to Two-dimensional Infrared (2D IR) Spectroscopy .....	103
5.1 Two-dimensional Fourier transform (2D FT) .....	103
5.2 2D IR Spectroscopy .....	106
5.3 Enhancement in 2D IR .....	119
5.4 Comparison .....	139
Conclusion .....	143
Acknowledgement .....	147
List of Symbols .....	149
List of Publications .....	153
Reference .....	154



# Introduction:

Attenuated total reflection (ATR)<sup>1</sup> techniques are widely used in spectroscopy due to their experimental simplicity and non-destructive nature<sup>2-8</sup>. In ATR, the radiation is propagating in a material with high refractive index, often referred to as the internal reflection element (IRE), and undergoes total internal reflection at the IRE surface. This surface is in contact with the sample so that the evanescent field<sup>9</sup> of the radiation can interact with the sample. In ATR absorption methods, the internally reflected radiation carries information about the absorption spectrum of the sample.

The most widely used range for the ATR technique is the mid-infrared spectral range<sup>10</sup>, i.e. from  $\sim 4000$  to  $\sim 200$   $\text{cm}^{-1}$ . The aim is usually to either carry out structural analysis from assigning the peaks to vibrational modes or to perform quantitative measurements, e.g. as a means of process analytical technology (PAT). However, there is a number of issues arising from complex, chemically, and physically inhomogeneous samples and extracting reliable information from their spectra. This is particularly true for strongly absorbing samples and media with a high refractive index such as carbon black<sup>11, 12</sup>, coal<sup>13</sup>, graphite, graphene, rubber<sup>14, 15</sup>, metal<sup>16-18</sup>, metal oxide<sup>19</sup>, etc<sup>20</sup>. When such samples are analyzed, the ATR spectrum is always affected by significant distortions<sup>21-24</sup>. As those distortions can originate from a multitude of physical and chemical phenomena, it is vitally important to understand the underlying mechanisms and to develop methods for their correction. Most of these issues are related to the fact that the refractive index is so high that the critical angle is higher than the one used in the ATR accessory; hence, the total internal reflection is affected.

In the present work, we focus on the analysis of mixtures of particles mixed with a solvent as suggested for the recently developed solvent infrared spectroscopy (SIRS) approach, which can be used to study the surface chemistry of nanomaterials<sup>25</sup>. Such systems are particularly interesting as they seem to be simple at first glance because the IRE-solvent interface appears to be dominating the evanescent field.

However, we will show that the reality is more complicated. For this purpose,

this doctoral thesis conducts a comprehensive exploration of distortion spectroscopy and surface-enhanced spectroscopy within the framework of attenuated total reflection Fourier transform infrared spectroscopy (ATR-FTIR)<sup>1, 10</sup>.

We always have questions first, then answers. But in the process of searching for answers, new questions will continue to arise, and new areas will continue to be expanded. This is how I do research and also why research is so fascinating. But when we find the answer, we have to start from some very basic and complicated theories to try to explain everything fundamentally. This is what this doctoral thesis demonstrates.

Chapter 1 first introduces wave optics based on Maxwell's equations. Then the chapter based on Maxwell's equations, Snell's law, and Fresnel's law, and explored the causes of spectral distortion and which parts caused the distortion. Next a model for mixtures comprising of a liquid and a solid is established. The effects of the distortion as well as potential misinterpretation of the data are discussed. Proof-of-concept experiments with mixtures of carbonaceous materials and toluene confirm the theoretically predicted observations.

Chapter 2 starts with an introduction to phase sensitive detection (PSD), Fourier transform (FT), Hilbert transform including Kramers-Kronig (KK) transform, and Lorenz-Drude model. Followed by the simulation and correction of the distorted ATR spectrum based on the KK transform, Inverse fast Fourier transform (IFFT), fast Fourier transform (FFT). Furthermore, we enhanced the original correction method to address these variations with phase delays varying across different wavenumbers. This improvement allowed us to obtain the corrected spectrum for the entire distorted spectrum in a single step, ensuring a more accurate and comprehensive correction. According to the analysis of the result, the right trends of the peak shift, which is blue shift rather than red shift in distorted original spectrum, are achieved.

Chapter 3 initiates with a systematic introduction from traditional transform methods to deep learning algorithms, including short-time Fourier transform (STFT), wavelet transform, convolutional neural network (CNN), recurrent neural network (RNN) including long short-term memory (LSTM), attention mechanism including Transformer. Followed by the simulation and correction of the distorted ATR spectrum based on LSTM and Transformer. In this work, several steps were taken: generating artificially distorted spectra using IFFT and FFT; subsequently, training models using

LSTM and Transformer as learning methods; consequently, distinguishing between distorted and normal experimental spectra; eventually, correcting the distorted spectra. The deep learning algorithms in this paper provide valuable guidance to researchers who encounter distorted spectra in experiments. This holds significant potential for differentiating and correcting various types of spectra, and even images.

Chapter 4 explains the principle of surface enhanced spectroscopy based on Maxwell's equations from two aspects: thin-layer theory and Surface plasmon polaritons (SPPs). Secondly, considering the influence of  $d$  on the basis of Otto and Kretschmann configuration, detailed steps are given for the calculation and simulation of surface plasmons in ATR, which is the basis of ATR surface enhanced spectroscopy in this thesis. Followed by the experiment of surface-enhanced spectroscopy of Rhodamine-6G based on ATR with Palladium (Pd) nanoparticles.

Chapter 5 introduces the 2D FT as a foundational topic before moving on to introduce two key approaches to 2D infrared spectra. After that ultrafast spectroscopy uncovered distorted and surface-enhanced spectra in 2D infrared spectra, similar to 1D infrared spectra. This chapter investigates the mechanisms by which third-order nonlinear spectroscopy methods produce surface-enhanced spectra near Brewster's angle. This phenomenon contrasts with the critical angle enhancement observed in one-dimensional infrared spectroscopy. Our research aims to provide a deeper understanding of these phenomena and their underlying principles, thereby enriching the field of two-dimensional infrared spectroscopy and advancing its applications in studying complex molecular interactions.

Since the theories and methods involved in this thesis span physics, chemistry, spectroscopy, linear optics and nonlinear optics, signal processing, and artificial intelligence, the relationships between the various concepts and methods are quite complicated, a brief relationship diagram to show the relationship between each part can be seen in the Fig. 1.0 below.

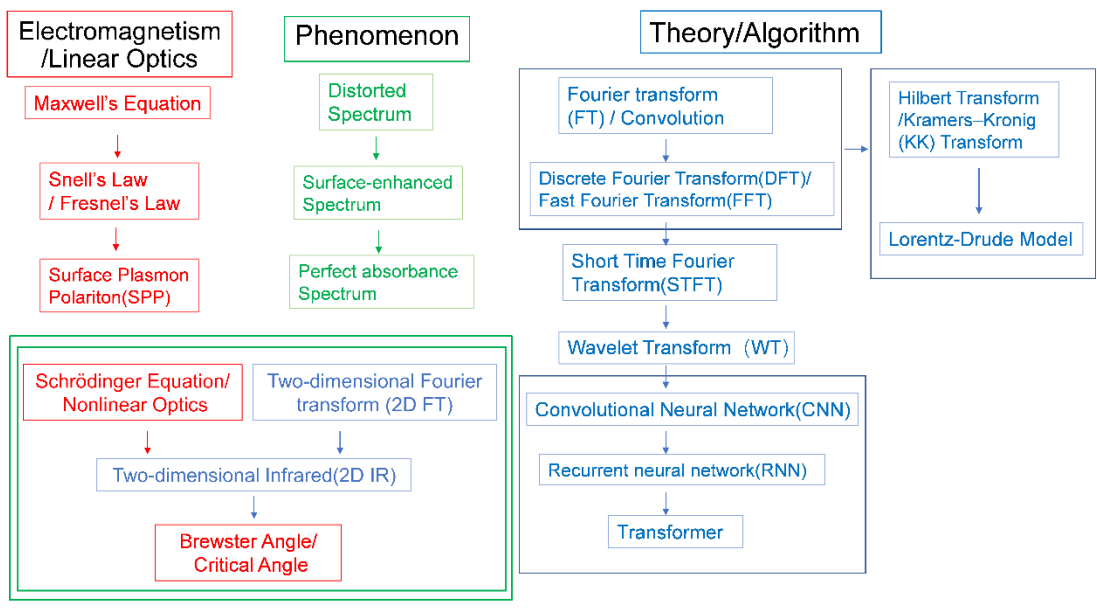


**Fig. 1.0** The relationship between the phenomena and principals involved in this doctoral thesis.

# 1. Theoretical calculation

## 1.1 Maxwell's Equations

Maxwell's equations are composed of the following four formulas<sup>26-34</sup>.

$$\nabla \times \vec{E} = -\frac{\partial \vec{B}}{\partial t} \quad \text{Faraday's law} \quad (1.1)$$

$$\nabla \times \vec{H} = \vec{J} + \frac{\partial \vec{D}}{\partial t} \quad \text{Ampere's circuital law} \quad (1.2)$$

$$\nabla \cdot \vec{D} = \rho_v \quad \text{Gauss's law} \quad (1.3)$$

$$\nabla \cdot \vec{B} = 0 \quad \text{Gauss's law for magnetic Field} \quad (1.4)$$

Faraday's law states that a changing magnetic field can generate an electric field.

Ampere's circuit law states that conducting an electric current can create a magnetic field and that a changing electric field can create a magnetic field.

Gauss's law means that an electric field is a source field, and a charge can generate an electric field.

Gauss's law for magnetic field means that the magnetic field is a field without sources.

All in all, Maxwell's equations explain the origins of electromagnetic fields<sup>31, 32</sup>.

The physical meanings of the symbols are shown in the table

List of Symbols.

In which<sup>34</sup>,

$$\nabla = \frac{\partial}{\partial x} \vec{i} + \frac{\partial}{\partial y} \vec{j} + \frac{\partial}{\partial z} \vec{k} \quad (1.5)$$

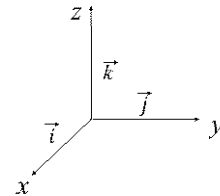


**Fig. 1.1** Unit vector  $(\vec{i}, \vec{j}, \vec{k})$  on the  $x, y, z$  axis.

The three following equations make up the constitutive relations, which describe how fields interact with materials<sup>31-33</sup>.

$$\vec{D} = \epsilon \vec{E} \quad \text{Electric response} \quad (1.6)$$

$$\vec{B} = \mu \vec{H} \quad \text{Magnetic response} \quad (1.7)$$

$$\vec{J} = \sigma \vec{E} \quad \text{Ohm's law} \quad (1.8)$$

In our discussion,  $\epsilon$ ,  $\mu$  and  $\sigma$  are scalars. But in anisotropic media, they're tensors. We'll introduce them respectively.

The permittivity  $\epsilon$  is a measure of the electric polarizability of a dielectric. And it indicates how well a medium stores electric energy in capacitors.  $\epsilon$  can be calculated

as<sup>33</sup>

$$\varepsilon = \varepsilon_0 \varepsilon_r = \varepsilon_0(1 + \chi_e) \quad (1.9)$$

$$\varepsilon_0 = 8.8541878176 \times 10^{-12} F/m; \quad \varepsilon_r = \frac{\varepsilon}{\varepsilon_0} = 1 + \chi_e.$$

The electric displacement field  $\vec{D}$  can be written as<sup>31, 32</sup>

$$\vec{D} = \varepsilon_0 \vec{E} + \vec{P} = \varepsilon_0 \vec{E} + \varepsilon_0 \chi_e \vec{E} \quad (1.10)$$

$\varepsilon_0 \vec{E}$  means the response of free space,  $\vec{P}$  means the response of material, which is defined as the polarization,  $\vec{P} = \varepsilon_0 \chi_e \vec{E}$ .

With regard to the response of material, we can divide them into linear and nonlinear.

For linear response, which means<sup>31, 32</sup>

$$\vec{P} = \varepsilon_0 \chi_e \vec{E} \quad (1.11)$$

$$\vec{D} = \varepsilon \vec{E} = \varepsilon_0 \varepsilon_r \vec{E} = \varepsilon_0(1 + \chi_e) \vec{E} \quad (1.12)$$

For nonlinear response, which means<sup>35, 36</sup>

$$\vec{P} = \varepsilon_0 \chi_e \vec{E} + \varepsilon_0 \chi_e^2 \vec{E}^2 + \varepsilon_0 \chi_e^3 \vec{E}^3 + \varepsilon_0 \chi_e^4 \vec{E}^4 + \dots \quad (1.13)$$

$$\vec{D} = \varepsilon_0(1 + \chi_e) \vec{E} + \varepsilon_0 \chi_e^2 \vec{E}^2 + \varepsilon_0 \chi_e^3 \vec{E}^3 + \varepsilon_0 \chi_e^4 \vec{E}^4 + \dots \quad (1.14)$$

In this chapter, we only discuss the linear case. In chapter 5, we'll discuss the nonlinear case.

The permeability  $\mu$  indicates how well a medium stores magnetic energy.

$$\mu = \mu_0 \mu_r = \mu_0(1 + \chi_m) \quad (1.15)$$

The electric response can be written as

$$\vec{B} = \mu \vec{H} = \mu_0 \mu_r \vec{H} = \mu_0(1 + \chi_m) \vec{H} \quad (1.16)$$

In which,  $\mu_r$  usually as 1 where the magnetic susceptibility  $\chi_m$  of most material is negligible.

The refractive index  $\hat{n}$  can be calculated as

$$\hat{n} = \sqrt{\mu_r \varepsilon_r} = \sqrt{(1 + \chi_m)(1 + \chi_e)} = \sqrt{\varepsilon_r} \quad (1.17)$$

we will introduce more specific later in chapter 1.6.

$$c = \frac{1}{\sqrt{\mu_0 \varepsilon_0}} \quad (1.18)$$

The parameter  $\sigma$ , with units of  $1/\Omega \cdot m$ , characterizes how effectively a material conducts electricity. But it's not important parameter in our case.



## 1.2 Wave Equation

If only a dielectric is present, without any metallic material or free electrons, Maxwell's Equations can be expressed in the following simplified form<sup>26, 33, 34, 37, 38</sup>:

$$\nabla \times \vec{E} = -\frac{\partial \vec{B}}{\partial t} \quad \text{Faraday's law} \quad (1.19)$$

$$\nabla \times \vec{H} = \frac{\partial \vec{D}}{\partial t} \quad \text{Ampere's circuital law} \quad (1.20)$$

$$\nabla \cdot \vec{D} = 0 \quad \text{Gauss's law} \quad (1.21)$$

$$\nabla \cdot \vec{B} = 0 \quad \text{Gauss's law for magnetic Field} \quad (1.22)$$

According to Gauss's law

$$\nabla \cdot \vec{D} = 0 \quad (1.23)$$

And electric response equation

$$\vec{D} = \epsilon \vec{E} \quad (1.24)$$

To get

$$\nabla \cdot \epsilon \vec{E} = \epsilon (\nabla \cdot \vec{E}) = 0 \quad (1.25)$$

And  $\epsilon$  is a constant, then we can get

$$\nabla \cdot \vec{E} = 0 \quad (1.26)$$

Add  $\nabla \times$  on both sides of Faraday's law to get

$$\nabla \times (\nabla \times \vec{E}) = -\nabla \times \frac{\partial \vec{B}}{\partial t} \quad (1.27)$$

Because

$$\vec{a} \times (\vec{b} \times \vec{c}) = (\vec{a} \cdot \vec{c}) \cdot \vec{b} - (\vec{a} \cdot \vec{b}) \cdot \vec{c} \quad (1.28)$$

For the left side of Eqn. 1.27

$$\nabla \times (\nabla \times \vec{E}) = \nabla(\nabla \cdot \vec{E}) - (\nabla \cdot \nabla) \cdot \vec{E} = -\nabla^2 \vec{E} \quad (1.29)$$

For the right side of Eqn. 1.27

$$-\nabla \times \frac{\partial \vec{B}}{\partial t} = -\frac{\partial}{\partial t} (\nabla \times \vec{B}) \quad (1.30)$$

Combine  $\vec{B} = \mu \vec{H}$ ,  $\nabla \times \vec{H} = \frac{\partial \vec{D}}{\partial t}$  and  $\vec{D} = \epsilon \vec{E}$  to get

$$-\nabla \times \frac{\partial \vec{B}}{\partial t} = -\mu \frac{\partial}{\partial t} (\nabla \times \vec{H}) = -\mu \frac{\partial}{\partial t} \left( \frac{\partial \vec{D}}{\partial t} \right) = -\mu \epsilon \frac{\partial^2 \vec{E}}{\partial t^2} \quad (1.31)$$

Combine Eqn. 1.29, Eqn. 1.30, and Eqn. 1.31 to obtain

$$\nabla^2 \vec{E} = \mu\epsilon \frac{\partial^2 \vec{E}}{\partial t^2} \quad (1.32)$$

Namely

$$\nabla^2 \vec{E} - \mu\epsilon \frac{\partial^2 \vec{E}}{\partial t^2} = 0 \quad (1.33)$$

Which is the wave equation for the electric field<sup>30</sup>.

Similarly, the wave equation of the magnetic field<sup>30</sup> is

$$\nabla^2 \vec{H} - \mu\epsilon \frac{\partial^2 \vec{H}}{\partial x^2} = 0 \quad (1.34)$$

For a monochromatic plane wave

$$\vec{E}(\vec{r}, t) = \vec{E}_0 \cdot e^{i(\omega t - \vec{k} \cdot \vec{r})} \quad (1.35)$$

$$\frac{\partial \vec{E}}{\partial t} = i\omega \vec{E}_0 \cdot e^{i(\omega t - \vec{k} \cdot \vec{r})} = i\omega \vec{E} \quad (1.36)$$

$$\frac{\partial^2 \vec{E}}{\partial t^2} = -\omega^2 \vec{E}_0 \cdot e^{i(\omega t - \vec{k} \cdot \vec{r})} = -\omega^2 \vec{E} \quad (1.37)$$

Then the wave equation for the electric field can be written as

$$\nabla^2 \vec{E} + \mu\epsilon\omega^2 \vec{E} = 0 \quad (1.38)$$

Similarly, the wave equation of the magnetic field can also be written as

$$\nabla^2 \vec{H} + \mu\epsilon\omega^2 \vec{H} = 0 \quad (1.39)$$

And for the wave vector  $\vec{k}$  satisfy the following conditions

$$\vec{k}^2 = \mu\epsilon\omega^2 \quad (1.40)$$

$$\nabla^2 \vec{E} + k^2 \vec{E} = 0 \quad (1.41)$$

$$\nabla^2 \vec{H} + k^2 \vec{H} = 0 \quad (1.42)$$

Eqn. 1.41 and Eqn. 1.42 are the Helmholtz equations<sup>38</sup>.

### 1.3 Boundary Conditions

When there is solely a dielectric present, meaning no metallic material or free electrons, Maxwell's Equations<sup>26, 39</sup> can be reduced to the following simplified form<sup>34, 37</sup>:

$$\nabla \times \vec{E} = -\frac{\partial \vec{B}}{\partial t} \quad \text{Faraday's law} \quad (1.43)$$

$$\nabla \times \vec{H} = \frac{\partial \vec{D}}{\partial t} \quad \text{Ampere's circuital law} \quad (1.44)$$

$$\nabla \cdot \vec{D} = 0 \quad \text{Gauss's law} \quad (1.45)$$

$$\nabla \cdot \vec{B} = 0 \quad \text{Gauss's law for magnetic Field} \quad (1.46)$$

Take a rectangle with infinitely thin thickness and length  $l$  at the interface of the material, according to the closed loop theorem

$$\vec{E}_{1t}l - \vec{E}_{2t}l = 0 \quad (1.47)$$

$t$  here is a tangential component and  $n$  is a normal component.

Then

$$\vec{E}_{1t} = \vec{E}_{2t} \quad (1.48)$$

Which means that the electric field is continuous in the tangential direction. From here we can derive the important Fresnel's law in chapter 1.4.

The following formulas can also be obtained in the same way.

$$\vec{H}_{1t} = \vec{H}_{2t} \quad (1.49)$$

$$\vec{D}_{1n} = \vec{D}_{2n} \quad (1.50)$$

$$\vec{B}_{1n} = B_{2n} \quad (1.51)$$

For the monochromatic plane wave from Eqn. 1.35, the electric field can be written as

$$\vec{E}(\vec{r}, t) = \vec{E}_0 \cdot e^{i(\omega t - \vec{k} \cdot \vec{r})} = \vec{E}_0 \cdot \cos(\omega t - \vec{k} \cdot \vec{r}) \quad (1.52)$$

$$\omega = 2\pi f \quad (1.53)$$

$$\omega = \frac{2\pi}{T} \quad (1.54)$$

$\vec{k}$  is the angular wave vector, indicating the direction of wave propagation.

$$|\vec{k}| = \frac{2\pi}{\lambda} \quad (1.55)$$

$$v = \frac{c}{n} = \frac{\omega}{\vec{k}} \quad (1.56)$$

$$\vec{k} = n \frac{\omega}{c} = n \vec{k}_0 \quad (1.57)$$

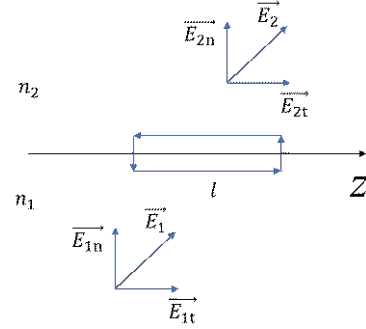


**Fig. 1.2** Schematic diagram of the closed loop theorem

For the vector  $\vec{X}$  the following formulas are all established

$$\nabla \times \vec{X} = i\vec{k} \times \vec{X} \quad (1.58)$$

$$\nabla \cdot \vec{X} = i\vec{k} \cdot \vec{X} \quad (1.59)$$

$$\frac{\partial \vec{X}}{\partial t} = i\omega \vec{X} \quad (1.60)$$

$$\frac{\partial^2 \vec{X}}{\partial t^2} = -\omega^2 \vec{X} \quad (1.61)$$

For Faraday's law

$$\nabla \times \vec{E} = -\frac{\partial \vec{B}}{\partial t} \quad (1.62)$$

Substituting Eqn. 1.58 into the left side gives

$$\nabla \times \vec{E} = i\vec{k} \times \vec{E} \quad (1.63)$$

Substituting Eqn. 1.60 into the right side gives

$$-i\omega \vec{E} = i\omega \vec{B} \quad (1.64)$$

Which means

$$\vec{k} \times \vec{E} = \omega \vec{B} \quad (1.65)$$

Similarly, as for Ampere's circuital law  $\nabla \times \vec{H} = \frac{\partial \vec{D}}{\partial t}$ ,

Eqn. 1.44 can be obtained

$$\vec{k} \times \vec{H} = -\omega \vec{D} \quad (1.66)$$

Combine  $\vec{B} = \mu \vec{H}$  and  $\vec{D} = \epsilon \vec{E}$  to get

$$\vec{k} \times \vec{E} = \omega \mu \vec{H} \quad (1.67)$$

$$\vec{k} \times \vec{H} = -\omega \epsilon \vec{E} \quad (1.68)$$

Simultaneously taking the modulo of Eqn. 1.67 and Eqn. 1.68 to obtain

$$k \cdot E = \omega \mu H \quad (1.69)$$

$$k \cdot H = \omega \epsilon E \quad (1.70)$$

Multiply the left and right sides of above two equations simultaneously to get

$$k^2 = \omega^2 \mu \epsilon \quad (1.71)$$

$$k = \omega \sqrt{\mu \epsilon} \quad (1.72)$$

Similarly,

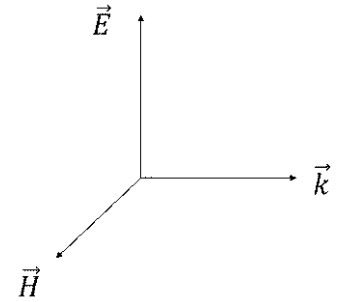


**Fig. 1.3**  $\vec{E}, \vec{H}, \vec{k}$

$$\frac{\vec{E}}{\vec{H}} = \sqrt{\frac{\mu}{\epsilon}} = \sqrt{\frac{\mu_0}{\epsilon_0}} \cdot \frac{1}{\sqrt{\epsilon_r}} \quad (1.73)$$

$$\frac{\vec{H}}{\vec{E}} = \sqrt{\frac{\epsilon}{\mu}} = \sqrt{\frac{\epsilon_0}{\mu_0}} \cdot \sqrt{\epsilon_r} \quad (1.74)$$

Meanwhile, for at the interface, the wave vector is continuous on the continuous component.

$$\vec{k}_{1z} = \vec{k}_{2z} = \vec{k}_{3z} \quad (1.75)$$

$$\vec{k}_1 \sin\theta_1 = \vec{k}_2 \sin\theta_2 = \vec{k}_3 \sin\theta_3 \quad (1.76)$$

And because  $\vec{k}_1 = \vec{k}_3$ , then

$$\theta_1 = \theta_3 \quad (1.77)$$

$$n_1 \vec{k}_0 \sin\theta_1 = n_2 \vec{k}_0 \sin\theta_2 \quad (1.78)$$

$$n_1 \sin\theta_1 = n_2 \sin\theta_2 \quad (1.79)$$

Snell's Law is obtained<sup>40</sup>.

## 1.4 Fresnel's Law

Transverse electric (TE) mode has magnetic field but no electric field in the direction of propagation<sup>31-33</sup>. Light polarized perpendicular to the incidence plane ( $x - z$ ) is  $s$ -light. Without considering time and only considering the direction of light wave propagation, monochromatic plane wave<sup>31, 32, 34</sup> Eqn. 1.35 can be expressed as follows

$$\vec{E}_1 = \vec{E}_{10} \cdot e^{-i\vec{k} \cdot \vec{r}} = \vec{E}_{10} \cdot e^{-i(k_{1x} \cdot x + k_{1z} \cdot z)} \quad (1.80)$$

$$\vec{E}_2 = \vec{E}_{20} \cdot e^{-i\vec{k} \cdot \vec{r}} = \vec{E}_{20} \cdot e^{-i(k_{2x} \cdot x + k_{2z} \cdot z)} \quad (1.81)$$

$$\vec{E}_3 = \vec{E}_{30} \cdot e^{-i\vec{k} \cdot \vec{r}} = \vec{E}_{30} \cdot e^{-i(k_{3x} \cdot x + k_{3z} \cdot z)} \quad (1.82)$$

The tangential component is continuous near the boundary

$$\vec{E}_{10} + \vec{E}_{20} = \vec{E}_{30} \quad (1.83)$$

$$\vec{H}_{1z} - \vec{H}_{2z} = \vec{H}_{3z} \quad (1.84)$$

$$\vec{H}_{1z} = \vec{H}_1 \cos \theta_1 \quad (1.85)$$

$$\vec{H}_{2z} = \vec{H}_2 \cos \theta_1 \quad (1.86)$$

$$\vec{H}_{3z} = \vec{H}_3 \cos \theta_2 \quad (1.87)$$

Eqn. 1.84 Turns to

$$\vec{H}_{10} \cos \theta_1 - \vec{H}_{20} \cos \theta_1 = \vec{H}_{30} \cos \theta_2 \quad (1.88)$$

According to Eqn. 1.74

$$\vec{H} = \sqrt{\frac{\epsilon_0}{\mu_0}} \cdot \sqrt{\epsilon_r} \cdot \vec{E} = \sqrt{\frac{\epsilon_0}{\mu_0}} \cdot n \cdot \vec{E} \quad (1.89)$$

Eqn. 1.88 can be changed as

$$\vec{E}_{10} n_1 \cos \theta_1 - \vec{E}_{20} n_1 \cos \theta_1 = \vec{E}_{30} n_2 \cos \theta_2 \quad (1.90)$$

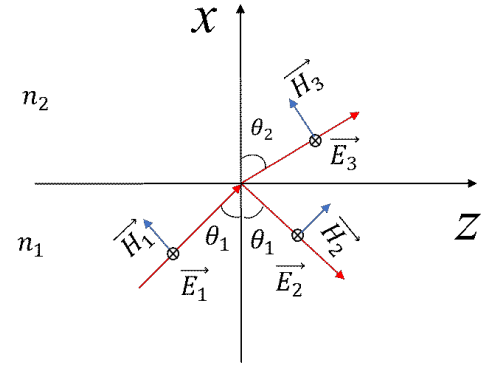


Fig. 1.4 TE mode

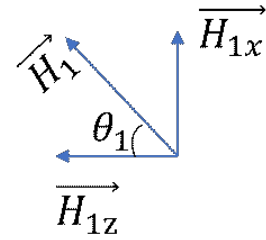


Fig. 1.5  $\vec{H}_1$ ,  $\vec{H}_{1x}$ ,  $\vec{H}_{1z}$

Simultaneous equations (Eqn.1.83 and Eqn.1.90) to get<sup>1</sup>

$$r_{TE} = \frac{\vec{E}_{20}}{\vec{E}_{10}} = \frac{n_1 \cos \theta_1 - n_2 \cos \theta_2}{n_1 \cos \theta_1 + n_2 \cos \theta_2} \quad (1.91)$$

$$t_{TE} = \frac{\vec{E}_{20}}{\vec{E}_{10}} = \frac{2n_1 \cos \theta_1}{n_1 \cos \theta_1 + n_2 \cos \theta_2} \quad (1.92)$$

Transverse magnetic (TM) mode<sup>33</sup>, also called *p* wave, has electric field but no magnetic field in the direction of propagation. Light propagated in TM mode is *p*-light.

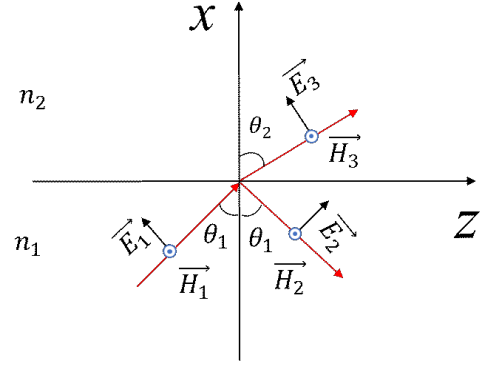


**Fig. 1.6** TM mode

Similarly, as for TM mode<sup>1</sup>

$$r_{TM} = \frac{\vec{E}_{20}}{\vec{E}_{10}} = \frac{n_2 \cos \theta_1 - n_1 \cos \theta_2}{n_2 \cos \theta_1 + n_1 \cos \theta_2} \quad (1.93)$$

$$t_{TM} = \frac{\vec{E}_{20}}{\vec{E}_{10}} = \frac{2n_1 \cos \theta_1}{n_1 \cos \theta_1 + n_2 \cos \theta_2} \quad (1.94)$$

Fresnel's law is obtained.

For light that has not been polarized, we usually think that the waves of TE and TM polarization states, namely *s*-light and *p*-light, each account for half<sup>1</sup>.

$$R_s = |r_s|^2 = \left| \frac{n_1 \cos \theta_1 - \sqrt{n_2^2 - n_1^2 \sin^2 \theta_1}}{n_1 \cos \theta_1 + \sqrt{n_2^2 - n_1^2 \sin^2 \theta_1}} \right|^2 \quad (1.95)$$

$$R_p = |r_p|^2 = \left| \frac{n_2^2 \cos \theta_1 - n_1 \sqrt{n_2^2 - n_1^2 \sin^2 \theta_1}}{n_2^2 \cos \theta_1 + n_1 \sqrt{n_2^2 - n_1^2 \sin^2 \theta_1}} \right|^2 \quad (1.96)$$

$$R = \frac{R_s + R_p}{2} \quad (1.97)$$

$$A = -\lg R \quad (1.98)$$

## 1.5 Total Internal Reflection and Evanescent Wave

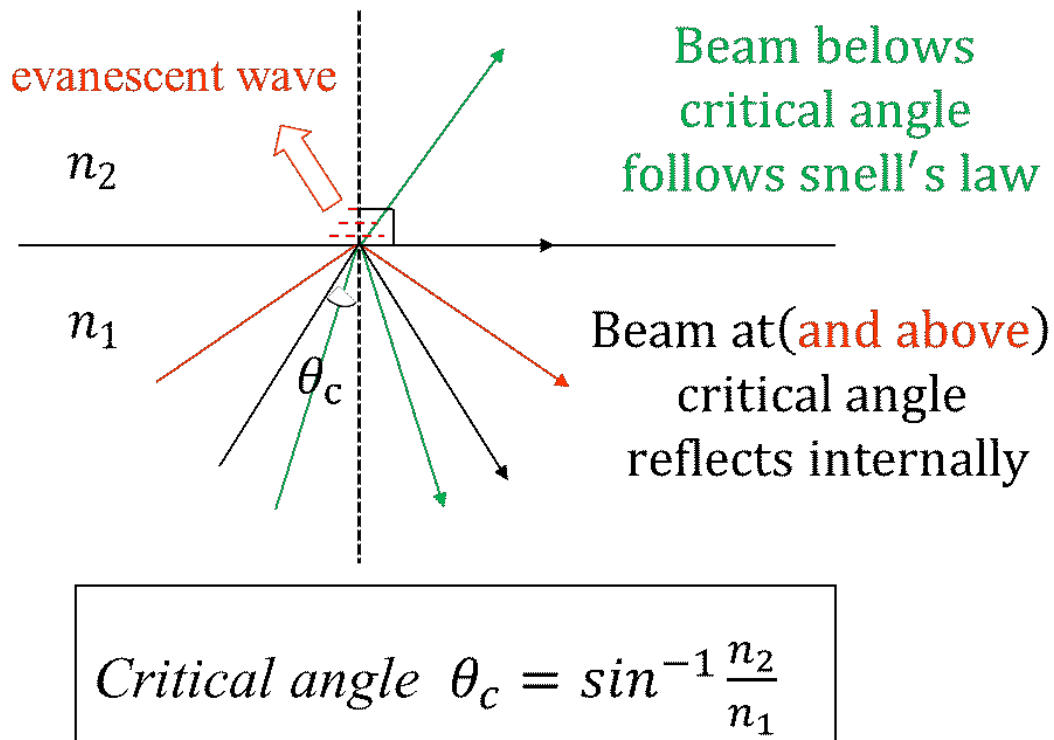


**Fig. 1.7** The refraction and reflection of light at different angles of incidence.

According to Snell's Law, when  $n_1 > n_2$ , at a certain incident angle the angle of refraction will be  $90^\circ$ . This angle of incidence is called the critical angle  $\theta_c$

$$\theta_c = \sin^{-1} \frac{n_2}{n_1} \quad (1.99)$$

If the angle of incidence exceeds the critical angle  $\theta_c$ , namely  $\theta_1 > \theta_c$ , no more light will enter the medium 2. That is, total reflection, also called total internal reflection occurs. However, the electric field and the magnetic field cannot be discontinuous at the boundary. We consider that there is a field at the interface that decays rapidly in the vertical direction in the medium 2. Such wave that enters the medium 2 and decay rapidly is called evanescent waves. With the influence of absorption, when light falls within an absorption band of material in the medium 2's frequency range, its reflection is diminished, whereas at frequencies significantly distant from an absorption band, all incident light is reflected. This is the origin of ATR<sup>1, 10, 41</sup>.

In additional, the amplitude of the evanescent wave decays to  $1/e$  of its maximum value at a distance  $d_p$  from the interface in attenuated total reflection<sup>1</sup>. This distance, called the penetration depth, is on the order of the wavelength of light.



$$d_p = \frac{1}{2\pi\nu\sqrt{n_1^2\sin^2\theta_1 - n_2^2}} \quad (1.100)$$

In attenuated total reflection, only the evanescent wave in the vertical direction enters the medium 2 and carries the information in the medium 2 back to the interface. Which is the basis of infrared absorption spectroscopy.

In ATR FTIR<sup>1</sup>, the refractive index of the crystal  $n_1$  and the entry angle  $\theta_1$  are usually fixed. Which means that when the refractive index  $n_2$  of the substance to be measured reaches a certain value, the refraction angle will be  $90^\circ$ . And we can calculate the critical refractive index

$$n_c = n_1 \frac{\sin \theta_1}{\sin \theta_2} = n_1 \sin \theta_1 \quad (1.101)$$

Especially when  $\theta_1 = 45^\circ$ ,  $n_1 = 2.3778$  (*Diamond*),  $n_c = 1.6814$ ;  
 $n_1 = 2.3990$  (*ZnSe*),  $n_c = 1.6963$ .

Once the refractive index of the substance to be measured is greater than the critical refractive index  $n_c$ , namely  $n_2 > n_c$ , it will no longer be internal reflection but refraction. And what is obtained is not the absorbance spectrum of the substance but the refraction spectrum.

If the substance to be measured is a mixture, especially in the case of inhomogeneous refractive index, once the refractive index of one or several of them is greater than the critical refractive index  $n_c$ , The mixed spectrum of absorption and refraction will be obtained. This is the reason for the distortion of the spectrogram, which is what we will focus on in the following papers.

## 1.6 Simulation of Distorted Spectrum

### 1. Obtaining $n(\nu)$ and $k(\nu)$ from absorption or reflection

In this section, we present the stepwise calculation procedure. For illustration purposes, we consider a mixture of carbon and toluene in order to show results based on real data.

First, the values for  $n(\nu)$  and  $k(\nu)$  need to be obtained from an absorption or reflection spectrum.

$$\hat{n}(\nu) = n(\nu) + ik(\nu) \quad (1.102)$$

The relationship between the  $n(\nu)$  and  $k(\nu)$  is KK relationship in chapter 2.3.

The  $k(\nu)$  value can be derived in a straightforward manner from<sup>12</sup>

$$A(\nu) = \frac{4\pi d\nu k(\nu)}{\ln 10} \quad (1.103)$$

$$k(\nu) = \frac{\ln 10 A(\nu)}{4\pi d\nu} \quad (1.104)$$

where  $d$  is the path length. The path length as such does not exist in ATR, but an effective path length can be determined from the penetration depth  $d_p$ . According to chapter 1.5

$$d_p = \frac{1}{2\pi\nu\sqrt{n_1^2\sin^2\theta_1 - n_2^2}} \quad (1.100)$$

This parameter can be converted to an effective path length  $d_{\text{eff}}$ , which is the path length that would lead to the same absorption in a transmission experiment. The latter assumes low absorption, the same assumption  $d_{\text{eff}}$  is derived from.  $d_{\text{eff}}$  depends on  $d_p$  and the polarization state of the light<sup>42, 43</sup>. In order to focus on the relevant math here, we simplify

$$d = 2d_p = \frac{1}{\pi\nu\sqrt{n_1^2\sin^2\theta_1 - n_2^2}} \quad (1.105)$$

and obtain

$$k(\nu) = \frac{\ln 10 A(\nu)}{4} \sqrt{n_1^2\sin^2\theta_1 - n(\nu)^2} \quad (1.106)$$

Furthermore,  $k(\nu)$  is connected with  $n(\nu)$  through the Kramers-Kronig relationship. Here, the method to calculate  $n(\nu)$  and  $k(\nu)$  from  $A(\nu)$  is according to Bertie and Satoru Nakashima<sup>44-46</sup>. It includes the following steps;

Step 1:  $n_\infty$  is calculated. (The refractive indices of toluene,  $n_{\text{To}}$ , and carbon,  $n_{\text{C}}$ , were taken from Myer et al.<sup>47</sup> and Sorensen et al.<sup>48</sup>, respectively). The calculation of  $n_\infty$  uses a modified Sellmeier equation:

$$n(\nu) = \sqrt{a + \frac{b}{\lambda^2 - c}} \quad (1.107)$$

where a, b, and c are constant numbers that are derived from fitting the equation to experimental data. It derives under the assumption of zero damping, i.e. without absorption. At this point,  $n(\nu)$  is only used to calculate  $n_\infty$ . It must not be confused with the final calculation of the  $n(\nu)$  spectrum. The resulting best-fit equation was used to find the refractive index at the highest energy data point in the experimental spectra. For our model system toluene/carbon, we obtain  $n_{\text{To}\infty} = n_{\text{To}(4000 \text{ cm}^{-1})} = 1.4707$  and  $n_{\text{C}\infty} = n_{\text{C}(4000 \text{ cm}^{-1})} = 1.79$ .

Step 2: replace  $n$  by  $n_{\text{To}\infty}$  to calculate  $k(\nu)$  by Eqn.1.106. If the refractive index  $n_\infty$  is too high (i.e. the square root in Eqn.1.106 becomes negative), then use Eqn. 1.108 instead of Eqn. 1.106 to have a starting value for the iteration process:

$$k_{j+1}(\nu) = k_j(\nu)(1 + \sqrt{k_j(\nu)}) \quad (1.108)$$

in which  $k_{j+1}(\nu)$  is the renew value from the old value  $k_j(\nu)$ .

Step 3: the obtained  $k(\nu)$  is used to calculate  $n(\nu)$  by the Hilbert transform;

Step 4: get the complex refractive index  $\hat{n}(\nu)$ .

Step 5: treat  $\hat{n}(\nu)$  as  $n_2$  and apply Fresnel's equations to get  $A(\nu)_{\text{cal}}$ .

Step 6: calculate the new  $k_{j+1}(\nu)$  by Eqn. 109

$$k_{j+1}(\nu) = k_j(\nu) \frac{A(\nu)}{A(\nu)_{\text{cal}}} \quad (1.109)$$

Repeat steps 3-5 until

$$\sum (A(\nu) - A(\nu)_{\text{cal}})^2 < 10^{-4} \quad (1.110)$$

Then stop calculation and get  $n(\nu)$  and  $k(\nu)$ .

In the low-wavenumber range, there may exist non-convergence using the above approach. This is attributed to strong absorption features and the real part of the refractive index  $n(\nu)$  changing significantly. In this case,  $k(\nu)$  from Myer et al.<sup>47</sup> is applied as Eqn. 1.104 is directly used for the calculation, and the fitting method is changed from Eqs. 1.109 to 1.111, which we found empirically:

$$k_{j+1}(\nu) = k_j(\nu) + \frac{A(\nu)}{500A(\nu)_{cal}} \quad (1.111)$$

Finally, the two pieces of data are spliced to get the complete data set. The measured  $n(\nu)$  and  $k(\nu)$  composite refractive index is not used as the experimentally measured  $n_{T_{0\infty}} = n_{T_{0(8000\text{ cm}^{-1})}} = 1.4749$  is far outside the experimental interval studied in this chapter.

Please refer to Fig. 1.8 for a basic flowchart.

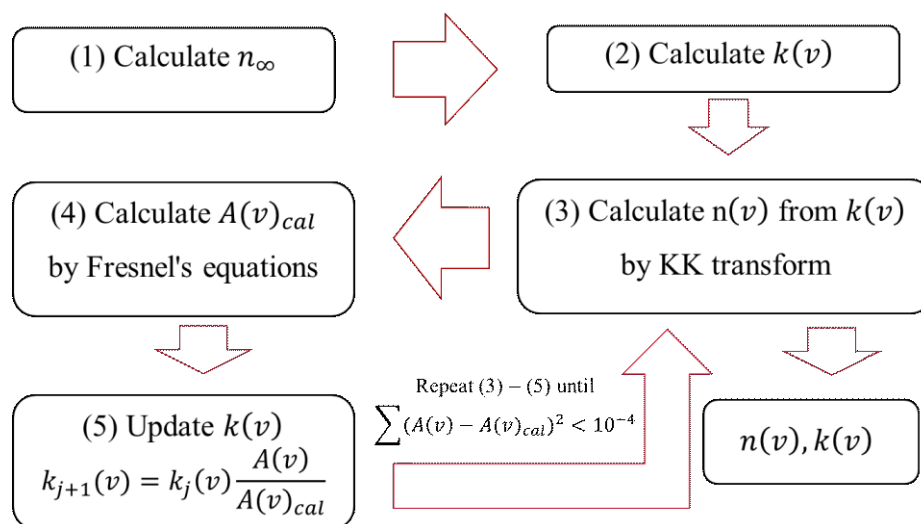


**Fig. 1.8** Flowchart for calculating the complex refractive index of  $n(\nu)$  and  $k(\nu)$  from the  $A(\nu)$  spectrum. Note that  $\hat{n}(\nu) = n(\nu) + ik(\nu)$ .

As the refractive index of carbon is larger than the critical refractive index, the corresponding complex refractive index cannot be calculated in this way. Therefore,  $A(\nu)$  is used to replace  $k(\nu)$  in order to calculate  $n(\nu)$ . We need to keep in mind that this contributes to the experimental error in the present work. Moreover, the complex refractive index is not calculated by ellipsometric or Surface Reflective Infrared (SRIR) measurements because these instruments cannot provide the same pressure as diamond ATR, which has a great influence on the experimental spectrum.

Fig.1.9 shows the  $n(\nu)$  and  $k(\nu)$  values of toluene calculated from  $A$  and  $n_\infty$ . The observed peak of absorbance is significantly red-shifted compared to  $k(\nu)$ , see Fig. 1.9B. The  $k(\nu)$  peak is consistent with the peak position in the transmission infrared spectrum. Although  $k(\nu)$  and the absorbance spectrum are similar, the positions of their peaks are not the same, so that the absorbance spectrum cannot be used directly. Generally, it must be noted that the measured peak positions in ATR-FTIR, Transmission-IR and reflection-IR spectra differ and that even for Ge as ATR crystal corrections are needed, although the deviations between  $k(\nu)$  and the absorbance spectrum are smaller in this case.

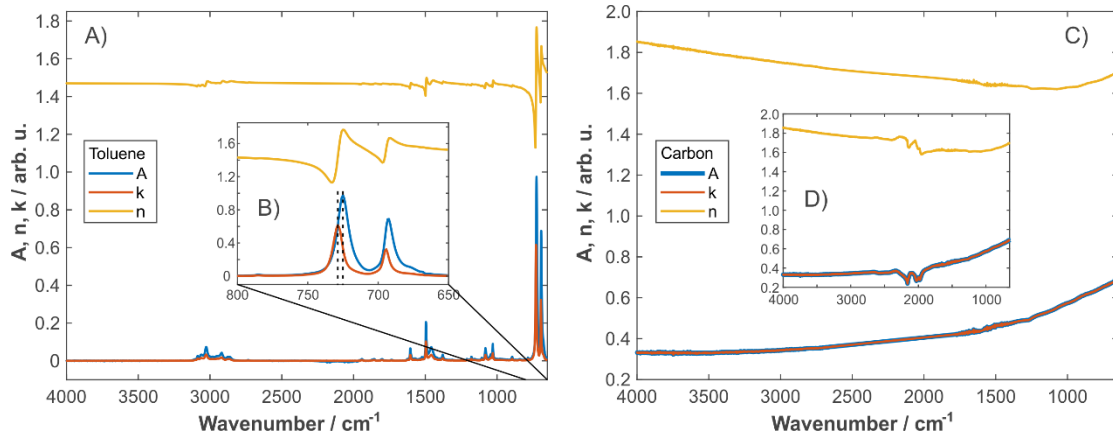


**Fig.1.9** Spectra of pure toluene and carbon. A) Overview  $A(\nu)$ ,  $n(\nu)$ ,  $k(\nu)$  of toluene; B) Zoomed in low wavenumber region of toluene spectra; C) Overview  $A(\nu)$ ,  $n(\nu)$ ,  $k(\nu)$  of carbon with diamond absorption removed; D)  $A(\nu)$ ,  $n(\nu)$ ,  $k(\nu)$  of carbon with diamond absorption displayed. The dashed lines in B) indicate the apparent peak shift between the measured absorbance spectrum and the derived  $k(\nu)$ .

The signatures around  $1800\text{-}2200\text{ cm}^{-1}$  in Fig. 1.9D are caused by 2-phonon absorptions of the IRE material diamond<sup>49, 50</sup>. This absorption feature is of great significance for determining whether the distortion of the spectrum is caused from optical reasons, that is, the non-attenuated total reflection caused by the excessive refractive index of the sample. Strictly, the refractive index of diamond should be treated as a complex number, but then we would have to switch to a more complex optical model that treats the ATR crystal as an incoherent layer. However, since most samples have no absorption in this wavenumber region and diamond does not exhibit

absorption signatures elsewhere in the considered spectral range, we treat diamond as a non-absorbing medium here. This assumption helps to keep the complexity of the calculation relatively small. When simulating or correcting the spectrum, this part can be directly replaced with a straight line or corresponding curve to reduce the simulation error.

## 2. Solid/liquid mixture infrared absorption spectrum model

The  $n(\nu)$  and  $k(\nu)$  data obtained by the above method are mixed to model and calculate the absorption spectrum in different ways. Medium 2 represents the mixed substances.

$$n_1 = 2.3778 \quad (1.112)$$

$$\hat{n}_{21}(\nu) = n_{21}(\nu) + ik_{21}(\nu) \quad (1.113)$$

$$\hat{n}_{22}(\nu) = n_{22}(\nu) + ik_{22}(\nu) \quad (1.114)$$

$\hat{n}_{21}(\nu)$  is the complex refractive index of the liquid, like toluene in our experiment,  $n_{21}(\nu)$  and  $k_{21}(\nu)$  are real and imaginary parts of  $\hat{n}_{21}(\nu)$ .  $\hat{n}_{22}(\nu)$  is the complex refractive index of the solid, with non-characteristic absorption but high refractive index, like it is the case for carbon black in the experiment. The refractive index of the mixture is then given by:

$$\hat{n}_2(\nu) = \hat{n}_{21}(\nu) + x\hat{n}_{22}(\nu) \quad (x = x_1, x_2) \quad (1.115)$$

For completeness, the following intuitive equation in liquid mixing is invalid in this situation:

$$\hat{n}_2(\nu) = (1 - x)\hat{n}_{21}(\nu) + x\hat{n}_{22}(\nu) \quad (1.116)$$

Liquid mixing does not necessarily follow the same trends as solid-liquid mixing. Eqn. 1.115, developed to describe the characteristics of solid-liquid mixtures, might not be applicable to liquid-only mixtures. Solid-liquid mixing often involves complex interactions due to the disparate physical states and properties of the components, such as differences in refractive index, light scattering, and absorption behavior. These factors contribute to spectral distortions unique to solid-liquid mixtures. If  $x$  would be the mole or volume fraction Eqn.116 should be (approximately) valid, but since eqn. Eqn. 1.115 much better describes the experimental findings,  $x$  cannot be identified with

one or the other. Since carbon black is insoluble in water and other solvents, this may be the reason that Eqn.115 is favorable over Eqn.116.

In the model, the complex refractive index is comprised of

$$n_2(\nu) = \text{real}(\hat{n}_2(\nu)) = n_{21}(\nu) + x_1 n_{22}(\nu) \quad (1.117)$$

$$k_2(\nu) = \text{imag}(\hat{n}_2(\nu)) = k_{21}(\nu) + x_2 k_{22}(\nu) \quad (1.118)$$

We substitute these equations into Fresnel's equations to yield the corresponding absorbance  $A$ , which can then be used to calculate the final simulated absorbance  $Ab$  (formally both  $Ab$  and  $A$  refer to absorbance, but  $Ab$  is simply used to distinguish the two in different situations):

$$Ab = A + yA_{22} + a \quad (0 \leq y) \quad (1.119)$$

where  $A_{22}$  corresponds to the absorbance of carbon black in the experiment. The obtained  $Ab$  spectrum is shown in Fig. 1.10.

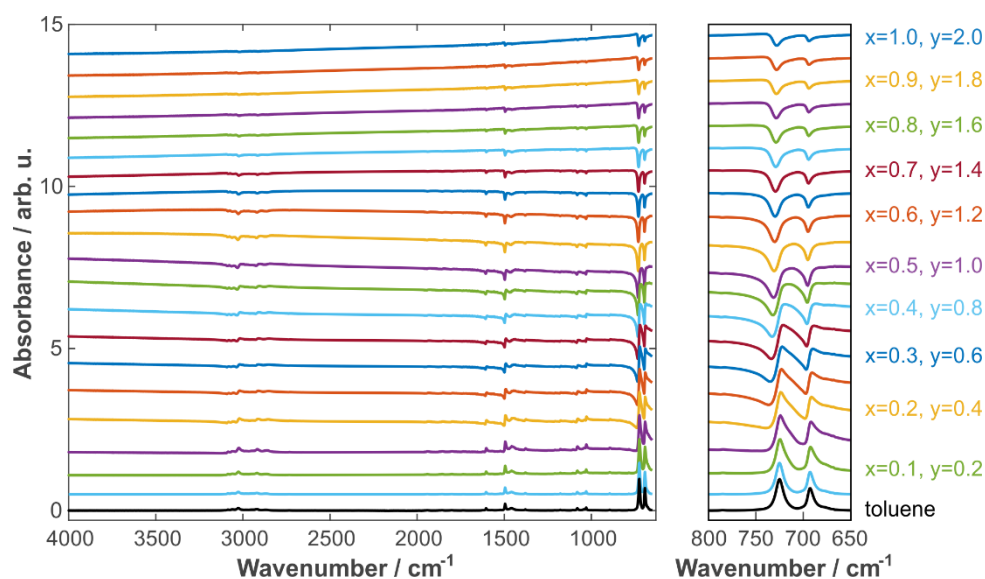


**Fig. 1.10** Simulated Absorbance spectrum with varying  $x$  and  $y$  using eqn.1.115 in combination with Fresnel's equations. The initial toluene spectrum is displayed at the bottom. The parameters  $x$  and  $y$  are increased in steps of 0.05 and 0.1, respectively. The left panel shows the overall spectrum and the right panel shows the enlarged region  $650\text{-}800\text{ cm}^{-1}$ . Spectra are displayed with offset for clarity.

Fig. 1.10 shows that with increasing  $x$ , that is, when the refractive index of the mixture sample gradually rises, the summit first redshifts and a concave part appears

on the left side of the peak (the concave part is difficult to observe in the beginning, so many researchers treat the spectrum as “normal” and regard the red-shifted peak as the result of intermolecular interactions). This is caused by the superposition of  $n(\nu)$  of the complex refractive index. Then the concave part becomes more and more obvious, and the normal peak becomes weaker, until central symmetry is maintained. The same effect can be observed when the incident angle of the radiation is changed: when the incident angle changes from large to small approaching the critical angle, the red-shift can be seen and the left side of the peak begins to appear concave. This was demonstrated by Amma et al.<sup>51</sup> However, for a given absorption transparent medium, the peak shape with one side recessed and the other protruding will continue to be maintained with decreasing incidence angle, just the degree of inclination will change.

Please note that in mixtures with a high refractive index and non-selective absorption, it is different from the selective absorption peak of a transparent medium. After the central symmetry, the peak of the recessed part will be more obvious. The peak from here began to change from center symmetry to the negative peak. Until the original positive peak completely disappeared, the negative peak appeared. The entire absorption spectrum will be overall inverted and show a blue shift. This phenomenon can be verified from the mixed graph of pure carbon black and toluene shown in Fig. 1.11. With increasing  $y$ , the baseline starts to tilt. In the low wavenumber regime, the baseline starts to rise, which is caused by the absorbance of carbon black, see Fig. 1.10 and Fig. 1.12. However, when it reaches a certain level, the low wavenumber baseline starts to drop again while the high wavenumber baseline slowly rises until it finally becomes the inverted, blue-shifted peak of the original liquid absorption peak. Of course, the increase of  $x_1$ ,  $x_2$  and  $y$  are almost synchronized, which shows that  $x_1$ ,  $x_2$  and  $y$  are not independent variables.

To summarize the above, when the light is refracted by the optically dense medium into the optically thin medium, the distortion of the spectrum caused by the real part  $n(\nu)$  of the complex refractive index might already occur before the calculated critical angle is reached. In turn, this means that when the refractive index of the sample is less



than the critical refractive index, the spectrum is already affected, that is, the peaks are red-shifted, and correction is needed to get the accurate peak position. Note that what we call redshift here should precisely be called a pseudo redshift, which is caused by the light itself, not due to the intermolecular interaction or other physicochemical phenomena in the sample. In many cases, this observed red-shift is an actual blue shift in the unaffected/corrected spectrum. Therefore, the effect under study can lead to severe misinterpretations of datasets.

When the mixture contains a substance with non-selective absorption and the refractive index of the sample is high enough, the infrared peaks of the sample can be observed anything from a positive to negative appearance and from red- to blue-shifted. This is particularly the case when the mixture contains carbonaceous substances such as carbon black, graphite, or graphene. These substances do not provide distinct absorption peaks in the infrared, so such peaks can be observed only when other organic substances are admixed. Unfortunately, carbon itself can cause the distortion of the baseline, the baseline will rise sharply at low wavenumbers, and because of its high reflectivity, the normal infrared spectrum is almost invisible when the content is higher than 20%. This is even true for Ge-ATR, i.e., under the condition that the refractive index is smaller than the critical refractive index of Ge.

### 3. Comparison of theory and experiment

In order to qualitatively test and validate the theoretical model and results presented above, a series of experiments with mixtures of carbon black and toluene were carried out. The exact composition at the IRE-sample interface is difficult to determine, but the experimental procedures were such that a clear variation of the carbon content at the IRE interface could be achieved, which is sufficient for our comparison. Fig. 1.11 shows the spectra obtained when different proportions of carbon black and toluene. The development of the experimental spectra with increasing carbon content agrees well with the theoretical trends revealed in Fig. 1.10. This demonstrates that the model includes all relevant effects.

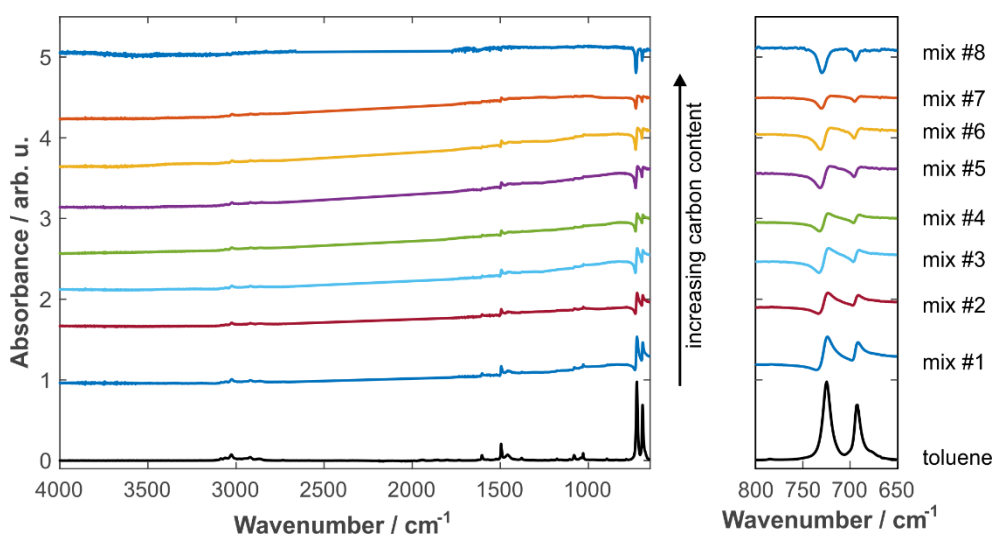


**Fig.1.11** Experimental Spectra of different mixtures containing carbon black and toluene. The spectrum of pure toluene is displayed at the bottom. The left panel shows the overall spectra and the right panel displays the enlarged region 650-800  $\text{cm}^{-1}$ . Spectra are displayed with offset for clarity.

The calculation and fitting method of the spectrum is a nonlinear fit to determine the parameters  $x_1$ ,  $x_2$ ,  $y$ , and  $a$ . The data of the mix #3 sample (see Fig. 1.11) are shown in Fig. 1.12 with the removed diamond absorption peaks between 1775-2661  $\text{cm}^{-1}$ .

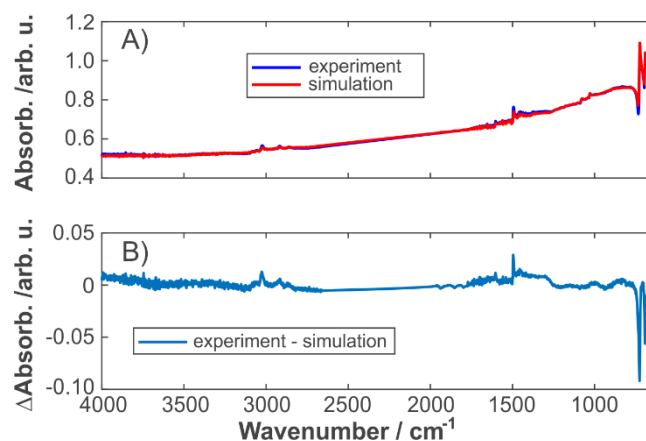


**Fig.1.12** A) Experimental and simulated spectra of the sample mix #3 and B) their difference spectrum.

The difference spectrum in Fig.4B shows small deviations from zero, which may be caused by the following: 1)  $A(\nu)$  was used instead of  $k(\nu)$  for calculating the complex refractive index of the carbon black; 2) Only the influence of the compound refractive index of the mixture was taken into consideration as the reason for the distortion. In fact, there are many factors that could influence the result including the solid carbon content, the solid-liquid ratio, the type of liquid, the shape and size of the solid, the solid-liquid molecular interactions, a numerical error, etc. As the spectrum simulated using to the above model shows a good agreement with the experiment and is capable of predicting the overall trends, we are confident that all relevant phenomena are included.

#### 4. Conclusions

The present work aims at better understanding the ATR spectra of complex mixtures, i.e. mixtures of organic or inorganic liquids with solids exhibiting a high refractive index. The ATR spectra of such mixtures are subject to severe distortions that can lead to misinterpretation of the data. We explored the reasons for the change of the spectrum near the critical angle and theoretically simulated the shape change and displacement of absorption peaks. The theoretical results were confirmed in experiments using toluene and carbon black as a model system. Moreover, the mixing law of  $n(\nu)$  of the complex refractive index and its impact on the resulting spectrum was studied. The proposed model allows the correction of distorted spectra and

therefore aids the correct interpretation of experimental results. The model and correction method, however, is not limited to the infrared spectral range. So, the method can be applied across in the entire spectrum. The development of further specific simulation procedures, elaboration on the curve correction, and the analysis of spectral calibration is the subject of ongoing work.

# 2. Introduction to Various Transforms

## 2.1 Phase-Sensitive Detection (PSD)

### 1. The trigonometric Fourier series<sup>52-55</sup>

A signal  $f(t)$  with a period of  $T$  can be expressed as a Fourier series expansion in the form of a trigonometric function in each period<sup>52, 53</sup>,

$$f(t) = a_0 + \sum_{k=1}^{\infty} (a_k \cos k\omega t + b_k \sin k\omega t) \quad (2.1)$$

Which means that any periodic signal can be composed of a constant term  $a_0$ , usually called a direct current(dc) component<sup>52</sup>, and the superposition of multiple trigonometric functions with different frequencies.

Where,

$$\omega = \frac{2\pi}{T} = 2\pi f \quad (2.2)$$

And  $k$  is frequency multiplier ( $k = 1, 2, 3 \dots$ );  $a_0, a_k, b_k$  are Fourier coefficients.

Especially,  $a_0$  can be treated as the result of  $k = 0$ ,<sup>52</sup>

$$a_0 = \frac{1}{T} \int_0^T f(t) dt \quad (2.3)$$

$$a_k = \frac{2}{T} \int_0^T f(t) \cos(k\omega t) dt \quad (2.4)$$

$$b_k = \frac{2}{T} \int_0^T f(t) \sin(k\omega t) dt \quad (2.5)$$

In addition,  $a_k$  and  $b_k$  can be expressed in polar coordinates as following,

$$a_k = c_k \sin\varphi_k \quad (2.6)$$

$$b_k = c_k \cos\varphi_k \quad (2.7)$$

Eqn. 2.1 can be expressed as

$$f(t) = a_0 + \sum_{k=1}^{\infty} (c_k \sin\varphi_k \cos k\omega t + c_k \cos\varphi_k \sin k\omega t) \quad (2.8)$$

Where  $c_k$  is the amplitude and  $\varphi_k$  is phase angle.<sup>52</sup>

$$c_k = \sqrt{a_k^2 + b_k^2} \quad (2.9)$$

Eqs. 2.1-2.9 are from “Quantitative modulated excitation Fourier transform infrared

spectroscopy<sup>52</sup> by Dieter Baurecht.

$$\varphi_k = \arctan \left( -\frac{b_k}{a_k} \right) \quad (2.10)$$

Combine sum-to-product formula

$$\sin(a + b) = \sin a \cos b + \cos a \sin b \quad (2.11)$$

Eqn. 2.8 can be further expressed on the basis of Eqn. 2.11 as

$$f(t) = a_0 + \sum_{k=1}^{\infty} c_k \sin(k\omega t + \varphi_k) \quad (2.12)$$

At this point, we can explain more specifically that any periodic signal that satisfies the Dirichlet condition can be decomposed into the sum of the dc component, the fundamental component and an infinite number of harmonic components<sup>53, 54, 56</sup>.

In which,  $a_0$  is the dc component,  $k = 1$  is the fundamental component,  $k > 1$  are higher harmonic components.  $\varphi_k$  can be treated as phase delay.

## 2. The complex exponential Fourier series<sup>56, 57</sup>

A signal  $f(t)$  with period  $T$  can also be expressed as the following Fourier series expansion in complex exponential form in each period<sup>57</sup>,

$$f(t) = \sum_{k=-\infty}^{\infty} d_k e^{ik\omega t} \quad (2.13)$$

$d_k$  are Fourier coefficients.

$$d_k = \frac{1}{T} \int_T f(t) e^{-ik\omega t} dt \quad (2.14)$$

And The relationship between the exponential form and the Fourier coefficient of the trigonometric function is as following.

$$d_k = \frac{c_k e^{i\varphi_k}}{2} \quad (2.15)$$

Corresponding calculation processing as following,

According to Euler's formula, as Fig.2.1

$$e^{ix} = \cos x + i \sin x \quad (2.16)$$

$$e^{-ix} = \cos x - i \sin x \quad (2.17)$$

$$\sin x = \frac{e^{ix} - e^{-ix}}{2i} \quad (2.18)$$

$$\cos x = \frac{e^{ix} + e^{-ix}}{2} \quad (2.19)$$

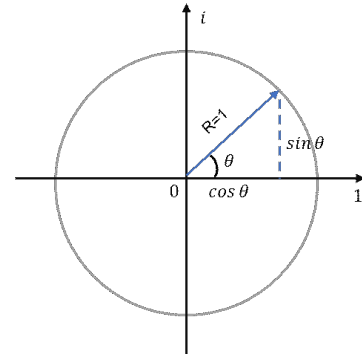


**Fig. 2.1** Euler's formula<sup>58</sup>

Eqn. 2.13 can be expressed as

$$\begin{aligned}
 f(t) &= a_0 + \sum_{k=1}^{\infty} \left( a_k \frac{e^{ik\omega t} + e^{-ik\omega t}}{2} + b_k \frac{e^{ik\omega t} - e^{-ik\omega t}}{2i} \right) \\
 &= a_0 + \sum_{k=1}^{\infty} \left( \frac{a_k - ib_k}{2} \right) e^{ik\omega t} + \sum_{k=1}^{\infty} \left( \frac{a_k + ib_k}{2} \right) e^{-ik\omega t} \quad (2.20)
 \end{aligned}$$

Set

$$d_k = \frac{a_k + ib_k}{2} \quad (2.21)$$

$$d'_k = \frac{a_k - ib_k}{2} \quad (2.22)$$

Then

$$f(t) = a_0 + \sum_{k=1}^{\infty} d'_k e^{ik\omega t} + \sum_{k=1}^{\infty} d_k e^{-ik\omega t} \quad (2.23)$$

We can introduce  $n = -k = -1, -2, \dots$

$$\begin{aligned}
 f(t) &= a_0 + \sum_{n=-1}^{-\infty} d'_{-n} e^{-in\omega t} + \sum_{k=1}^{\infty} d_k e^{-ik\omega t} \\
 &= a_0 + \sum_{k=-1}^{-\infty} d'_{-k} e^{-ik\omega t} + \sum_{k=1}^{\infty} d_k e^{-ik\omega t} \quad (2.24)
 \end{aligned}$$

Set

$$d'_{-k} = d_k, \quad k = -1, -2, \dots$$

$$f(t) = \sum_{k=-\infty}^{\infty} d_k e^{ik\omega t} \quad (2.25)$$

Where

$$d_0 = \frac{a_0}{2}, \quad k = 0$$

$$d_k = \frac{a_k + ib_k}{2}, \quad k = 1, 2, \dots \quad (2.26)$$

$$d_k = \frac{a_{-k} + ib_{-k}}{2}, \quad k = -1, -2, \dots \quad (2.27)$$

$$a_k = \frac{2}{T} \int_T f(t) \cos(k\omega t) dt \quad (2.28)$$

$$b_k = \frac{2}{T} \int_T f(t) \sin(k\omega t) dt \quad (2.29)$$

$$e^{ix} = \cos x + i \sin x \quad (2.30)$$

$$\begin{aligned} d_k &= \frac{1}{T} \int_T f(t) [\cos(k\omega t) + i \sin(k\omega t)] dt, \quad k = 1, 2, \dots \\ &= \frac{1}{T} \int_T f(t) e^{ik\omega t} dt, \quad k = 1, 2, \dots \end{aligned} \quad (2.31)$$

As well

$$d_k = \frac{1}{T} \int_T f(t) e^{ik\omega t} dt, \quad k = -1, -2, \dots \quad (2.32)$$

So

$$d_k = \frac{1}{T} \int_T f(t) e^{ik\omega t} dt \quad (2.33)$$

It should be pointed out that the complex exponential Fourier coefficients are usually not used in modulated excitation spectroscopy (MES)<sup>59</sup> or PSD<sup>52, 60</sup> described later. Because Fourier coefficients in their complex exponential form contain both real and imaginary components of the spectrum, which are intrinsically linked through KK relationship<sup>61-63</sup>. This relationship connects the real part, which reflects refraction, and the imaginary part, associated with absorption in a material's spectrum. In ATR-FTIR spectroscopy<sup>64</sup>, spectral distortion caused by refraction is viewed as undesirable, creating a need to correct or manage this distortion.

By performing a Fourier transform using complex exponential coefficients, both the real and imaginary parts, representing the inherent refractive and absorptive characteristics of the spectrum are captured. When using complex exponential Fourier coefficients for correcting or simulating distorted spectra, phase modulation across a broader range—typically from  $0 - 2\pi$  is often required. This approach allows it to be used to simulate or correct the distortions caused by refraction, often necessary in ATR-FTIR due to its reliance on internal reflection.

However, complex exponential coefficients are typically unnecessary for PSD. In PSD, due to symmetry, it is usually only necessary to modulate the phase within a narrow range (usually  $0 - \pi$ ) and use this phase information to extract the desired signal or reduce noise.



### 3. Fourier Trigonometric Function Expansion of Absorbance<sup>52</sup>

We have introduced the calculation formula for the absorption spectrum of a single substance in the chapter on Maxwell's Equations. In fact, the absorbance is a frequency-dependent coefficient, so it is often written as  $A(\nu)$ . When there are  $N$  substances in the component, the absorption spectrum of each substance can be represented by  $A_i(\omega), i = 1, 2 \dots N$ . But for simplicity, the following are omitted as  $A(\omega)$ .

Since the absorbance in the frequency domain is a state that corresponds to a specific phase angle, we usually use a  $90^\circ$  difference between the two states with the largest and smallest amplitudes of the examined absorbance. When we have different transients in the observed process, they will have maxima at different phases, one of the most important features of PSD to find them in a large background absorption. (Unlike what we will introduce in the later article on distorted spectra, we do not consider here the situation of distorted spectra due to the KK relationship. In other words, we only consider the imaginary part of the spectrum, which is the positive peak, and do not consider the real part, which is the distortion peak). If the real part is considered, and combined with the relevant knowledge of KK relationship, it can be seen that the two signals satisfying the KK relationship are orthogonal, that is, the phase angle is turned by  $90^\circ$ . Then, for the spectrum of substances, we only take the situation in ATR as an example to introduce the situation of the absorption spectrum. (Of course, this is completely applicable to other types of spectra or signals, but the calculation method may be slightly different).

If the absorption spectrum of a pure substance that satisfies the total reflection condition is the maximum value, it is the case where the phase delay is  $0^\circ$ , that is  $A^0(\omega)$ . Then, there is the corresponding case with  $90^\circ$  phase delay,  $A^{90^\circ}(\omega)$  satisfying the orthogonal relationship, namely KK relationship. Similarly, for the absorption spectrum  $A_k^0(\omega)$  of one of the components, there is also a component  $A_k^{90^\circ}(\omega)$  corresponding to the orthogonal relationship.

When we denote the total absorption spectrum recorded within a period  $T$  as  $A(\nu, t)$ . Then, like the above expansion for the signal, we can also express the absorption spectrum as the Fourier trigonometric function expansion, as<sup>52</sup>

$$A(\omega, t) = A_0(\omega) + \sum_{k=1}^{\infty} (A_k^{90^\circ}(\omega) \cos k\omega t + A_k^0(\omega) \sin k\omega t)$$

$$= A_0(\omega) + \sum_{k=1}^{\infty} A_k(\omega) \sin[k\omega t + \varphi_k(\omega)] \quad (2.35)$$

In which

$$A_0(\omega) = \frac{1}{T} \int_0^T A(\omega, t) dt \quad (2.36)$$

$$A_k^{90^\circ}(\omega) = A_k(\omega) \sin \varphi_k = \frac{2}{T} \int_0^T A(\omega, t) \cos(k\omega t) dt \quad (2.37)$$

$$A_k^{0^\circ}(\omega) = A_k(\omega) \cos \varphi_k = \frac{2}{T} \int_0^T A(\omega, t) \sin(k\omega t) dt \quad (2.38)$$

$A_k(\omega)$  is the amplitude, i.e. the signal maximum, is here the case of maximum absorbance.  $\varphi_k(\omega)$  is phase delay which relative with frequency here<sup>52</sup>.

## 4. Modulation Excitation Spectroscopy (MES)

Modulation Excitation (ME) refers to the introduction of a periodic change in the system, such as concentration, temperature, pressure or PH, etc. Modulation Excitation and phase-sensitive detection are usually used together in Modulation Excitation Spectroscopy (MES)<sup>65-67</sup>. That is, the corresponding spectrum is obtained on the basis of periodically changing a reaction condition, and then demodulated by PSD. The purpose is to filter out unnecessary background noise and absorption changes that does not result from the excitation of the sample<sup>65</sup>. Moreover, constant parts of absorption (dc) are also suppressed. By using ME-PSD, only the response signals consistent with the periodic variables are retained. This has gained wide application in heterogeneous catalysis. Next, let's take the catalyst on the surface of ATR-FTIR as an example where the concentration of the sample over the catalyst changes periodically. Continuously record the changes of the spectrum to obtain a time series of spectra. The recorded time series of spectra can then be demodulated by PSD to obtain phase resolved spectra. The corresponding schematic is shown below.

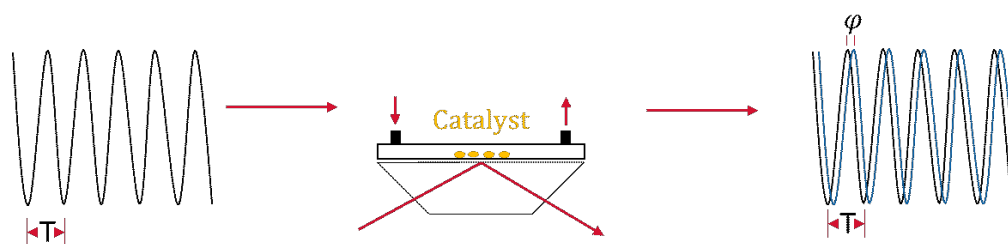


**Fig. 2.2** Principle of MES in ATR-FTIR.

Of course, the periodic modulation waveform can be various, such as Sine, Cosine, Square, Triangular and so on. However, in the process of concentration adjustment, it is more common to use a square wave, because it is easier to control during the experiment by only controlling the two states of one of the substances, namely adding or not adding, that is, 1 and 0. There are also many kinds of instruments used for detection, such as ATR-FTIR<sup>68-72</sup>, diffuse reflectance Fourier transform spectroscopy(DRIFTS)<sup>73-75</sup>, Raman, X-ray diffraction (XRD)<sup>76</sup>, X-ray absorption spectroscopy (XAS)<sup>77</sup>, etc.

## 5. Phase-Sensitive Detection (PSD)

The PSD<sup>78</sup> in ME is different from the usual signal detection (usually in lock-in amplification)<sup>65</sup>. We will introduce the PSD in ME first, and introduce the PSD in lock-

in amplification later.

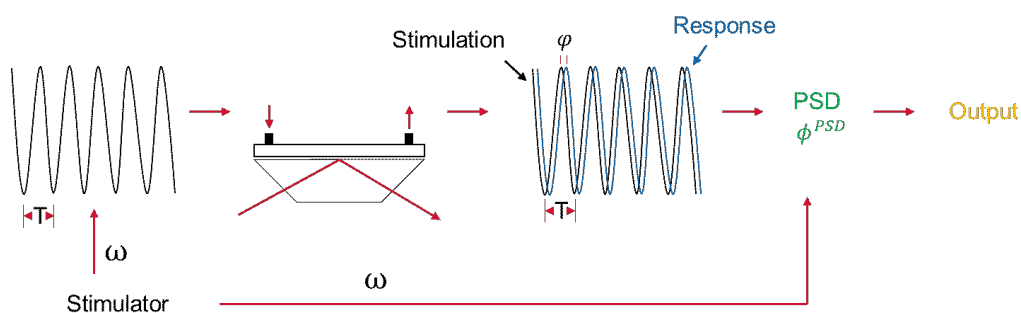


**Figure. 2.3** ME with PSD.

As we have introduced the situation of ME before, now PSD is used to demodulate the spectrum acquired in ME. The specific process is shown in Fig. 2.3.

That is, use a periodically changing external stimulus to record the time-varying spectrum on the instrument, and then use the same simulation parameters as the stimulation period  $T$  (or frequency  $\omega$ ) to multiply the measured time-domain spectrum to obtain the corresponding frequency-domain Spectrum, and finally, the so-called phase domain spectra are obtained by changing the phase angle from  $0 - 180^\circ$  (ie  $0 - \pi$ ). Finally, those spectra only contain absorbances that change periodically with the stimulus.

The relevant calculation formula is shown in Eqn. 2.39<sup>52</sup>

$$A_k^{\phi_k^{PSD}}(\nu) = \frac{2}{T} \int_0^T A(\nu, t) \sin(k\omega t + \phi_k^{PSD}) dt; \quad k = 1, 2, 3 \dots \quad (2.39)$$

In which,  $A_k^{\phi_k^{PSD}}(\nu)$  is the phase -resolved modulation spectrum, usually with  $k = 1$  corresponding to the fundamental state.  $\phi_k^{PSD}$  is artificially phase angle setting<sup>52</sup>.

In fact, the process of multiplying the time-varying spectrum with an analog function is more similar to the time-domain multiplication and frequency-domain convolution in the Fourier transform that we will introduce later. From frequency domain spectroscopy to phase domain spectroscopy (that is, the process of changing the phase angle from  $0-180^\circ$ ) actually involves two processes of inverse fast Fourier transform

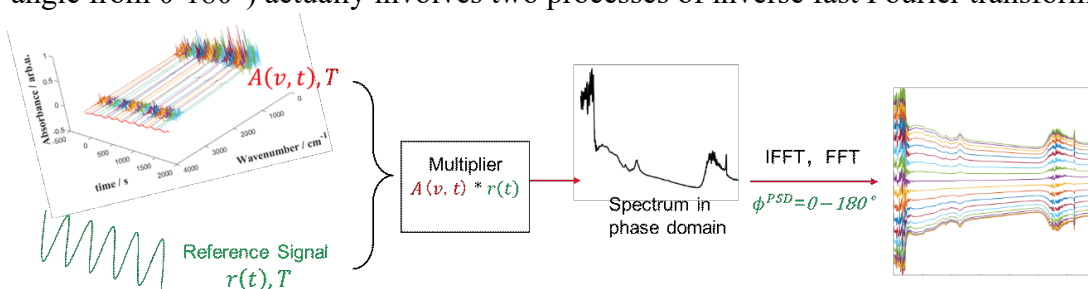


**Fig.2.4** Processing of PSD.

and fast Fourier transform (FFT)<sup>79</sup>. As shown in Fig. 2.4.

But it should be pointed out that the so-called inverse Fourier transform and Fourier transform here only use the imaginary part, while the real part is ignored (that is, only  $\sin x$  is used instead of  $e^{ix}$ ). So, the so-called Fourier transform and inverse Fourier transform here are not real full versions of Fourier transform and inverse Fourier transform. The difference between using only the imaginary part of  $\sin x$  and using  $e^{ix}$  to change the phase angle is shown in Fig. 2.5. The corresponding equation is shown as Eqn. 2.40.

$$A_k^{\phi_k^{PSD}}(v) = \frac{2}{T} \int_0^T A(v, t) e^{i(k\omega t + \phi_k^{PSD})} dt; \quad k = 1, 2, 3 \dots \quad (2.40)$$

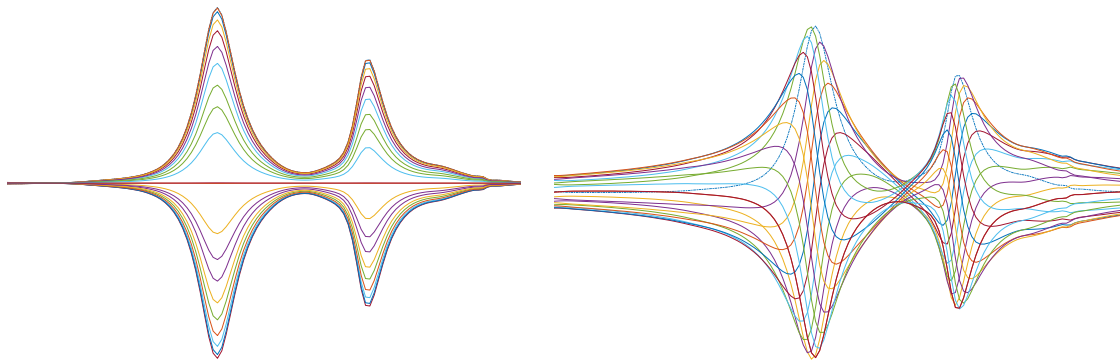


**Fig. 2.5** Phase demodulation with  $\sin x$  and  $e^{ix}$ .

It is very obvious that there is no "twisted peak" when the phase angle difference is  $90^\circ$  due to the absence of orthogonal real parts (we will explain in detail later in the KK transformation). Compared to using the full version of the complex exponential  $e^{ix}$  form, the trigonometric function formula only needs to change half of the phase angle, that is, from  $0 - \pi$ , to obtain the desired result.

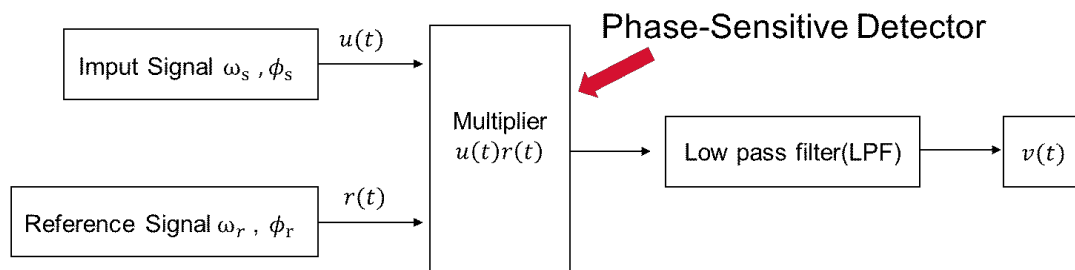


**Fig. 2.6** Principal diagram of PSD / digital lock-in amplifier.

Next, we will introduce the PSD in signal detection and the difference with the PSD in ME. Fig. 2.6 is a simple lock-in amplifier<sup>80, 81</sup> that includes a PSD. Usually, the signal to be tested and the reference signal are input into the phase-sensitive detector

and multiplied therein, and the corresponding noise-filtered signal is obtained through a low-pass filter (LPF). There is a process of multiplying the reference signal in both PSD processes, the difference is that there is no low-pass filtering process in the MES process. When using a lock-in amplifier for demodulation in modulation excitation (ME) experiments, the order of the signal to be detected (usually the fundamental tone,  $k = 1$ ) is set before the measurement<sup>52</sup>. The output consists normally of two signals, one representing  $\phi = 0^\circ$  (in-phase) and the other  $\phi = 90^\circ$  (quadrature), which can be used to calculate other phase lags later. However, this approach has a significant limitation. By focusing only on the fundamental frequency, you lose higher-order responses. These higher-order responses occur when<sup>52, 82</sup>:

- The excitation is not purely sinusoidal, causing harmonics.
- The system response is non-linear, leading to complex behaviors.

Therefore, critical information about nonlinear effects or other dynamic properties of the system may be ignored. To address this limitation, multi-harmonic lock-in amplifiers or Fourier-based methods can be explored to capture a wider range of signal frequencies<sup>52</sup>.

## 2.2 Fourier Transform (FT)

Fourier transform (FT)<sup>38, 83, 84</sup> is a method that can convert time-domain signals and frequency-domain signals into each other. Eqs. 2.41 and 2.42 shows the continuous Fourier transform<sup>75</sup>

$$F(f) = \int_{-\infty}^{\infty} f(t)e^{-i2\pi ft} dt \quad (2.41)$$

$$f(t) = \int_{-\infty}^{\infty} F(f)e^{i2\pi ft} df \quad (2.42)$$

The above formula can be abbreviated as  $f(t) \leftrightarrow F(f)$ , or  $f(t) \Leftrightarrow F(f)$ . Sometimes we also express  $F$  as the Fourier transform of  $f$ , and  $F^{-1}$  as the inverse Fourier transform of  $f$ .

The Fourier transform can also be expressed in the form of angular frequency

$$F(\omega) = \int_{-\infty}^{\infty} f(t)e^{-i\omega t} dt \quad (2.43)$$

$$f(t) = \frac{1}{2\pi} \int_{-\infty}^{\infty} F(\omega)e^{i\omega t} d\omega \quad (2.44)$$

where  $\omega = 2\pi f$  is the angular frequency (*rad/s*).

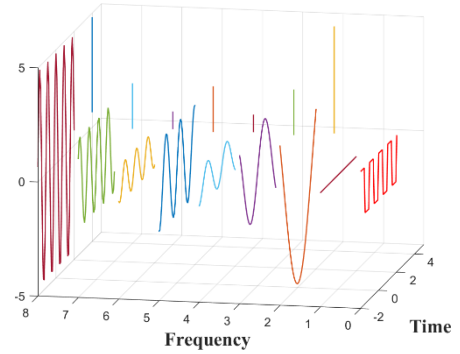


**Fig. 2.7** Fourier transform

Among the many basic properties of the Fourier transform, there are two most important properties for us, one is the differential property; the other is the convolution property.

### 1. Differential properties of Fourier transform

A. For  $\lim_{|t| \rightarrow \infty} f(t) = 0$ , if the Fourier transform corresponding to  $f(t)$  is  $F(\omega)$ , that is,  $f(t) \leftrightarrow F(\omega)$ , then  $f(t)$  differential  $f'(t)$  corresponding to the Fourier transform is  $i\omega F(\omega)$ , namely

$$f'(t) \leftrightarrow i\omega F(\omega) \quad (2.45)$$

Mathematical proof is as follows

$$\begin{aligned} F[f'(t)] &= \int_{-\infty}^{\infty} f'(t)e^{-i\omega t} dt = \int_{-\infty}^{\infty} e^{-i\omega t} df(t) \\ &= [e^{-i\omega t} f(t)]|_{-\infty}^{+\infty} - \int_{-\infty}^{\infty} f(t) de^{-i\omega t} \end{aligned}$$

$$\begin{aligned}
&= 0 - \int_{-\infty}^{\infty} f(t)e^{-i\omega t} (-i\omega) dt \\
&= i\omega \int_{-\infty}^{\infty} f(t)e^{-i\omega t} dt = i\omega F(\omega) \quad (2.46)
\end{aligned}$$

Correspondingly, we can achieve

$$f^{(n)}(t) \leftrightarrow (i\omega)^n F(\omega) \quad (2.47)$$

When  $|t| \rightarrow \infty$ ,  $f'(t) = f''(t) = \dots = f^{(n-1)}(t) = 0$ .

B.

$$(-it)f(t) \leftrightarrow F'(\omega) \quad (2.48)$$

$$(-it)^{(n)}f(t) \leftrightarrow F^{(n)}(\omega) \quad (2.49)$$

Equation above can also be written as

$$t^n f(t) \leftrightarrow i^n F^{(n)}(\omega) \quad (2.50)$$

The differential nature of the Fourier transform is very useful for us to solve the differential equation to obtain the Lorentz-Drude model in Chapter 2.3.

### 1. Convolutional of the Fourier transform<sup>85</sup>

Convolution is defined as follows

$$f(t) * g(t) = \int_{-\infty}^{\infty} f(t - \tau)g(\tau)d\tau = \int_{-\infty}^{\infty} f(\tau)g(t - \tau)d\tau \quad (2.51)$$

Where  $*$  means convolution, and the convolution theorem means that the Fourier transform of the function convolution is the product of the Fourier transform of the function, such as Eqn. 2.52. It means that the convolution in the time domain corresponds to the product in the frequency domain

$$F\{f * g\} = F\{f\} \cdot F\{g\} \quad (2.52)$$

The same Eqn. 2.53 also exists, indicating that the convolution in the frequency domain corresponds to the product in the time domain

$$F\{f \cdot g\} = F\{f\} * F\{g\} \quad (2.53)$$

Eqn. 2.51 can also be written

$$f * g = F^{-1}\{F\{f\} \cdot F\{g\}\} \quad (2.54)$$

In the Fourier transform, convolution in the time domain corresponds to product in the frequency domain. In the signal processing process, the principle of the filter is to use a specific time-domain signal  $g(t)$  to convolve with the original signal  $f(t)$ , which means that the spectral function  $G(\omega)$  corresponding to  $g(t)$  needs to be compared with  $f(t)$  is multiplied by the corresponding spectral function  $F(\omega)$ . If



$G(\omega)$  is 0 at some frequency components, it means that the product of  $F(\omega) \cdot G(\omega)$  corresponding to this frequency is 0. Then the value of the obtained new signal at this frequency is also 0. Then for the signal  $f(t)$ , it is like filtering out certain frequencies after convolution with  $g(t)$ . Therefore,  $g(t)$  is called a filter.

In this thesis, the convolution theorem is not only related to the calculation of Hilbert Transform and KK Transform, but also the basis of deep learning, especially CNN algorithm.

## 2. Discrete Fourier Transform (DFT)<sup>83, 86</sup> and Fast Fourier transform (FFT)<sup>79, 83</sup>

When it comes to signal processing<sup>85</sup>, especially in computer programming, we usually use Discrete Fourier Transform (DFT)<sup>87</sup>. This implies that the Fourier transform is discrete in both the time domain and the frequency domain. And the sequences of the discrete Fourier transform in both the time domain and the frequency domain are of finite length, which is more in line with the actual situation of our sampling and signal processing.

The discrete Fourier transform means transform a sequence of  $N$  complex numbers  $\{x_n\} = x_0, x_1, \dots, x_{N-1}$  to another sequence  $\{X_k\} = X_0, X_1, \dots, X_{N-1}$ . For the convenience of understanding,  $\{x_n\}$  and  $\{X_k\}$  can be regarded as  $f(t)$  and  $F(w)$  in Eqn. 2.43 and Eqn. 2.44 respectively.

$$X_k = \sum_{n=0}^{N-1} x_n \cdot e^{-\frac{i2\pi}{N}kn} \quad (2.55)$$

According to Euler's formula as

$$e^{ix} = \cos x + i \sin x \quad (2.56)$$

To get

$$X_k = \sum_{n=0}^{N-1} x_n \cdot [\cos\left(\frac{2\pi}{N}kn\right) - i \cdot \sin\left(\frac{2\pi}{N}kn\right)] \quad (2.57)$$

At the same time, in order to speed up the calculation, the Cooley–Tukey algorithm<sup>88</sup> reduces the amount of calculation from  $O(N^2)$  to  $O(N \log_2 N)$  by recursively decomposing the original array into smaller arrays. This calculation method significantly reduces the amount of computation, so it is also called Fast Fourier transform (FFT)<sup>89</sup>.

Just like its name, FFT speeds up calculation, greatly reduces calculation and

measurement time, and enables Fourier transform to be more widely used in different fields. The focus of this paper is Fourier transform infrared spectroscopy (FTIR), which is based on the fast Fourier transform method to measure data.

## 2.3 Hilbert Transform

### 1. The Hilbert transform

The Hilbert transform<sup>90</sup> is a calculation method defined in mathematics and signal processing<sup>91</sup>. The Hilbert transform of a function or signal  $f(t)$  can be considered as the convolution of  $f(t)$  with the function  $\frac{1}{\pi t}$ ,<sup>92</sup> such as Eqn. 2.58

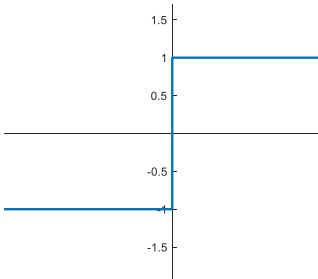
$$\mathcal{H}[f(t)] = \hat{f}(t) = f(t) * \frac{1}{\pi t} = \frac{1}{\pi} \int_{-\infty}^{\infty} \frac{f(\tau)}{t - \tau} d\tau \quad (2.58)$$

$\mathcal{H}$  represents apply Hilbert transform on  $f(t)$ . And  $\hat{f}(t)$  is the Hilbert transformation corresponding to  $f(t)$ .

Combined with the convolution theorem, we can get

$$\mathcal{H}[f(t)] = \hat{f}(t) = f(t) * \frac{1}{\pi t} \leftrightarrow F(f)[-isgn(f)] = \begin{cases} -iF(f) & f \geq 0 \\ iF(f) & f < 0 \end{cases} \quad (2.59)$$

where  $sgn$  is the signum function, as showed in Fig. 2.8



$$sgn(t) = \begin{cases} 1 & t > 0 \\ 0 & t = 0 \\ -1 & t < 0 \end{cases} \quad (2.60)$$

The Hilbert transform can be treated as Fourier transform the signal first and then shift the phase of the transform result by  $90^\circ$ .

**Fig. 2.8**  $sgn(t)$

The Hilbert transform is used in our study to relate the real and imaginary parts of the spectrum. Hilbert transform has an important property. The Hilbert transform of the  $cos$  signal is a  $sin$  signal, and the Hilbert transform of the  $sin$  signal is  $-cos$ . Which is essential for us to understand the correction of distorted spectra in the frequency domain.

This sentence is expressed by the formula as

If

$$f(t) = \cos(2\pi f_0 t + \theta) \quad (2.61)$$

We can get

$$H[f(t)] = \hat{f}(t) = \sin(2\pi f_0 t + \theta) \quad (2.62)$$

Similarly, if

$$f(t) = \sin(2\pi f_0 t + \theta) \quad (2.63)$$

Then

$$H[f(t)] = \hat{f}(t) = -\cos(2\pi f_0 t + \theta) \quad (2.64)$$

At the same time, we can easily infer that the Hilbert transform of the baseband signal is multiplied by  $\cos$  is to directly change  $\cos$  to  $\sin$ . Namely, if

$$f(t) = m(t) \cos(2\pi f_0 t) \quad (2.65)$$

where  $m(t)$  is the baseband signal, and the bandwidth  $w < f$ , then

$$\mathcal{H}[f(t)] = \hat{f}(t) = m(t) \sin(2\pi f_0 t) \quad (2.66)$$

Of course, in signal processing,  $f(t)$  is usually a function in the time domain. But in our research, the calibration curve is a function in the frequency domain. However, it is not difficult to understand the nature of the Fourier transform in Chapter 2.1 to link the time domain and the frequency domain.

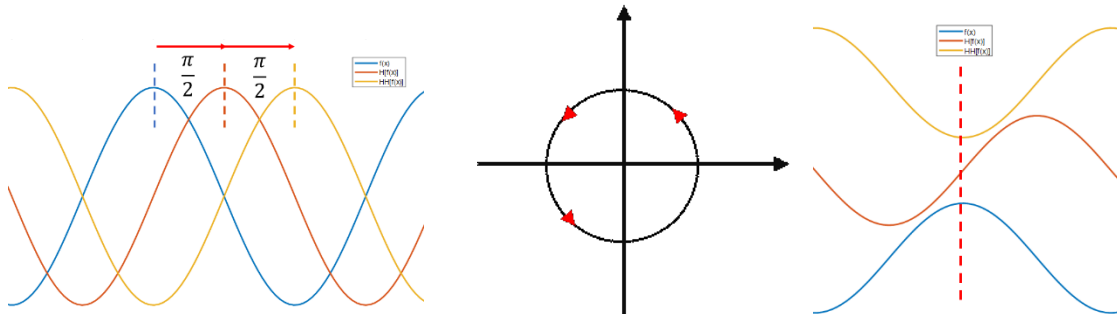


**Fig. 2.9**  $f(t)$ ,  $\mathcal{H}[f(t)]$  and  $\mathcal{H}[\mathcal{H}[f(t)]]$  (Left, Right); angle of  $f(t)$ ,  $\mathcal{H}[f(t)]$  and  $\mathcal{H}[\mathcal{H}[f(t)]]$ (Middle).

As shown in Fig. 2.9 are  $f(x) = \cos x$  completes first Hilbert transform and second Hilbert transform. Which is the process of  $\cos x \rightarrow \sin x \rightarrow -\cos x$ . It is easy to see that each Hilbert transform for  $\cos x$  is translated to the right side of  $\frac{\pi}{2}$ . If combined with Euler's formula<sup>93</sup>

$$e^{i\theta} = \cos \theta + i \sin \theta \quad (2.67)$$

We can easily get the conclusion that each Hilbert transform for  $\cos x$  is the transformation for  $\theta = \frac{\pi}{2}$  in a clockwise direction as shown in Fig.2. 9 (Middle). At the same time, according to Euler's formula, it can also be considered as changing from the

real part to the imaginary part, and from the imaginary part to the opposite number of the real part.

If we look at Hilbert transform in another way, which means comparing the peak spectrum of  $\cos x$  separately as shown in Fig. 2.9 (Right). Then it is easy to find that  $\cos x$  has experienced the process of positive peak, convex and concave twisted peak, at the end inverted peak. Whereas in the Fourier transform, we know that various graphs, in our case is infrared spectrum, can be considered as a combination of  $\sin(kx)$  and  $\cos(kx)$  ( $k$  for different frequencies), or it can be said to be a combination of  $\cos(kx)$ . The reason why the distorted spectrum can be corrected into a normal spectrum by using the Hilbert transform is that it uses an operation like changing  $\cos x$  to  $\sin x$ . The fundamental reason lies in the transformation is using Fourier transform with a fixed angle of  $\theta = \frac{\pi}{2}$  (at this time, the angle of distortion can be considered as  $\theta = \frac{\pi}{2}$  or  $\theta = -\frac{\pi}{2}$ ). Of course, this is also doomed to pure Hilbert transform or Kramers–Kronig transform, that is, the Fourier transform with a fixed angle  $\theta = \frac{\pi}{2}$  cannot accurately correct the distorted spectrum (sometimes the twisted angle is not necessarily  $\theta = \frac{\pi}{2}$  or  $\theta = -\frac{\pi}{2}$ ). So, we need to change the correction angle according to the spectral distortion.

Secondly, another property about  $f(t)$  and  $\hat{f}(t)$  is very important for the Kramers–Kronig transform<sup>94,95</sup> we will introduce next is  $\hat{f}(t)$  is opposite to the parity of  $f(t)$ . That is, if  $f(t)$  is an odd function, then  $\hat{f}(t)$  is an even function, namely

$$\hat{f}(-t) = \frac{1}{\pi} \int_{-\infty}^{\infty} \frac{f(\tau)}{-t - \tau} d\tau = \frac{1}{\pi} \int_{-\infty}^{\infty} \frac{-f(-\tau)}{-t - \tau} d\tau = \frac{1}{\pi} \int_{-\infty}^{\infty} \frac{f(\tau)}{t - x} d\tau = \hat{f}(t) \quad (2.68)$$

## 2. Kramers–Kronig transform

Kramers–Kronig (KK) transform<sup>62, 63, 96-99</sup>, that is, Kramers–Kronig relations, is essentially a Hilbert transform of a square-integrable function with causality<sup>61</sup>. In short, KK transform can be considered as a special case of Hilbert transform, like a square is to a rectangle.

KK transform is often used to analyze the properties of physical systems<sup>91</sup>, such as electrical circuits and optical systems<sup>61, 100</sup>. If the Fourier transform is related to the time domain and the frequency domain, KK transform is related to the real part and the imaginary part. In our case, the real part and the imaginary part of the frequency domain are mainly considered.

Kramers–Kronig transform can be expressed as<sup>61</sup>

$$\hat{x}(f) = x_1(f) + ix_2(f) \quad (2.69)$$

$$x_1(f) = \frac{1}{\pi} P \int_{-\infty}^{\infty} \frac{x_2(f')}{f' - f} df' \quad (2.70)$$

$$x_2(f) = -\frac{1}{\pi} P \int_{-\infty}^{\infty} \frac{x_1(f')}{f' - f} df' \quad (2.71)$$

where P denotes the Cauchy principal value. Its integral area is formed by removing the extreme point  $f'$  of the integrand with a minimal semicircle. Which is the entire upper half complex plane (with real axis) except for the point  $f'$  in Fig. 2.10.

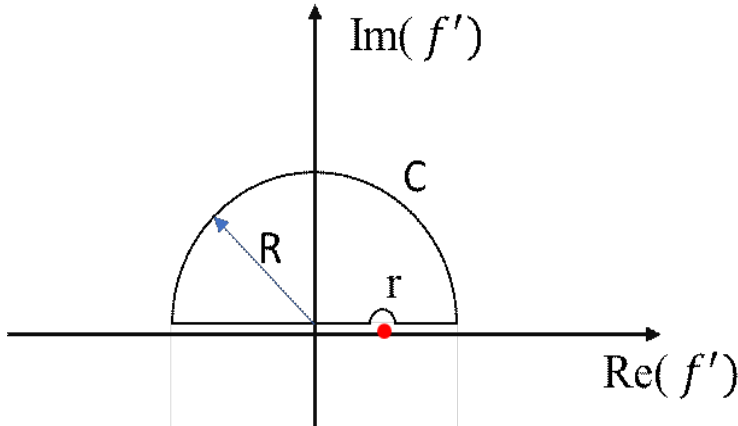


**Fig. 2.10** Integral region of  $x_1(f)$  ( $R \rightarrow \infty, r \rightarrow 0$ ).

Kramers–Kronig transform, which can be obtained from Cauchy's residue theorem of complex integration<sup>101</sup>. And Kramers–Kronig is the key to connect the real part and the imaginary part.

Let's back to the KK transform. Since time starts from 0 in physical systems and signal processing systems, we can know that the time domain function  $\hat{x}(t)$

corresponding to  $\hat{x}(f)$  is a real function. That is when  $t < 0$ ,  $\hat{x}(t) = 0$ . Then we can get  $\hat{x}(-f) = \hat{x}^*(f)$ , \* is complex conjugate. So, the real part  $x_1(f)$  of  $\hat{x}(f)$  is an even function, and the imaginary part  $x_2(f)$  is an odd function. Which also corresponds to the parity before and after the function transformation in the Hilbert transformation.

So

$$x_1(f) = \frac{1}{\pi} P \int_{-\infty}^{\infty} \frac{x_2(f')}{f' - f} df' = \frac{1}{\pi} P \int_{-\infty}^{\infty} \frac{(f' + f)x_2(f')}{f'^2 - f^2} df' \quad (2.72)$$

$$= \frac{1}{\pi} P \int_{-\infty}^{\infty} \frac{f'x_2(f')}{f'^2 - f^2} df' + \frac{f}{\pi} P \int_{-\infty}^{\infty} \frac{x_2(f')}{f'^2 - f^2} df' \quad (2.73)$$

∴  $x_2(f)$  is an odd function,  $\int_{-\infty}^{\infty} \frac{x_2(f')}{f'^2 - f^2} df' = 0$

∴  $x_1(f)$  is an even function,

$$\int_{-\infty}^{\infty} \frac{f'x_2(f')}{f'^2 - f^2} df' = 2 \int_0^{\infty} \frac{f'x_2(f')}{f'^2 - f^2} df' \quad (2.74)$$

$$x_1(f) = \frac{2}{\pi} P \int_0^{\infty} \frac{f'x_2(f')}{f'^2 - f^2} df' \quad (2.75)$$

Correspondingly<sup>102</sup>,

$$x_2(f) = -\frac{2f}{\pi} P \int_0^{\infty} \frac{x_1(f')}{f'^2 - f^2} df' \quad (2.76)$$

In physics, there is linear KK relationship and nonlinear KK relationship. Here we only consider the linear KK relationship. In the physical medium, the linear KK relationship also includes<sup>61, 103</sup>

1. Response function (reflection spectrum<sup>104, 105</sup>, transmission spectrum);
2. Electrical characteristic parameters<sup>91, 106</sup> (complex polarizability and complex permittivity, electrical impedance);
3. Magnetic characteristic parameters<sup>107</sup>;
4. Optics Characteristic parameters<sup>103, 108, 109</sup> (complex refractive index and complex permittivity, photoconductivity, etc.);
5. Acoustic characteristic parameters (adiabatic compressibility coefficient, acoustic refractive index, scattering function) and other fields of application.

Here, we only discuss the complex refractive index and complex permittivity of substances and some applications in reflection spectrum according to the research content.

The frequency is usually represented by  $\nu$ . Compared with Eqs. 2.76 and 2.77

without a constant term, when we use KK transform, it is necessary to add a constant when calculating the real part  $x_1(f)$ . This constant means that the tendency at infinity of  $x_1(f)$  is not 0 but a certain limit value. Which does not affect the KK transform itself.

For the complex permittivity  $\varepsilon_r(\nu)$  of a substance, it can be expressed as

$$\varepsilon_r(\nu) = \varepsilon'_r(\nu) + i\varepsilon''_r(\nu) \quad (2.77)$$

Where  $\varepsilon_r(\nu)$  is equivalent to  $\hat{x}(f)$ , and the real part  $\varepsilon'_r(\nu)$  and imaginary part  $\varepsilon''_r(\nu)$  are respectively equivalent to  $x_1(f)$  and  $x_2(f)$ . and the corresponding KK relations or KK transform can be expressed as

$$\varepsilon'_r(\nu) = 1 + \frac{2}{\pi} P \int_0^\infty \frac{\nu' \varepsilon''_r(\nu')}{\nu'^2 - \nu^2} d\nu' \quad (2.78)$$

$$\varepsilon''_r(\nu) = -\frac{2\nu}{\pi} P \int_0^\infty \frac{\varepsilon'_r(\nu')}{\nu'^2 - \nu^2} d\nu' \quad (2.79)$$

And the complex refractive index  $\hat{n}(\nu) = \sqrt{\varepsilon_r(\nu)}$  consists of real part  $n(\nu)$  representing refraction and imaginary part  $k(\nu)$  representing absorption. And real part  $n(\nu)$  and imaginary part  $k(\nu)$  also obey the KK relations.

$$\hat{n}(\nu) = n(\nu) + ik(\nu) \quad (2.80)$$

$$n(\nu) = n_\infty + \frac{2}{\pi} P \int_0^\infty \frac{\nu' k(\nu')}{\nu'^2 - \nu^2} d\nu' \quad (2.81)$$

$$k(\nu) = -\frac{2\nu}{\pi} P \int_0^\infty \frac{n(\nu')}{\nu'^2 - \nu^2} d\nu' \quad (2.82)$$

The spectrum of  $n(\nu)$  and  $k(\nu)$  is showed in Fig.2.11.

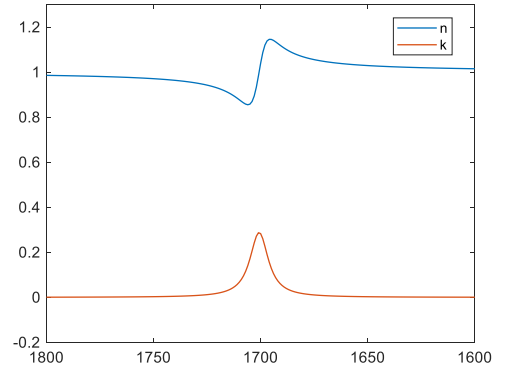


**Fig. 2.11**  $n(\nu)$  and  $k(\nu)$ .

According to the above understanding of the Hilbert transform, it can be found that in fact the KK relationship can be considered as a Fourier transform with a difference of  $90^\circ$ . The two components that constitute the KK relationship can be considered as two mutually orthogonal components, and can be expressed in polar coordinates, that is, magnitude and phase.

## 2.4 Lorentz-Drude Model

### 1. The Lorentz Oscillator<sup>33, 110</sup>

When an electromagnetic wave expressed by

$$\vec{E} = \vec{E}_0 e^{-i(\omega t - kz)} \quad (2.83)$$

Here we assumed that  $z = 0$ ,

$$\vec{E} = \vec{E}_0 e^{-i\omega t} \quad (2.84)$$

Then

$$f(t) = -q\vec{E} = -q\vec{E}_0 e^{-i\omega t} \quad (2.85)$$

In fact,  $q$  represents the charge of an electron, which can be represented by  $e$ , but in order to avoid confusion with Euler's number ( $e$ ), we still use  $q$  here.

Calculate the polarization  $\vec{p}$  for a single atom. Which can be expressed in Fig.2.12.

$$m\ddot{x}(t) + m\gamma\dot{x}(t) + kx(t) = f(t) \quad (2.86)$$

For time-harmonic fields:

$$x(t) = \vec{X}_0 e^{-i\omega t} \quad (2.87)$$

and  $m = m_e$

$$\dot{x}(t) = -i\omega \cdot \vec{X}_0 e^{-i\omega t} = -i\omega x(t) \quad (2.88)$$

$$\ddot{x}(t) = -\omega^2 \cdot \vec{X}_0 e^{-i\omega t} = -\omega^2 x(t) \quad (2.89)$$

Eqn. 2.107 can be written as

$$(-m_e\omega^2 - m_e i\gamma\omega + k)x(t) = -q\vec{E} \quad (2.90)$$

$$x(t) = \frac{q}{k - m_e\omega^2 - m_e i\gamma\omega} \vec{E} \quad (2.91)$$

Set  $\omega_0 = \sqrt{\frac{k}{m_e}}$ , which means resonance frequency here.

$$x(t) = \frac{q/m_e}{\omega_0^2 - \omega^2 - i\gamma\omega} \vec{E} \quad (2.92)$$

And finally, the polarization  $\vec{p}$  for a single atom is as following:

$$\vec{p} = qx(t) = \frac{q^2/m_e}{\omega_0^2 - \omega^2 - i\gamma\omega} \vec{E} \quad (2.93)$$

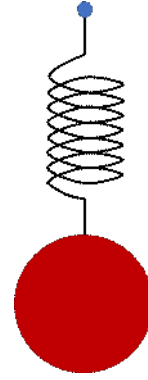


Fig. 2.12 A mass on a spring.



Then we can calculate the polarization of the medial in unit volume  $\vec{P}$

$$\vec{P} = N\vec{p} = \frac{Nq^2/m_e}{\omega_0^2 - \omega^2 - i\gamma\omega} \vec{E} \quad (2.94)$$

$N$  is the number of atoms per unit volume.

Meanwhile, the polarization is also defined as  $\vec{P} = \epsilon_0\chi_e\vec{E}$ ,  $\epsilon_0$  is the vacuum permittivity.

And

$$\vec{D} = \epsilon_0\vec{E} + \vec{P} = \epsilon_0\vec{E} + \epsilon_0\chi_e\vec{E} = \epsilon_0(1 + \chi_e)\vec{E} \quad (2.95)$$

In here, the relative permittivity  $\epsilon_r$  is frequency-dependent, also called the dielectric function

$$\epsilon_r = \frac{\epsilon}{\epsilon_0} = (1 + \chi_e) \quad (2.96)$$

Combine Eqs 2.94, 2.95 and 2.96, We can get

$$\epsilon_r = \frac{\epsilon}{\epsilon_0} = 1 + \frac{Nq^2}{m_e\epsilon_0} \frac{1}{\omega_0^2 - \omega^2 - i\gamma\omega} \quad (2.97)$$

Set  $\omega_p = \sqrt{\frac{Nq^2}{m_e\epsilon_0}}$ , which is called the plasma frequency<sup>12</sup>.

$$\epsilon_r = \frac{\epsilon}{\epsilon_0} = 1 + \frac{\omega_p^2}{\omega_0^2 - \omega^2 - i\gamma\omega} \quad (2.98)$$

Eqn. 2.98 was called as the classic damped harmonic oscillator model, also called as Lorentz model.

It should notice the relative permittivity  $\epsilon_r(\nu)$  is complex as well. The real part of  $\epsilon_r'(\nu)$  and imaginary part  $\epsilon_r''(\nu)$  follows Kramers–Kronig relations as we have already discussed.

$\nu$  here means frequency, is the same as  $\omega$ ;  $\nu_0$  is the same as  $\omega_0$ ;  $S$  replaces  $\omega_p$ .<sup>12</sup>

$$\epsilon_r(\nu) = \epsilon_r'(\nu) + i\epsilon_r''(\nu) \quad (2.99)$$

$\epsilon_r$  can be split from Eqn. 2.99 to 2 parts with real and imag as well.

$$\epsilon_r(\nu) = 1 + \frac{S^2(\nu_0^2 - \nu^2)}{(\nu_0^2 - \nu^2)^2 + \gamma^2\nu^2} + i \frac{S^2\gamma\nu}{(\nu_0^2 - \nu^2)^2 + \gamma^2\nu^2} \quad (2.100)$$

Then

$$\epsilon_r'(v) = 1 + \frac{S^2 (v_0^2 - v^2)}{(v_0^2 - v^2)^2 + \gamma^2 v^2} \quad (2.101)$$

$$\epsilon_r''(v) = \frac{S^2 \gamma v}{(v_0^2 - v^2)^2 + \gamma^2 v^2} \quad (2.102)$$

As showed in Fig 2.11<sup>111</sup> (  $S^2 = 10000$ ,  $v_0 = 1700$ , and  $\gamma = 10$  with the unit  $1/cm$ ).

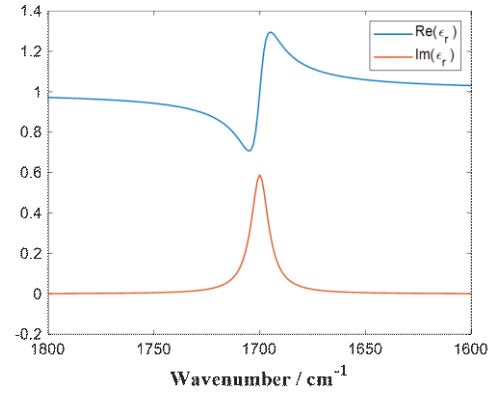


**Fig. 2.13**  $\epsilon_r'(v)$  and  $\epsilon_r''(v)$

Which also can be used to calculate the real and imag parts of refractive index  $\epsilon_r(v)$ .

And combine Eqn. 2.103 as following

$$\hat{n}(v) = \sqrt{\mu_r \epsilon_r} = \sqrt{\epsilon_r(v)} = n(v) + ik(v) \quad (2.103)$$

## 2. Drude model for metals

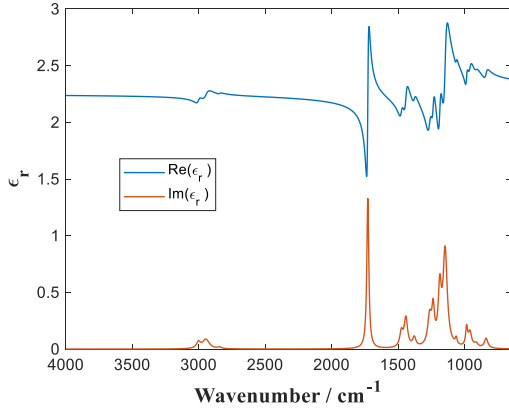
In most metal the restoring force is 0 because they have free electrons rather than bound by the nucleus. So, we consider  $\omega_0 = 0$  for metal as the Drude model<sup>112</sup>. In this case,  $\epsilon_r$  can be written as

$$\epsilon_r = 1 - \frac{\omega_p^2}{\omega^2 - i\gamma\omega} \quad (2.104)$$

## 3. General equation of Lorentz-Drude model

Eqn. 2.98 and Eqn. 2.104 are also called Lorentz-Drude model<sup>112</sup>.

Lorentz-Drude model can be used to calculate complex refractive index  $\hat{n}(\nu)$  as well.



But it is worth noting that Eqn 2.98 and Eqn. 2.104 are only used for the calculation of  $\epsilon_r$  assuming a single frequency peak. If a substance has many absorption peaks, it needs a lot of parameters to determine. For example, in the case of  $N$  absorption peaks.

**Fig. 2.14**  $\epsilon_r'(\nu)$  and  $\epsilon_r''(\nu)$  with  $N$  peaks<sup>113</sup>.

$$\epsilon_r = \epsilon_r(\infty) + \sum_{j=1}^N \frac{\omega_{p,j}^2}{\omega_{0,j}^2 - \omega^2 - i\omega\gamma_j} \quad (2.105)$$

In which,  $\epsilon_r(\infty)$  is the contribution of all at higher wavenumber situated oscillators for infinite wavelength, i.e., zero wavenumber.

Sometimes it is also written as

$$\epsilon_r = \epsilon_r(\infty) + \sum_{j=1}^N \frac{S_j^2}{\nu_j^2 - \nu^2 - i\nu\gamma_j} \quad (2.106)$$

The above two formulas express the same meaning. Spectrum as showed in Fig. 2.14 and corresponding parameters values are from the reference<sup>113</sup>.

Both the Lorentz-Drude model and KK transform can be used to relate the real and imaginary parts of  $\epsilon_r$  and  $\hat{n}(\nu)$ . The difference is that the KK can be used for continuous calculations, while the Lorentz-Drude model cannot.

## 2.5 Simulation and Correction

With  $n_1 = 2.41$ , and applied  $n(\nu)$  and  $k(\nu)$  of Toluene as complex  $n_2$ . And changing  $\theta_1$  within  $0^\circ$ - $90^\circ$ , the simulation spectrums within  $650$ - $800\text{cm}^{-1}$  are showed in Fig.2.15A. After considering  $n_{T\infty} = n_{To(4000\text{cm}^{-1})} = 1.4707$ , it is not difficult to find by Eqn.1.99 that  $\theta_c \approx 37.61^\circ$ . Which perfectly explained the abnormality of absorption spectrum below  $40^\circ$ . It's obviously related to the real part  $n(\nu)$  of the complex refractive index of Toluene (To), but it should be noted that, for ATR, the peak position values of the absorption spectrum and the complex refractive index spectrum are not completely consistent. There are a series of references for specific calculation process. For a better comparison, we introduce the absorption spectrum obtained under the experimental conditions with  $\theta_1 = 45^\circ$ .

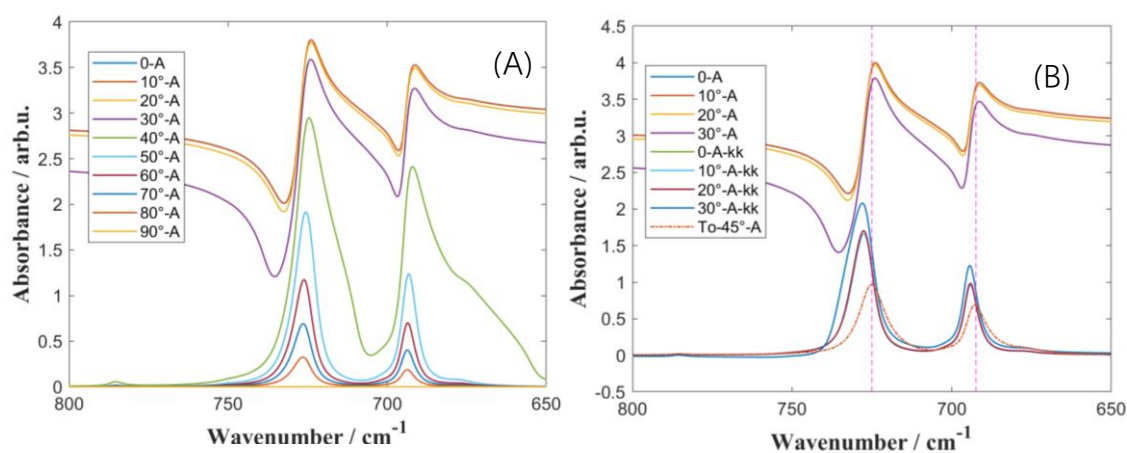


**Fig. 2.15** Comparison of the simulation spectrum with the incident angle within  $0^\circ$ - $90^\circ$  within  $650$ - $800\text{cm}^{-1}$  (A); Comparison of the simulation spectrum with the incident angle lower than the critical angle and experiment spectrum with  $\theta_1 = 45^\circ$ , corresponding corrected spectrum by KK transform within  $650$ - $800\text{cm}^{-1}$  (B).

Indeed, if the incident angle falls below the critical angle or even when the distortion peak near the critical angle exhibits a red shift compared to the normal peak observed with an incident angle higher than the critical angle, correction is imperative. However, it's essential to clarify a common misconception. The distortion peak primarily arises from the refractive part, namely the real part  $n(\nu)$ , which is commonly referred to as anomalous dispersion. Contrary to common belief, the distorted spectrum primarily encompasses the refraction property rather than the absorption property. Consequently, these distorted peaks necessitate transformation into normal peaks

through methods such as Kramers-Kronig (KK) <sup>44, 97, 98</sup> transformation. The corrected curves illustrating this transformation are depicted in Fig. 2.15B. This corrective approach ensures that the refractive properties inherent in the distorted peaks are appropriately accounted for, leading to the generation of accurate spectra suitable for subsequent analysis and interpretation.

If we consider the raised portion of the original spectrum as an absorption peak, the spectrum will appear red-shifted compared to the experimental peak observed at  $\theta_1 = 45^\circ$ . Conversely, some papers treat the recessed portion in Fig. 1B as another absorption peak. However, when the experimental value is taken as the reference, the corrected peak exhibits a noticeable blue shift instead of a red shift. It's important to note that the concave and convex sections of the original spectrum can be interpreted as the real part of the spectrum, rather than representing two distinct absorption peaks (though this simplification may not be entirely accurate and is primarily for ease of understanding). This interpretation becomes apparent when the spectrum is obtained directly through KK transformation to yield a symmetrical spectrum.

Fig. 2.16 presents information from spectrograms at all incident angles with correct positioning. This comprehensive visualization aids in understanding the spectral characteristics across different incident angles, providing valuable insights for further analysis and interpretation.

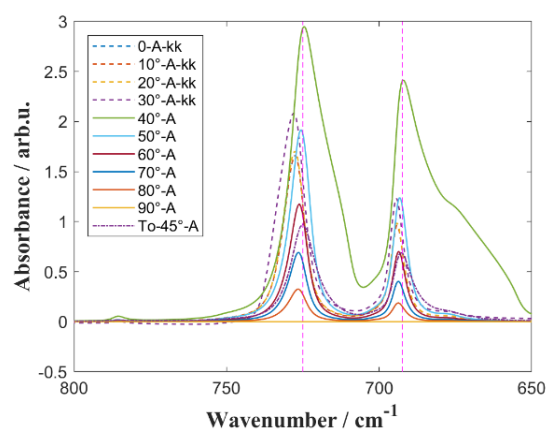


**Fig. 2.16** Comparison of the original spectrum with the incident angle higher than the critical angle and the corrected spectrum with the incident angle lower than the critical angle.

As depicted in Fig. 2.16, when the incident angle surpasses the critical angle, a reduction in the incident angle results in a gradual redshift of the peak position alongside a gradual increase in peak height. Conversely, when the incident angle falls below the critical angle, the peak position continues to redshift while the peak height gradually decreases. However, it's crucial to note that the corrected peak, relative to the experimental peak, exhibits a blue shift rather than a red shift.

Regarding scenarios near the critical angle, further insights can be gleaned from

Milan's book<sup>1</sup>, particularly in Fig. 9.2.

Nevertheless, it's pertinent to acknowledge that conventional approaches, such as simple KK transformation, may not yield optimal calibration curves when dealing with the curve of  $n(\nu)$  and  $k(\nu)$  mixing and distortion. This limitation is particularly pronounced in scenarios involving multiphase mixing, such as the spectrum of high refractive index solid-liquid mixing. Previous articles have elucidated the principles and simulations of spectrum distortion, highlighting the inadequacy of simple KK transformation in achieving a perfect calibration curve.

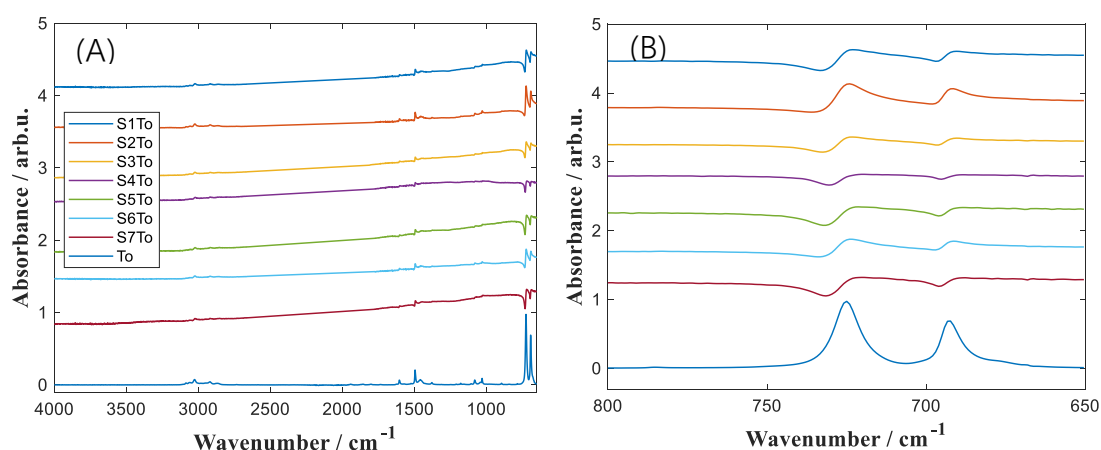


**Fig. 2.17** Spectra of samples in toluene and pure toluene(A) and partial spectra within 650-800 $\text{cm}^{-1}$  (B).

The original spectra, as depicted in Fig. 2.17, highlight a critical consideration: to mitigate the influence of the Internal Reflection Element (IRE) itself on the spectrum, all mixture spectra in this study have been corrected within the range of 1775-2661  $\text{cm}^{-1}$ . The significant negative peak observed within this interval stems from the depression caused by the absorption of diamond, a phenomenon detailed in previous articles.

It is evident that none of the peak positions illustrated in Fig. 2.17 can be deemed accurate. Similar to the observations in Fig. 2.17B, the convex portions of the uncorrected spectrum exhibit a red shift when compared to the peak of the pure solvent. This discrepancy underscores the necessity for correction methodologies to account for spectral distortions arising from factors such as IRE absorption and refractive index

variations within the sample.

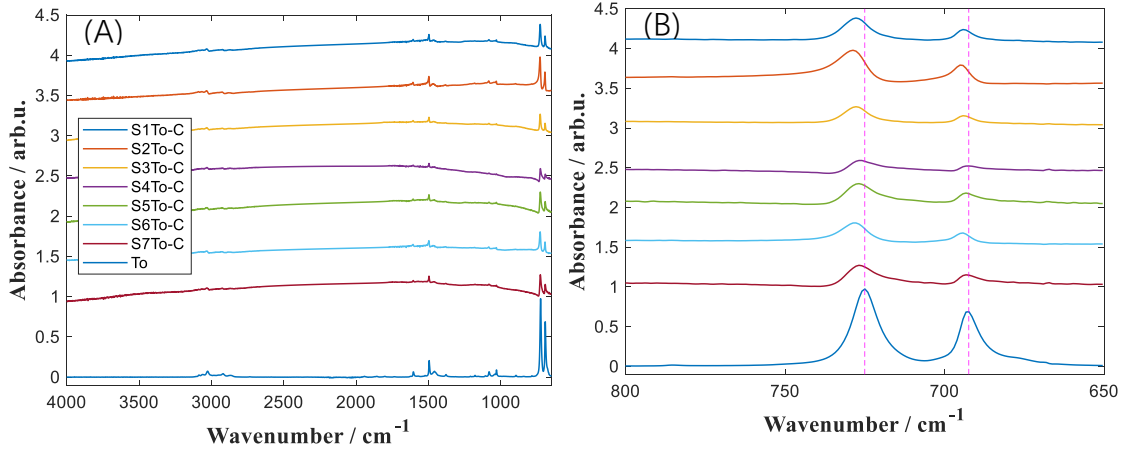


**Fig. 2.18** Spectra in Fig.3 after correcting by KK transform (A) and partial spectra within 650-800cm<sup>-1</sup> (B).

As depicted in Fig. 2.18, even after applying the KK transformation, the corrected spectrum retains the influence of refraction peaks. This phenomenon arises due to the complex nature of the distortion observed in the original spectrum, which stems from a combination of refraction and absorption phenomena within the solid-liquid mixture.

When simple KK transformation is applied, the absorption peaks present in the original spectrum are converted into refraction peaks. However, this transformation does not fully eliminate the refraction effects, leading to interference in the resulting spectrum. This underscores the intricacies involved in correcting distorted spectra and highlights the need for more sophisticated correction methodologies that can effectively address the combined effects of refraction and absorption.

In this case, the method used by Gökçen Tek was adopted<sup>114</sup>. Firstly, select the interval to be corrected. Secondly, correct the baseline. Thirdly, using inverse fast Fourier transformation (IFFT)<sup>79</sup> and check for the most symmetric line shape of the peak by changing  $\phi$  from  $-\pi$  to  $\pi$ , which means phase index from -314 to 314, to get the best phase index  $\phi_b$  with minimum of the difference between the absorption peaks at equal distances from the center frequency after fast Fourier transformation (FFT)<sup>53</sup>. Finally, use Eqn.12 to get the final corrected spectrum.

$$A_{\phi_b}(w) = 2 * real(A(w)e^{i\phi_b}) \quad (2.107)$$

The method described above addresses the challenge of separating the mixed absorption peak from the real and imaginary parts of the spectrum. Originally proposed to resolve peak distortion resulting from reflection on the surface of a metal layer, this approach proves applicable to the context of this paper as well. The calibration results

obtained through this method are illustrated in Fig.2.19.

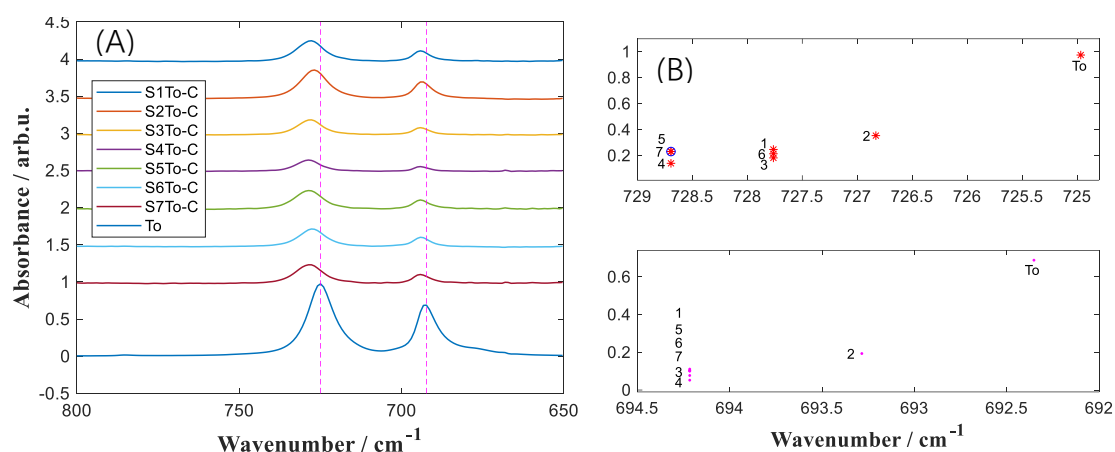


**Fig. 2.19** Spectra within in Fig.4 after correcting method by Gökçen Tek (A) and specific dashed peak shift (B).

From Fig. 2.19, it becomes apparent that the absorbance peak generally exhibits a blue shift relative to the Toluene peak after correction. However, it's noteworthy that many scientific researchers erroneously conclude a red shift in such spectra analysis, neglecting the crucial aspect of correction. This oversight compromises the rigor of their conclusions, particularly when analyzing intermolecular interactions.

The distortion observed in the spectrum primarily stems from light transmission through the medium, influenced by the complex refractive index. Therefore, attributing this distortion to intermolecular interactions is inherently flawed. In conjunction with Fig. 2.17, it can be inferred that the distortion in the original spectrum correlates with the magnitude of the real part of the composite refractive index of the mixture. Consequently, a greater distortion in the original spectrum tends to manifest as a more pronounced blue shift in the corrected spectrum.

The challenge with this method is that even within the same spectrum, the degree of phase delay can vary across different wavenumbers. This can be likened to the varying depth of an evanescent wave.

The amplitude of the evanescent wave decays to  $1/e$  of its maximum value at a distance  $d_p$  in Eqn. 1.100 from the interface.

$$d_p = \frac{1}{2\pi\nu\sqrt{n_1^2\sin^2\theta_1 - n_2^2}} \quad (1.100)$$

Spectral distortion can also occur when the incident angle is near the critical angle in 2D IR spectroscopy.<sup>115</sup> However, the focus in 2D IR is typically on vibrations within a narrower wavenumber range, allowing for the phase delay at the highest symmetrical



peak to be used as a representative value for other peaks. But this approach becomes problematic when dealing with broader wavenumber spans and varying degrees of distortion, such as the mixed distortion peak of Carbon and Toluene. In these cases, using the phase delay from the highest distortion peak for the entire spectrum is not suitable.

When correcting the baseline, narrower ranges with fewer variations are easier to manage, while a broader spectrum with complex distortions, including concave and convex lines, poses greater difficulty. The simple baseline correction method used in the Gökçen Tek's method becomes insufficient for correcting distorted spectra across the entire wavenumber range. To address this, a more intricate baseline correction approach is needed<sup>116</sup>. Building upon the Gökçen Tek correction method, with the integration of PSD<sup>52, 66, 67, 73, 75, 117</sup>, a more globally applicable correction method was developed.

The entire correction method involves two main steps:

1. Calibrate the baseline across the entire spectrum as in Fig.2.20A.
2. Adjust  $\phi$  (phase shift) from  $-\pi$  to  $\pi$ , based on Eqn.12, as shown in Fig. 2.20B.

This allows for finding the maximum and minimum values for each wavenumber. The difference between these values provides a general correction, leading to the final calibrated spectrum as in Fig.2.20C.

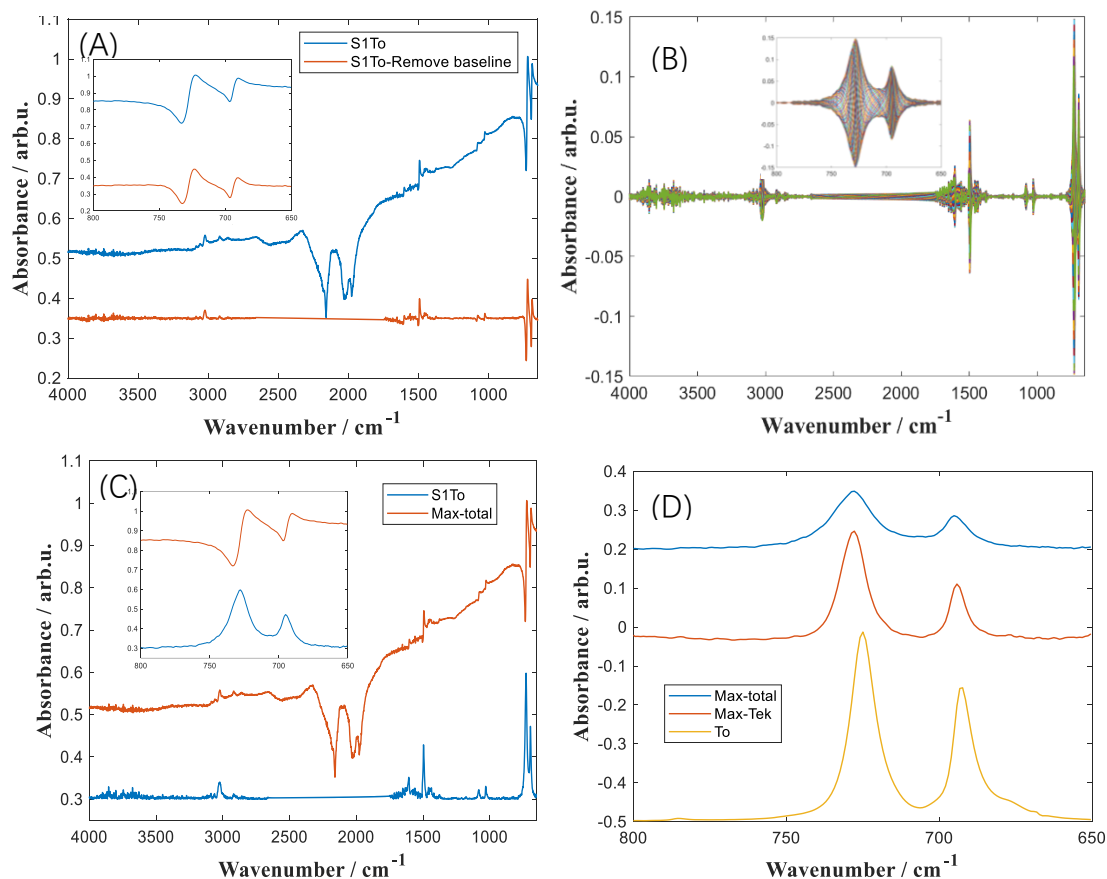


**Fig. 2.20** Comparison between distorted spectrum of S1To and the spectrum of S1To after correcting baseline(A); Changing  $\phi$  from  $-\pi$  to  $\pi$  of spectrum of S1To after correcting baseline(B); Comparison between distorted spectrum of S1To and the spectrum of S1To after correcting by using max total method (C); Comparison between the spectrum of S1To after correcting with 2 methods and Toluene(D).

It's important to note that while this method can determine a more accurate peak position, it may not yield the most accurate peak shape. This is because this method effectively generates multiple phase delay envelopes, allowing for greater flexibility in correction but potentially leading to less precise peak profiles. Fig. 2.20D displays the corrected spectra from two different correction methods, alongside the spectrum for pure Toluene for comparison.

## Conclusions

In this study, the calibration of pure solvent spectra serves as the starting point for employing various Kramers-Kronig (KK) transformation techniques to rectify ATR spectra originating from high refractive index carbon and solvent mixtures. To correct the distortion in the spectrum of a mixture, we accounted for differences in phase delay

across various wavenumbers. By applying Inverse Fast Fourier Transform (IFFT) and Fast Fourier Transform (FFT), combined with techniques from the Phase Sensitive Detection (PSD) process, we achieved one-time correction of the entire spectrum. This integrated approach addresses the complexities arising from phase delay variations, allowing for a comprehensive and efficient correction of distorted spectra in a single step, improving the accuracy of spectral analysis and reducing the need for segmental corrections. Through this calibration process, correct spectra are derived and subsequently analyzed from multiple perspectives. The paper highlights that the distortion of spectra, particularly prominent at low wavenumbers and regions of high absorption, is attributed to the refraction and absorption phenomena inherent in solid-liquid mixtures. These effects are encapsulated by the real and imaginary components of the complex refractive index, respectively. Notably, while the original spectrum exhibits a redshift in absorption relative to the solvent, the calibrated spectrum undergoes a blue shift, with the magnitude of this shift positively correlated with the absorption intensity of the pure solvent spectrum. Furthermore, the degree of spectral distortion correlates with the prominence of the blue shift. This research bears critical significance not only for spectral correction and the acquisition of accurate spectra but also for advancing our understanding of substance properties and solid-liquid interactions.

Moreover, by considering both Specular Reflectance (SR) and ATR, representing internal and external reflection, respectively, through the lens of Fresnel's law, a novel perspective emerges. It is discerned that the partial or total absence of total internal reflection within the experimental wavenumber range (due to incident angles falling below the critical angle or refractive indices exceeding the critical refractive index) constitutes Specular Reflectance-induced Internal Reflection (SRIR). Ultimately, employing diverse KK transformation methodologies facilitates the derivation of correct spectra, thereby significantly broadening the applicative scope of ATR and laying a solid groundwork for the accurate characterization of high refractive index materials.

# 3. From Fourier Transform to Deep Learning

## 3.1 Extension of Fourier Transform

### 1. Short Time Fourier Transform (STFT)

The Fourier transform (FT)<sup>57</sup> loses the information of the time domain part in the process of converting the time domain to the frequency domain. When both the frequency domain and the time domain information are needed, we can use the Windowed Fourier transform, also called Short Time Fourier Transform (STFT)<sup>118-120</sup>.

STFT can be described as follows

$$G(\omega, u) = \int_{-\infty}^{\infty} f(t)g(t - u)e^{-i\omega t} dt \quad (3.1)$$

Where  $g(t - u)$  is the window function.

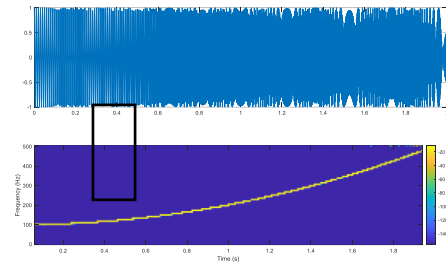


**Fig. 3.1** STFT

The short-time Fourier transform is the Fourier transform multiplied by a window function. This can also be considered as dividing the time signal into different short signals of the same time, and then performing Fourier transform in each short time to obtain the spectrum signal in the corresponding time. This also embodies time-varying information in the transformations that reveal the spectrum.

Since the window length is fixed, STFT has the problem of single time resolution. To solve it we introduce the wavelet transform.

### 2. Wavelet Transform<sup>121</sup>

The wavelet<sup>122-125</sup> can be expressed by the following formula

$$\psi_{a,b}(t) = \frac{1}{\sqrt{a}}\psi\left(\frac{t-b}{a}\right) \quad a, b \in \mathbb{R} \quad (3.2)$$

where  $a, b$  are scale and position parameters respectively.

There are different kinds of wavelets we can apply. For example, Morlet Wavelet<sup>126-128</sup>, is given by:

$$\psi(t) = e^{-i\omega t} e^{-\frac{t^2}{2}} = k_0 \cdot \cos(\omega t) \cdot e^{-\frac{t^2}{2}} \quad (3.3)$$

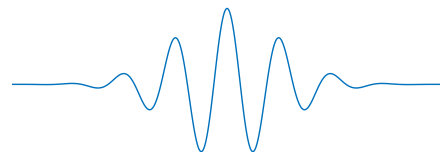


**Fig. 3.2** Morlet Wavelet

Wavelet Transform has different resolutions at different times when analyzing signals. It provides low time resolution at high frequencies and high time resolution at low frequencies. It can also be considered as the Fourier transform that is multiplied by a window, but the window at this time is not fixed, and the window is inversely proportional to the frequency.

Wavelet transform can be divided into continuous and discontinuous wavelet transform. In what follows, we will use continuous wavelet transform to illustrate the relationship between time resolution and frequency resolution.

### 2.1 Continuous Wavelet Transform (CWT)

The Continuous Wavelet Transform(CWT)<sup>127, 129</sup> is given by Eq. 3.4

$$CWT(a, b) = \langle f, \psi_{a,b} \rangle = \frac{1}{\sqrt{a}} \int_{-\infty}^{\infty} f(t) \cdot \psi^* \left( \frac{t-b}{a} \right) dt \quad (3.4)$$

$$\Delta t \cdot \Delta \omega \geq \frac{1}{2\pi} \quad (3.5)$$

$\Delta t$ ,  $\Delta \omega$  can be treated as time resolution and frequency resolution respectively,  $f(t)$  is the signal. This means that when we get very high frequency resolution, the corresponding time resolution is low, and when we have high time resolution, the frequency resolution is low.

Just like the Fourier transform, the wavelet transform also has a corresponding inverse transform. For a continuous wavelet transform, its inverse is a continuous wavelet transform. By combining CWT and ICWT we can use them for spectral analysis of signals or spectrum in MATLAB, python and so on. Of utmost significance is the utilization of Continuous Wavelet Transform (CWT) coefficients in the form of a scalogram, which can serve as input data for a deep neural network used in signal classification tasks.<sup>130</sup>

CWT also has the problem of excessive calculation.

### 2.2 Discrete Wavelet Transform (DMT)

The wavelet is discrete in Discrete Wavelet Transform(DMT)<sup>131</sup>. That is, the scale and shift parameters are discretization as following.

$$\psi_{m,k}(t) = \frac{1}{\sqrt{2^m}} \psi \left( \frac{t-k2^m}{2^m} \right) \quad m, k \in \mathbb{R} \quad (3.6)$$

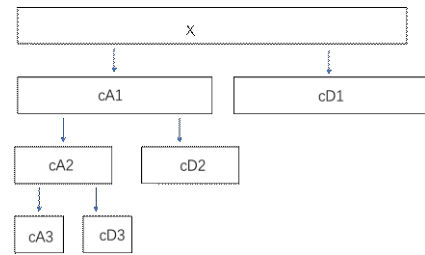


**Fig. 3.3** Decomposing data process.

Where  $m, k$  are the scale and shift parameters respectively.

Correspondingly, Discrete Wavelet Transform can be written as

$$DWT(m, k) = \langle f, \psi_{m,k} \rangle = \frac{1}{\sqrt{2^m}} \int_{-\infty}^{\infty} f(t) \cdot \psi^* \left( \frac{t - k2^m}{2^m} \right) dt \quad (3.7)$$

Eqn. 3.7 means decomposing the data into high and low frequencies of equal length each time in the frequency domain, which is also similar to having two equal-length window samples at each node. This is illustrated in Fig. 3.3.

Just like convolution in Fourier transform, convolution in time domain corresponds to product in the frequency domain. The convolution of the wavelet and the original function in the time domain is also the product of the corresponding frequency domain, which is why the discrete wavelet transform can achieve high-pass and low-pass filtering.

Why do I introduce so many contents that seem to have nothing to do with my research? Although I have not directly applied the above data processing methods in my research, these are the bridges connecting Fourier transform and deep learning. Because convolution, as a very useful mathematical method, which not only plays a significant role in traditional calculations and signal processing, but, and even more importantly, it plays a pivotal role in deep learning algorithms.

Whether it is windowed Fourier transform or wavelet transform, this is a method of extracting part of the information in the data through convolution using a window function, or a method similar to a window function. And the convolutional neural network algorithm takes this method to the extreme.

In short, STFT derives the characteristics of data by using window functions of equal length, and WT is a means to obtain the characteristics of data by using window functions of different lengths. The size change of the  $\psi$  function can be regarded as a way to obtain different data characteristics. It is only one kind of  $\psi$  that can be selected each time in wavelet transform, which means that the characteristics of each selected data are also of a specific type. That's why Wavelet Scattering can be thought as an equivalent to a convolutional neural network<sup>130</sup>. The convolutional neural network uses different window functions to obtain different characteristics of the data through convolution and learns during the training process.

## 3.2 Convolutional Neural Network (CNN)

### 1. Introduction of CNN<sup>132, 133</sup>

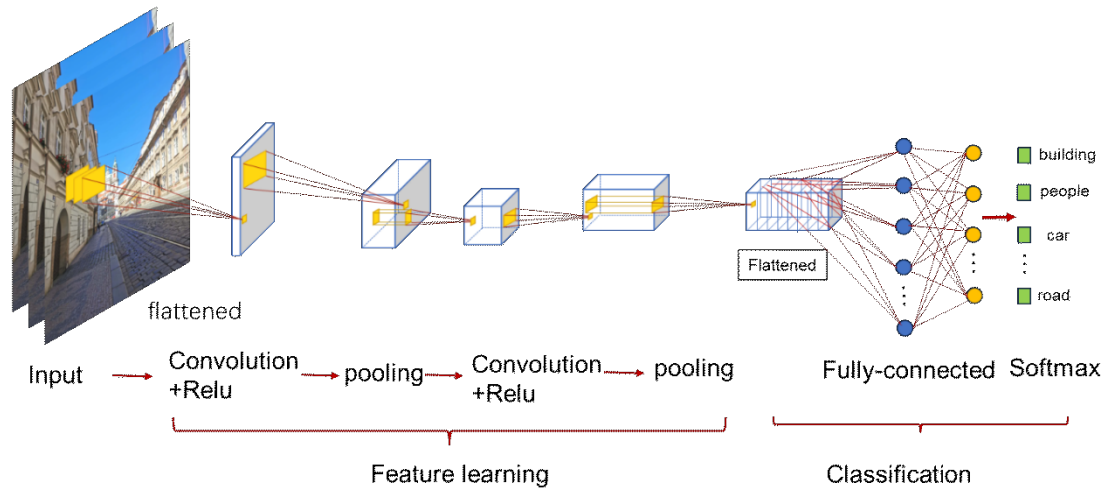


**Fig. 3.4** Calculation program of CNN<sup>134</sup>

The algorithm of CNN<sup>132, 133, 135-138</sup>, as shown in Fig.3.4, is composed of two parts, feature learning and classification<sup>139</sup>. Each of these components will be expounded upon separately.

Within feature learning, convolution plays a pivotal role.

We can regard the convolution kernel as a wavelet in wavelet transform. But it is worth noting that unlike the wavelet transform, the similar wavelet here is two-dimensional just like 2D Fourier transform what we'll introduce in Chapter 5.1 (of course, there are also data with one-dimensional or three-dimensional, here only two-dimensional image data is used as an example). As showed in Fig. 3.5, and the convolutional kernel size is fixed as 3\*3 (or 5\*5 or other sizes). Convolution kernel is used to extract the main information of the data by finding the similarity between the convolution kernel and the data. The difference between the convolution kernel in CNN and the Fourier convolution will be described in detail in section 2. Different features of the data are obtained by different types of convolution kernels, such as horizontal stripes, vertical stripes or circles in the picture, etc. Which is also the most important part of the deep learning black box properties.

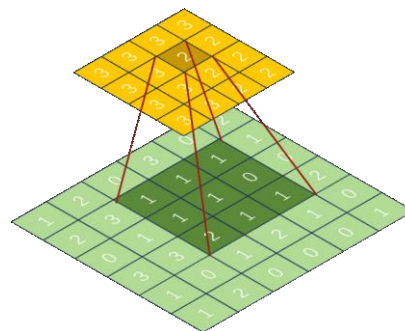


**Fig. 3.5** Convolution with a 3\*3 kernel.<sup>134</sup>

The Rectified Linear Unit (ReLU)<sup>140</sup> function selectively activates data based on convolution-derived outcomes, as illustrated in Fig. 3.5.

The subsequent step involves pooling, aiming to acquire locally optimal and representative data from the output of a convolution layer using diverse methods such as maximum<sup>141, 142</sup>, minimum, or average<sup>143</sup> value computation<sup>144</sup>. The amalgamation of these pooled data points results in the creation of a new two-dimensional dataset.

This iterative process is applied to the new dataset, extracting fundamental features from the lower layers. Diverse results are then combined to obtain more intricate features, capturing nuanced global information, as depicted in Fig. 3.6, which illustrates the calculation program of feature learning.

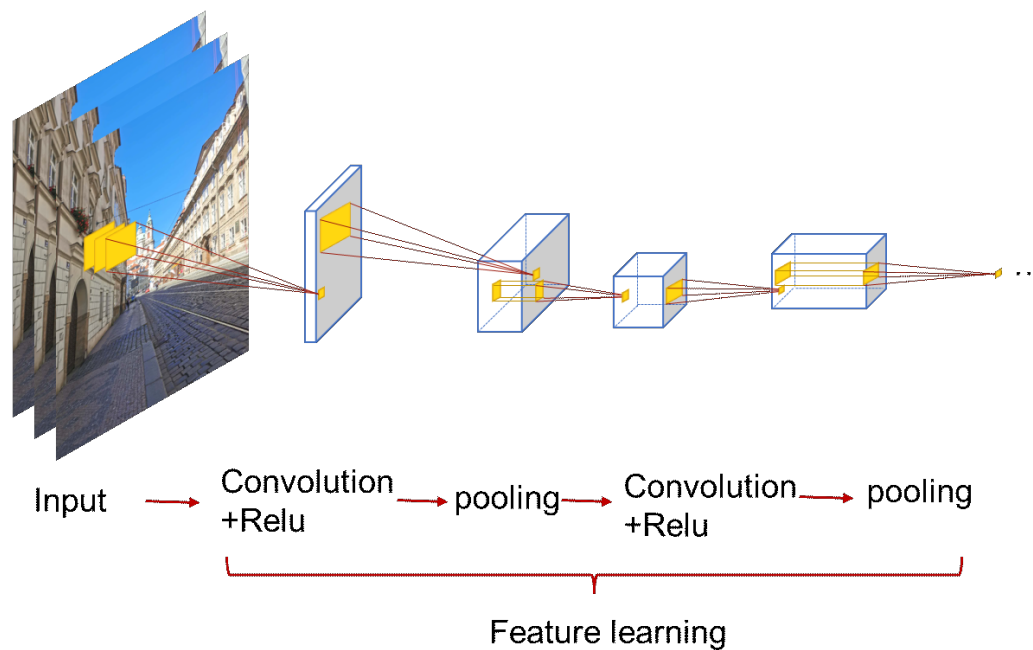


**Fig. 3.6** Calculation program of feature leaning.<sup>134</sup>

After the convolutional layer has fully obtained the data information, we next introduce the classification.

The global and local information are combined by full connected layer through mapping distributed features to sample label space. In short, all the data obtained in the feature learning step are integrated into one data as output to achieve the screening purpose<sup>145</sup>.

The Softmax function<sup>133, 138</sup> is employed to map the output of the preceding step to the data space of (0,1), thereby enhancing the accuracy of classification.

Through these aforementioned steps, the final result, whether it pertains to data



classification or labeling, is obtained.

## 2. Convolutions in Convolutional Neural Networks

In the Fourier transform, convolution is defined as follows

$$f(t) * g(t) = \int_{-\infty}^{\infty} f(t - \tau)g(\tau)d\tau = \int_{-\infty}^{\infty} f(\tau)g(t - \tau)d\tau \quad (3.8)$$

The above definition refers to the convolution in the continuous Fourier transform, and its application is mainly in the time domain and frequency domain transform.

But in the neural network algorithm, it is used less and more in one domain, so it is also written as

$$(f * g)(n) = \int_{-\infty}^{\infty} f(n - \tau)g(\tau)d\tau = \int_{-\infty}^{\infty} f(\tau)g(n - \tau)d\tau \quad (3.9)$$

Then for the discrete Fourier transform, the convolution is defined as

$$(f * g)(n) = \sum_{\tau=-\infty}^{\infty} f(\tau)g(n - \tau) \quad (3.10)$$

In the Fourier transform, convolution in the time domain corresponds to product in the frequency domain. We have mentioned that a time-domain signal  $f(t)$  can be filtered after being convolved with another specific function  $g(t)$ . In fact, the same is true for the neural network algorithm. After the original data  $f(n)$  is convolved with a specific  $f(n)$ , since some data in  $F(f)$  that do not conform to the type of  $F(g)$  will become 0, the obtained new  $(f * g)$  means that a certain part of  $f(n)$  is extracted to meet the characteristics of  $g(n)$ .

The above is for the case of one-dimensional data. For two-dimensional discrete convolution, it is defined as

$$(f * g)(m, n) = \sum_i \sum_j f(i, j)g(m - i, n - j) \quad (3.11)$$

$f$  refers to the input data matrix, and  $g$  is the weight coefficient matrix, which is commonly referred to as the convolution kernel.

$f$  is an  $m * n$  pixel matrix, and  $g$  is a convolution kernel of  $x * x$  ( $x$  is generally an odd number).

After  $f(m, n)$  is convolved with different  $g(x, x)$ , different types of information in  $f(m, n)$  can be extracted, such as horizontal texture, vertical texture, circular texture

and so on.

Hence, the operation performed by a convolutional neural network is essentially analogous to applying a spatial filter in image processing. Nevertheless, it's important to emphasize that the convolution kernel and the original matrix are not directly multiplied; instead, each corresponding element is computed after a  $180^\circ$  rotation around the central element.

In CNN, we first consider the local information independently at the bottom layer and then use the most representative local data to obtain a new round of features on the basis of obtaining obvious local features. Finally, consider the big picture. This approach is very beneficial for spatial information processing, which is why we use 2D data to explain CNN. However, this method does not take into account the order of local data, so CNN is not so suitable when it comes to considering the impact of previous data on subsequent data, such as text data, voice data, and so on. However, language translation or speech recognition, emotional classification of different texts, music generation, etc. all put new requirements on the algorithm, so we need to introduce a new deep learning algorithm<sup>145</sup>, which is the recurrent neural network (RNN) and its enhanced Long Short-Term Memory (LSTM)<sup>146</sup> algorithm to process the sequence model.

Of course, we are also very curious, how does the convolution kernel meet different needs to find the most suitable features? Because we mainly want to understand CNN in combination with convolution in this part, and this part involves the parameter update problem in training neural network, we will explain it in detail in the next chapter in conjunction with the recurrent neural network (RNN) algorithm.

### 3.3 The Recurrent Neural Network (RNN)

Before introducing The Recurrent Neural Network (RNN)<sup>147-153</sup> algorithm, I would like to explain some basic details.

#### A. The Sequence Model

A model that involves sequential data either as its input or output is referred to as a sequential model<sup>151, 154</sup>. We will take Recurrent Neural Network (RNN) as an example. For more detailed course explanations, please refer to Andrew Ng's Deep Learning Course, other relative papers or books<sup>155</sup>.

#### B. Notation

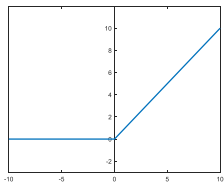
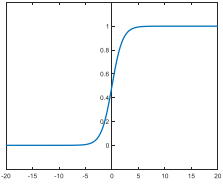
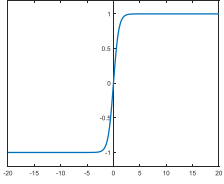
The language was first digitized in the lexicon, and each word has a specific position in the lexicon. We use  $N$  data to represent  $N$  words. Each word is represented by an  $N$ -dimensional vector<sup>156</sup> (which facilitates subsequent matrix calculations).

When we need to translate a sentence, we first need to divide the words in the sentence according to their step in the sentence (rather than the position in the dictionary), usually represented by  $t$ .

#### C. Activation function

The activation function determines whether a neuron should be activated highlighting whether the calculation result should be retained, and how it should be retained and passed down. Some common activation functions are shown in Table 3.1.

**Table 3.1** Common Activation Functions<sup>154, 157, 158</sup>

Name	Relu	Sigmoid	Tanh	Softmax
Eqn.	$f(x) = \begin{cases} 0 & (x \leq 0) \\ x & (x > 0) \end{cases}$	$f(x) = \frac{1}{1 + e^{-x}}$	$\tanh(x) = \frac{1 - e^{-2x}}{1 + e^{-2x}}$	$S_i = \frac{e^i}{\sum_j e^i}$
Plot				

The Softmax function takes the layer's output and transforms it into a value within the range of (0,1) while also ensuring normalization, where the sum of all elements equals 1<sup>154</sup>. This allows it to be directly interpreted as a probability distribution, and the category with the highest probability is chosen as the prediction target.

#### D. Cross Entropy<sup>159</sup>

$$CE = - \sum_{y_i} y_i \log \hat{y}_i \quad (3.12)$$

$y_i$  is the real probability distribution,  $\hat{y}_i$  is the predicted probability distribution,  $\log$  is usually  $\log_2$  in the algorithm.

In the classification problem, because only one of the classification labels has a true value of 1, and the rest are 0, the cross-entropy can also be written as

$$CE = -\log \hat{y}_i \quad (3.13)$$

For the dichotomous case, which can also be written as

$$CE = -y_i \log \hat{y}_i - (1 - y_i) \log (1 - \hat{y}_i) \quad (3.14)$$

And in the algorithm, cross entropy is usually used as a standard logistic regression loss function, so it is also called cross entropy loss function (Cross Entropy Loss<sup>160</sup>). In Recurrent Neural Network (RNN),  $y_i$  refers to the real label  $y^{(t)}$  at  $t$  step, and  $\hat{y}_i$  to the calculated predicted label  $\hat{y}^{(t)}$  at  $t$  step.

#### 1. The Recurrent Neural Network (RNN)<sup>147, 149-152, 154, 161</sup>

Similar to CNN, RNN also performs calculations at each position in sequence, but instead of using the local small window of convolution, it uses shared parameters to calculate the hidden state  $a^{(t-1)}$  and the input data  $x^{(t)}$  of the current step for calculation. Just like when people are reading, RNN is also processing information in order. For example, RNN is processing a piece of data at the  $t$  step, which summarizes all the information collected by  $t$  step, as shown in Fig. 3.7.

The specific calculations involved are below

$$a^{(t)} = \tanh (W_{ax}x^{(t)} + W_{aa}a^{(t-1)} + b_a) \quad (3.15)$$

$$\hat{y}^{(t)} = \text{softmax}(W_{ya}a^{(t)} + b_y) \quad (3.16)$$

Where  $W_{ax}$ ,  $W_{aa}$ ,  $b_a$ ,  $W_{ya}$ ,  $b_y$  are weight and biases respectively, and are the same at each step.

$a^{(t-1)}$  is the hidden state at  $t - 1$  step,  $x^{(t)}$  is the input value at  $t$  step,  $a^{(t)}$  is the hidden state at  $t$  step,  $a^{(0)} = 0$ ,  $\hat{y}^{(t)}$  is the output value at  $t$  step.

For the convenience of calculation, we usually use matrix notation in which Eqn. 3.15 becomes

$$a^{(t)} = \tanh ([W_{ax} : W_{aa}][x^{(t)}, a^{(t-1)}] + b_a) \quad (3.17)$$

Or

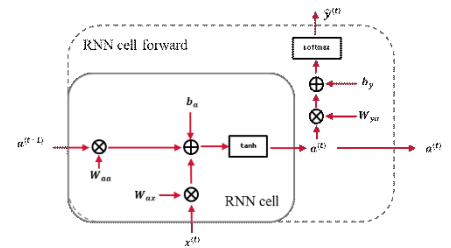


**Fig. 3.7** RNN cell

$$a^{(t)} = \tanh ([W_{ax} : W_{aa}] [x^{(t)} : a^{(t-1)}] + b_a) \quad (3.18)$$

Sometimes  $[W_{ax} : W_{aa}]$  can also be written as  $W_a$ .

In RNN,  $a^{(t-1)}$  represents the network's memory of  $t - 1$  and previous information. Then Eqn. 3.17 means that the calculation result of the hidden layer  $a^{(t)}$  contains the input  $x^{(t)}$  of  $t$  step and the information of  $t - 1$  step and before. And Eqn. 3.16 means that the output  $\hat{y}^{(t)}$  at  $t$  step is determined according to the information contained in the hidden layer  $a^{(t)}$ , which means that  $\hat{y}^{(t)}$  not only contains the current step. The information of  $t$  also includes all the information before  $t$  step, so the network will remember the information before  $t$  and apply it to the current output  $\hat{y}^{(t)}$ .

At the same time, the hidden layer  $a^{(t)}$  will be used as the input of  $t + 1$  step to participate in the calculation of the next step, which means that the network processes the information at  $t + 1$  step based on the information summarized at  $t$  step, and updates the hidden layer  $a^{(t+1)}$ , and get the output  $\hat{y}^{(t+1)}$  of  $t + 1$  at the same time; which repeats, as shown in Fig. 3.8.

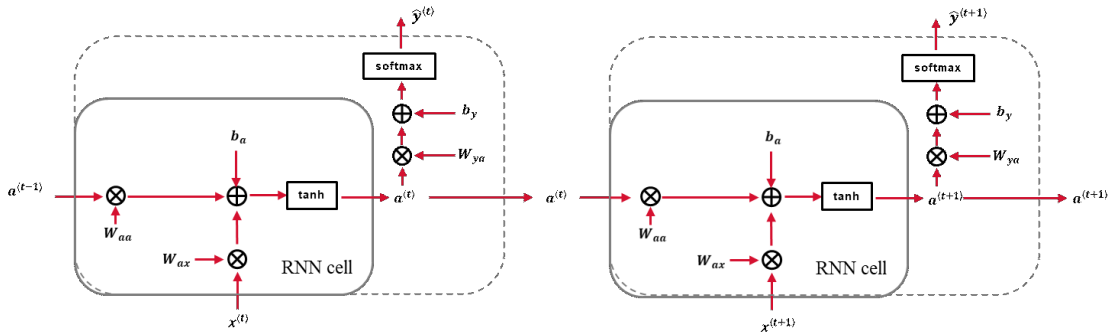


**Fig. 3.8** RNN over multiple time steps.

We will now explain the back propagation, that is, the problem of parameter update.

Through the initial values of the calculation parameters  $W_{ax}$ ,  $W_{aa}$ ,  $b_a$ ,  $W_{ya}$ ,  $b_y$ , we get the calculation output value corresponding to each step from  $\hat{y}^{(1)}$  to  $\hat{y}^{(t)}$ . However, they are expectedly deviate from the true output values from  $\hat{y}^{(1)}$  to  $\hat{y}^{(t)}$ . Then it's necessary to use the Cross Entropy Loss introduced before to calculate the loss function between the calculated value and the actual value.

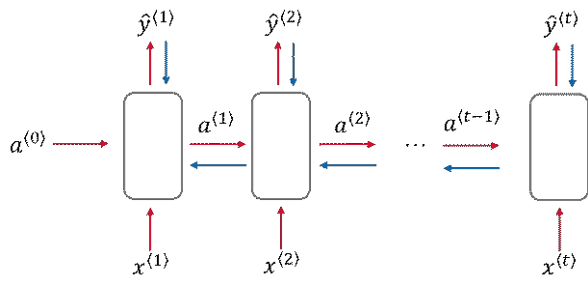


**Fig. 3.9** Calculation process of loss function

The genesis of these loss functions can be traced back to inaccuracies in the initial parameter settings and the ongoing updates

during computation. To mitigate this, we employ a backpropagation approach, reiteratively utilizing the loss function to discern the impact of each calculation parameter on the output value. This involves calculating the partial derivatives of the Cross Entropy Loss with respect to each parameter. Subsequently, these derivatives guide the update process for the calculation parameters, allowing for a refined adjustment that aligns with the optimization goal. In essence, the continuous backpropagation of the loss function serves as a corrective mechanism, enhancing the precision of the model through systematic parameter updates, as shown in Fig. 3.9. Then forward step again to get the new output value from  $\hat{y}^{(1)}$  to  $\hat{y}^{(t)}$ , calculate the loss function again, and backpropagate to update the calculation parameters. Repeat this until the calculated output value consistent with the actual value is obtained. This is how the calculation parameters are updated, and finally can complete the task we need.

To summarize, we set the initial value of the random parameter, use RNN algorithm to obtain the calculated output value, and then compare the actual value with the calculated value, and then reverse the influence of the initial value on the calculated value, update the parameters, calculate again, and continue to iterate until a satisfactory output value is finally obtained. This process is similar to CNN, RNN, and Transformer.

There are many different and more complex types of RNNs<sup>162</sup>, such as multi-layers RNN that adds more neural networks before the output layer<sup>154</sup>, or there are bidirectional RNNs<sup>162, 163</sup> in one program that read data from two directions, etc. The above two forms of RNN can well solve the problem of RNN data weight imbalance, which can be stated as, previous data can have an impact on subsequent data, while the data at the rear cannot affect the previous data.

RNN has a vanishing gradient<sup>164</sup> and exploding gradient<sup>165</sup> problems<sup>166, 167</sup>.

The term "exploding gradient" signifies that parameter values grow excessively large, potentially leading to overflow and resulting in non-numeric values<sup>165</sup>. This

problem can be addressed through gradient pruning and clipping, which involves scaling the gradients when they surpass a predefined threshold.

Vanishing gradient phenomenon<sup>164, 166</sup> occurs as the network's depth increases, causing the impact of the initial hidden layer on the output of subsequent computations to diminish progressively. In the process of backpropagation, we use the chain rule to obtain partial derivatives to update the calculation parameters. Which also means that the weight update of the first few layers will become so small that the previous neural network cannot work, which is the problem of gradient disappearance<sup>166</sup>. In the natural language model, RNN is not good at processing long sentences, and the previous information will be forgotten after a few cycles.

The gradient problem can be solved by introducing GRU<sup>168, 169</sup> and LSTM architectures.

Our focus here is on LSTM<sup>153, 154</sup>.

## 2. Long short-term memory (LSTM)<sup>146, 153, 170</sup>

LSTM cell is shown in Fig. 3.11. Compared with RNN, LSTM only has one more long-term memory.

(For specific applications, see chapter 3.5. In which, the introduction of the following LSTM cells is the same.)

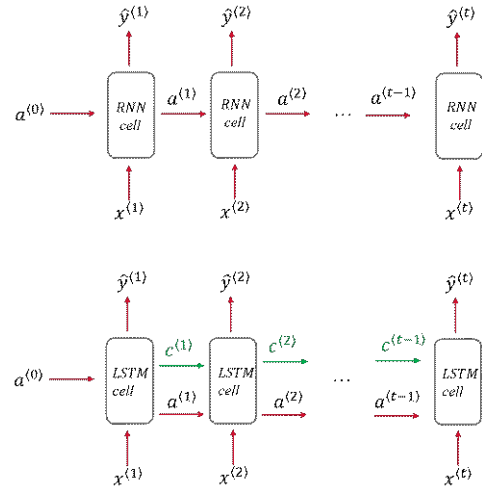


**Fig. 3.10** Comparison between RNN and LSTM

$$\Gamma_f^{(t)} = \sigma(W_f[a^{(t-1)}, x^{(t)}] + b_f) \quad (3.19)$$

$$\Gamma_u^{(t)} = \sigma(W_i[a^{(t-1)}, x^{(t)}] + b_i) \quad (3.20)$$

$$\hat{c}^{(t)} = \tanh(W_c[a^{(t-1)}, x^{(t)}] + b_c) \quad (3.21)$$

$$c^{(t)} = \Gamma_f^{(t)} \cdot c^{(t-1)} + \Gamma_u^{(t)} \cdot \hat{c}^{(t)} \quad (3.22)$$

$$\Gamma_o^{(t)} = \sigma(W_o[a^{(t-1)}, x^{(t)}] + b_o) \quad (3.23)$$

$$a^{(t)} = \Gamma_o^{(t)} \cdot \tanh(c^{(t)}) \quad (3.24)$$

$$\hat{y}_{pred}^{(t)} = \text{softmax}(W_y a^{(t)} + b_y) \quad (3.25)$$

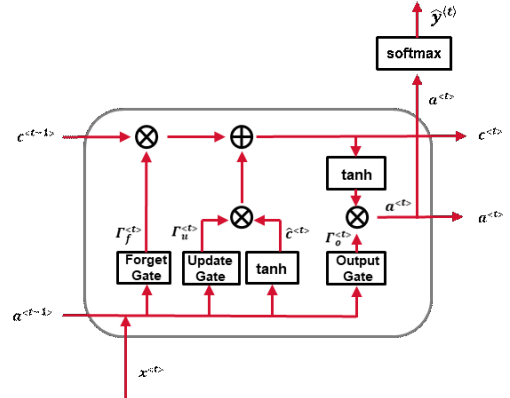


**Fig. 3.11** LSTM Cell

Please find List of Symbols for the meaning of each parameter. Eqs. 3.19-3.25 are working equations of the LSTM cell we briefly describe the operation of the cell below.

First,  $\Gamma_f^{(t)}$  (forget gate)<sup>171</sup> is calculated as Eqn.3.19 by the input data of  $t$  step  $x^{(t)}$  and the hidden state from the previous cell  $a^{(t-1)}$ . If  $\Gamma_f^{(t)}$  is close to 0, the information in  $c^{(t-1)}$  will be forgotten, if  $\Gamma_f^{(t)}$  is close to 1, the information in  $c^{(t-1)}$  it will be kept. Second,  $\Gamma_u^{(t)}$  (update gate) is also calculated as Eqn.3.20 by  $x^{(t)}$  and  $a^{(t-1)}$ .  $\hat{c}^{(t)}$  (candidate value) is as shown in Eqn.3.21 as well. It should notice that  $\hat{c}^{(t)}$  (candidate value) is not  $c^{(t)}$  (the cell state in  $t$  step). Above steps are selecting which data in the input information of  $t$  step are important.

Third, the cell state in  $t$  step  $c^{(t)}$  is updated as Eqn.3.22 by using the forget gate  $\Gamma_f^{(t)}$  to connect the previous cell state  $c^{(t-1)}$  and the update gate  $\Gamma_u^{(t)}$  to connect the candidate value  $\hat{c}^{(t)}$ . This step is to update the data that can be stored in long-term memory.

Forth,  $\Gamma_o^{(t)}$  (output gate) is also calculated as Eqn.3.23 by  $x^{(t)}$  and  $a^{(t-1)}$ . This is to select which data we want to output at  $t$  step.

Fifth, the hidden state  $a^{(t)}$  is determined as Eqn.3.24 by the output gate  $\Gamma_o^{(t)}$  and the cell state  $c^{(t)}$ . This step is to update the data that can be stored in short-term memory.

At the last step, prediction for  $t$  step  $\hat{y}_{pred}^{(t)}$  is gotten in Eqn.3.25 by the hidden state  $a^{(t)}$ .

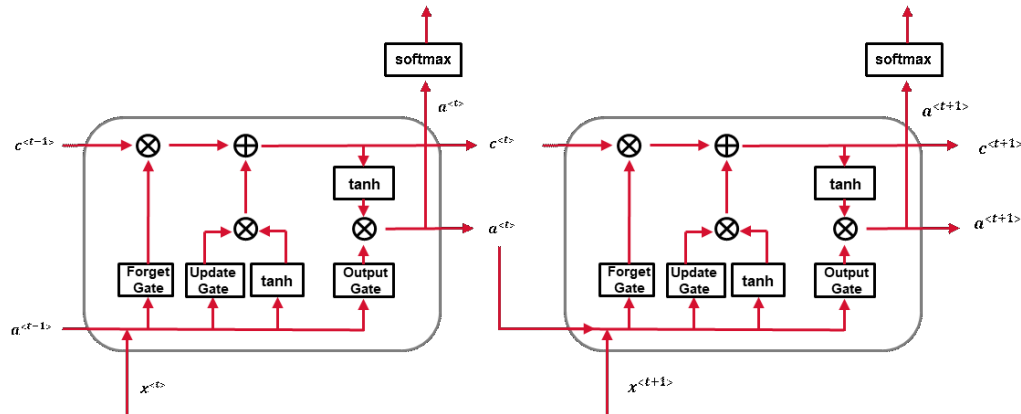


**Fig. 3.12** LSTM over multiple time steps.

Fig. 3.12 describes the process of passing parameters between adjacent LSTM cells. It can be seen from the figure that in the process from  $t$  step to  $t + 1$  step, both the cell state  $c^{(t)}$  and the hidden state  $a^{(t)}$  are passed to the next step as parameters of the previous step. But it is worth noting that the content of  $c^{(t)}$  and  $a^{(t)}$  are different, namely long-term memory and short-term memory, respectively. Which is also the



origin of the LSTM name.

LSTM can solve the problem of gradient disappearance in RNN to a certain extent<sup>154</sup>. LSTM has played an important role in natural language models. But LSTM also has limitations, that is, it relies heavily on forgetting gates<sup>169</sup>. Because once there are too many steps and the forgetting gate is updated too fast, the long-term memory cannot be transmitted very far. In machine translation, LSTM can remember about 30 words<sup>172</sup>. If the sentence is longer, it will be difficult for LSTM. A new algorithm, an attention mechanism can theoretically remember infinitely long information as long as the computing power is sufficient. One of the most influential attention mechanism algorithms is the Transformer.

### 3.4 Transformer

#### 1. Sequence to Sequence Model<sup>173</sup>

Before the Attention Mechanism, the machine translation model used more Sequence-to-Sequence Model as shown in Fig. 3.13. It usually consists of two parts,

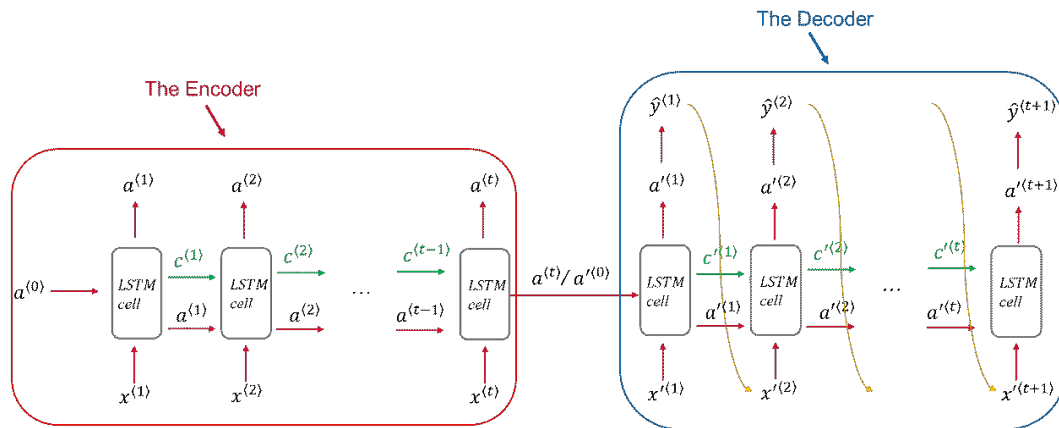


**Fig. 3.13** Encoder and decoder with LSTM.<sup>148</sup>

the encoder and the decoder<sup>163, 174</sup>. It is easy to find that the encoder<sup>175</sup> is similar to LSTM described before, except that the output value of each step is omitted. And the decoder part is similar as well, except that the hidden state at the beginning is no longer  $a^{(0)}$ , but the output of the hidden state  $a^{(t)}$  in encoder. ' here indicates the parameters of the decoder. Another difference is that we use the output  $\hat{y}^{(1)}$  calculated by the previous step as the input  $x'^{(2)}$  for the next step in decoder. Whereas  $x'^{(1)}$  is a blank symbol. And the output of the last step  $\hat{y}^{(t+1)}$  is a terminal symbol. So, the decoder has one more step than the encoder.

But as we mentioned at the end of LSTM section, if the data length is too long,

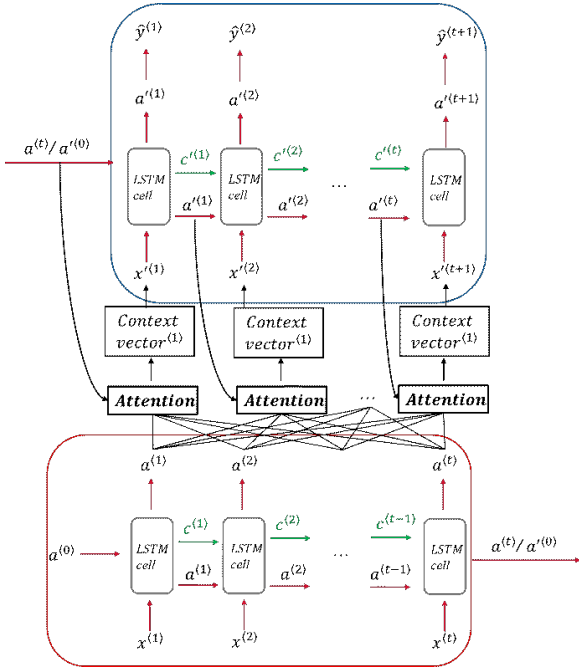


**Fig. 3.14** Attention Mechanism with LSTM

**2. Attention Mechanism**<sup>163, 177, 178</sup>

The attention mechanism is designed to imitate the human way to process data. That is, when processing massive amounts of information, it selectively focuses on some information while ignoring other information<sup>177</sup>. There are many different types of attention mechanisms, we only use the traditional attention mechanism mentioned above to illustrate.

As mentioned before, the data to be processed by Attention is only hidden states.

Suppose at  $t$  step, the Attention needs to process all hidden states from  $a^{(1)}$  to  $a^{(t)}$  of the

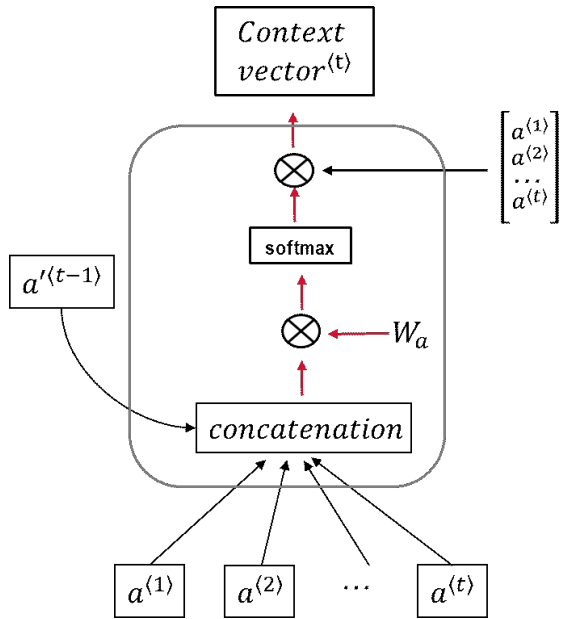


**Fig. 3.15** The Attention Mechanism.

encoder and the hidden state  $a'^{(t-1)}$  of the previous step in decoder. We can take out the attention part separately, and only make a simplification as shown in Fig. 3.15.

The data processing process is as follows

1. Calculate the degree of correlation between the hidden states from  $a^{(1)}$  to  $a^{(t)}$  of the encoder and the hidden state  $a'^{(t-1)}$  in decoder by multiply  $W_a$  and use

LSTM cannot handle it well for a long time<sup>175</sup>. Here we need to introduce the Attention Mechanism, as shown in Fig. 3.14.

This part looks complicated, but it's just an attention model was added between encoder and decoder<sup>175, 176</sup>. The data to be processed by Attention actually consists of two parts: information contained in all hidden states of the encoder, namely from  $a^{(1)}$  to  $a^{(t)}$  and the hidden state in decoder of the previous step  $a'^{(t-1)}$  (see the black arrow part in Fig. 3.14).

softmax to get each hidden states weights. This step is to find out the similarity between certain data in the outputting target data and each data in the inputting source.

2. Use all hidden states from encoder as a vector to multiply the weighted sum of the similarity obtained in the previous step to obtain the context vector in  $t$  step.

In traditional attention mechanism, we can easily find that this method is finding the similarity between the target data and the source data. Next, we will introduce a new concept: self-attention. In this method, the attention mechanism looks for the similarity between the internal elements of source data or target data.

### 3. Self-attention Mechanism<sup>179-181</sup>

It is worth noting that starting from 3. Self-attention Mechanism to 5. Transformer are the introduction to the Transformer algorithm, which comes from Vaswani's paper "Attention is all you need"<sup>180</sup>.

$$Attention(Q, K, V) = \text{softmax} \left( \frac{QK^T}{\sqrt{d_k}} + M \right) V \quad (3.26)$$

$Q$  is the matrix of queries.

$K$  is the matrix of keys.

$V$  is the matrix of values.

$M$  is the optical of mask.

$d_k$  is the dimension of the keys.

The calculation flow chart of the self-attention mechanism is shown in Fig. 3.16.

The calculation steps are

$$q^{(t)} = x^{(t)} W_q \quad (3.27)$$

$$k^{(t)} = x^{(t)} W_k \quad (3.28)$$

$$v^{(t)} = x^{(t)} W_v \quad (3.29)$$

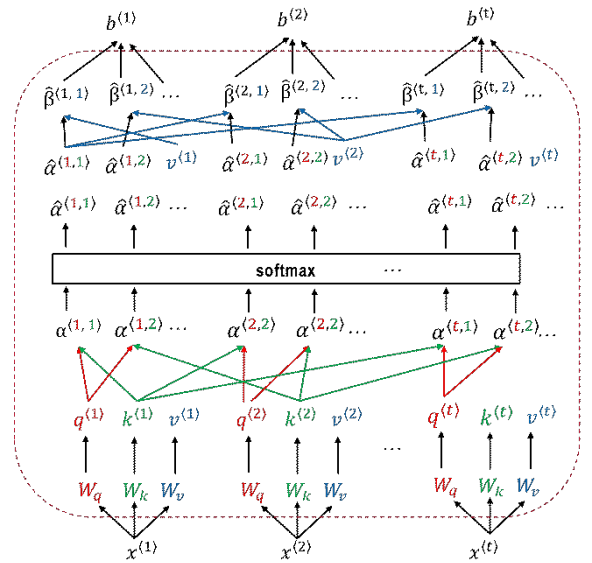


**Fig. 3.16** Self-attention Mechanism.

Eqs.3.27 - 3.29. mean to establish the connection between input data across various dimensions.

$$\alpha_{1,t} = q^{(1)} \cdot k^{(t)} / \sqrt{d_k} \quad (3.30)$$

$$\alpha_{2,t} = q^{(2)} \cdot k^{(t)} / \sqrt{d_k} \quad (3.31)$$

...

$$\hat{\alpha}_{1,t} = \text{softmax}(\alpha_{1,t}) = \text{softmax}(q^{(1)} \cdot k^{(t)} / \sqrt{d_k}) \quad (3.32)$$

$$\hat{\alpha}_{2,t} = \text{softmax}(\alpha_{2,t}) = \text{softmax}(q^{(2)} \cdot k^{(t)} / \sqrt{d_k}) \quad (3.33)$$

...

$$b^{(1)} = \sum_i \hat{\alpha}_{1,t} \cdot v^i \quad (3.33)$$

$$b^{(2)} = \sum_i \hat{\alpha}_{2,t} \cdot v^i \quad (3.34)$$

#### 4. Multi-head self-Attention<sup>180</sup>

Multi-head self-Attention is basically the same as self-attention. The main difference is that the data of  $Q, K, V$  are split into  $n$  head as Fig. 3.17.

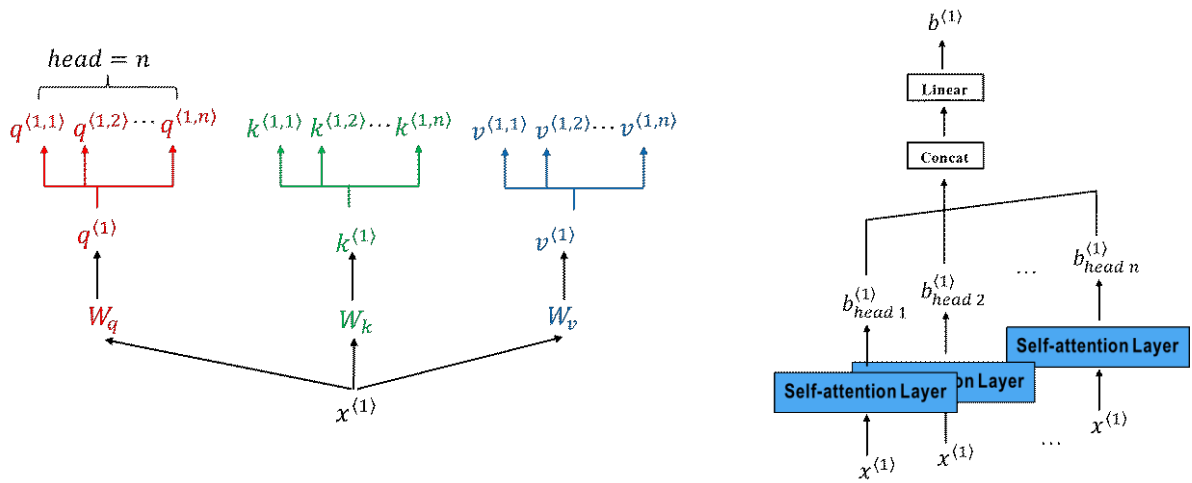


**Fig. 3.17** Multi-head self-Attention Mechanism<sup>180</sup>.

We only take  $x^{(1)}$  as an example to illustrate the calculation process as shown in Fig.3.17. It is easy to see that compared to self-attention, Multi-head self-Attention performs much more steps as follows,

1. first splits the parameters  $Q, K, V$  into  $n$  heads,
2. performs self-attention calculations separately,
3. concatenates the obtained results,
4. substitutes the data into the linear layer to get  $b^{(1)}$ .

The calculation formula is as follows.

$$\text{Multihead}(Q, K, V) = \text{Concat}(\text{head}_1, \text{head}_2, \dots, \text{head}_n)W^O \quad (3.35)$$

Where  $\text{head}_i = \text{Attention}(QW_i^Q, KW_i^K, VW_i^V)$

## 5. Transformer<sup>180</sup>

In order to solve the problem of cyclic operation and parallel operation in traditional attention, a new algorithm was proposed, which is the famous Transformer<sup>180</sup>. In this model, LSTM is abandoned. And the combination of self-attention and feed-forward neural network is used instead. that is, "Attention is all you need"<sup>180</sup>. Of course, encoder-decoder is used as the framework to process data. The structure of a Transformer is shown in Fig. 3.18.

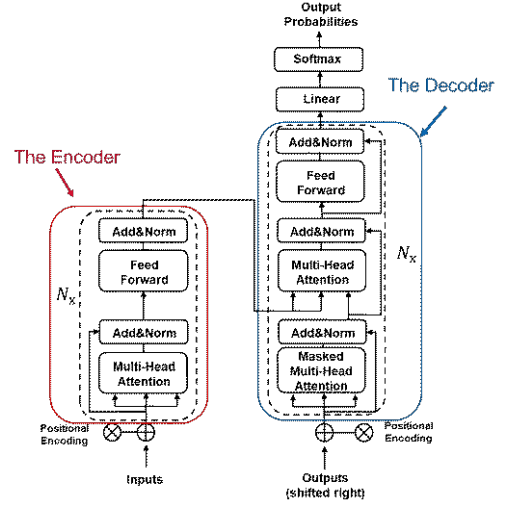


**Fig. 3.18** Transformer.<sup>180</sup>

The following is an introduction to the calculation process of Transformer.

Since the position information is not included in the transformer operation, it is necessary to add positional encoding at the very beginning.

$$PE_{(pos,2i)} = \sin\left(\frac{pos}{10000^{\frac{2i}{d}}}\right) \quad (3.36)$$

$$PE_{(pos,2i+1)} = \cos\left(\frac{pos}{10000^{\frac{2i}{d}}}\right) \quad (3.37)$$

$d$  is the dimension of the word embedding and positional encoding<sup>180</sup>.

$pos$  is the position of the word<sup>180</sup>.

$i$  refers to each of the different dimensions of the positional encoding<sup>180</sup>.

After positional encoding is the encoder.

Put the original data together with the location information into the encoder.

In addition to multi-head attentions, as we mentioned earlier, the encoder also includes Add&Norm<sup>182</sup> and Feed forward neural network.

The Add&Norm layer is to add the output result of multi-head attention to the data before inputting multi-head attention together. The purpose is to speed up the gradient calculation in training. Then normalize the sum of the above data to stabilize the training.

Feed forward neural network is a two-layer fully connected linear layer, usually using Relu as the activation function.

Perform Add&Norm again to complete the calculation of the encoder.

The input of the Decoder is the same as that of the encoder. The following is the

operation process of the data in decoder.

1. After the data enters the decoder, a masked multi-head attention will be performed. The only difference between this part and multi-head attention is the use of mask tensors. Which means the result of  $QK^T$  only displays the data in the lower left triangle. This is to prevent transformer from obtaining information after the current time during parallel computing.
2. The result of calculation needs to be operated by Add&Norm as well.
3. Use the value  $V$  and key  $K$  from the encoder calculation result and the query  $Q$  obtained by the decoder to perform subsequent calculations.
4. Use the above  $Q$ ,  $K$  and  $V$  data, which combines the encoder and decoder, to perform calculations like whole previous encoder. It is worth noticing that this multi-head attention is where the input data and target data mapping meet. The main idea of this part is to obtain the correct output by finding out the corresponding relationship between the input data and the target data by giving the target data different weights. The last step is to put the calculation result of the decoder into a linear layer and use softmax to get the final probability data to obtain the final target data.

$N_x$  in the encoder and the decoder represents multi-layer stacking to obtain more information of different dimensions.

The self-attention in Transformer is like the convolution in CNN. Similarly, multi-head attention is similar to multi-channel convolution in CNN, which uses multiple convolution kernels for operations. And the Add&Norm layer in the transformer is somewhat comparable to shortcut of ResNet in CNN. These structures enable Transformer to remember more information over long distances than RNN or LSTM. Whether it is on sequence data such as natural language processing or matrix data such as image processing, Transformer has powerful capabilities.

There are many improved versions of Transformer, among which the most widely used is bidirectional encoder representation transformer (BERT)<sup>183</sup>, and other large language model<sup>184</sup>, which has achieved excellent results in natural language processing.

## 3.5. Simulation, Classification, and Correction with Deep Learning

### 1. Simulation

First, according to the correction method used in the past, we made certain adjustments to get simulation spectrum. Phase delay  $\phi$  were changed to get a series of  $\phi_b$  by applying IFFT according to the literature<sup>14</sup>. As contrast, here we chose a series specific phase index is based on simulated spectrum like the distorted spectrum after FFT.

Second, Eqn. 2.128 was used to get the distorted simulated spectra of different states.

Next, the mixed spectrum of the distorted and normal spectra was achieved, by varying the above distorted and normal spectra in different percentages (the total percentage is 100%).

$$A_{\text{mix}}(w) = aA_{\phi_b}(w) + (1 - a)A(w) \quad (0 < a < 1) \quad (3.38)$$

Finally, by adding different proportions of twisted baselines (specifically, the absorption spectra of some substances whose refractive index is higher than the ATR critical refractive index, such as carbon black, graphene, etc.), the final simulated twisted spectrum was obtained as Fig. 3.19.

$$A_{\text{si}}(w) = A_{\text{mix}}(w) + mB(w) \quad (3.39)$$

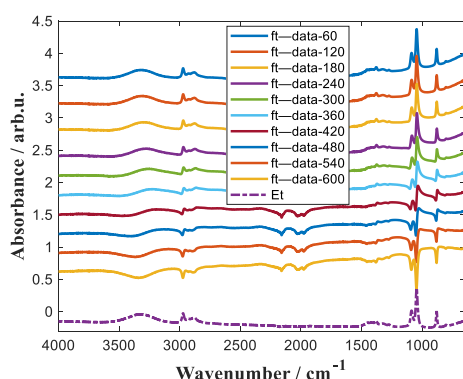


**Fig. 3.19** Distorted simulated spectrum(Toluene and Carbon black) by IFFT and FFT as training data.

## 2. Classification and correction

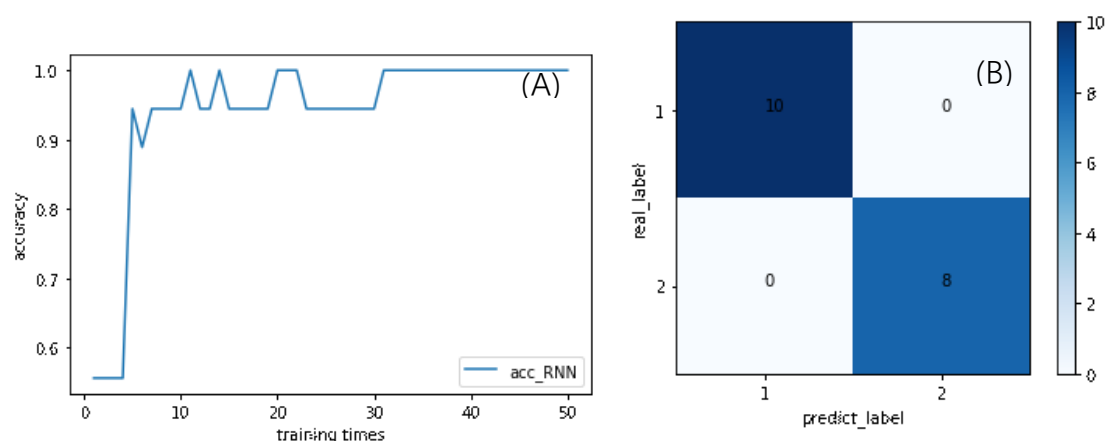


**Fig 3.20** Accuracy of Classification by LSTM (A); Classification result by LSTM (B).

As depicted in Fig. 3.20, the classification results obtained by LSTM indicated that after approximately 31 training iterations, the accuracy rate reaches approximately 100%. which demonstrated effective differentiation between distorted and normal spectra. However, it's important to acknowledge that this high accuracy may be attributed, in part, to the limited experimental data available in our study.

Following the successful differentiation of distorted spectra from normal ones, the subsequent focus lies on correcting the distorted spectra. The conventional method of correcting spectra using IFFT and FFT, derived from Peter Hamm's paper<sup>114</sup>, has been employed in our previous work to achieve accurate spectra correction. Nevertheless, this method presents drawbacks, notably the requirement for segment-wise corrections due to varying degrees of distortion in each peak. Although the PSD maximum difference method can be employed to calibrate the peak, the resulting peak shape remains an envelope rather than a precise absorption peak. Additionally, the baseline of distorted spectra is often elevated to different extents due to the influence of high refractive index substances, necessitating baseline correction prior to applying the IFFT and FFT methods. This baseline correction process, especially when dealing with the superposition of uneven distortion across different wavelength ranges, poses a significant challenge. These limitations considerably restrict the widespread application of this method.

In contrast, when employing deep learning methods, such as neural networks, these concerns are alleviated. Through the process of machine learning, all influencing



factors are integrated to produce a single learning outcome, akin to operations within a black box. Furthermore, neural network algorithms facilitate faster correction speeds and can operate in batch mode. However, it's important to note that the training and testing data utilized in our calibration are derived from simulations of the IFFT and FFT processes. Although traditional methods may be computationally cumbersome, they serve as the foundation for our ability to utilize deep learning algorithms for spectrum correction.

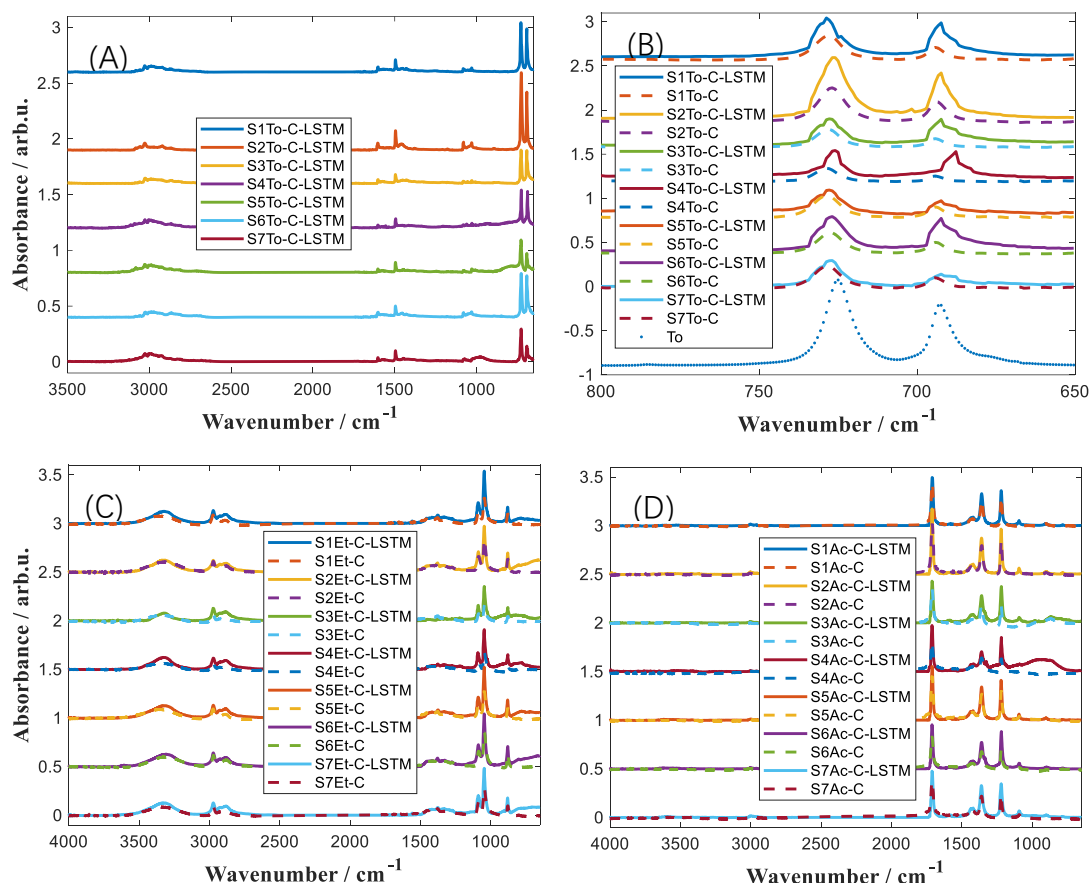


**Fig 3.21** Corrected spectrum by LSTM ( A ); Comparison corrected spectrum between two methods ( B, C, D ).

According to the corrected spectrum depicted in Fig. 21A, LSTM was utilized to rectify the seven mixed distorted spectra of carbon black and toluene, yielding accurate spectra. Subsequently, in Fig. 3.21B, it is evident that the spectrum obtained via LSTM closely resembles the corrected spectrum derived from traditional methods, albeit with subtle differences in peak heights. Figures 21C and 21D illustrate the comparison of calibration results for mixtures of carbon black and ethanol, as well as acetone, obtained through LSTM and the IFFT/FFT methods, respectively. Remarkably, the corrected

spectra from both LSTM and traditional methods exhibit nearly identical overlap. This observation suggests that despite LSTM operating as a black box within our approach, its results closely align with those obtained through the calculation and correction of spectra based on physical principles.

The Transformer as introduced in chapter 3.4. In the context of spectral correction, only the encoder part of the Transformer is utilized for classification purposes. Our experimentation revealed that compared to LSTM, the Transformer model is more sensitive to parameter selection. Inadequate parameter selection can lead to loss convergence issues, where the loss function becomes trapped at specific values, hindering further descent.

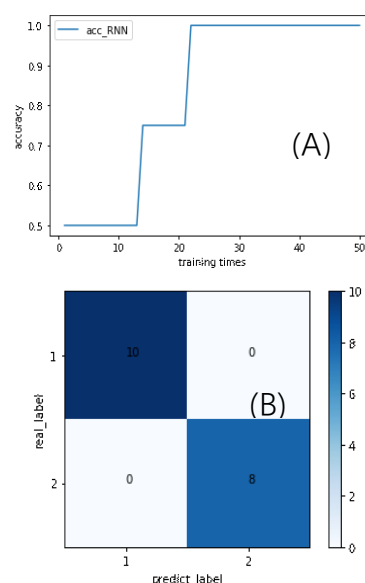


**Fig. 3.22** Accuracy (A) and Classification result by Transformer (B).

Fig. 3.22A illustrates the accuracy rate and training time of the Transformer model during the classification process. Notably, after 23 training iterations, the accuracy rate reaches nearly 100%. Subsequently, Fig. 3.22B presents the classification results achieved by the Transformer model. Both LSTM and Transformer models exhibit considerable potential and demonstrate exceptionally high accuracy in spectral classification tasks. Nonetheless, it's important to acknowledge the potential for overfitting due to the limited dataset. However, this underscores the broader applicability of deep learning not only in distinguishing distorted spectra but also in identifying and classifying substances across various spectral domains. This not only pertains to infrared spectra but extends to spectra across different modalities, laying the groundwork for increased automation in analytical chemistry through machine learning methodologies.

Similar to Fig. 3.22, Fig. 3.23 presents a comparison between the traditional method and the rectification outcomes achieved using Transformer, denoted as "T." .

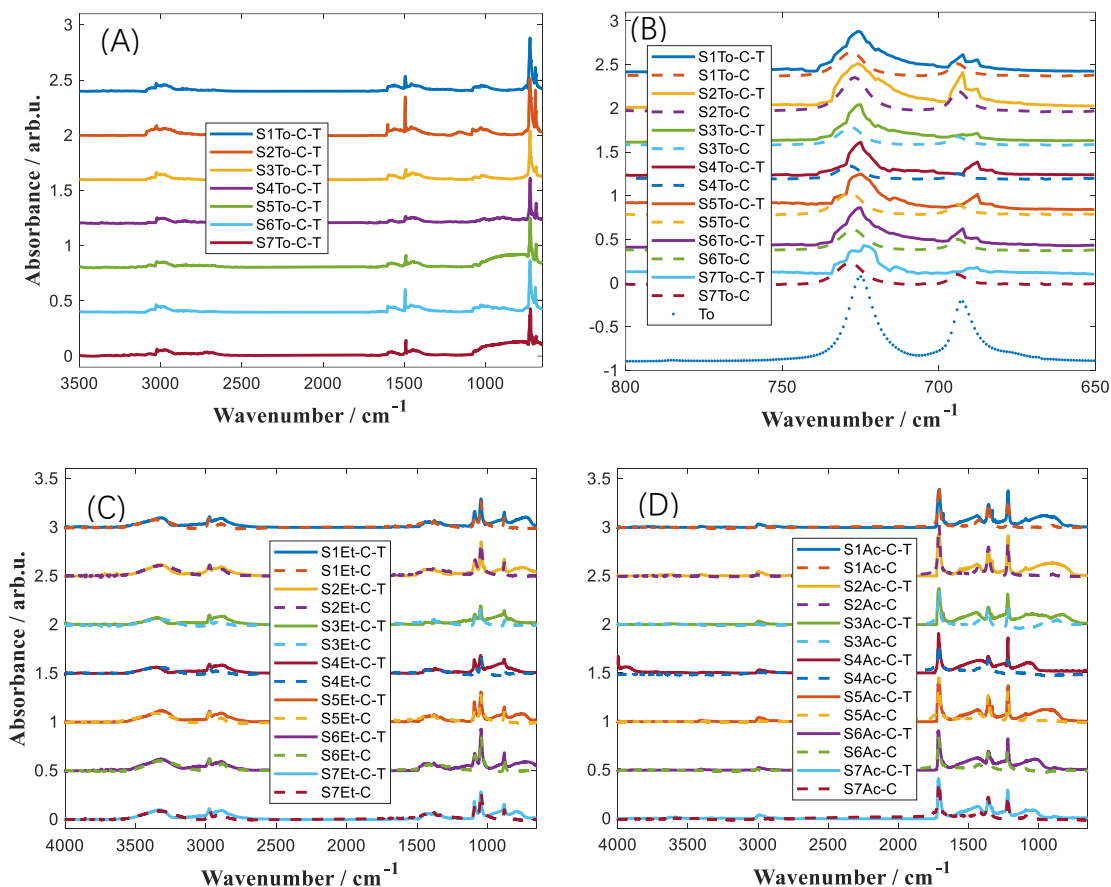


**Fig. 3.23** Corrected spectrum by Transformer (A); Comparison corrected spectrum between two methods (B,C,D).

From Fig. 3.23A, it is evident that Transformer encounters challenges in correcting the baseline, which may potentially be attributed to computational limitations. This issue becomes more pronounced in the calibration map depicted in Figure 3.23D. However, despite these challenges, both LSTM and Transformer exhibit robust correction capabilities compared to traditional methods.

In the traditional approach, the typical procedure involves first removing the absorption peaks caused by Diamond, followed by addressing the inclined baseline, and ultimately employing KK transformation to attain the corrected peaks. Notably, in this process, removing the baseline proves particularly challenging as it encompasses not only the baseline tilt caused by carbon black but also distorted absorption peaks, including inverted peaks resulting from partial reflection.

Conversely, deep neural network algorithms, such as LSTM and Transformer, can simultaneously address both baseline and peak distortion issues, thereby yielding reliable correction outcomes. This capability allows for the consideration of multiple

spectral artifacts in a unified framework, leading to improved correction results compared to traditional methods.

### **3. Conclusion**

Initially, we simulated distorted spectra by employing the IFFT and FFT methods, varying the degree of distortion for individual substances. Subsequently, we incorporated the distorted baseline obtained from experimentation to derive the final mixed distorted spectra. In our experiments, we employed two distinct methodologies, LSTM and Transformer, to classify and rectify spectra. Ultimately, we identified the most effective model to classify and correct experimental data, achieving correction results comparable to traditional methods but with significantly improved speed and batch correction capability.

In summary, both LSTM and Transformer models have exhibited robust capabilities in discriminating and rectifying distorted ATR spectra, thereby laying a solid groundwork for their broader application. However, further research is warranted to optimize these procedures. Additionally, given the limited input data, potential overfitting issues necessitate careful consideration and mitigation in future endeavors.

# 4. Surface - Enhanced Spectrum

## 4.1 Calculation

Following the introduction of distorted spectroscopy, this chapter will center its attention on surface-enhanced spectroscopy utilizing theoretical calculations and experimental analysis in the infrared (IR) domain<sup>185</sup>.

### 1. Fresnel's equations<sup>17</sup>

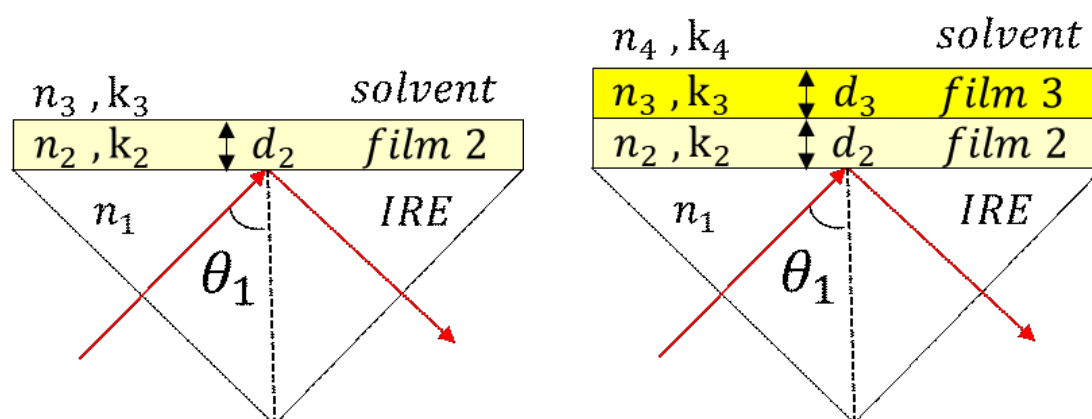


**Fig.4.1** The internal reflection element (IRE) has a single-layer metal (substance with a negative relative permittivity) thin layer model(left) and a double-layer thin film model on the surface(right).

As illustrated in Fig. 4.1, we commence by simplifying the model, treating the middle layer as an ideal layered structure. An assumption is made that all thin layers are isotropic.

Referencing the introductory content in Chapter 1, it is established that calculations are rooted in Maxwell's equations, necessitating the contemplation of electric and magnetic field continuity at the phase boundary. Specific calculations are derivable through matrices or Fresnel's equations. The matrix method, pioneered by Hansen and Abelès<sup>186</sup>, proves instrumental in computing overall reflectance for scenarios involving combinations of absorbing and non-absorbing isotropic layers at varying angles of incidence<sup>17</sup>. This method finds significant applications in absorption, reflection, and refraction calculations for diverse materials, thicknesses, and angles of incidence. While the calculation method based on Fresnel's equations is more straightforward to

comprehend than the matrix method, it is limited in its applicability to anisotropic materials.

Subsequently, we will employ Fresnel's equations to calculate single/multi-layer thin structures with predetermined thickness<sup>33, 51, 187</sup>.

$$\hat{n}_i = n_i + k_i \quad (i = 1,2,3,4) \quad (4.1)$$

$$m_1 = \hat{n}_1 \cos \theta_1 \quad (4.2)$$

$$m_i = \sqrt{\hat{n}_i^2 - \hat{n}_1^2 \sin^2 \theta_1} \quad (i = 2,3,4) \quad (4.3)$$

$$r_{ij,s} = \frac{m_i - m_j}{m_i + m_j}, \quad r_{ji,s} = \frac{m_j - m_i}{m_i + m_j} = -r_{ij,s}, \quad t_{ij,s} = \frac{2m_i}{m_i + m_j}, \quad t_{ji,s} = \frac{2m_j}{m_i + m_j} \quad (4.4)$$

$$r_{ij,p} = \frac{\hat{n}_i^2 m_j - \hat{n}_j^2 m_i}{\hat{n}_i^2 m_j + \hat{n}_j^2 m_i}, \quad r_{ji,p} = \frac{\hat{n}_j^2 m_i - \hat{n}_i^2 m_j}{\hat{n}_i^2 m_j + \hat{n}_j^2 m_i} = -r_{ij,p},$$

$$t_{ij,p} = \frac{2\hat{n}_i^2 m_j}{\hat{n}_i^2 m_j + \hat{n}_j^2 m_i}, \quad t_{ji,p} = \frac{2\hat{n}_j^2 m_i}{\hat{n}_i^2 m_j + \hat{n}_j^2 m_i} \quad (4.5)$$

$$\phi_2 = 2\pi v d_2 m_2 = 2\pi v d_2 \sqrt{\hat{n}_2^2 - \hat{n}_1^2 \sin^2 \theta_1} = 2\pi \frac{d_2}{\lambda} m_2 \quad (4.6)$$

$$t_{ij,p} = \frac{2\hat{n}_i^2 m_j}{\hat{n}_i^2 m_j + \hat{n}_j^2 m_i}, \quad t_{ji,p} = \frac{2\hat{n}_j^2 m_i}{\hat{n}_i^2 m_j + \hat{n}_j^2 m_i} \quad (4.7)$$

$$\phi_2 = 2\pi v d_2 m_2 = 2\pi v d_2 \sqrt{\hat{n}_2^2 - \hat{n}_1^2 \sin^2 \theta_1} = 2\pi \frac{d_2}{\lambda} m_2 \quad (4.8)$$

$$r_{123} = \frac{r_{12} + r_{23} \exp(2i\phi_2)}{1 + r_{12} r_{23} \exp(2i\phi_2)}, \quad r_{321} = \frac{r_{32} + r_{21} \exp(2i\phi_2)}{1 + r_{32} r_{21} \exp(2i\phi_2)},$$

$$t_{123} = \frac{t_{12} t_{23} \exp(i\phi_2)}{1 + r_{12} r_{23} \exp(2i\phi_2)}, \quad t_{321} = \frac{t_{32} t_{21} \exp(i\phi_2)}{1 + r_{32} r_{21} \exp(2i\phi_2)}, \quad (4.9)$$

For 3 layers

$$R = R_{123} = |r_{123}|^2 \quad (4.10)$$

For 4 layers

$$\phi_3 = 2\pi v d_3 m_3 = 2\pi v d_3 \sqrt{\hat{n}_3^2 - \hat{n}_1^2 \sin^2 \theta_1} \approx \phi_2 \quad (4.11)$$

$$R = R_{1234} = R_{123} + \frac{T_{123} R_{31} T_{321} \exp(4i\phi_3)}{1 - R_{321} R_{31} \exp(4i\phi_3)} \quad (4.12)$$

$$A = -lgR \quad (4.13)$$

In which

$$T = \frac{T_{123} T_{31} \exp(2i\phi_3)}{1 - R_{321} R_{31} \exp(4i\phi_3)} \quad (4.14)$$

$$R_{ij} = |r_{ij}|^2, T_{ij} = |t_{ij}|^2 \quad (4.15)$$

$\hat{n}_1, \hat{n}_2, \hat{n}_3$  and  $\hat{n}_4$  mean the complex refractive index of medium 1, 2, 3 and 4 respectively.  $n$  and  $k$  are the real part and imaginary part of refractive index.  $\theta_1$  is the angle of incidence.  $d_2$  and  $d_3$  are the thickness of the medium 2 and 3.  $\nu$  is the wavenumber ( $\text{cm}^{-1}$ ).  $i$  is the imaginary unit.  $r$  and  $t$  are the reflection coefficient and the transmission coefficient, respectively.  $s$  and  $p$  are the polarization of incidence light. For example,  $r_{12,s}$  is the reflections arising from the interfaces between incidence medium (medium 1) and layer (medium 2) with s-polarized incident light. For incident light that is not polarized, it can be regarded as 50% mixed light of s-polarized and p-polarized.

$R$  and  $T$  are the overall reflectance and transmission of the system respectively. The parameter  $A$  is eventually the absorbance calculated from the reflectance.

The preceding calculation offers a robust simulation of the ideal thin layer, wherein our consideration is confined to the complex refractive index ( $\hat{n}$ ). However, it is crucial to recognize that the refractive index is fundamentally determined by the complex dielectric constant ( $\epsilon_r$ ). When the real part ( $\epsilon'_r$ ) of the complex dielectric constant assumes a negative value, specific conditions can give rise to the generation of surface plasmon<sup>188-190</sup> resonances.<sup>191</sup> This phenomenon yields a notably pronounced surface-enhanced spectral effect. In the subsequent section, we will provide a concise overview of the principles underlying surface plasmon generation and implement adjustments to traditional calculations, incorporating considerations for the thickness of the thin layer.

## 2. Surface plasmon polaritons (SPPs)

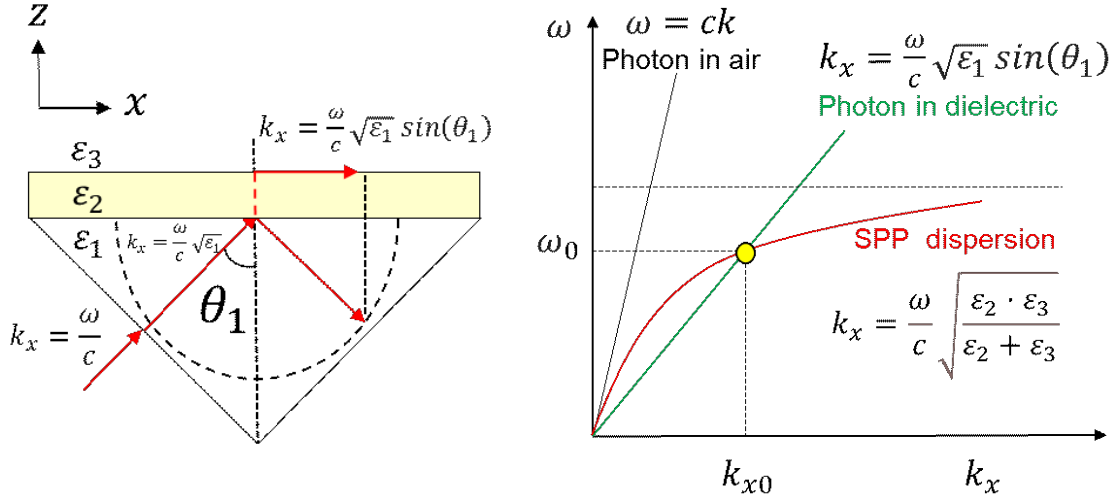


**Fig. 4.2** Demonstration of surface plasmon excitation on the surface of ATR metal (negative relative constant substance) (left), Calculation of the conditions for surface plasmon generation(right).

As shown in Fig. 4.2, which means coupling of photons into surface plasmon polaritons can be achieved using a coupling medium such as a prism or grating to match the photon and surface plasmon polariton (SPP)<sup>192-195</sup> wave vectors (and thus match their momenta) as Eqs. 4.16-4.22. A prism can be positioned against a thin metal film in the Kretschmann configuration<sup>196</sup> or very close to a metal surface in the Otto configuration<sup>192</sup>. In this case, only the transverse magnetic wave, which is p-polarized/TM wave was taken into consideration. According to Maxwell's equation, the dispersion relation for the wave at the interface is shown as Eqn.4.20.

$$k_x = \frac{\omega}{c} \sqrt{\epsilon_1} \sin(\theta_1) \quad (4.16)$$

$$\frac{k_{z2}}{\epsilon_2} + \frac{k_{z3}}{\epsilon_3} = 0 \quad (4.17)$$

$$k_x^2 + k_{z2}^2 = \epsilon_2 \left(\frac{\omega}{c}\right)^2 \quad (4.18)$$

$$k_x^2 + k_{z3}^2 = \epsilon_3 \left(\frac{\omega}{c}\right)^2 \quad (4.19)$$

$$k_{x0} = \frac{\omega}{c} \sqrt{\frac{\epsilon_2 \cdot \epsilon_3}{\epsilon_2 + \epsilon_3}} \quad (4.20)$$



$$k_x = \frac{\omega}{c} \sqrt{\frac{\varepsilon_2 \cdot \varepsilon_3}{\varepsilon_2 + \varepsilon_3}} = \frac{\omega}{c} \sqrt{\varepsilon_1} \sin(\theta_1) \quad (4.21)$$

$$\sqrt{\frac{\varepsilon_2 \cdot \varepsilon_3}{\varepsilon_2 + \varepsilon_3}} = \sqrt{\varepsilon_1} \sin(\theta_1) \quad (4.22)$$

Where,  $c$  is speed of light.  $\omega$  is angular frequency, in which  $\omega = 2\pi\nu$ .  $\varepsilon_1$ ,  $\varepsilon_2$  and  $\varepsilon_3$  mean the relative primitivity of medium 1, 2 and 3 respectively. in which  $\varepsilon_i = \hat{n}_i^2$  ( $i = 1, 2, 3$ ).  $\varepsilon_1 = \hat{n}_1^2 = 2.3778$  (Diamond)<sup>95</sup>,  $\varepsilon_3 = \hat{n}_3^2 = 1$  (Air).  $\varepsilon_2$  is complex relative primitivity described by the model as following.

$$\varepsilon_2(\nu) = \varepsilon_{Au}(\omega) = \varepsilon_\infty + \frac{\omega_p^2}{\omega^2 + i\Gamma\omega} + G_1(\omega) + G_2(\omega) \quad (4.23)$$

Usually, the complex relative primitivity can be described by the Lorentz-oscillator model according to chapter 2.4 as well

$$\varepsilon(\nu) = \varepsilon_\infty + \sum_{j=1}^N \frac{S_j^2}{v_j^2 - \nu^2 - i\nu\gamma_j} \quad (4.24)$$

The aforementioned equations are commonly employed in the computation of surface plasmon generation conditions. Nevertheless, these formulations typically neglect the consideration of the thickness of the metallic layer, specifically the thin layer characterized by a negative dielectric constant. It is noteworthy that existing literature and computational outcomes suggest that alterations in the thickness of the thin layer result in a significant variance in the frequency/wavenumber associated with its heightened absorption<sup>185, 197, 198</sup>. This discrepancy indicates that the frequency generated by the surface plasmon is distinct from that of the surface plasmon and is intricately linked to the thickness of the thin layer.

$$r_{123} = r_{12} \frac{k_x - k_{x0} + r_{12}^{-1} K_0 \exp(-2jk_{z0}d)}{k_x - k_{x0} + r_{12} K_0 \exp(-2jk_{z0}d)} \quad (4.25)$$

$$k_{res} = \frac{\omega}{c} \sqrt{\frac{\varepsilon_r \cdot \varepsilon_b}{\varepsilon_r - \varepsilon_b}} - r_{12}^{-1}(k_{x0}) K_0 \exp(-2jk_{z0}d) \quad (4.26)$$

$$K_0 = \frac{\omega}{c} \left( \frac{2}{\varepsilon_r + \varepsilon_b} \right) \left( \frac{\varepsilon_r \cdot \varepsilon_b}{\varepsilon_r - \varepsilon_b} \right)^{3/2} \quad (4.27)$$

$$k_{z0} = -\frac{\omega}{c} \frac{\varepsilon_m}{\varepsilon_m - \varepsilon_d} \quad (4.28)$$

$$\varepsilon_r = -real(\varepsilon_2) \quad (4.29)$$

$$\varepsilon_b = real(\varepsilon_3) \quad (4.30)$$

Henceforth, as elucidated by Sophocles J. Orfanidis in "Electromagnetic Waves and Antennas"<sup>199</sup> incorporating the thickness of the thin layer and employing an approximation of the reflection calculation akin to Eqn.4.25 yields the aforementioned outcome. This outcome closely aligns with results derived from matrix calculations. Specifically, when configuring the incident angle ( $\theta_1$ ) to  $14.9^\circ$  (marginally exceeding the critical angle,  $\theta_c = 14.8^\circ$ ), a pronounced absorption phenomenon at a particular wavelength becomes readily achievable. Upon combining Eqn. 4.16 with Eqn.4.20, the conditions for exciting Surface Plasmon Polaritons (SPPs) can be ascertained, taking into consideration the thickness of the metal layer characterized by negative relative permittivity. These conditions are succinctly expressed as Eqn. 4.31.

$$k_{res} = \frac{\omega}{c} \sqrt{\frac{\varepsilon_r \cdot \varepsilon_b}{\varepsilon_r - \varepsilon_b}} - r_{12}^{-1}(k_{x0})K_0 \exp(-2jk_{z0}d) = \frac{\omega}{c} \sqrt{\varepsilon_1} \sin(\theta_1) \quad (4.30)$$

Upon establishing the thickness, one can readily determine the incident angle conducive to SPP generation, along with the corresponding wavelength or wavenumber associated with the onset of SPP generation.

$$\theta_1 = \arcsin \left\{ \left[ \frac{\omega}{c} \sqrt{\frac{\varepsilon_r \cdot \varepsilon_b}{\varepsilon_r - \varepsilon_b}} - r_{12}^{-1}(k_{x0})K_0 \exp(-2jk_{z0}d) \right] * \frac{c}{w\sqrt{\varepsilon_1}} \right\} \quad (4.31)$$

The corresponding result is shown in Fig. 4.3.

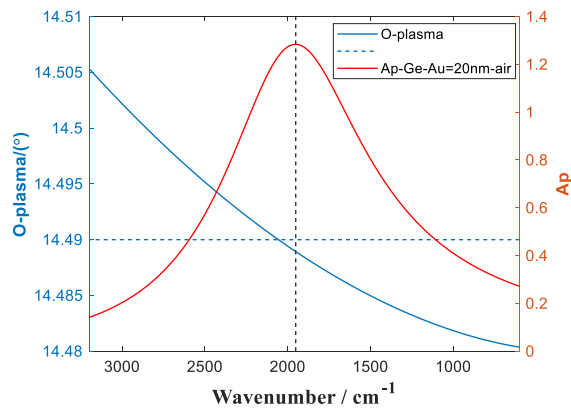


**Fig. 4.3** Incidence angle of surface plasmon generated at a fixed thickness and ATR spectrum at a fixed angle of  $14.49^\circ$  (both calculated values)

This observation provides a partial explanation for the emergence of surface enhancement spectra in the context of utilizing metal thin film ATR<sup>185, 200-204</sup>. The induction of surface plasmons results in discernible alterations in the baseline and conspicuous peaks in the absorption spectrum. Furthermore, the pronounced effect of the high refractive index of the thin layer is noteworthy. As illustrated in chapter 4.2, simulation data indicates that, with an incident angle slightly surpassing the critical angle, control can be exerted over the thickness of the high refractive index thin layer (non-metal, where the real part of the relative permittivity is positive). Consequently, the surface enhancement spectrum's thickness can be determined. Nevertheless, owing to the elevated refractive index of the thin layer, the absorption spectrum can experience a twofold enhancement, yet fails to yield absorption peaks akin to surface plasmons.

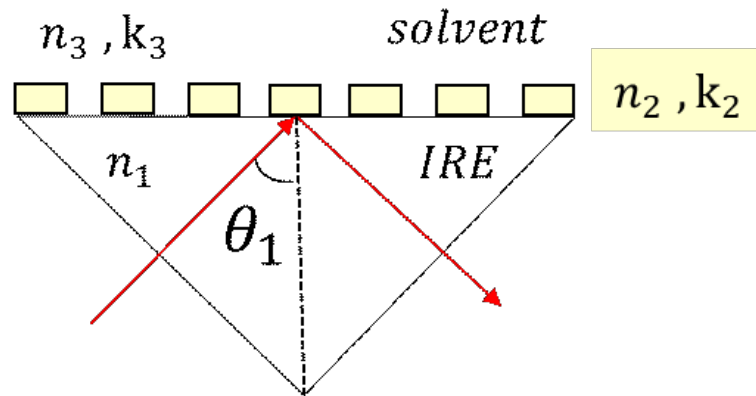


**Fig.4.4** Demonstration of surface plasmon excitation on the surface of ATR metal with grating.

The corresponding SPP is calculated as follows

$$k_x = \frac{\omega}{c} \sqrt{\varepsilon_1} \sin(\theta_1) + m \frac{2\pi}{\Lambda} \quad (4.32)$$

$$\frac{\omega}{c} \sqrt{\varepsilon_1} \sin(\theta_1) + m \frac{2\pi}{\Lambda} = \pm \frac{\omega}{c} \sqrt{\frac{\varepsilon_2 \cdot \varepsilon_3}{\varepsilon_2 + \varepsilon_3}} \quad (4.33)$$

Where  $m$  is the diffraction order,  $\Lambda$  is the grating period,  $n$  the refractive index of the surrounding medium. Compared with Eqn. 4.21, Eqn. 4.32 adds  $m \frac{2\pi}{\Lambda}$  as the contribution of the wave vector.

Regrettably, the application of the aforementioned formula necessitates a uniform and known thickness of the thin layer or the shape of grating, a condition that is readily achievable in the case of surfaces coated with metals such as gold or other conventional

materials<sup>205-208</sup>. However, when dealing with nanomaterials or emerging semiconductor materials, challenges arise due to diverse material morphologies, unevenness, and the impracticality of achieving uniform thickness<sup>209, 210</sup>. This is particularly evident in instances where experimental conditions are stringent, or when resorting solely to photolithography technology. Although the previously mentioned calculation effectively addresses the impact of thickness on surface plasmons, it fails to accommodate materials exhibiting irregular thickness and scattering on the surface, rather than forming a coherent film. Consequently, a computational approach employing the Finite-Difference Time-Domain (FDTD)<sup>211-214</sup> method becomes imperative. This involves modeling the experimental materials within software such as Lumerical to simulate and analyze the behavior of the materials under consideration.

### 3. The Finite-Difference Time-Domain (FDTD) method<sup>214, 215</sup>

The Finite-Difference Time-Domain (FDTD)<sup>214-216</sup> method, rooted in the numerical solution of Maxwell's equations as described in Chapter 1, offers a versatile and accurate approach to simulate the complex interactions of electromagnetic fields with nanostructures.

The FDTD method discretizes both time and space, allowing the numerical solution of Maxwell's equations<sup>215, 216</sup>. The electric and magnetic fields are represented on a grid, and their values are updated iteratively over discrete time steps. The update equations for the electric and magnetic fields are given by:

$$\frac{\partial \vec{E}}{\partial t} = \frac{1}{\epsilon} \nabla \times \vec{H} - \vec{J} \quad (4.34)$$

$$\frac{\partial \vec{H}}{\partial t} = \frac{1}{\mu} \nabla \times \vec{E} \quad (4.35)$$

In the context of surface-enhanced spectroscopy, the FDTD simulations<sup>217</sup> facilitate the exploration of plasmonic resonances<sup>218</sup>, field enhancements, and near-field distributions surrounding metallic nanostructures. The parameters in the FDTD simulation settings encompass the physical structure, simulation area, boundary conditions, light source characteristics, as well as monitor and script commands. This methodology has transitioned from its initial one-dimensional (1D) formulation to its current three-dimensional (3D) configuration. These simulations yield valuable insights into the underlying mechanisms of surface-enhanced Raman scattering (SERS)<sup>219</sup> and surface-enhanced infrared absorption (SEIRA)<sup>191, 197</sup>. Due to the constraints pertaining to the scope of the research objects, the ensuing discussion will focus exclusively on the SEIRA aspect.

## 4.2 Simulation

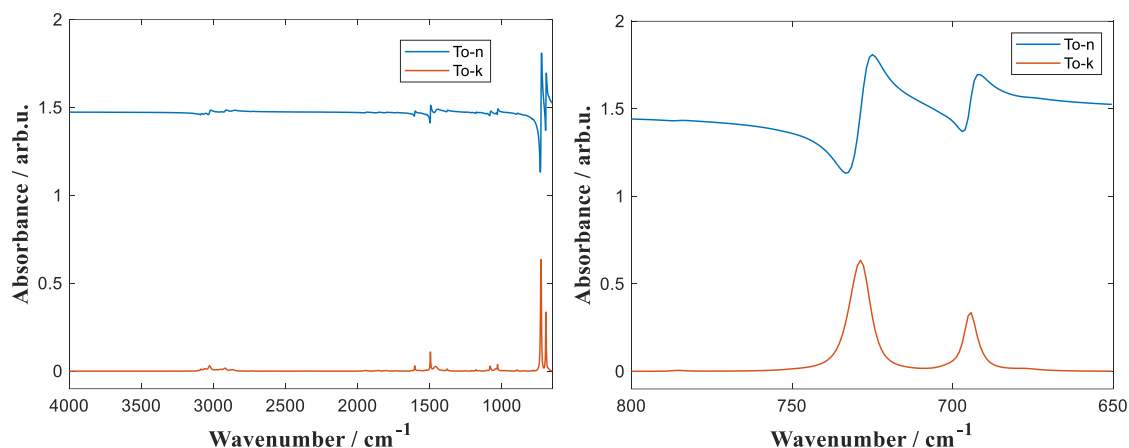


**Fig. 4.5** Complex reflective index ( $n$  presents refraction and  $k$  presents absorbance) of Toluene in  $650 - 4000\text{cm}^{-1}$ (left),  $650 - 800\text{cm}^{-1}$ (right).

Subsequently, the infrared spectrum of Toluene serves as the subject of analysis, wherein calculations and simulations are conducted based on Eqs. 4.1-4.15 from Chapter 4.1 to derive the infrared absorption spectra under various conditions. As illustrated in Fig. 4.1,  $n_1$  denotes the internal reflection element (IRE) of ATR, with  $n_{Ge} = 4.0$ ,  $n_{Diamond} = 2.39$ ; Different high refractive index materials, such as Au, Pt, Carbon Black, etc., are employed as the intermediate layer ( $n_2$ ). Toluene, functioning as the third layer solvent, exhibits a complex refractive index that varies with wavenumber, as depicted in Fig. 4.5.

The parameters manipulated during the computational process include: initially, maintaining the thickness ( $d_2$ ) constant while altering the incident angle  $\theta_1$  to observe the resulting absorption spectrum; subsequently, incrementing the thickness ( $d_2$ ) appropriately and varying the incident angle ( $\theta_1$ ) to obtain a distinct absorption spectrum; finally, setting the incident angle slightly above the critical angle, maintaining it fixed ( $\theta_1$ ), and adjusting the thickness ( $d_2$ ) to acquire the absorption spectrum. Throughout this procedure, different types of  $n_1$  and  $n_2$  are also encompassed within the investigation and comparison.

Regrettably, owing to the constraints of experimental conditions, this segment of the study cannot be experimentally executed; however, all refractive index data are derived from calculations based on experimental measurements.

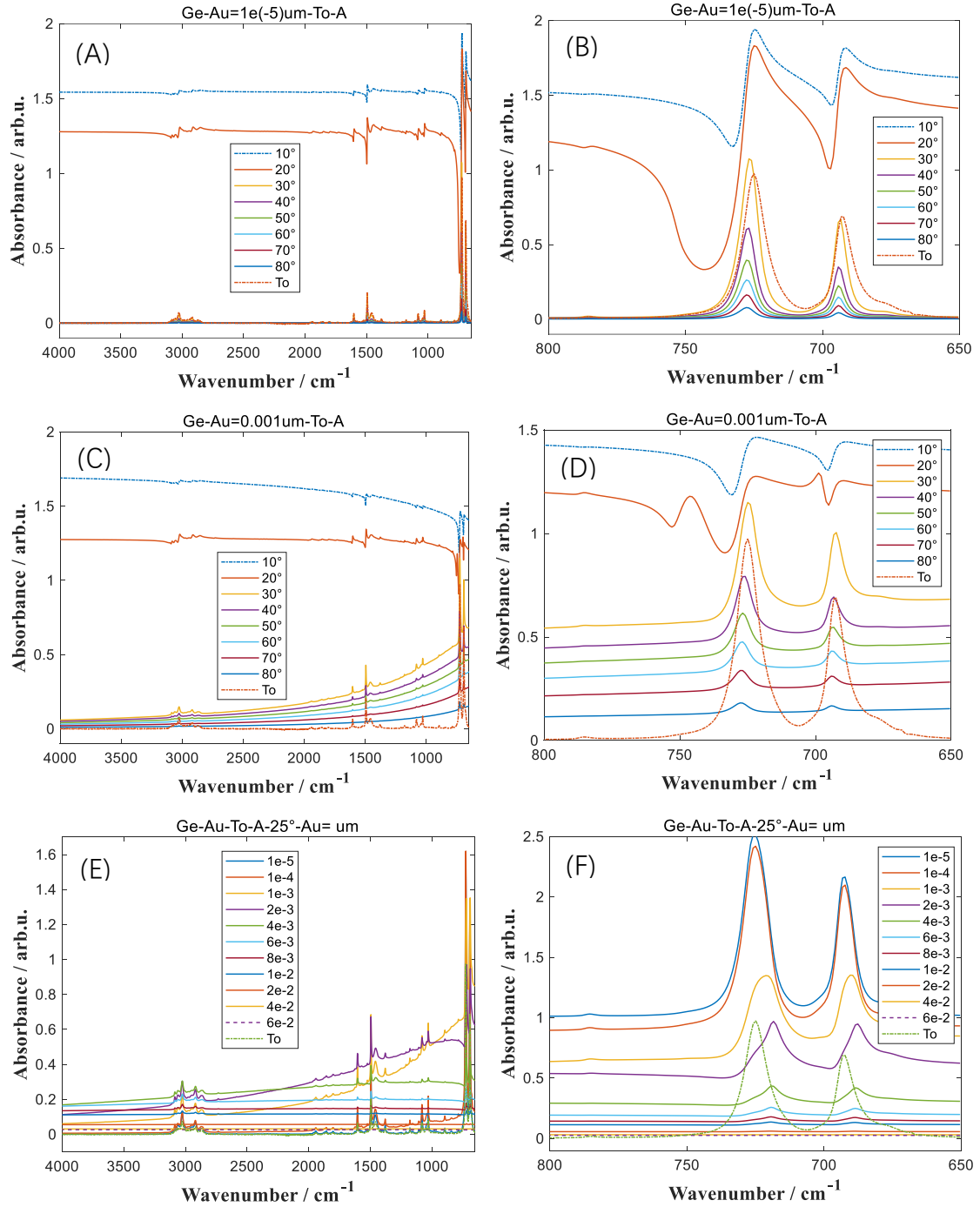


**Fig. 4.6** Complex reflective index ( $n$  presents refraction and  $n$  presents absorbance) of Toluene in  $650 - 4000\text{cm}^{-1}$ (left),  $650 - 800\text{cm}^{-1}$ (right). Set  $d_{Au} = 10^{-5}\text{um} = 0.01\text{nm}$  with changing the incident angle  $\theta_1 = 10^\circ - 80^\circ$  (A, B);  $d_{Au} = 10^{-3}\text{um} = 1\text{nm}$  with changing the incident angle  $\theta_1 = 10^\circ - 80^\circ$  (C, D);  $\theta_1 = 25^\circ$ ,  $d_{Au} = 10^{-5} - 6 * 10^{-2}\text{um} = 0.01 - 60\text{nm}$  (E, F).

In the depicted Fig. 4.6A, B, the incident angle  $\theta_1$  exerts a significant influence, particularly in proximity to  $\theta_c$ , where the absorption spectrum undergoes pronounced changes. Specifically, when  $\theta_1 < \theta_c$ , the absorption spectrum closely resembles the

imaginary part ( $k$ ) of the complex refractive index. Conversely, when  $\theta_1 > \theta_c$ , the absorption spectrum exhibits similarities to the real part ( $n$ ) of the complex refractive index. With an increase in the thickness ( $d_2$ ), the baseline of the absorption spectrum starts to elevate (Fig. 4.6C, D), particularly in the vicinity of  $\theta_c$ , resembling phenomena observed in experimental observations.

Under the condition of a fixed incident angle ( $\theta_1 = 25^\circ$ , slightly exceeding  $\theta_c$ ), varying  $d_2$  allows for the observation of the surface enhancement spectrum to a certain extent (Fig. 4.6E, F).



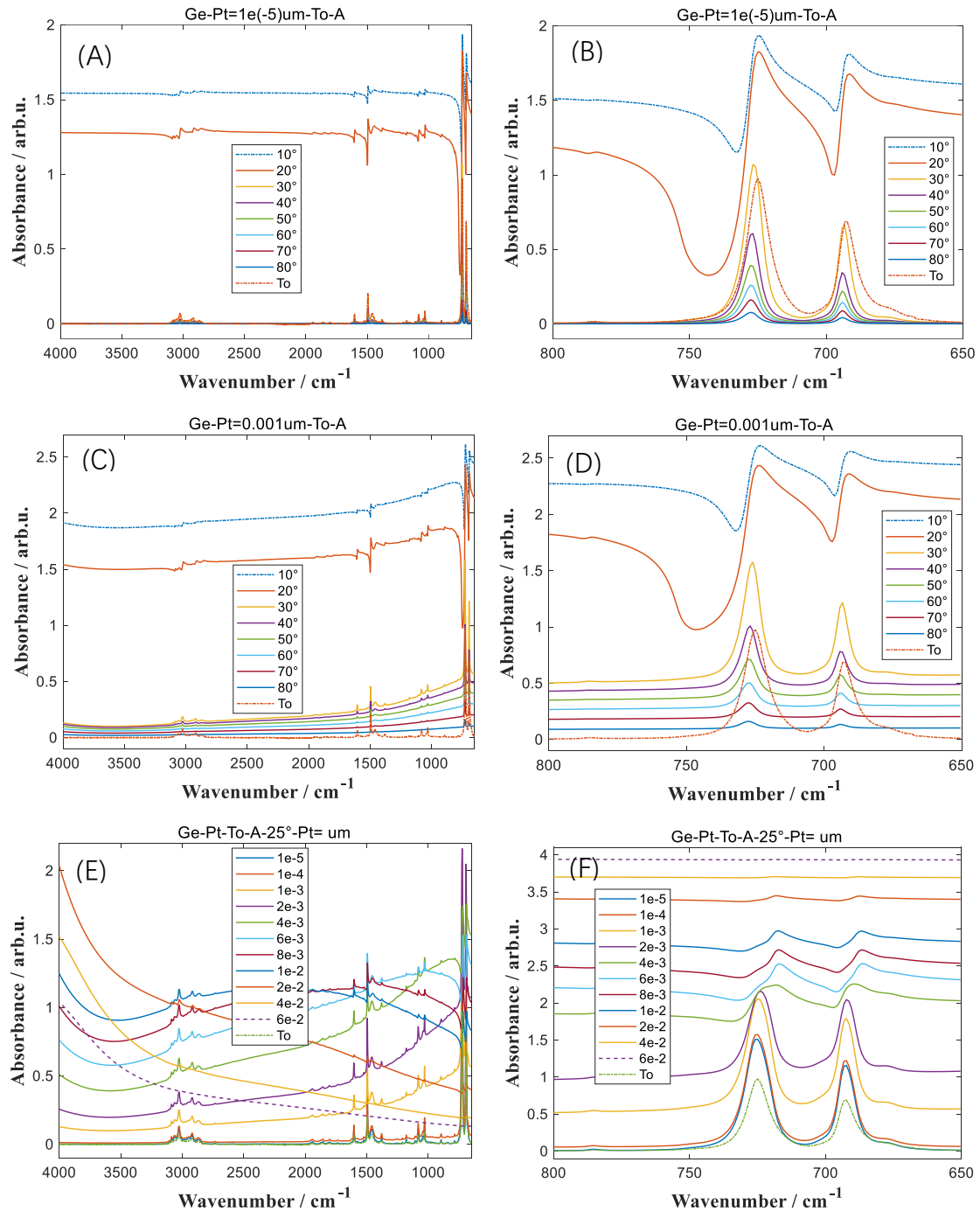


**Fig. 4.7** Complex reflective index ( $n$  presents refraction and  $n$  presents absorbance) of Toluene in  $650 - 4000\text{cm}^{-1}$ (left),  $650 - 800\text{cm}^{-1}$ (right). Set  $d_{Pt} = 10^{-5}\text{um} = 0.01\text{nm}$  with changing the incident angle  $\theta_1 = 10^\circ - 80^\circ$  (A, B);  $d_{Pt} = 10^{-3}\text{um} = 1\text{nm}$  with changing the incident angle  $\theta_1 = 10^\circ - 80^\circ$  (C, D);  $\theta_1 = 25^\circ$ ,  $d_{Pt} = 10^{-5} - 6 \times 10^{-2}\text{um} = 0.01 - 60\text{nm}$  (E, F).

Upon transitioning the material of the second layer from Au to Pt, a phenomenon akin to the aforementioned conclusion becomes apparent. It is noteworthy that when maintaining  $\theta_1 = 25^\circ$  and varying  $d_2$  within the range of  $650 - 4000\text{cm}^{-1}$ ,

heightened volatility is observable with Pt serving as the intermediate layer. This observation aligns with phenomena expounded upon in the literature by Thomas<sup>12, 220</sup>.

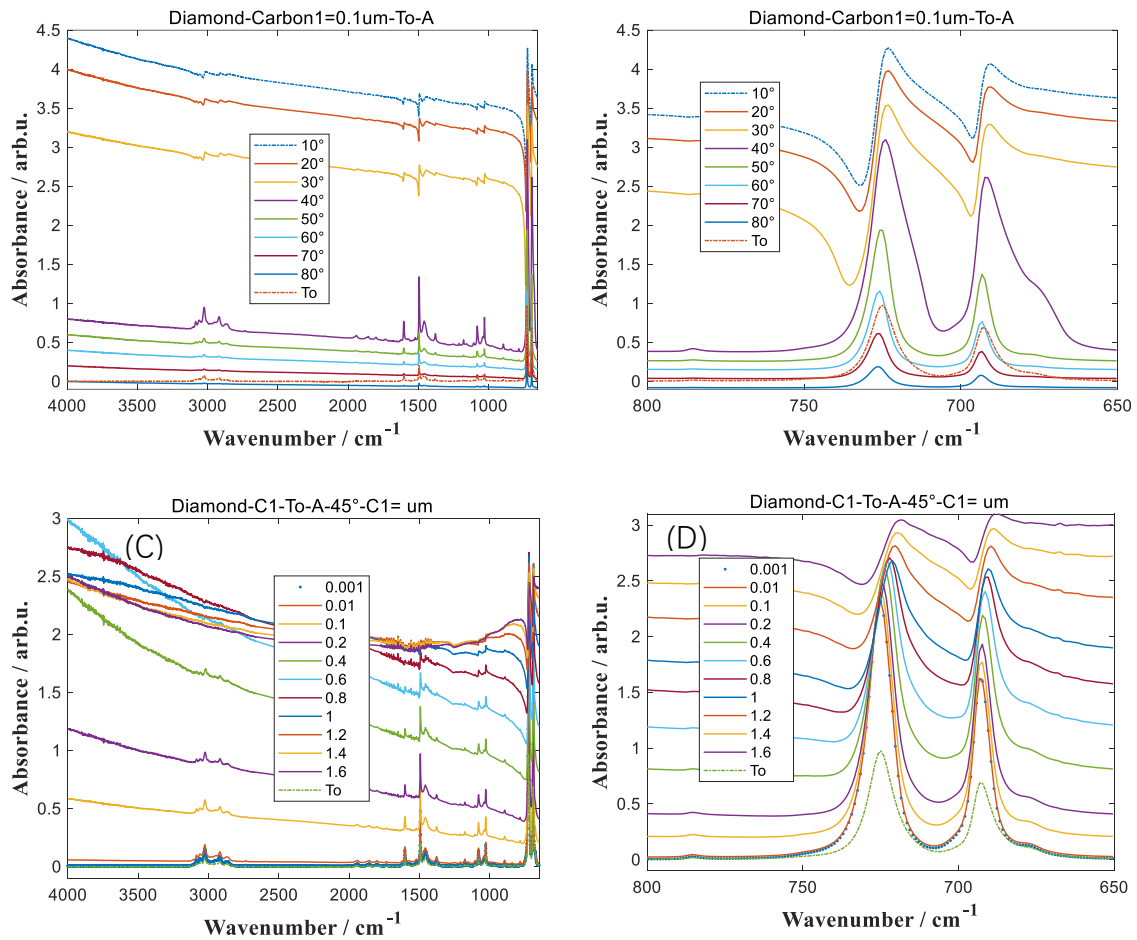


**Fig. 4.8** Complex reflective index ( $n$  presents refraction and  $n$  presents absorbance) of Toluene in  $650 - 4000\text{cm}^{-1}$ (left) , $650 - 800\text{cm}^{-1}$ (right). Set  $d_{C1} = 10^{-5}\text{um} = 0.01\text{nm}$  with changing the incident angle  $\theta_1 = 10^\circ - 80^\circ$  (A, B);  $d_{C1} = 10^{-3}\text{um} = 1\text{nm}$  with changing the incident angle  $\theta_1 = 10^\circ - 80^\circ$  (C, D);  $\theta_1 = 25^\circ$ ,  $d_{C1} = 10^{-5} - 6 * 10^{-2}\text{um} = 0.01 - 60\text{nm}$  (E, F).

Owing to the substantial refractive index disparity, the observation of the surface enhancement spectrum proves challenging when Carbon Black serves as the middle layer, particularly when utilizing Ge as  $n_1$ . To address this, Diamond is employed as the Internal Reflection Element (IRE), with the incident angle set at  $\theta_1 = 45^\circ$ .

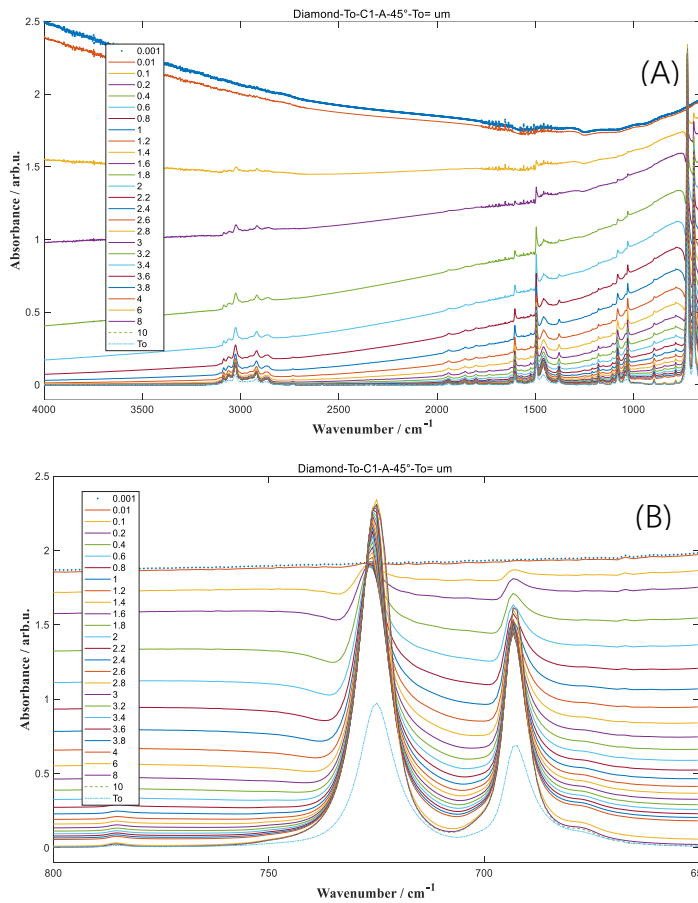


**Fig. 4.9** Compare the absorbance spectrum with thickness change in Diamond-Carbon black-Toluene system ( $\theta_1 = 45^\circ$ ) (A), and the absorbance spectrum of pure Toluene in Diamond-ATR (B).  $\theta_1 = 45^\circ$ ,  $d_{C1} = 10^{-3} - 10\mu\text{m} = 1 - 10000\text{nm}$ .

Simultaneously, adopting Carbon Black as the third layer and Toluene as the second layer yields a comparable enhanced spectrum. However, it is imperative to highlight that the highest Improvement Factor for surface enhancement in this scenario is approximately 2.

### 4.3 Experiment

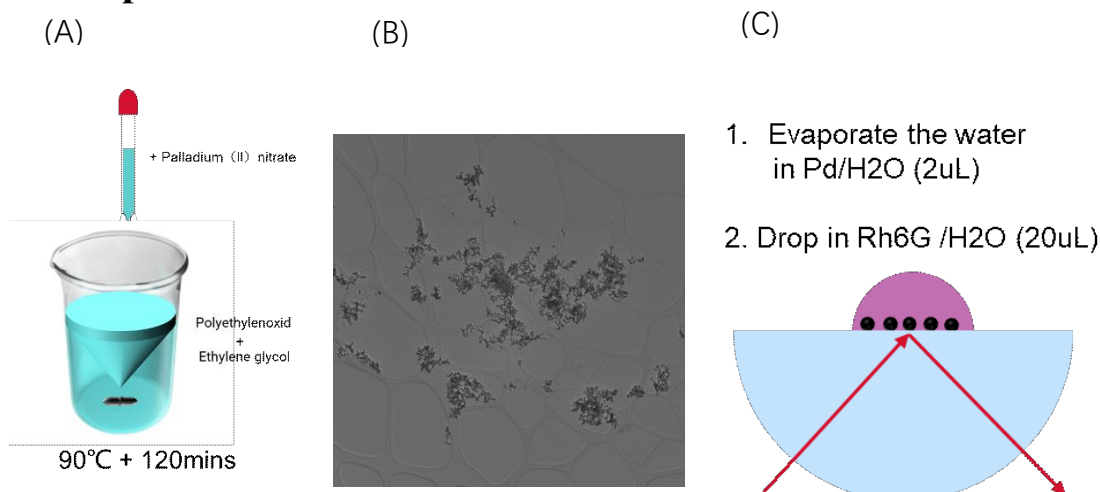


**Fig 4.10.** Process of Pd production ( A ); TEM of Pd ( B ); experimental procedure of Pd and Rh6G ( C ).

The procedure for acquiring nano-Pd through water bath synthesis is depicted in Fig.4.10A, and the corresponding Transmission Electron Microscopy (TEM) image for Pd is presented in Figure 4.10B.

Subsequently, Pd was employed as the particle to induce surface plasmon resonances in the experiment. The experimental procedure is illustrated in Fig.4.10C, and the resulting surface-enhanced spectrum was obtained<sup>221</sup>.

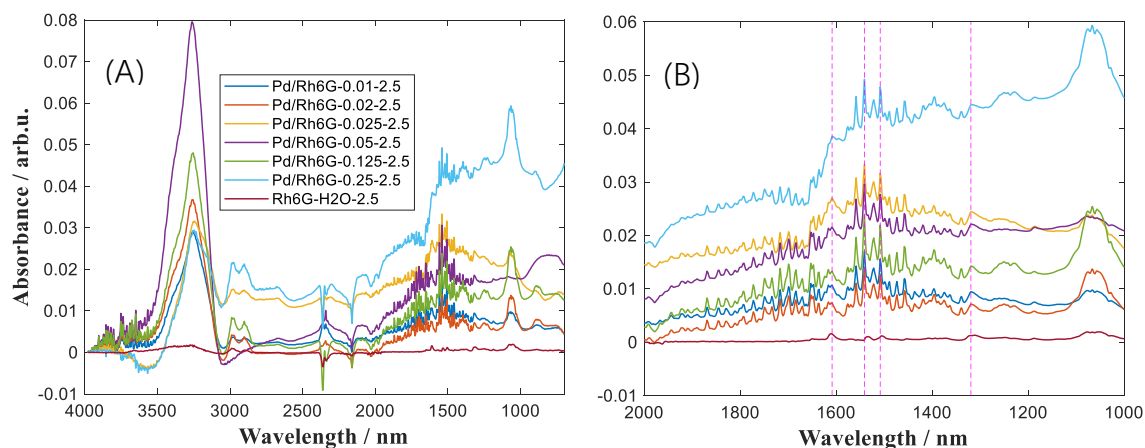


**Fig 4.11** Comparison between the spectra of Rhodamine 6G(2.5mg/ml) with different concentration of Pd,  $650 - 4000\text{cm}^{-1}$ (left) ,  $1000 - 2000\text{cm}^{-1}$ (right).

As depicted in Fig 4.11, even at elevated concentrations of Rhodamine 6G, such as 2.5g/L, its infrared absorption peak remains inconspicuous. However, in the presence of Pd as a substrate, a marked enhancement of the absorption peak becomes evident. Notably, within a specified range, an increase in the concentration of Pd/Rhodamine

6G corresponds to an augmented tendency of absorption peak enhancement. This observation aligns with the findings articulated by Hu in her published paper<sup>222</sup>.

Regarding the negative peak observed within the absorption peak, such as at 2500cm<sup>-1</sup>, it finds explication in the perspectives presented in the cited reference literature. Specifically, the higher refractive index of Pd (as illustrated in Fig 4.10C) surpasses the critical refractive index of Diamond-ATR. Consequently, the elevated refractive index of the sample induces localized refraction phenomena on the surface. However, due to the limited quantity used, the distortion of the final spectrum and the shift of the peak value are not overtly pronounced. Given that higher concentrations of Pd lead to a more substantial baseline drift, our consideration is confined to a maximum value of 0.05mg/ml, as informed by experimental outcomes and recorded literature<sup>222</sup>.

The enhancement factor is as shown in Eqn. 4.36

$$e_{EF} = \frac{I_{GEIRA}}{I_0} \quad (4.36)$$

$I_{GEIRA}$  and  $I_0$  are the peak heights corresponding to the characteristic peaks of Rhodamine 6G with and without Pd.

We can easily obtain the enhancement factor corresponding to the characteristic absorption peak of Rhodamine 6G, as shown in Table 4.1.

**Table 4.1** The enhancement factor of Rh6G in typical peaks.

Pd/(mg/mL)*	Wavenumber/(cm <sup>-1</sup> )			
	1608 v(-CN)	1541 v(ring)	1508 v(ring)	1319 v(-CN)
0.01	6.85	16.24	13.06	7.54
0.02	4.75	13.28	10.69	5.69
0.025	17.31	31.76	26.52	19.45
0.05	13.83	28.26	23.22	17.59
0.125	8.52	22.68	18.38	11.36
0.25	24.72	46.96	40.04	35.38

\* Rh6G = 2.5 mg/mL

Similarly, we derive the enhancement factors corresponding to the characteristic absorption peaks, as depicted in Fig 4.12.

The enhancement effect demonstrates a gradual increase with the rise in Pd

concentration. Nevertheless, instances arise where the enhancement effect at lower concentrations surpasses that observed at higher concentrations. For instance, the enhancement effect at 0.025 mg/mL exceeds that at 0.05 mg/mL and 0.125 mg/mL. We attribute this phenomenon to the possibility of uneven mixing of the concentration during sonication.

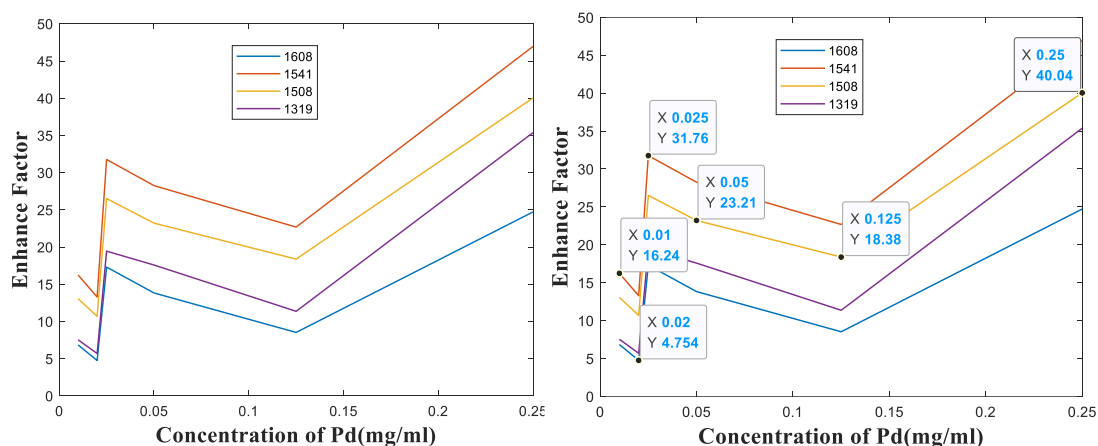


**Fig.4.12** Enhance factor in 4 typical wavenumbers with different concentration of Pd.

Analogously, with the Pt concentration held constant at 0.05 mg/mL, employing varying concentrations of Rh6G yields the surface enhancement spectrum depicted in Fig 4.13.

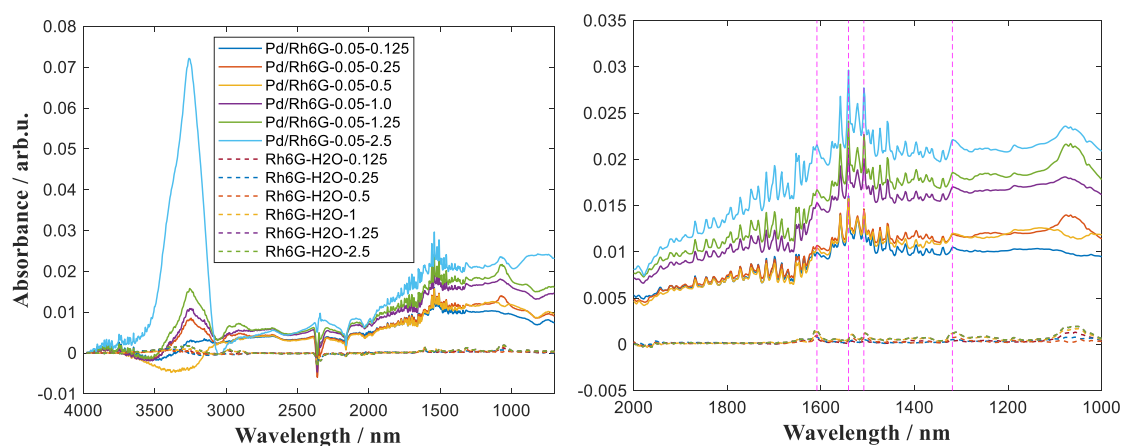


**Fig 4.13** Comparison between the spectra of Rhodamine 6G with different concentrations of Rhodamine 6G.

The enhancement coefficients corresponding to the characteristic peaks are detailed in Table 4.2.

**Table 4.2** The enhancement factor of Rh6G in typical peaks.

Rh6G /(mg/mL)*	Wavenumber/(cm <sup>-1</sup> )			
	1608 v(-CN)	1541 v(ring)	1508 v(ring)	1319 v(-CN)
0.125	16.48	46.41	37.89	25.23
0.25	13.15	36.87	30.55	22.62
0.5	10.73	23.46	18.32	16.08
1	11.12	20.07	16.58	14.31
1.25	10.72	23.01	18.99	14.77
2.5	11.77	21.72	18.69	15.31

\* Pd = 0.05 mg/mL

Observing Fig 4.14, it becomes evident that the surface enhancement coefficient increases with decreasing concentrations of Rh6G.

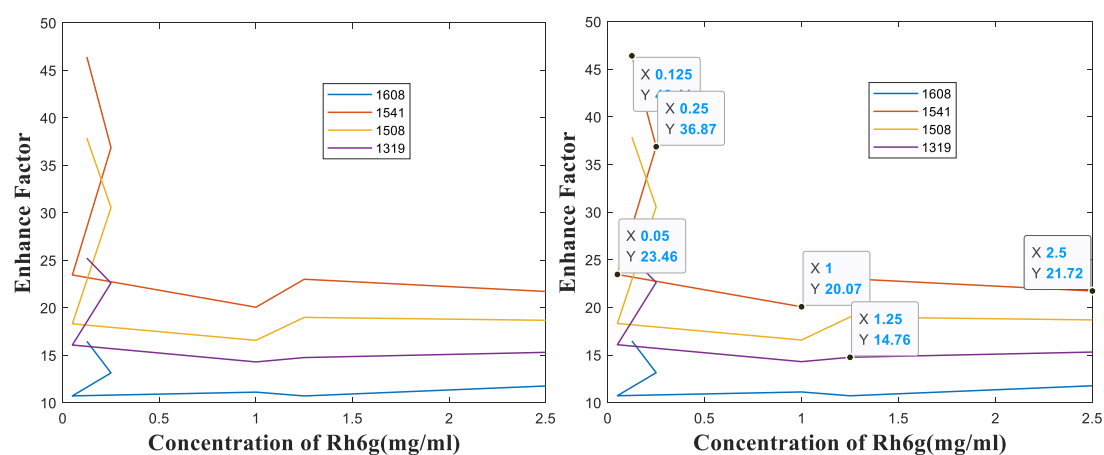


**Fig 4.14** Enhance factor in 4 typical wavenumbers with different concentration of Rhodamine 6G.

## **Conclusions**

Through calculations of ATR spectroscopy and detailed simulations, our study demonstrates that high refractive index mixtures achieve limited spectral enhancement when the incident angle slightly exceeds the critical angle. Conversely, materials with a negative real part of the relative dielectric constant, such as metals, exhibit significant surface-enhanced spectra near the critical angle due to surface plasmon generation. Notably, our research uniquely considers the influence of metal film thickness on these effects.

In experiments with palladium (Pd) and Rhodamine 6G, we observed that the enhancement factor increased with higher Pd concentrations and decreased with higher Rhodamine 6G concentrations. These findings advance our understanding of infrared-enhanced spectroscopy and its potential integration with two-dimensional infrared-enhanced spectroscopy, providing a foundation for further exploration in optimizing spectral enhancements across various materials.



# 5. Introduction to Two-dimensional Infrared (2D IR) Spectroscopy

## 5.1 Two-dimensional Fourier transform (2D FT)

According to Chapter 2.1, it is easy to get 1D FT<sup>83</sup> as Eqs. 5.1 and 5.2.

$$F(\omega) = \int_{-\infty}^{\infty} f(t)e^{-i\omega t} dt, \quad (5.1)$$

$$f(t) = \frac{1}{2\pi} \int_{-\infty}^{\infty} F(\omega)e^{i\omega t} d\omega, \quad (5.2)$$

in which  $F(\omega)$  is spectrum in frequency domain, and  $f(t)$  is spectrum in time domain. Here,  $F(\omega)$  is the 1D spectrum of  $f(t)$ , which shows the components of the original signal  $f(t)$  at each frequency  $\omega$ .

Combine KK transform, Eqn. 2.43 can also be expressed as

$$F(\omega) = \int_{-\infty}^{\infty} f(t)e^{-i\omega t} dt = F_r(\omega) + F_i(\omega) , \quad (5.3)$$

$F_r(\omega)$  is the real part of spectrum and  $F_i(\omega)$  is the its imaginary part, whereas  $|F(\omega)|$  (or  $\sqrt{F_r^2(\omega) + F_i^2(\omega)}$ ) is the amplitude spectrum, and  $\tan^{-1}\left(\frac{F_i(\omega)}{F_r(\omega)}\right)$  is the phase spectrum<sup>38</sup>.

According to Euler's formula,

$$e^{i\omega x} = \cos(\omega x) + i \sin(\omega x) , \quad (5.4)$$

$$f(t) = \frac{1}{2\pi} \int_{-\infty}^{\infty} [F(\omega) \cos(\omega x) + iF(\omega) \sin(\omega x)] d\omega , \quad (5.5)$$

then  $f(t)$  can be understood as linear combinations of countless trigonometric functions (i.e. one-dimensional orthogonal basis) with different  $\omega$ -directions and frequencies.

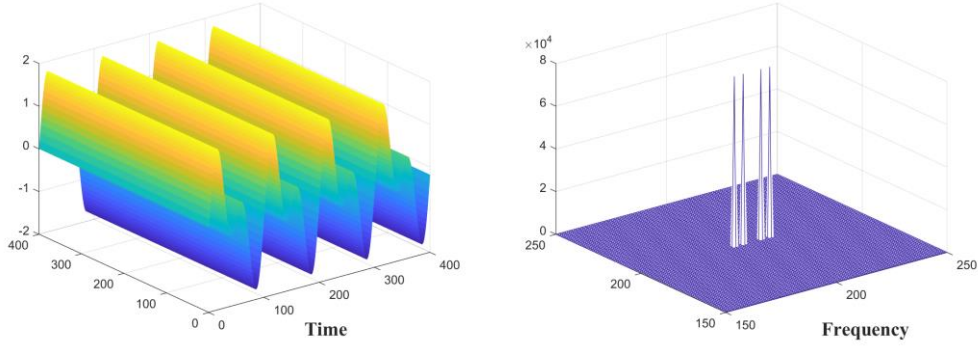


**Fig. 5.1** 1D Fourier transform, time domain (left); Frequency domain (right).

Unlike the 1D Fourier transform given in Fig. 5.1, in which time domain and frequency domain are in the same coordinate system. In Fig. 5.2, the graphs of time domain and frequency domain are displayed in two dimensions. 2D Fourier transform will be introduced as following.

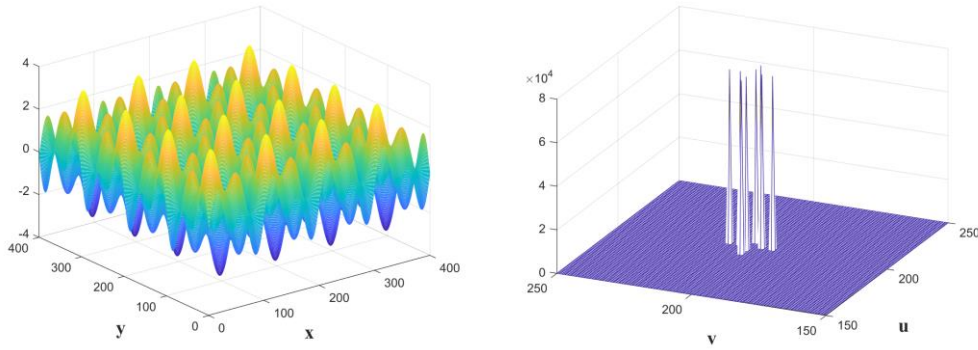


**Fig. 5.2** 2D Fourier transform,  $f(x, y)$  (left);  $F(u, v)$  (right).

A 2D spectrum  $f(x, y)$  is continuous and non-periodic. In the 2D FT<sup>223, 224</sup>, we use two coordinate systems to represent the time domain  $(x, y)$  and frequency domain  $(u, v)$  respectively. It also has properties similar to 1D spectral transformation. It can be clearly seen from the figure that 2D FT simply adds another dimension to the respective  $y$ -axis ( $v$ -axis) on the basis of 1D FT. The corresponding formula can be expressed as following:

$$F(u, v) = \int_{-\infty}^{\infty} \int_{-\infty}^{\infty} f(x, y) e^{-i\omega(ux+vy)} dx dy = F_r(u, v) + F_i(u, v), \quad (5.6)$$

$$f(x, y) = \int_{-\infty}^{\infty} \int_{-\infty}^{\infty} F(u, v) e^{i\omega(ux+vy)} du dv . \quad (5.7)$$

Here,  $F(u, v)$  is the 2D spectrum in frequency domain of  $f(x, y)$ .  $F(u, v)$  indicates the components of  $f(x, y)$  at both  $x$ - and  $y$ -directions for frequency  $u$  and  $v$  respectively, which also contain real and imaginary parts:

$$e^{i\omega(ux+vy)} = [\cos(ux) \cos(vy) - \sin(ux) \sin(vy)] \\ + i[\sin(ux) \cos(vy) + \sin(vy) \cos(ux)] \quad . \quad (5.8)$$

Then  $f(x, y)$  can be understood as a linear combination of countless products of sine and cosine functions of  $x$  and  $y$  (i.e., a 2D orthogonal basis). These orthogonal bases are also periodic functions in the plane.

The 2D FT is separable, that is, it can be separated into two 1D FTs. For example, using MATLAB, the function of the two-dimensional fast Fourier transform (2D FFT) is in the form of  $y = fft2(x) = fft[fft(x)]$ .

The order of integration in 2D FT is commutative:

$$F(u, v) = 2D FT [f(x, y)] \\ = \int_{-\infty}^{\infty} e^{-i\omega(vy)} dy \left[ \int_{-\infty}^{\infty} f(x, y) e^{-i\omega(ux)} dx \right] \\ = \int_{-\infty}^{\infty} F(u, y) e^{-i\omega(vy)} dy \quad . \quad (5.9)$$

Similarly, 2D FT can also be similarly performed through 2D FFT and convolution calculations.

## 5.2 2D IR Spectroscopy

Two predominant methodologies characterize contemporary usage of 2D Infrared (2D IR) Spectroscopy. The first approach involves the conversion of 1D spectrum into symmetrical 2D spectrums. This innovative technique was introduced by Isao Noda<sup>225, 226</sup>. We will only briefly introduce it here. The second method entails the direct application of nonlinear optical experiments to discern the correlation between chemical bond vibration modes, resulting in the acquisition of asymmetric 2D spectra, (asymmetry is not absolute). The focus of the present chapter, as well as subsequent chapters, will be directed towards a comprehensive exploration of the latter method.

### 1. 2D IR by Isao Noda<sup>225, 226</sup>

We will now start the introduction of the first method, devised and advanced by Isao Noda. This method pertains to the conversion of a series of 1D spectra into 2D spectra. Its utility lies in the analysis of diverse conditions, including temperature, pressure, time, and other factors, to discern the impact on the spectrum.<sup>227</sup> This entails an investigation into the similarity or dissimilarity of spectral intensity changes induced by external perturbations to the sample.<sup>226</sup>

The computational procedure unfolds as follows.

In the context of this method, let it be posited that a collection of  $m$  spectra, denoted as  $A(v_k, t_i)$ , has been acquired in the presence of external disturbances.<sup>227</sup> These disturbances encompass variables representative of diverse factors, such as temperature, pressure, time, and so on. Here,  $v_k$  denotes the wave number associated with the  $k$ -th sampling point, serving as a frequency or wavenumber coordinate. Concurrently,  $t_i$  signifies the outcome corresponding to the  $i$ -th disturbance ( $i = 1, 2 \dots m$ ).<sup>225-227</sup>

Then, the final dynamic spectrum  $\tilde{A}(v_k, t_i)$  can be expressed as<sup>225-227</sup>

$$\tilde{A}(v_k, t_i) = \begin{cases} A(v_k, t_i) - \bar{A}(v_k) & \text{for } 1 \leq i \leq m \\ 0 & \text{otherwise} \end{cases} \quad (5.10)$$

Where  $\bar{A}(v_k)$  is the reference spectrum, usually the average spectrum, which is

$$\bar{A}(v_k) = \frac{1}{m} \sum_{i=1}^m A(v_k, t_i) \quad (5.11)$$

The calculation formulas of synchronous and asynchronous 2D correlation spectra  $\Phi(v_1, v_2)$  and  $\Psi(v_1, v_2)$  are as follows<sup>225-227</sup>

$$\Phi(v_1, v_2) = \frac{1}{m-1} \sum_{i=1}^m \tilde{A}(v_1, t_i) \cdot \tilde{A}(v_2, t_i) \quad (5.12)$$

$$\Psi(v_1, v_2) = \frac{1}{m-1} \sum_{i=1}^m \tilde{A}(v_1, t_i) \cdot \sum_{j=1}^m N_{ij} \tilde{A}(v_2, t_j) \quad (5.13)$$

$N_{ij}$  is the Hilbert-Noda transformation matrix<sup>225-227</sup>,

$$N_{ij} = \begin{cases} 0 & \text{for } 1 \leq i \leq m \\ \frac{1}{\pi(j-i)} & \text{otherwise} \end{cases} \quad (5.14)$$

The Hilbert transform produces a new set of spectra that are orthogonal (i.e. 90° out of phase) to the original  $t$  correlated spectra<sup>228</sup>.

The aforementioned information, Eqs 5.10-5.15, are entirely articulated within Isao Noda's papers<sup>225, 227</sup>.

Fundamentally, the synchronized 2D correlation spectrum  $\Phi(v_1, v_2)$  is actually the result of multiplying a series of spectral matrices  $A(v_k, t_i)$  with its own transpose and dividing by  $(m-1)$ . To illustrate this concept, we employ the simulated Toluene infrared absorption spectrum on the Diamond-ATR. In this instance, the variable  $t$  represents the alteration of the incident angle (respectively 0°, 10° ... 90°,  $m = 10$ ). The cumulative spectrum, when  $t$  is varied across different incident angles, is denoted as a  $160 \times 10$  matrix, as depicted in Fig. 5.3 (Left).

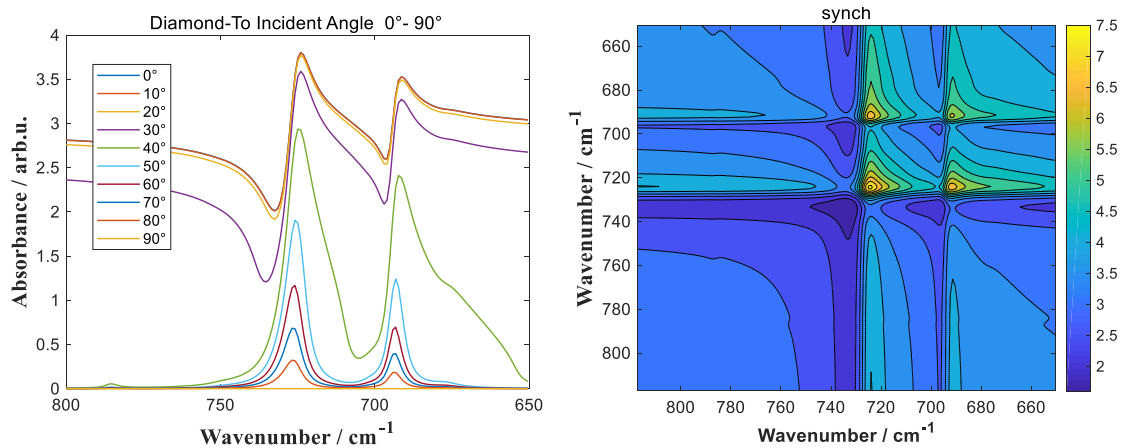


**Fig. 5.3** 1D spectrum of Toluene based on Diamond- ATR with incident angles from 0° to 90°(Left), synchronous 2D spectrum (Right).

Then the corresponding synchronous 2D spectrum, as shown in Fig. 5.3 (Right), is a  $160 \times 160$  matrix. The derivation of  $160 \times 160$  matrix, representing the synchronous 2D spectrum, involves the multiplication of a  $160 \times 10$  matrix (representing the 1D spectrum) by the transpose of a  $160 \times 10 \cdot 10 \times 160$  matrix, followed by division by  $(m - 1)$ . The main calculation process can be expressed as

$$A_{160 \times 10} \cdot A'_{10 \times 160} / 9 = \tilde{A}_{160 \times 160}^{\text{Syn}} \quad (5.15)$$

While the method yields a conversion of a series of 1D spectra into 2D spectra, it does not encompass additional information compared to the original one-dimensional spectrum. Furthermore, due to the symmetry of the resulting two-dimensional spectrum about the diagonal axis, only half of the image is necessary to accurately represent the entirety of the content.

The asynchronous 2D spectrum employs a comparable methodology as in Fig. 5.4, with the exception that the Hilbert transformation is applied to the influencing factor, denoted as  $t$ . Hilbert transformation as defined in Equation 2.58 in Chapter 2.2.

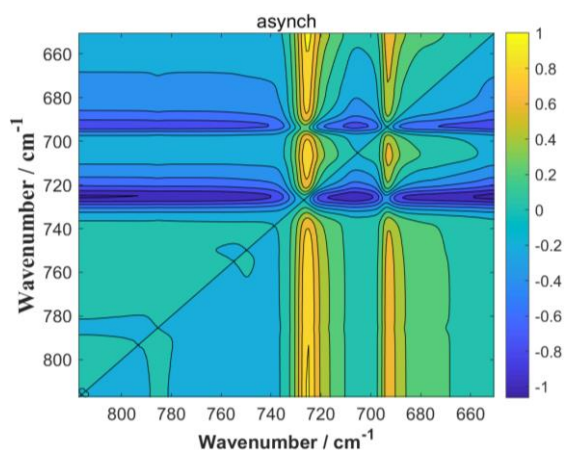


**Fig. 5.4** Asynchronous 2D spectrum

$$\mathcal{H}[f(t)] = \hat{f}(t) = f(t) * \frac{1}{\pi t} = \frac{1}{\pi} \int_{-\infty}^{\infty} \frac{f(\tau)}{t - \tau} d\tau \quad (5.16)$$

Initially, the process involves obtaining a  $10 \times 10$  orthogonal matrix ( $90^\circ$  out of phase with the original influencing factors  $t$ ). Subsequently, the original  $160 \times 10$  matrix is multiplied by the aforementioned orthogonal matrix, followed by the multiplication with the transposed  $10 \times 160$  matrix of the original matrix, resulting in a  $160 \times 160$  matrix, namely  $160 \times 10 \cdot 10 \times 10 \cdot 10 \times 160$ , which is then divided by  $(m - 1)$ .

$$A_{160 \times 10} \cdot t_{10 \times 10} \cdot A'_{10 \times 160} / 9 = \tilde{A}_{160 \times 160}^{\text{Asyn}} \quad (5.17)$$

It is worth noting that the Hilbert transformation here is not a transformation on the original spectra. Which is different from what we used in the correction in Chapter 2. The Hilbert transformation here refers to the Hilbert transformation on  $t$ , rather than

the spectrum. Since this conversion also results in a 2D spectrum that is symmetrical about the diagonal axis, only half of the image can reflect all the information.

While the 2D spectrum obtained through this approach has inherent limitations, the potential lies in leveraging the insights from Chapter 3 on deep learning. This idea could offer a novel perspective, expanding the application horizon. Specifically, drawing parallels to image recognition and natural language models within the realm of deep learning, the 1D spectrum aligns more closely with natural language processing (NLP)<sup>229</sup> models like RNN, LSTM, and Transformer. In contrast, the 2D spectrum bears resemblance to image recognition and is better suited for models such as CNN and Vision-Transformer. This suggests that in situations where processing data in the 1D spectrum proves challenging, the application of image recognition models may offer a solution by elevating the dimensionality without altering the original information.

## 2. 2D IR with nonlinear optics

Now we will focus on 2D infrared spectroscopy<sup>230-235</sup> that uses nonlinear optics to detect chemical bond vibrations<sup>236</sup>. It is imperative to clarify that in the subsequent discussions, the term "2DIR" specifically alludes to this particular methodology.

2D IR<sup>237, 238</sup> has emerged as a powerful technique for probing the structural and dynamic properties of molecules in a variety of scientific disciplines. This method extends the capabilities of traditional one-dimensional infrared spectroscopy by providing additional information about molecular interactions, dynamics, and coupling.

In contrast to 1D infrared spectrum, 2D IR introduces an additional frequency dimension<sup>239</sup>. Nevertheless, within the 2D IR, phenomena such as distorted spectra and surface-enhanced spectra, akin to those observed in 1D linear spectra, are also present. This similarity arises because the frequency distribution on the  $x$ -axis (pump) in 2D IR is exactly the same as the frequency measured by 1D infrared spectrum. The key distinction lies in the fact that 1DIR captures solely the initial vibration frequency, while 2D IR quantifies signal intensity variations over time in the two-dimensional frequency space<sup>240</sup>.

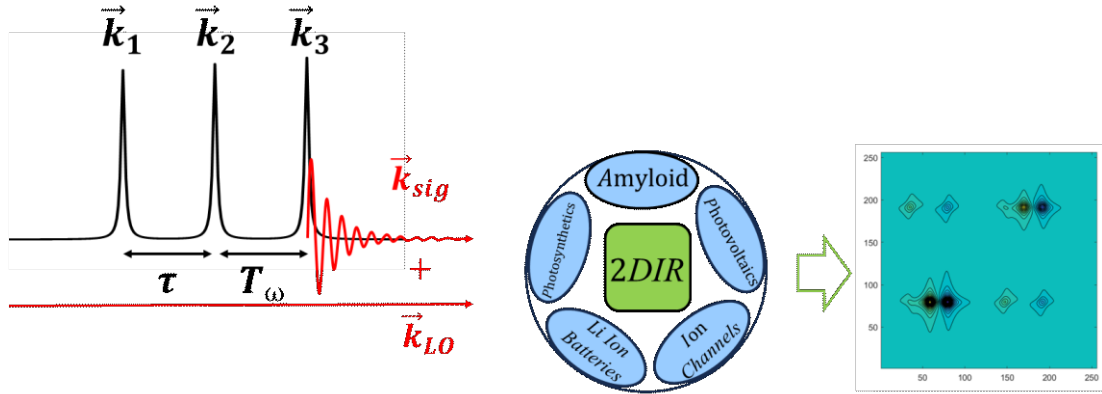


**Fig. 5.5** Schematic diagram of the principle and application of 2D IR spectroscopy<sup>241</sup>.

Despite the relatively intricate principles governing 2D IR spectroscopy, to sum it up in one sentence, 2D IR spectroscopy was obtained by perform Fourier transform on third-order nonlinear optical signals  $S(\tau, T_\omega, t_3)$  in the time domain. Which can be expressed as Eqn. 5.18 or 5.19

$$S(\omega_\tau, \omega_m, T_\omega) \propto \int_0^\infty dt \int_0^\infty dt_3 e^{\mp i\omega_m t_3 \mp i\omega_\tau \tau} \cdot S(\tau, T_\omega, t_3) \quad (5.18)$$

Which can be also written as

$$S(\omega_\tau, \omega_m, T_\omega) \propto \int_0^\infty \int_0^\infty S(\tau, T_\omega, t_3) \cdot e^{\mp i\omega_m(t_3+\tau)} dt_3 d\tau \quad (5.19)$$



In which,  $\omega_\tau$  is the excitation frequency,  $\tau$  is the excitation frequency coherence time after emission,  $\omega_m$  is the emission frequency,  $t_3$  is the emission coherence time,  $T_\omega$  is the reaction time (population time). The sign ( $\mp$ ) of phase is matched by phase (phase match, the vector sum of the incident beam) is determined.

Certainly, it is apparent that the above computational procedure closely parallels the 2D FT introduced in Chapter 5.1. However, during experimental investigations, two distinct methodologies are typically employed to perform the Fourier transform to obtain the 2D spectrum, thereby constituting a significant divergence among various approaches in 2D IR<sup>242</sup>.

1)  $\omega_\tau$  and  $\omega_m$  are both derived through instrumental Fourier transform, involving the utilization of an instrument, such as a grating or etalon, to spectrally disperse the incident light and ascertain the frequencies. This approach is known as the narrow pump/broad probe (pump/probe) method. As illustrated in Figure 5.6, the pump-pump direction typically aligns, while the probe direction differs. The ultimate detector is exclusively configured to capture signals along the probe direction. Which is characterized by the relative simplicity and ease of operation of the experimental apparatus. However, its limitations include a restricted frequency range dictated by the broadband light frequency, leading to less precise outcomes.<sup>237</sup>

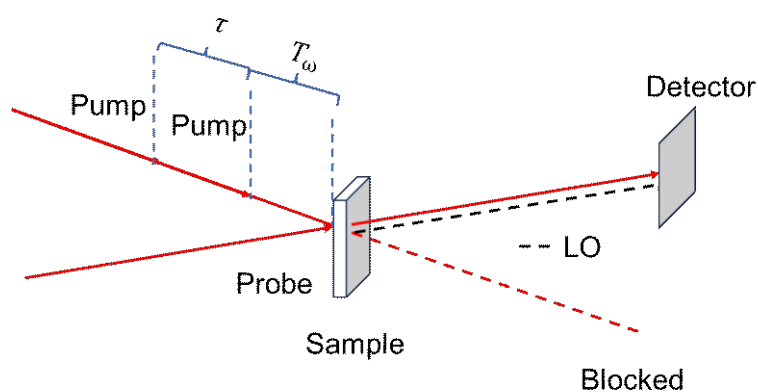


**Fig. 5.6** Schematic diagram of pump-probe used for 2D IR detection.

2) The derivation of  $\omega_\tau$  involves the application of mathematical Fourier transform, while  $\omega_m$  is obtained through instrumental Fourier transform. Specifically, this entails time-domain scanning to procure the coherence pattern, followed by employing mathematical techniques to transform the coherence pattern into frequency data—a process commonly referred to as coherence method. As depicted in Figure 5.7, the pump-pump-probe configuration and the detection direction of the final signal

collectively constitute a parallelogram. This approach is commonly referred to as the "CARS-Box" geometry.<sup>238, 243</sup> The advantage of this method is high frequency resolution and time resolution. However, its drawbacks encompass high cost, operational intricacy, and extended measurement durations.

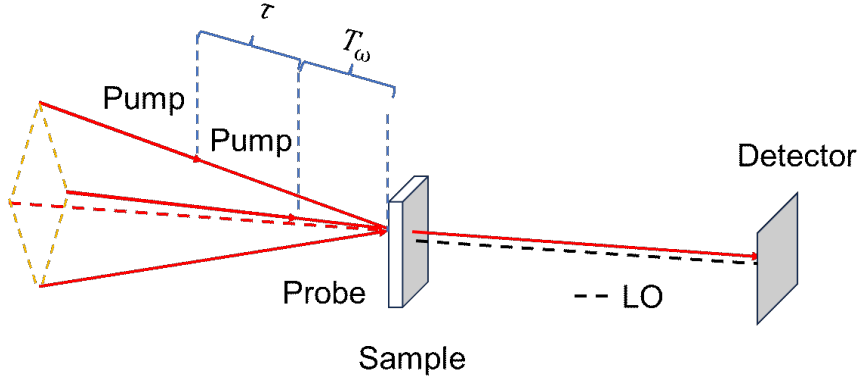


**Fig. 5.7** Box-CARS geometry used for 2D IR detection.

Next, we will elaborate on the calculation process of third-order nonlinear optical signals  $S(\tau, T_\omega, t_3)$  by combining the Schrödinger equation and relevant knowledge of nonlinear optics.

### 3. Calculation process of 2D IR with nonlinear optics<sup>237</sup>

In the discussion about Maxwell's equations in Chapter 1, we briefly mentioned that the response of materials to electric fields is divided into linear and nonlinear situations (Eqs. 1.11-1.14), that is,

$$\vec{P} = \epsilon_0 \chi_e \vec{E} \quad (5.20)$$

$$\vec{D} = \epsilon \vec{E} = \epsilon_0 \epsilon_r \vec{E} = \epsilon_0 (1 + \chi_e) \vec{E} \quad (5.21)$$

For nonlinear response, which means<sup>244</sup>

$$\vec{P} = \epsilon_0 \chi_e \vec{E} + \epsilon_0 \chi_e^2 \vec{E}^2 + \epsilon_0 \chi_e^3 \vec{E}^3 + \epsilon_0 \chi_e^4 \vec{E}^4 + \dots \quad (5.22)$$

$$\vec{D} = \epsilon_0 (1 + \chi_e) \vec{E} + \epsilon_0 \chi_e^2 \vec{E}^2 + \epsilon_0 \chi_e^3 \vec{E}^3 + \epsilon_0 \chi_e^4 \vec{E}^4 + \dots \quad (5.23)$$

Prior to Chapter 5, our focus has been on linear responses. Now, we are tasked with introducing nonlinear scenarios. In the context of 2D IR, where three ultrafast laser beams (pump-pump-probe) are employed to examine the sample, our consideration shifts to the third-order nonlinear response. Here, we must integrate the classical time-dependent electron field with the quantum mechanics governing molecular vibration states. Given this foundation, the temporal response of the material to the external

electric field  $\vec{E}$  is to be addressed.

$$\widehat{W}(t) = -\hat{\mu}E(t) \quad (5.24)$$

In which  $\widehat{W}$  represents the quantum mechanical operator corresponding to the interaction energy between the laser pulse and the molecule.  $\hat{\mu}$  is the molecule's dipole, indicates how well a medium stores magnetic energy.  $\hat{\mu}$  and  $E(t)$  are both scalars. And the calculations in Eqn. 5.24 have been normalized.

The following content, including Equations 5.24–5.68, is derived from the book *Concepts and Methods of 2D Infrared Spectroscopy* by Hamm, Peter and Martin, Zanni<sup>237</sup>. This section presents a concise explanation of the calculation principles underlying nonlinear 2D IR spectroscopy. These principles are essential for understanding the subsequent development of 2D enhanced spectroscopy. A mixed state of molecules is described here,

$$\widehat{H}(t) = \widehat{H}_0 + \widehat{W}(t) = \widehat{H}_0 - \hat{\mu}E(t) \quad (5.25)$$

Among these elements,  $\widehat{H}_0$  represents the principal component,  $\widehat{W}(t)$  stands as the perturbation Hamiltonian, with the condition  $\widehat{W}(t) \ll \widehat{H}_0$ . This assumption is made under the premise that the eigenstate of  $\widehat{H}_0$  is denoted as  $|n\rangle$ .

The molecular eigenstates  $|n\rangle$  of  $\widehat{H}_0$  are determined by solving the time-independent Schrödinger equation:<sup>237</sup>

$$\widehat{H}_0|n\rangle = E_n|n\rangle \quad (5.26)$$

And for  $|\psi\rangle$  can be decided by the time-independent Schrödinger equation,

$$i\hbar \frac{\partial}{\partial t} |\psi(t)\rangle = \widehat{H}(t)|\psi(t)\rangle = \widehat{H}(t)|\psi(t)\rangle - |\psi(t)\rangle\widehat{H}(t) = [\widehat{H}(t), |\psi(t)\rangle] \quad (5.27)$$

Which also written as

$$\frac{\partial}{\partial t} |\psi(t)\rangle = -\frac{i}{\hbar} \widehat{H}(t)|\psi(t)\rangle \quad (5.28)$$

In the absence of an external laser beam,  $\widehat{H}_0$  remains time independent. Consequently, we can provide the solution for the state  $|\Psi(t)\rangle$  as follows:

$$|\psi(t)\rangle = \sum_n c_n(t) |n\rangle \quad (5.29)$$

In which  $c_n$  is the probability amplitude.

This implies that prior to the laser's arrival, the system exists in the ground state. Subtract Eqn.5.26 from Eqn.5.29 to get

$$\frac{dc_m(t)}{dt} = -\frac{i}{\hbar} \sum_n H_{mn}c_n(t) \quad (5.30)$$

The mixed state of the molecule is described by a density matrix as

$$\rho = \sum_s p_s |\psi_s\rangle\langle\psi_s| \quad (5.31)$$

Here,  $\rho$  represents the density matrix (or density operator), and  $|\psi_s\rangle$  denotes the eigenstate corresponding to the density operator. This eigenstate can be interpreted as a specific state within the ensemble, characterized by a particular probability.  $p_s$  represents the associated eigenvalue, which can be understood as the probability of occupying the corresponding state. And

$$\sum_s p_s = 1 \quad (5.32)$$

$$\begin{aligned} i\hbar \frac{d}{dt} \rho &= \sum_s p_s i\hbar \left( \frac{d}{dt} |\psi_s\rangle\langle\psi_s| + |\psi_s\rangle \frac{d}{dt} \langle\psi_s| \right) = \sum_s p_s (\hat{H} |\psi_s\rangle\langle\psi_s| + |\psi_s\rangle\langle\psi_s| \hat{H}) \\ &= \hat{H} \rho - \rho \hat{H} = [\hat{H}, \rho] \end{aligned} \quad (5.33)$$

Which can be expressed equivalently as:

$$\frac{d}{dt} \rho = -\frac{i}{\hbar} [\hat{H}, \rho] \quad (5.34)$$

This is *the Liouville–von Neumann equation*.

We define the operator  $\hat{A}$  as:<sup>245</sup>

$$\hat{A} = \sum_s a_s |\psi_s\rangle\langle\psi_s| \quad (5.35)$$

Then the expected value of operator  $\langle\hat{A}\rangle$  is

$$\langle\hat{A}\rangle = \sum_s p_s \langle\psi_s|\hat{A}|\psi_s\rangle = \sum_s \langle\psi_s|\hat{\rho}\hat{A}|\psi_s\rangle = Tr(\hat{\rho}\hat{A}) \equiv \langle\hat{\rho}\hat{A}\rangle \quad (5.36)$$

In most of case  $\hat{A}$  is  $\hat{\mu}$ , which means

$$\langle\hat{\mu}\rangle = Tr(\hat{\rho}\hat{\mu}) \equiv \langle\hat{\rho}\hat{\mu}\rangle \quad (5.37)$$

From Eqn. 5.31

$$\rho_{nm} = \sum_s p_s c_n^s c_m^{s*} = \langle c_n^s c_m^{s*} \rangle \quad (5.38)$$

$\langle c_n^s c_m^{s*} \rangle$  of the density operator  $\hat{\rho}$  are related to a coherence  $|n\rangle\langle m|$  between states  $|n\rangle$  and  $|m\rangle$

$$\langle\hat{\mu}\rangle = \sum_{nm} \langle c_n^s c_m^{s*} \rangle u_{mn} = \sum_{nm} \rho_{nm} u_{mn} \quad (5.39)$$

Let's back to Eqn. 5.25,

$$\hat{H}(t) = \hat{H}_0 + \hat{W}(t) = \hat{H}_0 - \hat{\mu}E(t) \quad (5.35)$$

with

$$\hat{H}_0|n\rangle = E_n|n\rangle \quad (5.2)$$

Here the energy and density matrices are defined as follows:

$$|n\rangle_I = e^{i\omega_n t}|n\rangle \quad (5.40)$$

$$|\psi(t)\rangle\langle\psi(t)| = e^{-\frac{i}{\hbar}\hat{H}_0(t-t_0)}|\psi_I(t)\rangle\langle\psi_I(t)|e^{+\frac{i}{\hbar}\hat{H}_0(t-t_0)} \quad (5.41)$$

Or

$$\rho(t) = e^{-\frac{i}{\hbar}\hat{H}_0(t-t_0)}\rho_I(t)e^{+\frac{i}{\hbar}\hat{H}_0(t-t_0)} \quad (5.42)$$

Then the corresponding *Liouville–von Neumann equation* is

$$\frac{d}{dt}\rho_I(t) = -\frac{i}{\hbar}[\widehat{W}_I(t), \rho_I(t)] \quad (5.43)$$

where  $\widehat{W}_I(t)$  is the perturbation Hamiltonian

Correspondingly,

$$\widehat{W}(t) = e^{-\frac{i}{\hbar}\hat{H}_0(t-t_0)}\widehat{W}_I(t)e^{+\frac{i}{\hbar}\hat{H}_0(t-t_0)} \quad (5.44)$$

Write Eqn. 5.34 in integral form

$$\rho_I(t) - \rho_I(t_0) = -\frac{i}{\hbar} \int_{t_0}^t [\widehat{W}_I(\tau), \rho_I(\tau)] d\tau \quad (5.45)$$

It can be solved by iterative calculation

$$\begin{aligned} \rho_I(t) = \rho_I(t_0) + \sum_{n=1}^{\infty} \left(-\frac{i}{\hbar}\right)^n \int_{t_0}^t d\tau_n \int_{t_0}^{\tau_n} d\tau_{n-1} \dots \int_{t_0}^{\tau_2} d\tau_1 \\ [\widehat{W}_I(\tau_n), [\widehat{W}_I(\tau_{n-1}), \dots [\widehat{W}_I(\tau_1), \rho_I(t_0)] \dots]] \end{aligned} \quad (5.46)$$

Substitute into Eqn.5.42 to get

$$\begin{aligned} \rho(t) = \rho^{(0)}(t) + \sum_{n=1}^{\infty} \left(-\frac{i}{\hbar}\right)^n \int_{t_0}^t d\tau_n \int_{t_0}^{\tau_n} d\tau_{n-1} \dots \int_{t_0}^{\tau_2} d\tau_1 \\ \cdot e^{-\frac{i}{\hbar}\hat{H}_0(t-t_0)} [\widehat{W}_I(\tau_n), [\widehat{W}_I(\tau_{n-1}), \dots [\widehat{W}_I(\tau_1), \rho(t_0)] \dots]] e^{+\frac{i}{\hbar}\hat{H}_0(t-t_0)} \end{aligned} \quad (5.47)$$

Then

$$\rho(t) = \rho^{(0)}(t) + \sum_{n=1}^{\infty} \rho^{(n)}(t) \quad (5.48)$$

Substituting Eqn. 5.24 into it, we can get

$$\begin{aligned} \rho^{(n)}(t) = -\left(-\frac{i}{\hbar}\right)^n \int_{t_0}^t d\tau_n \int_{t_0}^{\tau_n} d\tau_{n-1} \dots \int_{t_0}^{\tau_2} d\tau_1 E(\tau_n)E(\tau_{n-1}) \dots E(\tau_1) \\ \cdot e^{-\frac{i}{\hbar}\hat{H}_0(t-t_0)} [\hat{\mu}_I(\tau_n), [\hat{\mu}_I(\tau_{n-1}), \dots [\hat{\mu}_I(\tau_1), \rho(t_0)] \dots]] e^{+\frac{i}{\hbar}\hat{H}_0(t-t_0)} \end{aligned} \quad (5.49)$$

With

$$\hat{\mu}_I(t) = e^{-\frac{i}{\hbar}\hat{H}_0(t-t_0)}\hat{\mu}e^{+\frac{i}{\hbar}\hat{H}_0(t-t_0)} \quad (5.50)$$

The macroscopic polarization,  $P(t)$ , which is given by the expectation value of the dipole operator  $\hat{\mu}$  and extract the molecular response,  $R(t)$ .

The macroscopic polarization  $P(t)$  is the convolution of the external laser's electric field  $E(t)$ . with the response function  $R(t)$ . The content of convolution was introduced in Chapter 2.1.

$$P(t) \propto \int_{-\infty}^{\infty} R(t_1)E(t-t_1) dt_1 \quad (5.51)$$

$P(t)$  can be calculated as

$$P(t) = Tr\langle\rho(t)\hat{\mu}\rangle \equiv \langle\rho(t)\hat{\mu}\rangle \quad (5.52)$$

Then for  $n$  order  $P^{(n)}(t)$  can be expressed as

$$P^{(n)}(t) = Tr\langle\rho^{(n)}(t)\hat{\mu}\rangle \equiv \langle\rho^{(n)}(t)\hat{\mu}\rangle \quad (5.53)$$

Substitute Eqn. 5.49 into Eqn. 5.53, let  $t_0 \rightarrow -\infty$ ,  $\tau_1 = 0$ ,  $t_1 = \tau_2 - \tau_1, \dots, t_n = t - \tau_n$  to get

$$\begin{aligned} P^{(n)}(t) = & -\left(-\frac{i}{\hbar}\right)^n \int_{-\infty}^t d\tau_n \int_{-\infty}^{\tau_n} d\tau_{n-1} \dots \int_{-\infty}^{\tau_2} d\tau_1 \\ & \cdot E(t-t_n)E(t-t_n-t_{n-1}) \dots E(t-t_n-t_{n-1}-\dots-t_1) \\ & \cdot \langle\hat{\mu}(t)[\hat{\mu}(\tau_n), [\hat{\mu}(\tau_{n-1}), \dots [\hat{\mu}(\tau_1), \rho(-\infty)] \dots]]\rangle \quad (5.54) \end{aligned}$$

For the convolution of  $n$  electric fields can be represented by the  $n$ -order nonlinear response  $R^{(n)}$ . Then

$$\begin{aligned} P^{(n)}(t) = & -\left(-\frac{i}{\hbar}\right)^n \int_{-\infty}^t d\tau_n \int_{-\infty}^{\tau_n} d\tau_{n-1} \dots \int_{-\infty}^{\tau_2} d\tau_1 \\ & \cdot E(t-t_n)E(t-t_n-t_{n-1}) \dots E(t-t_n-t_{n-1}-\dots-t_1) \\ & \cdot R^{(n)}(t_n, t_{n-1}, \dots, t_1) \quad (5.55) \end{aligned}$$

As we mentioned before, 2D IR is third-order nonlinear optics. Then third-order response functions  $R^{(3)}(t_1, t_2, t_3)$ , through the possible Feynman diagrams (did not contains here), contains the rephasing diagram ( $R_{1,2,3}$ ) and the non-rephasing diagram( $R_{4,5,6}$ ),

$$R_4(t_1, t_2, t_3) \propto i\mu_{01}^4 e^{-i\omega_{01}t_1} e^{-\frac{t_1}{T_2}} e^{-\frac{t_2}{T_1}} e^{-i\omega_{01}t_3} e^{-\frac{t_3}{T_2}} \quad (5.56)$$

$$R_1(t_1, t_2, t_3) \propto i\mu_{01}^4 e^{+i\omega_{01}t_1} e^{-\frac{t_1}{T_2}} e^{-\frac{t_2}{T_1}} e^{-i\omega_{01}t_3} e^{-\frac{t_3}{T_2}} \quad (5.57)$$

$$R_{1,2,3} = 2i\mu_{01}^4 [e^{-i\omega_{01}(t_3-t_1)} - e^{-i(\omega_{01}-\Delta)t_3-i\omega_{01}t_1}] e^{-\frac{t_1+t_3}{T_2}} \quad (5.58)$$

$$R_{4,5,6} = 2i\mu_{01}^4 [e^{-i\omega_{01}(t_3+t_1)} - e^{-i(\omega_{01}-\Delta)t_3+i\omega_{01}t_1}] e^{-\frac{t_1+t_3}{T_2}} \quad (5.59)$$

Accordingly, the corresponding third-order macroscopic polarization is<sup>246</sup>

$$P^{(3)}(t_3, t_2, t_1) \propto \int_{-\infty}^{\infty} dt_3 \int_{-\infty}^{\infty} dt_2 \int_{-\infty}^{\infty} dt_1 \sum_n R_n(t_3, t_2, t_1) E_3(t-t_3) \\ \cdot E_2(t-t_3-t_2) E_1(t-t_3-t_2-t_1) \quad (5.60)$$

The macro signal field  $E_{sig}(t)$  is generated by the macroscopic polarization  $P(t)$ . There is a  $90^\circ$  phase difference between  $E_{sig}(t)$  and  $P(t)$  in the frequency domain, which corresponds to multiplying by  $i$  in the time domain. This part is similar to the Hilbert transform. See chapter 2.2 for details.

$$E_{sig}(t) = iP(t) \quad (5.61)$$

$$E_{sig}^{(3)}(t) = iP^{(3)}(t_3, t_2, t_1) = iTr\langle \rho^{(n)}(t) \hat{\mu} \rangle \quad (5.62)$$

Then the final detected signal is

$$S(t_1, t_2) = \int_0^{\infty} |E_{sig}^{(3)}(t_3; t_1, t_2)|^2 dt_3 \quad (5.63)$$

When adding a laser pulse as the so-called local oscillator (LO), the result can be obtained as:

$$S(t_{LO}; t_1, t_2) \propto \int_0^{\infty} |E_{LO}(t_3 - t_{LO}) + E_{sig}^{(3)}(t_3; t_1, t_2)|^2 dt_3 \\ \approx I_{LO} + 2\mathcal{R} \int_0^{\infty} |E_{LO}(t_3 - t_{LO}) * E_{sig}^{(3)}(t_3; t_1, t_2)|^2 dt_3 \quad (5.64)$$

In an ideal scenario, laser pulses are utilized.

$$E(t) \propto \delta(t) e^{\pm i\omega t \mp ik\vec{r} \mp i\phi} \quad (5.65)$$

Then the obtained third-order signal field is

$$E_{sig}^{(3)}(t_1, t_2, t_3) \propto e^{i(\mp i\vec{k}_1 \pm \vec{k}_2 + \vec{k}_3)\vec{r}} e^{i(\mp i\phi_1 \pm \phi_2 + \phi_3)} \sum_n iR_n(t_1, t_2, t_3) \quad (5.66)$$

Where the symbols  $+$ ,  $-$  are depended on  $R_n$  (the rephasing diagrams or the non-rephasing diagrams).

The signal obtained after passing the heterodyne detection (this part will be introduced in detail in Chapter 5.3) is

$$S(t_1, t_2, t_3) \propto E_{LO} * E_{sig}^{(3)} \propto e^{i(\mp i\phi_1 \pm \phi_2 + \phi_3 - \phi_{LO})} \sum_n iR_n(t_1, t_2, t_3) \quad (5.67)$$

After 2D FT

$$\begin{aligned}
S(\omega_3, t_2, \omega_1) &\propto \int_0^\infty \int_0^\infty e^{i\omega_1 t_1 + i\omega_3 t_3} \cdot S(t_1, t_2, t_3) dt_1 dt_3 \\
&= \int_0^\infty \int_0^\infty e^{i\omega_1 t_1 + i\omega_3 t_3} \cdot \sum_n iR_n(t_1, t_2, t_3) dt_1 dt_3 \quad (5.68)
\end{aligned}$$

That is also written as:

$$S(\omega_\tau, \omega_m, T_\omega) \propto \int_0^\infty \int_0^\infty S(\tau, T_\omega, t_3) \cdot e^{\mp i\omega_m(t_3 + \tau)} dt_3 d\tau \quad (5.19)$$



## 5.3 Enhancement in 2D IR

### 1. Calculation in 1D

In the preceding section, a comprehensive examination was conducted on the generation principles of 2D IR signal and its associated computations. As revealed in the literature, akin to the one-dimensional infrared (1D IR) spectra, 2D IR spectra also exhibit spectral distortion and signal enhancement<sup>115, 247-249</sup>. The fundamental cause for the phenomenon of spectral distortion in both 1D and 2D spectra lies in the application of ATR-FTIR for sample testing, where the refractive index of the substance being measured is either partially or entirely greater than the critical refractive index. However, a distinct enhancement is observed in the realm of 2D IR, specifically, the spectral enhancement phenomenon near the Brewster Angle. This phenomenon diverges significantly from the behavior observed in 1D spectra.

Drawing insights from Fayer's discourse<sup>250, 251</sup>, a remarkable enhancement in the signal-to-noise (S/N) ratio is evident in this geometry compared to a conventional transmission pump-probe geometry signal. The heightened S/N ratio is attributed to the substantial modulation of the local oscillator (LO) field induced by the nonlinear signal field. This chapter delves into the principles and influencing factors of this phenomenon, building upon the existing literature. Subsequently, the subsequent chapter will elaborate on the constraints of this enhancement and highlight distinctions from the enhanced spectrum observed in 1D.

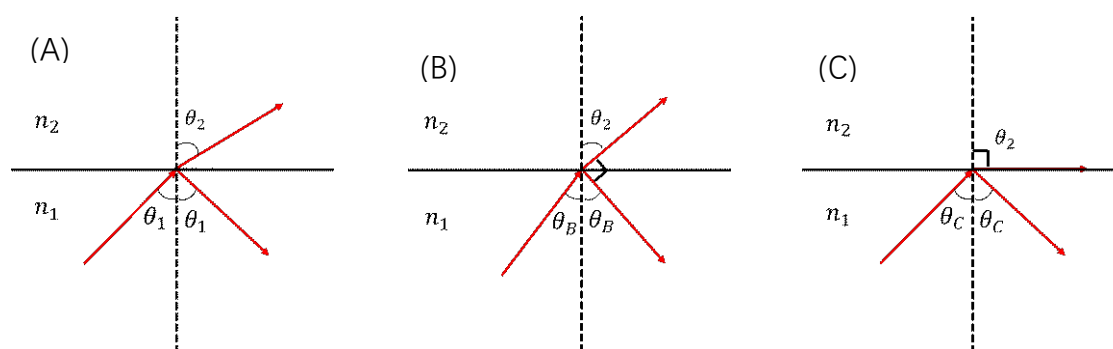


**Fig. 5.8** Snell's law(A), Brewster angle (B) and Critical angle (C)

According to Snell's law, as showed in Fig. 5.8A

$$n_1 \sin\theta_1 = n_2(\omega) \sin\theta_2 \quad (5.69)$$

If the angle between the reflected light and the refracted light measures  $90^\circ$ , the incident angle  $\theta_1$  at this specific juncture is designated as the Brewster Angle  $\theta_B$ , as

illustrated in Figure 5.8B.

$$\theta_B = \tan^{-1} \left( \frac{n_2}{n_1} \right) \quad (5.70)$$

And Brewster Angle  $\theta_B$  exists whether light is incident from an optically dense medium to an optically sparse medium or from an optically sparse medium to an optically dense medium. We first conclude that there is a maximum surface enhancement of the two-dimensional nonlinear infrared spectrum near Brewster Angle  $\theta_B$ . See later chapters for specific derivation and explanation.

If the angle between the refracted light and the normal is  $90^\circ$ , i.e.,  $\theta_2 = 90^\circ$ , at this juncture, the incident light undergoes total internal reflection. The incident angle  $\theta_1$  at this moment is denoted as the critical angle  $\theta_C$ , as showed in Fig. 5.8C.

$$\theta_C = \sin^{-1} \left( \frac{n_2}{n_1} \right) \quad (5.71)$$

It is noteworthy that this circumstance occurs when light travels from an optically dense medium to an optically sparse medium, i.e.,  $n_1 > n_2$ .

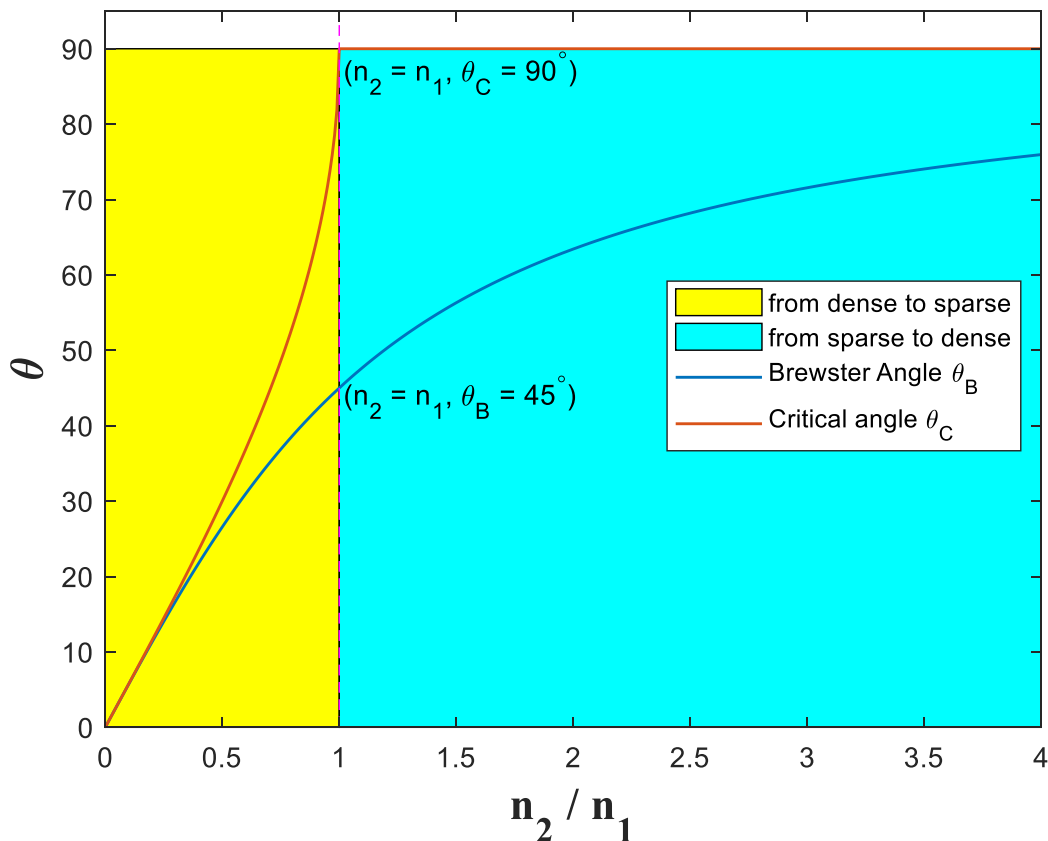


**Fig. 5.9** Relationship between  $\frac{n_2}{n_1}$  and  $\theta_B$ ,  $\theta_C$ .

As depicted in Fig. 5.9, the comprehensive illustration delineates two distinct segments: the transition of light intensity from dense to sparse (depicted in yellow) and

from sparse to dense (depicted in blue). These segments are further partitioned by angles  $\theta_B$  and  $\theta_C$ . Following the elucidation of the fundamental operational principle, Fresnel's law, an examination of each delineated region ensues sequentially. Moreover, it is readily discernible from Fig. 5.9 that  $\theta_C > \theta_B$ .

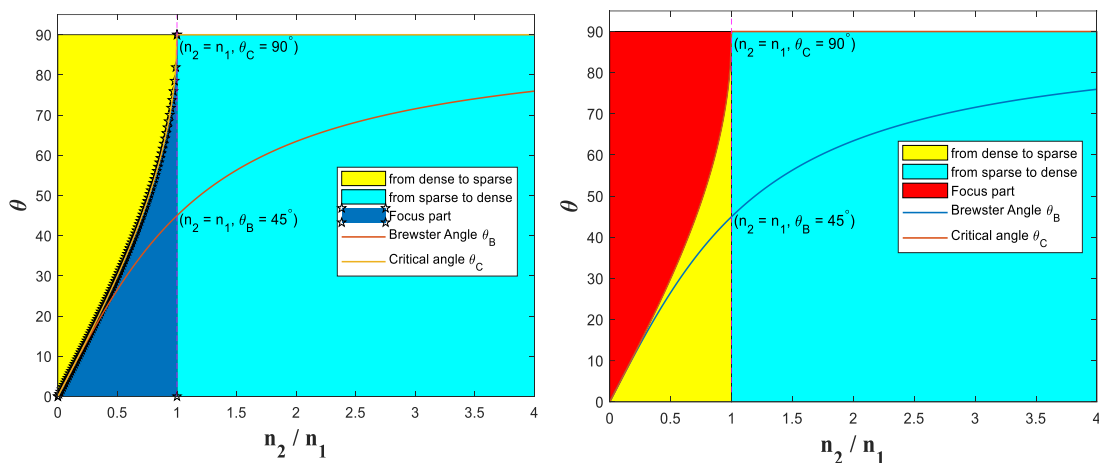


**Fig. 5.10** Relationship between  $\frac{n_2}{n_1}$  and  $\theta_B$ ,  $\theta_C$  with highlighted area of distorted spectrum in ATR (left) and with highlighted area of surface-enhanced spectrum in ATR (right).

Drawing from the insights presented in Chapter 1, it becomes evident that within ATR<sup>114</sup>, that is, when light is incident from an optically dense medium to an optically sparse medium, when  $\theta_1 \leq \theta_C$ , the resulting spectrum may exhibit distortion or even inversion. Area as depicted in the left portion of Fig. 5.10, highlighted by the dark blue focal region enveloped by asterisks.

Conversely, informed by the discourse in Chapter 4, it is established that under ATR conditions, provided the prerequisites for surface plasmon excitation are satisfied, an enhanced spectrum can be attained<sup>248, 252, 253</sup>. This is exemplified by the red focus area in the right segment of Figure 5.10. (For the present discussion, the focus is on bulk phenomena, excluding considerations of isolated surface plasmons arising from metal nanoparticles.)

It is noteworthy that the augmented and distorted spectra elucidated previously persist across both 1D ATR-FTIR spectroscopy and 2D ATR-FTIR spectroscopy methodologies.

Utilizing the formula derived from Maxwell's equations in Chapter 1, we can perform the following calculations:

$$r_s = \frac{n_1 \cos \theta_1 - n_2 \cos \theta_2}{n_1 \cos \theta_1 + n_2 \cos \theta_2} \quad (5.72)$$

$$r_p = \frac{n_2 \cos \theta_1 - n_1 \cos \theta_2}{n_2 \cos \theta_1 - n_1 \cos \theta_2} \quad (5.73)$$

$$R_s = |r_s|^2 \quad (5.74)$$

$$R_p = |r_p|^2 \quad (5.75)$$

$$R = \frac{R_s + R_p}{2} \quad (5.76)$$

$$A_s = -lgR_s \quad (5.77)$$

$$A_p = -lgR_p \quad (5.78)$$

$$A = -lgR \quad (5.79)$$

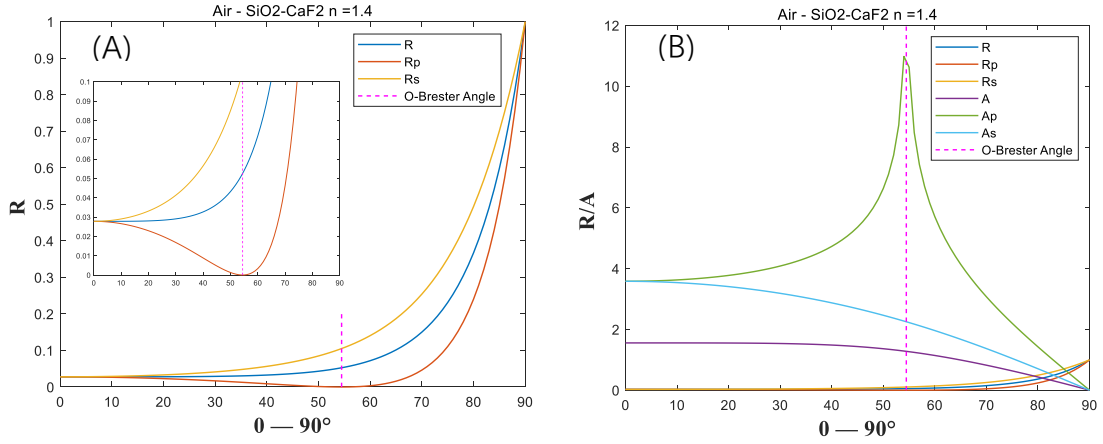


**Fig. 5.11** R and A with  $n_1 = 1$ ,  $n_2 = 1.4$ .

When considering the condition where light is propagating from an optically sparse medium to an optically dense medium, specifically light incidence from air into  $\text{SiO}_2$ , with refractive indices  $n_1 = 1$  and  $n_2 = 1.4$ , and varying the incident angle from  $0^\circ$  to  $90^\circ$ , the corresponding refraction and absorption diagrams can be derived, as illustrated in Fig. 5.11.

The observations from Figure 5.11 clearly indicate significant changes in the emission and absorption of p-polarized light in close proximity to the Brewster angle. This noteworthy alteration serves as a crucial foundation for the subsequent discussion on the observable enhancements near the Brewster angle in 2D IR, which will be explored in the following section.

Indeed, it is pertinent to highlight that when light traverses from an optically dense medium to an optically sparse medium, the phenomenon of Brewster angle remains

significant as showed in Fig.5.12. Notably, for p-polarized light, the emission and absorption characteristics in proximity to the Brewster angle undergo substantial alterations. Furthermore, it is imperative to acknowledge that analogous enhancement effects are observable in the context of 2D IR spectroscopy.

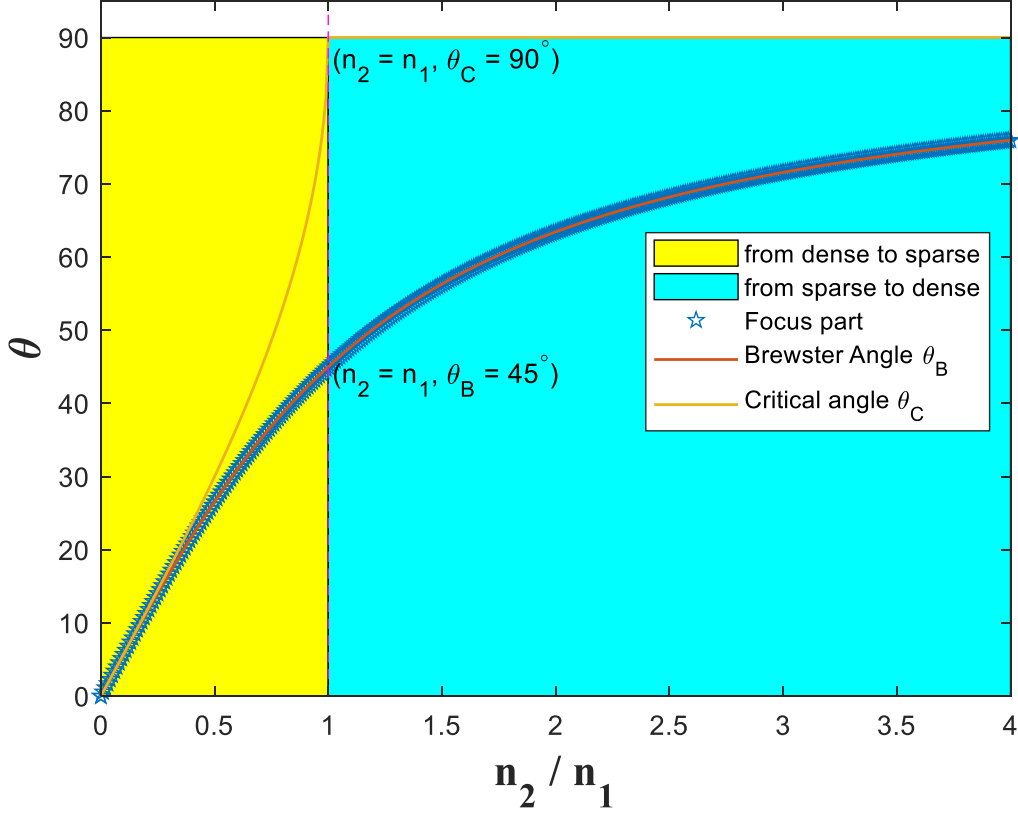


**Fig. 5.12** Relationship between  $\frac{n_2}{n_1}$  and  $\theta_B$ ,  $\theta_C$  with highlighted curve of surface-enhanced spectrum in 2D IR.

However, it merits attention that the condition  $\theta_B < \theta_C$  pertains to light transitioning from an optically dense medium to an optically sparse medium. In the context of ATR, when there is absorption by the substance, the resulting signal may exhibit distortion. Therefore, it is not advisable to utilize the signal obtained under such circumstances as an indicator of enhanced signal quality.

For 3 layers, the calculation is the same like in Chapter 4 as follows

$$\hat{n}_i = n_i + k_i \quad (i = 1,2,3) \quad (5.80)$$

$$m_1 = \hat{n}_1 \cos \theta_1 \quad (5.81)$$

$$m_i = \sqrt{\hat{n}_i^2 - \hat{n}_1^2 \sin^2 \theta_1} \quad (i = 2,3,4) \quad (5.82)$$

$$r_{ij,s} = \frac{m_i - m_j}{m_i + m_j}, \quad r_{ji,s} = \frac{m_j - m_i}{m_i + m_j} = -r_{ij,s}, \quad t_{ij,s} = \frac{2m_i}{m_i + m_j}, \quad t_{ji,s} = \frac{2m_j}{m_i + m_j} \quad (5.83)$$

$$r_{ij,p} = \frac{\hat{n}_i^2 m_j - \hat{n}_j^2 m_i}{\hat{n}_i^2 m_j + \hat{n}_j^2 m_i}, \quad r_{ji,p} = \frac{\hat{n}_j^2 m_i - \hat{n}_i^2 m_j}{\hat{n}_i^2 m_j + \hat{n}_j^2 m_i} = -r_{ij,p},$$

$$t_{ij,p} = \frac{2\hat{n}_i^2 m_j}{\hat{n}_i^2 m_j + \hat{n}_j^2 m_i}, \quad t_{ji,p} = \frac{2\hat{n}_j^2 m_i}{\hat{n}_i^2 m_j + \hat{n}_j^2 m_i} \quad (5.84)$$

$$\phi_2 = 2\pi v d_2 m_2 = 2\pi v d_2 \sqrt{\hat{n}_2^2 - \hat{n}_1^2 \sin^2 \theta_1} = 2\pi \frac{d_2}{\lambda} m_2 \quad (5.85)$$

$$r_{123} = \frac{r_{12} + r_{23} \exp(2i\phi_2)}{1 + r_{12} r_{23} \exp(2i\phi_2)} \quad (5.86)$$

$$t_{123} = \frac{t_{12} t_{23} \exp(i\phi_2)}{1 + r_{12} r_{23} \exp(2i\phi_2)} \quad (5.87)$$

$$R = R_{123} = |r_{123}|^2 \quad (5.88)$$

$$T = T_{123} = \left| \frac{n_1}{n_3} t_{123} \right|^2 \quad (5.89)$$

## 2. Enhancement in 2D IR

Building upon the knowledge from the preceding chapter, it is understood that 2D IR operates on the principles of third-order nonlinear optics. The specific spectrum enhancement principles of Eqs 5.90-5.105 are detailed in the literatures<sup>245, 250, 251</sup>. In which the signal light field is generated by the joint action of two pump light fields and a probe light field that is:

$$|E_{sig}| \propto |E_{pr}| |E_{pu}|^2 \quad (5.90)$$

The final signal S is modulated by adding a signal from the local oscillator (LO) field on the basis of the third-order signal light field, this can be expressed as:

$$S_1(\omega) \propto |E_{LO}(\omega) + E_{sig}(\omega)|^2 = |E_{LO}(\omega)|^2 + 2\text{Re}E_{sig}(\omega)E_{LO}(\omega) + |E_{sig}(\omega)|^2$$

$$\approx |E_{LO}(\omega)|^2 + 2\text{Re}E_{sig}(\omega)E_{LO}(\omega) \quad (5.91)$$

The omission of  $|E_{sig}(\omega)|^2$  is justified by the condition  $|E_{sig}(\omega)| \ll |E_{LO}(\omega)|$ .

Given that the pump light undergoes periodic obstruction by the optical cutter, resulting in the absence of third-order optical signal generation, only the LO signal is detected during these intervals. This is expressed as:

$$S_2(\omega) \propto |E_{LO}(\omega)|^2 \quad (5.92)$$

Subsequently, the ultimate signal is given by:

$$S(\omega) = \frac{S_1(\omega)}{S_2(\omega)} \propto \frac{\text{Re}E_{sig}(\omega)E_{LO}(\omega)}{|E_{LO}(\omega)|^2} \quad (5.93)$$

For transmission

$$E_{LO}(\omega) = E_{pr}(\omega) \quad (5.94)$$

The corresponding transmitted final signal can be expressed as:

$$S_t(\omega) \propto \frac{ReE_{sig}(\omega)E_{pr}(\omega)}{|E_{pr}(\omega)|^2} \quad (5.95)$$

For reflections

$$E_{LO}(\omega) = r(\omega) E_{pr}(\omega) \quad (5.96)$$

$r(\omega)$  is reflectance

$$S_r(\omega) \propto \frac{ReE_{sig}(\omega)(\omega)E_{pr}(\omega)}{|r(\omega)E_{pr}(\omega)|^2} = -\frac{ReE_{sig}(\omega)E_{pr}(\omega)}{r(\omega)|E_{pr}(\omega)|^2} \quad (5.97)$$

$$S_t(\omega) \propto -S_r(\omega) r(\omega) \quad (5.98)$$

Alternatively, it can be written as:

$$S_r(\omega) \propto -\frac{1}{r(\omega)} S_t(\omega) \quad (5.99)$$

Then the signal increase factor between the reflection spectrum and transmission spectrum is

$$R_{Enhance} = -\frac{1}{r(\omega)} \quad (5.100)$$

If the refractive index  $n_2(\omega)$  is changing with wavelength (or wavenumber), then this equation can be written as

$$r_p(\omega) = \frac{n_2(\omega)\cos\theta_1 - n_1\cos\theta_2}{n_2(\omega)\cos\theta_1 + n_1\cos\theta_2} \quad (5.101)$$

Then

$$R_{Enhance} = -\frac{1}{r(\omega)} \quad (5.102)$$

When the influence of s-polarized light is not taken into account.

However, when considering the leakage of s-polarized light, under these circumstances, the signal light does not interfere with the s light. The leaked s-polarized light does not impact  $ReE_{sig}(\omega)E_{pr}(\omega)$  but solely influences  $|E_{pr}(\omega)|^2$ . Let  $m$  denotes the leakage coefficient of s-polarized light, signifying:

$$m = \frac{|E_{pr,s}(\omega)|}{|E_{pr,p}(\omega)|} \quad (5.103)$$

Here, we consider  $m = 0.0001$ ,

Then

$$S_r(\omega) \propto -\frac{r_p(\omega)}{|r_p(\omega)|^2 + m|r_s(\omega)|^2} S_t(\omega) = -\frac{r_p(\omega)}{R_p + mR_s} S_t(\omega) \quad (5.104)$$

Then

$$R_{Enhance} = -\frac{r_p(\omega)}{R_p + mR_s} \quad (5.105)$$

The parameter  $R_{Enhance}$  holds significant relevance with respect to the Brewster angle and is evident in transitions from optically dense to optically sparse media as well as vice versa. However, owing to its association with LO modulation, this particular form of surface enhancement is exclusive to 2D IR spectroscopy, and is not observable within the realm of one-dimensional infrared 1D IR spectroscopy.



### 3. Brewster angle

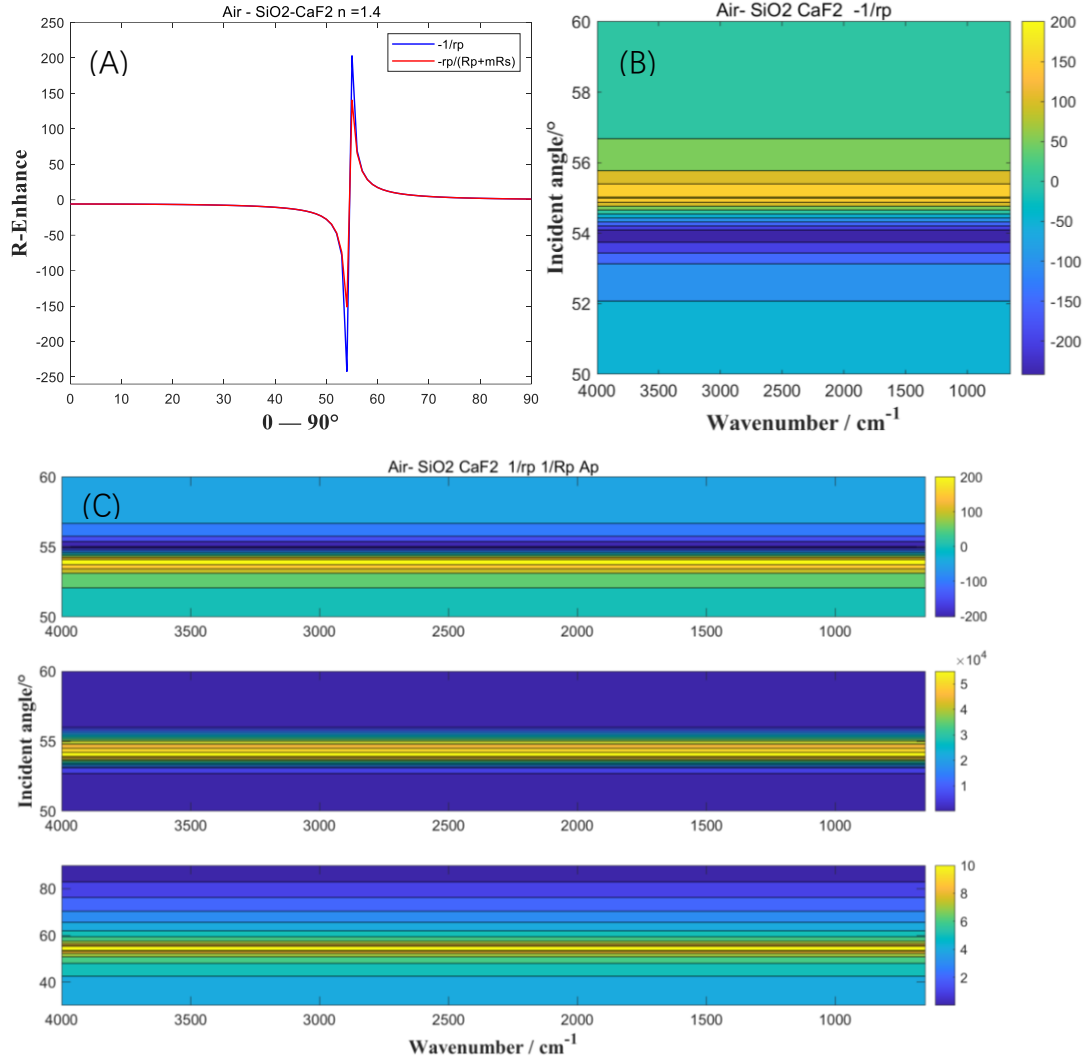


**Fig. 5.13**  $R_{Enhance}$  changing with incident angle  $\theta_1 = 0^\circ - 90^\circ$  (A) ( $n_1 = 1$ ,  $n_2 = 1.4$ );  $R_{Enhance}$  changing with wavenumber and incident angle  $\theta_1 = 50^\circ - 60^\circ$  (B);  $\frac{1}{r_p}$ ,  $\frac{1}{R_p}$  and  $A_p$  changing with wavenumber and incident angle (C).

As observed prominently in Fig. 5.13,  $\theta_{Brewster\ Angle} = 54.46^\circ$ , near the Brewster Angle,  $R_{Enhance}$  undergoes significant variations, aligning with the description provided by Fayer in the paper<sup>251</sup>. This observation also concurs with the explanation presented in our preceding chapter.

It is important to note that in this context, we maintain the assumption that  $n_2(\omega) = 1.4$  remains a constant value. Furthermore, the anisotropy of the material and alterations in the refractive index due to the incident laser are not taken into consideration. It is crucial to acknowledge that, in reality, these factors could introduce added complexity to the situation. For a detailed calculation process, please refer to the

supporting information provided in Fayer's papers<sup>250, 251, 254</sup>.

Next, we will analyze the implications of varying the value of  $n_2(\omega)$  with changes in  $\omega$ .<sup>255</sup>

$$n_2(\omega) = \sqrt{1.33973 + \frac{0.69913\lambda^2}{\lambda^2 - 0.09374^2} + \frac{0.11994\lambda^2}{\lambda^2 - 21.18^2} + \frac{4.3518\lambda^2}{\lambda^2 - 38.46^2}} \quad (5.106)$$

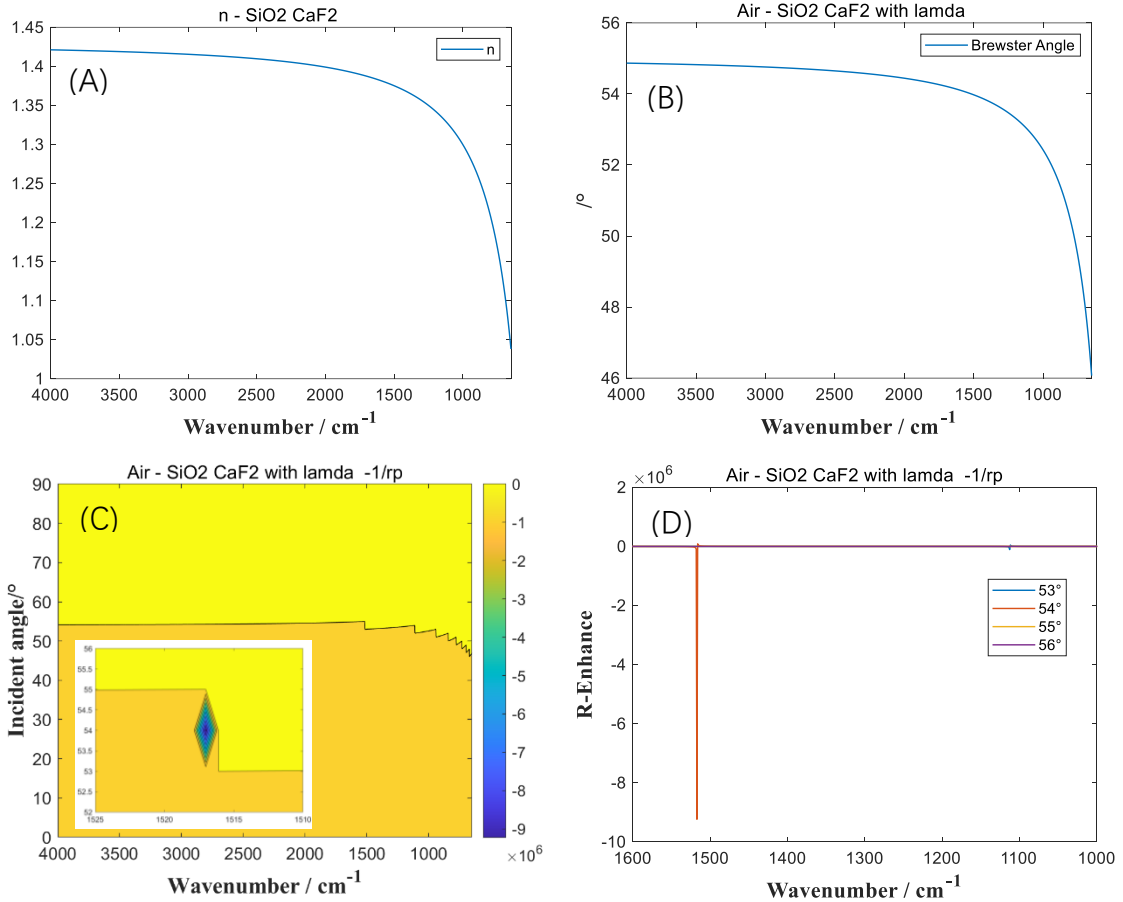


**Fig. 5.14**  $n_2(\omega)$ (A) and  $\theta_B(\omega)$ (B) changing with wavenumber;  $R_{Enhance}$  changing with wavenumber and incident angle(C);  $R_{Enhance}$  changing with wavenumber(D).

As evident from Fig. 5.14, the alteration of  $n_2(\omega)$  with  $\omega$  results in a corresponding change in  $\theta_B(\omega)$ . This, in turn, leads to variations in the maximum value of  $R_{Enhance}$  with  $\omega$  at different incident angles. While most of the aforementioned aspects have been discussed in detail, we will refrain from delving into further intricacies at this juncture.

The initial point we intend to clarify is that the underlying reason for the variation in  $R_{Enhance}$  with  $\omega$  lies in the changes of  $n_2(\omega)$ , leading to the attainment of  $\theta_B(\omega)$  at different  $\omega$  values. It is crucial to note that this phenomenon does not alter the fact that  $R_{Enhance}$  is maximized near the Brewster angle. To simplify matters and avoid

complexity, we will refrain from further emphasis on this particular scenario in our subsequent discussions.

The focus of our subsequent discussion centers on the addition of a Carbon((Sample 1 discussed in Chapter 1)) thin layer to the interface(normally gold is used in simulation<sup>256</sup>), as illustrated in Fig. 5.15.

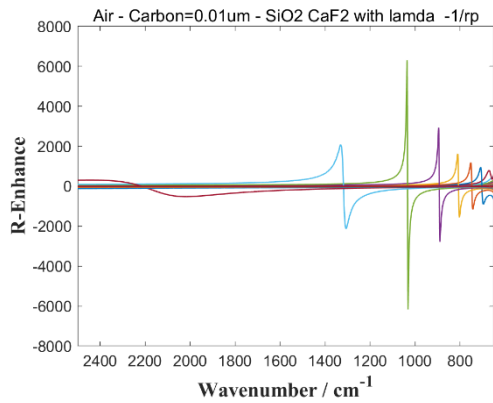
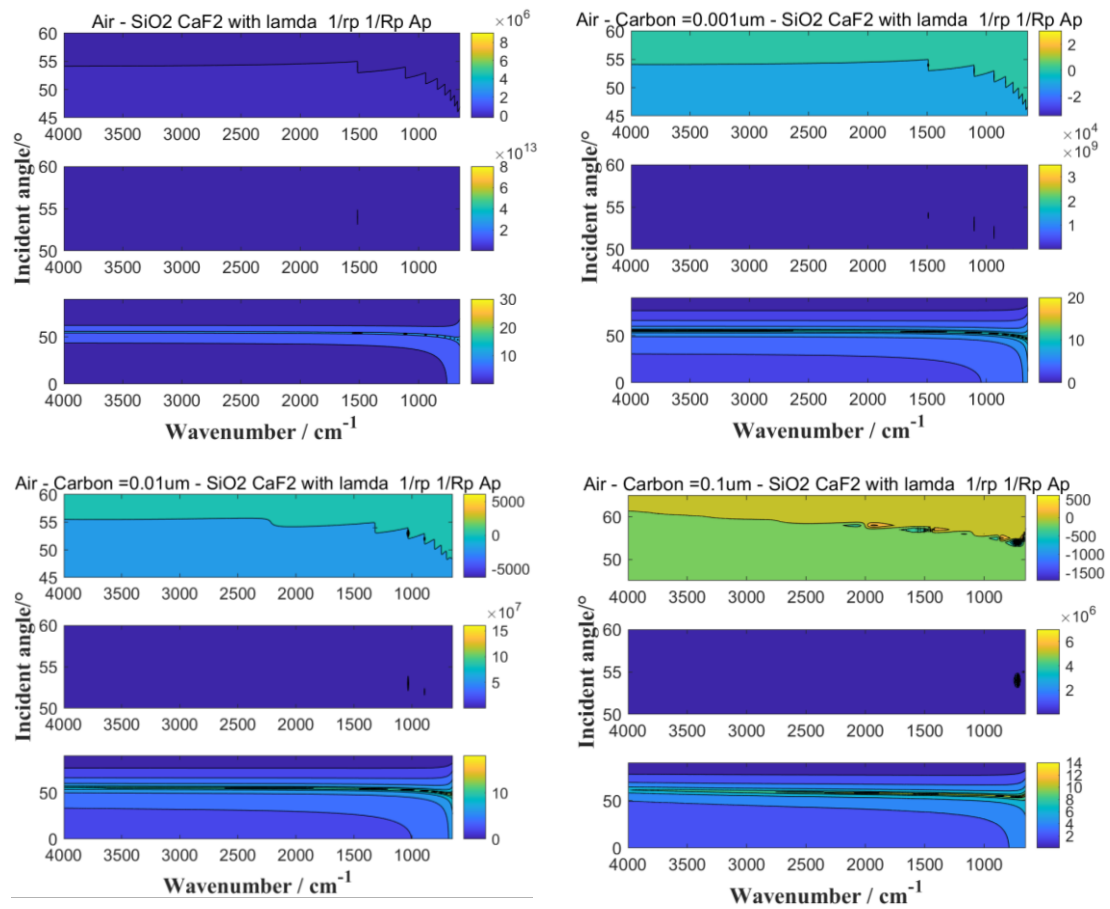


**Fig. 5.15.**  $R_{Enhance}$  changing with wavenumber and thickness( $d$ ).



The evident variation in  $R_{Enhance}$  near the Brewster Angle, reaching both maximum and minimum values on both sides, is notable in Fig. 5.15. However, it's crucial to highlight that the magnitude of  $R_{Enhance}$  is entirely different when the thickness varies.

It is important to highlight that in Fig. 5.15 our comparison extends beyond the values of  $R_{Enhance} = -\frac{1}{r_p(\omega)}$ ; we also consider the values of  $\frac{1}{r_p}$ ,  $\frac{1}{R_p}$  and  $A_p$ . We present an initial observation that, when focusing solely on angle-dependent  $A_p$ , the observed trend aligns with the trend of  $\frac{1}{r_p}$ . This alignment is inherent as  $A_p$  is fundamentally derived from  $\frac{1}{r_p}$ .

Combining the preceding calculations and the corresponding Fig. 5.15, it becomes evident that  $\frac{1}{r_p}$ ,  $\frac{1}{R_p}$ , and  $A_p$  are fundamentally equivalent, albeit with differing orders of magnitude in the calculations.

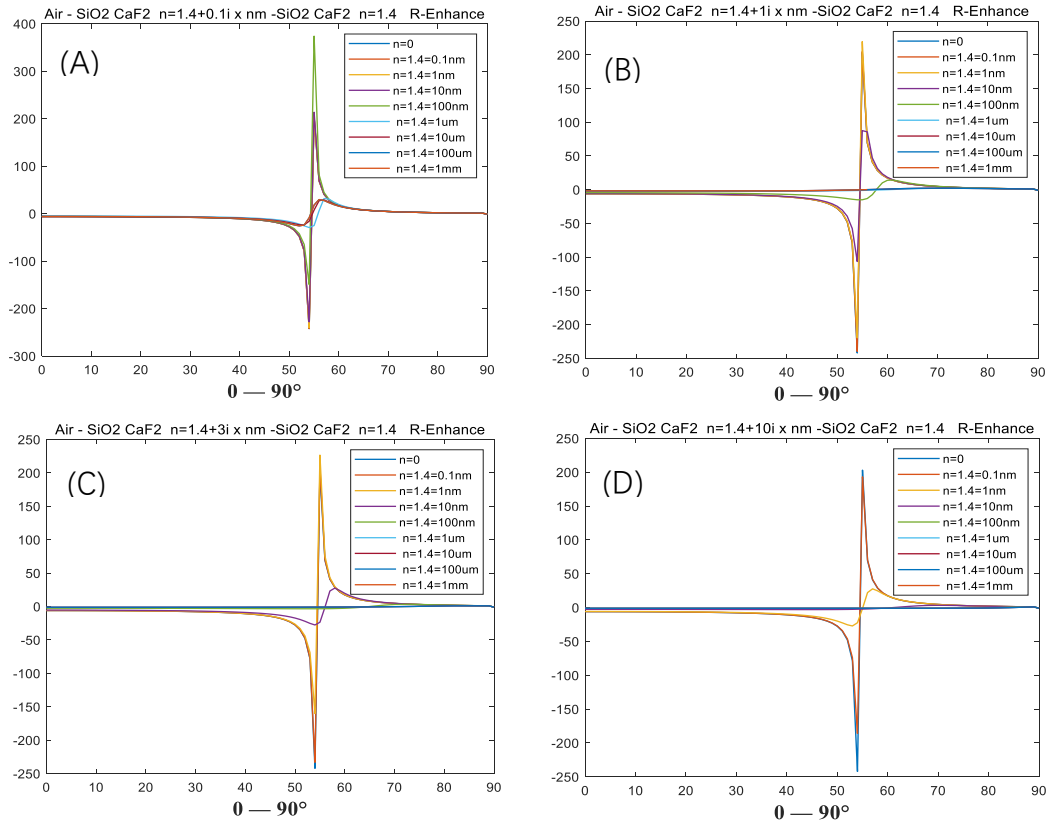


**Fig. 5.16**  $R_{Enhance}$  changing with incident angle, thickness ( $d$ ) and absorption coefficients ( $k$ ). Set  $n = 1.4 + 0.1i(A)$ ;  $n = 1.4 + 1i(B)$ ;  $n = 1.4 + 3i(C)$ ;  $n = 1.4 + 10i(D)$ .

Subsequently, to enhance clarity in illustrating the influence of the thickness and

refractive index of the intermediate dielectric layer on R-Enhance, we maintain the assumption that  $n_{SiO_2CaF_2}(\omega) = 1.4$ , noting that this corresponds to the third layer. The refractive index of the intermediate layer is represented as  $n_2 = n + ik = 1.4 + ik$ . The summarized findings are depicted in Fig.5.16

We conducted a comparative analysis across various absorption coefficients ( $k$ ). Notably, when  $k = 0.1$  with a thickness ( $d$ ) of 100nm,  $R_{Enhance}$  attains its maximum value. Similarly, at  $k = 1$  and  $d = 0.1nm$ ,  $R_{Enhance}$  reaches its maximum. Furthermore, for  $k = 3$  and  $d = 1nm$ ,  $R_{Enhance}$  achieves its highest value. Additionally, for cases where  $k \geq 10$  and there is no specified thickness,  $R_{Enhance}$  attains its maximum value. Importantly, the conclusion remains consistent even when altering the refractive index ( $n$ ).

As highlighted by Fayer in the paper, adopting  $\frac{d}{\lambda}$  as the abscissa and exclusively considering the scenario where the incident angle is  $\theta = 54^\circ$  (approximating the Brewster angle), at a wavenumber of approximately  $\sim 2025\text{ cm}^{-1}$  (the specific choice of wavenumber is not a critical factor at this juncture), the calculated signal diagram for the reflection situation is depicted in Fig. 5.16.

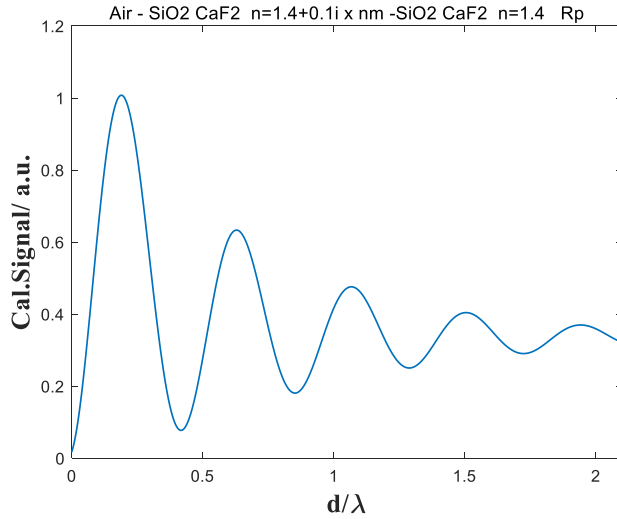


**Fig. 5. 17** Reflection pattern signal fields of different thicknesses with  $\theta = 54^\circ$  at  $\sim 2025\text{ cm}^{-1}$ .

In reality, if  $\frac{d}{\lambda}$  continues to increase, the signal will persist in oscillating until it eventually decays to zero. However, the fundamental nature of this phenomenon is attributed to the calculation process of  $R_p$ .

Referring to Eqs. 5.85 ~ 5.88, it can be deduced that:

$$R \propto \exp(4i\phi_2) \propto \exp\left(i\frac{d_2}{\lambda}\right) = \cos\left(\frac{d_2}{\lambda}\right) + i\sin\left(\frac{d_2}{\lambda}\right) \quad (5.107)$$

Therefore, the intrinsic cause of the cyclic oscillation and decay in the signal is determined by the periodic function concerning  $\frac{d}{\lambda}$ . This phenomenon is present at any wavenumber and for any incident angle with phase delay.

As our primary focus is not solely on the enhancement phenomenon near the Brewster angle, and considering that this aspect has been thoroughly addressed, we will refrain from providing further elaboration on it in the subsequent chapters.

In the subsequent section, we will delve into and the surface enhancement spectrum as it transitions from an optically dense medium to an optically sparse medium.

#### 4. Optically dense to optically sparse

In the preceding section, we explored the scenario of light transitioning from an optically sparse medium to an optically dense medium. Now, we shift our focus to the transition from an optically dense medium to an optically sparse medium, assuming the medium to be diamond with  $n_{Diamond} = 2.41$  and  $n_{SiO_2CaF_2} = 1.4$ . Through calculations, the obtained results are illustrated in the figure.

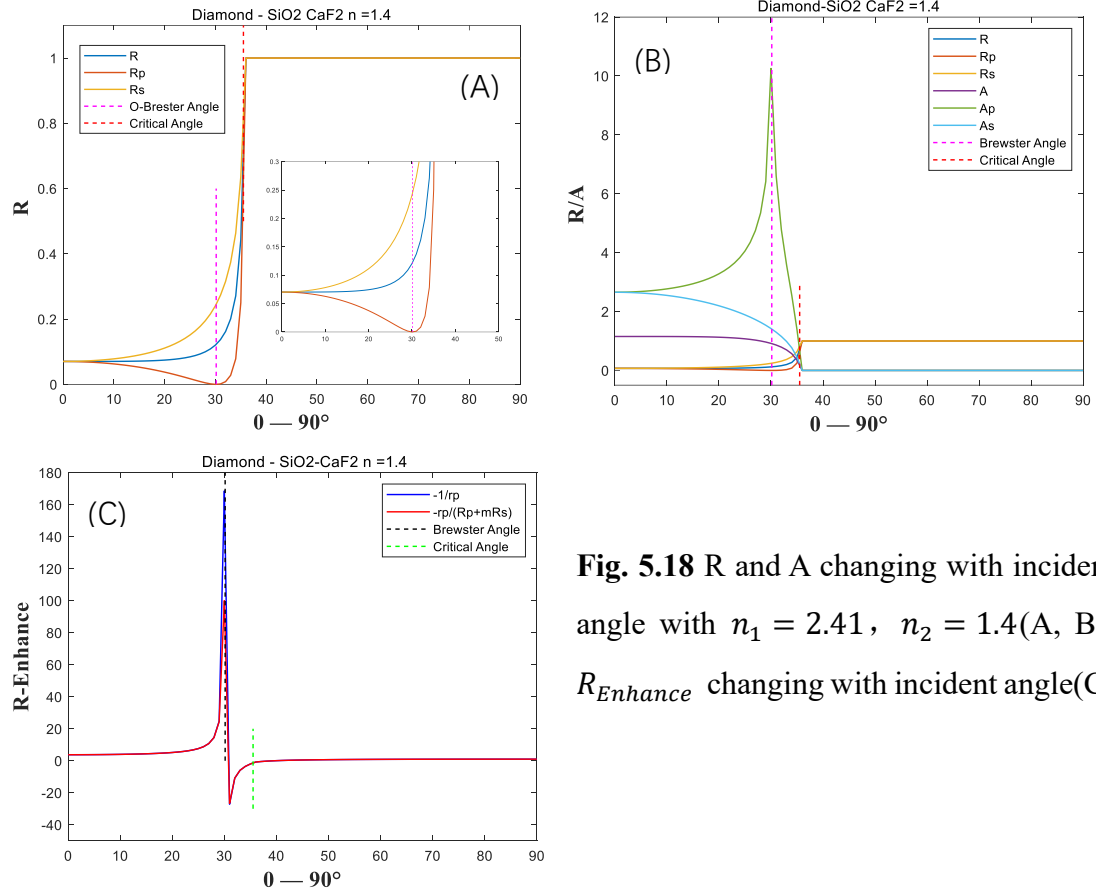


**Fig. 5.18** R and A changing with incident angle with  $n_1 = 2.41$ ,  $n_2 = 1.4$ (A, B);  $R_{Enhance}$  changing with incident angle(C).

As depicted in Fig. 5.18, it is evident that when light transitions from the optically dense medium to the beam medium, both the Brewster Angle  $\theta_B$  and the Critical Angle  $\theta_C$  are present. And normally  $\theta_C \geq \theta_B$

Having previously explored the distorted spectrum near the Critical Angle in Chapters 1 and 2, and delved into the surface-enhanced spectrum in Chapter 4, we now turn our attention to the Brewster Angle  $\theta_B$  and examine the enhancement near  $\theta_B$  when transitioning from optically dense to optically sparse media. Similar to the previous section, we can derive analogous  $R_{Enhance}$  values, but now with opposite directions in both positive and negative axes.

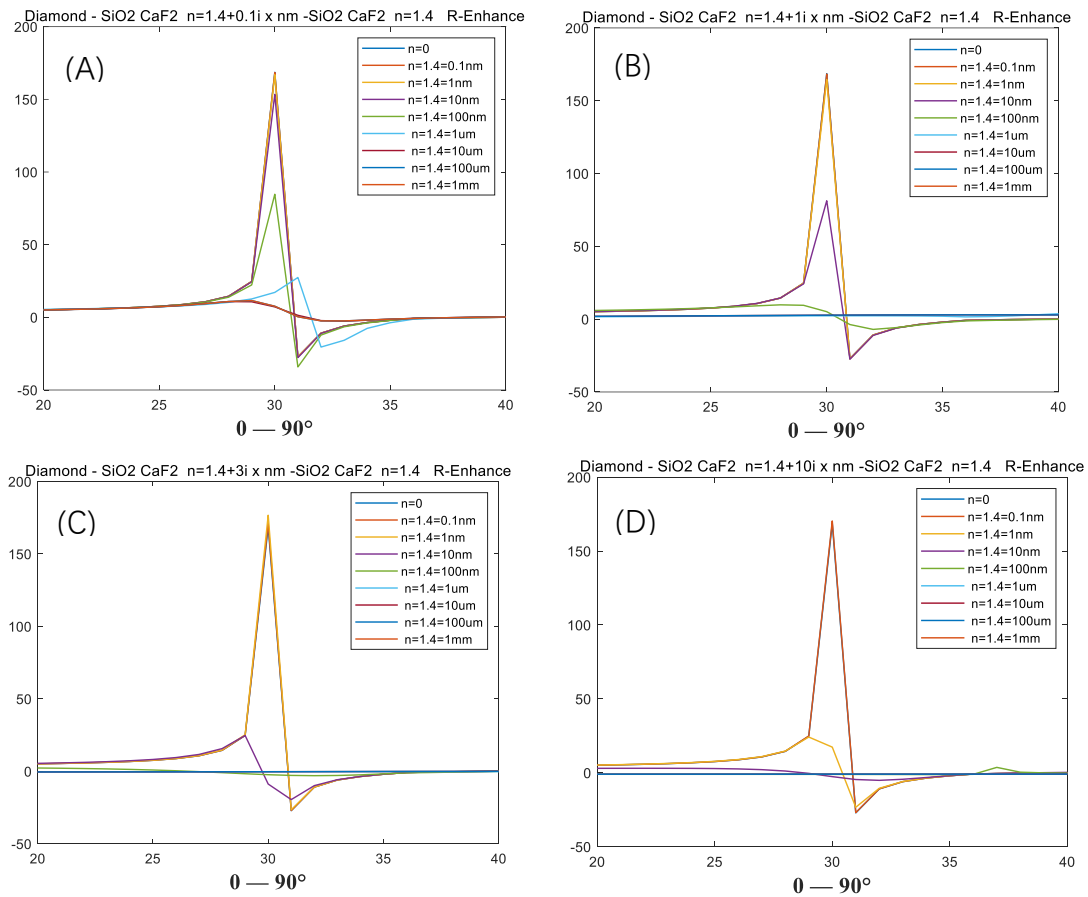


**Fig. 5.19**  $R_{Enhance}$  changing with incident angle, thickness ( $d$ ) and absorption coefficients ( $k$ ). Set  $n = 1.4 + 0.1i(A)$ ;  $n = 1.4 + 1i(B)$ ;  $n = 1.4 + 3i(C)$ ;  $n = 1.4 + 10i(D)$ .

We conducted a comparative analysis considering various absorption coefficients ( $k$ ) for the intermediate layer in Fig. 5.19. Notably, when  $k = 0.1$ ,  $R_{Enhance}$  attains its maximum value at different thicknesses ( $d$ ). It's important to note that, due to variations in the refractive index of both the input and refractive media from the preceding section,  $R_{Enhance}$  achieves its maximum value. While there are slight differences in the specific maximum values, they are generally obtained at extremely thin thicknesses, such as  $d = 1nm$  or  $d = 0.11nm$ . However, unlike incidents from air, the scenario of  $R_{Enhance}$  undergoes changes when altering the refractive index ( $n$ ) of the intermediate layer.



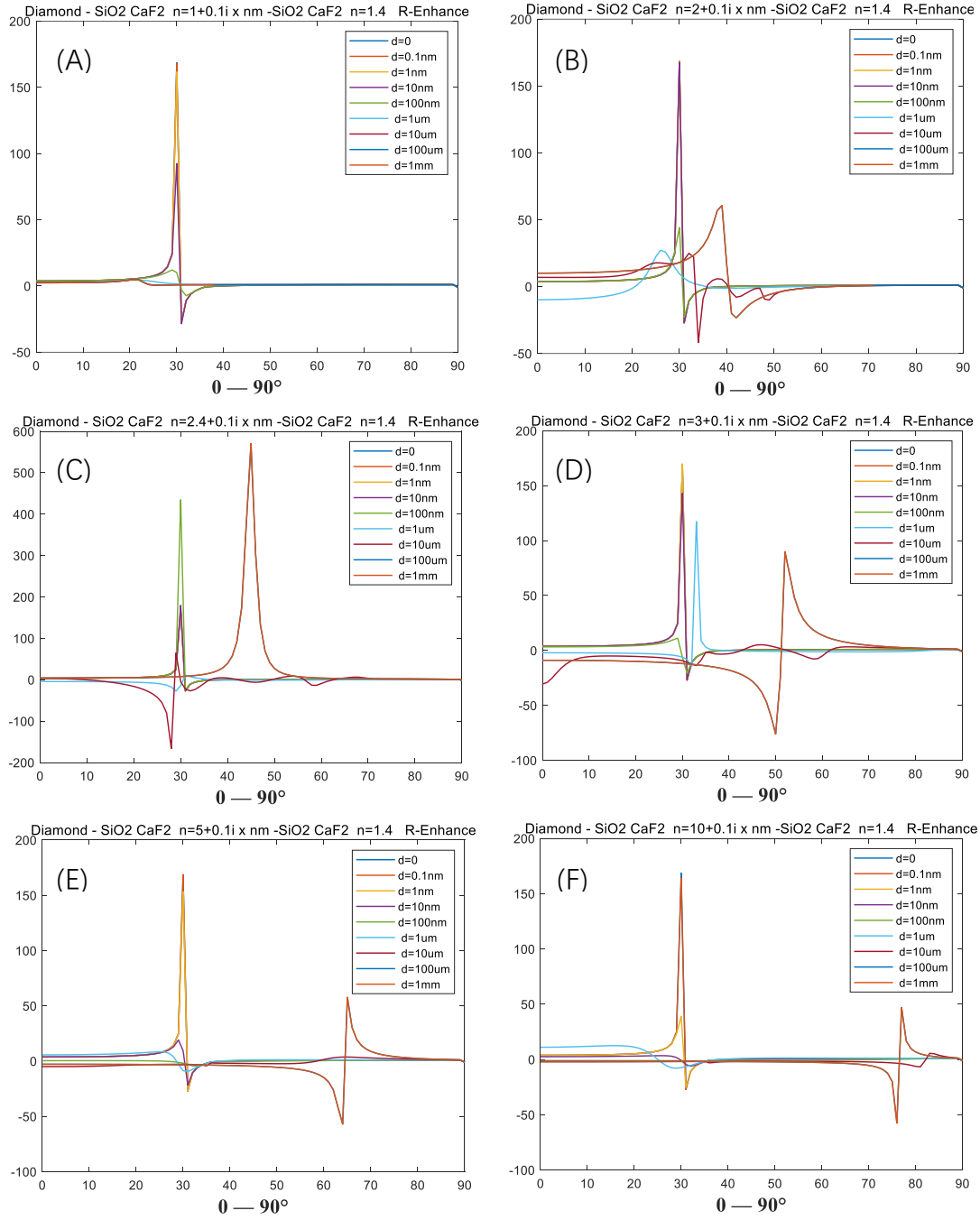


**Fig. 5.20**  $R_{Enhance}$  changing with incident angle, thickness ( $d$ ), refractive index ( $n$ ). Set  $n = 1 + 0.1i$ (A);  $n = 2 + 0.1i$ (B);  $n = 2.4 + 0.1i$ (C);  $n = 3 + 0.1i$ (D);  $n = 5 + 0.1i$ (E);  $n = 10 + 0.1i$ (F).

Diverging from the previous section, we extend our consideration to additional cases, specifically those involving a continuously changing refractive index ( $n$ ) of the intermediate layer ( $n_2 = n + ik$ ). When the refractive index of the intermediate layer ( $n$ ) is less than  $n_1$ , its impact on  $R_{Enhance}$  is confined to the data size. Additionally, when the refractive index ( $n$ ) of the intermediate layer approaches the refractive index

of the incident medium,  $n_1 = 2.41$  ( $2 < n < 3$ ),  $R_{Enhance}$  exhibits notable fluctuations.

In scenarios where the refractive index of the intermediate layer significantly exceeds that of the incident medium ( $n > 5$ ), for small thicknesses ( $d$ ), it can still be treated as a thin layer. Conversely, for large thicknesses, it is regarded as an independent second layer.

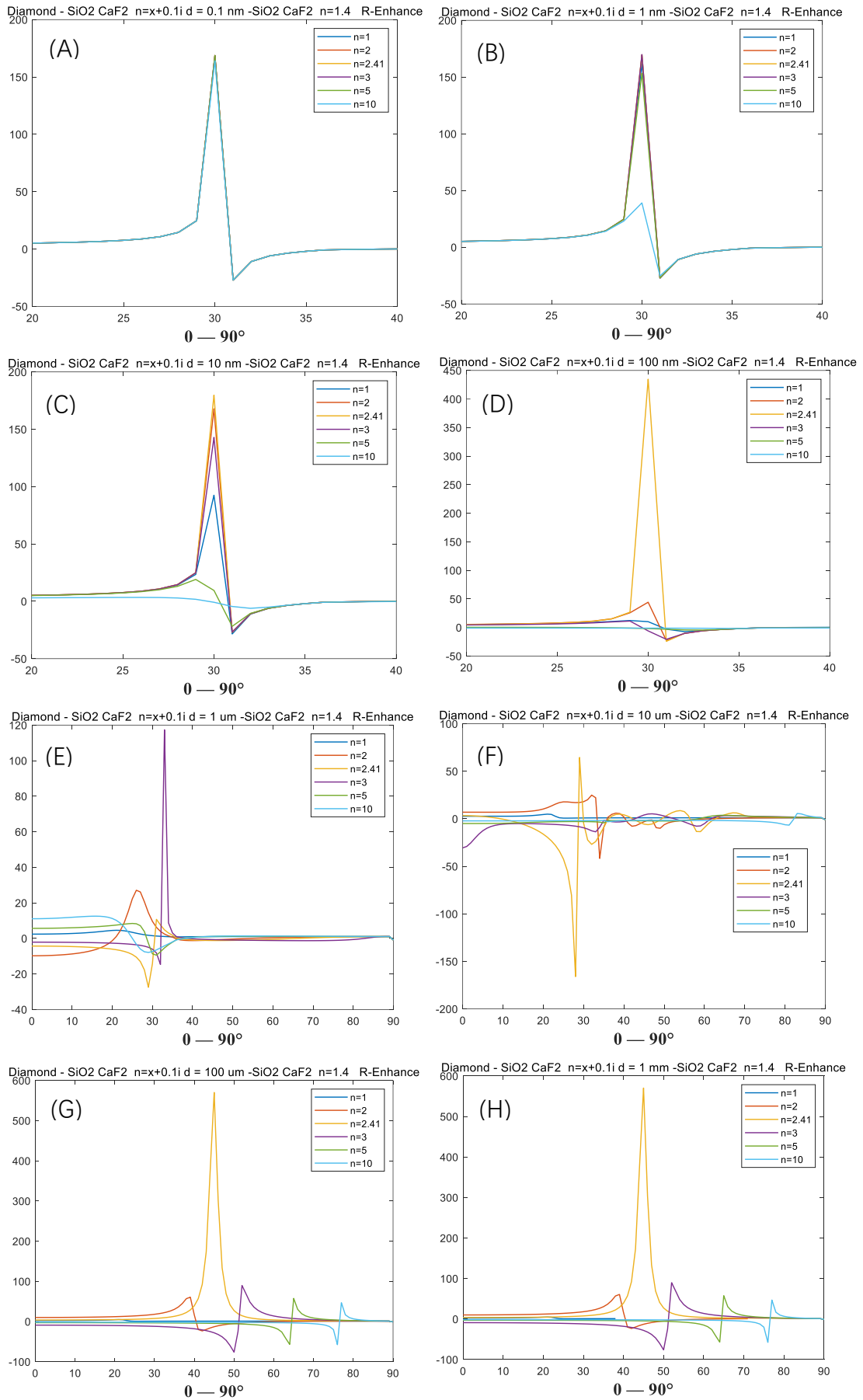


**Fig. 5.21**  $R_{Enhance}$  changing with incident angle, thickness ( $d$ ), refractive index ( $n$ ).

Set  $d = 0.1nm$  (A) ;  $d = 1nm$  (B) ;  $d = 10nm$  (C) ;  $d = 100nm$  (D);  $d = 1\mu m$  (E);  $d = 10\mu m$  (F) ;  $d = 100\mu m$  (G);  $d = 1mm$  (H).

The distinct observation from Fig 5.21 is that, with the continued increase in the refractive index ( $n$ ) of the intermediate layer, the thin-layer paradigm persists for cases with small thickness ( $d < 1nm$ ), allowing us to disregard the impact of the intermediate layer. However, when  $d$  is larger ( $d > 10\mu m$ ), it should be treated as an independent second layer, reiterating the previously discussed transition from an optically sparse to an optically dense medium.

In the range of  $10nm < d < 100nm$ , although the refractive index ( $n$ ) of the intermediate layer can exert some influence, the overall trend of  $R_{Enhance}$  remains relatively consistent. The most intriguing scenario emerges in the case of  $1nm < d < 10\mu m$ , where the thickness is close to half-wavelength. In this instance, as the refractive index ( $n$ ) continues to rise,  $R_{Enhance}$  undergoes a distinct transformation, presenting a wholly different state.

## 5.4 Comparison

In Chapter 4, we conducted a comparative analysis of the impact of thin layers with varying thicknesses and shapes on ATR-FTIR surface enhancement. Of particular significance was the observation of the enhancement mechanism near the critical angle. Subsequently, in Chapter 5, Section 3, we delved into the influence of the Brewster angle on the 2D enhancement mechanism IR<sup>257</sup>. The objective now is to elucidate the relationship and function between these two phenomena, and this will be addressed in the current chapter.

It is noteworthy that our discussion exclusively revolves around the enhancement mechanism under variable incident angles, specifically excluding considerations of transmission enhancement.

First and foremost, we draw the conclusion that the primary contributor to the enhancement observed in the Brewster Angle effect is the unique nature of the 2D spectrum. This enhancement effect, derived from the interplay of incident angles generated by the pump and probe, undergoes a significant transformation in proximity to the Brewster angle. Notably, altering thickness at the same angle does not exert the most pronounced impact. Specifically, the changes in  $\frac{1}{r_p}$ ,  $\frac{1}{R_p}$  and  $A_p$  are most substantial in the vicinity of the Brewster Angle.

The enhancement associated with the critical angle exhibits greater resemblance to the refractive index and thickness of the medium. While the alteration in spectral enhancement may not be most prominent near the critical angle, the change induced by variations in thickness has the most significant influence in close proximity. Specifically, the change in  $A_{pd}/A_p$  are most substantial in the vicinity of the critical angle. (Here,  $A_{pd}$  denote absorption with a thin layer).

Subsequently, we will bifurcate the scenario into two distinct situations: incident from an optically dense medium to an optically sparse medium, and incident from an optically sparse medium to an optically dense medium. Each situation will be discussed individually.

In the first scenario, where an optically dense medium is incident on an optically sparse medium.

In accordance with the data presented in Figure 5.20, it is evident that the most substantial alterations in the ratios  $r_p/r_{pd}$  and  $R_p/R_{pd}$  occur at the Brewster Angle ( $\theta_B = 35.51^\circ$ ,  $\theta_c = 30.15^\circ$ ). This observation aligns consistently with the findings expounded upon in the preceding chapter.

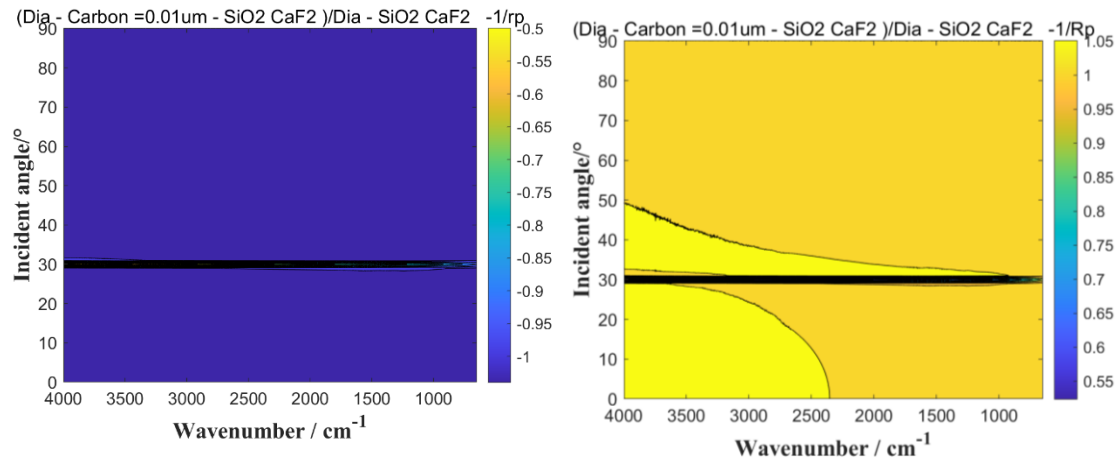


**Fig. 5.22**  $r_p/r_{pd}$  and  $R_p/R_{pd}$  changing with wavenumber and incident angle ( $n_{Diamond} = 2.41$ , Carbon is sample 1 from Chapter1). The difference is  $n_{SiO_2CaF_2} = 1.4$ (Left);  $n_{SiO_2CaF_2}$  changing with wavenumber (Right)

However, a noteworthy observation emerges in Fig.5.22. As the incident angle approaches the Critical Angle ( $\theta_B = 35.51^\circ$ ,  $\theta_c = 30.15^\circ$ ), the ratio  $A_{pd}/A_p$  abruptly becomes indeterminate.

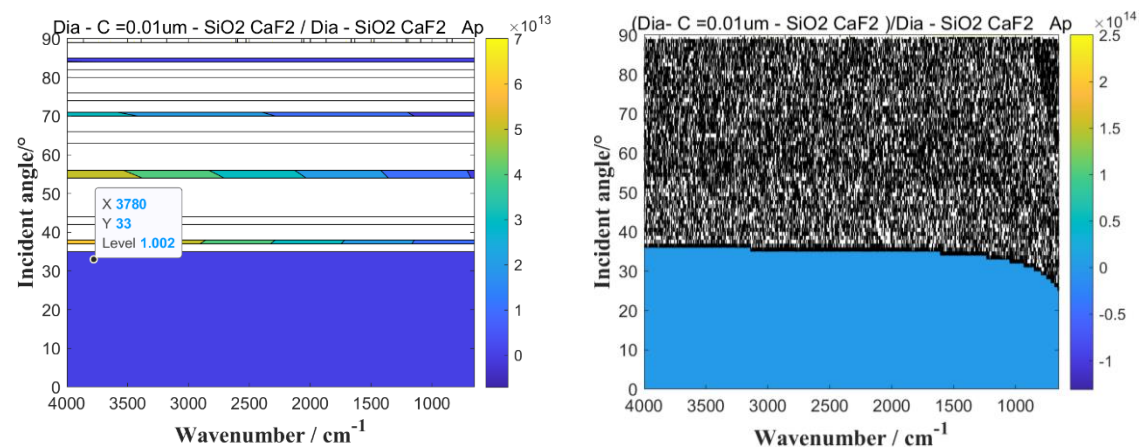


**Fig. 5.23**  $A_{pd}/A_p$  changing with wavenumber and incident angle ( $n_{Diamond} = 2.41$ , Carbon is sample 1 from Chapter1). The difference is  $n_{SiO_2CaF_2} = 1.4$  (Left);  $n_{SiO_2CaF_2}$  changing with wavenumber (Right).

This occurrence is attributed to the fact that, without accounting for absorption

conditions,  $R_p$  undergoes total reflection when the incident angle surpasses the Critical Angle, resulting in a value of 1, while  $A_p$  is 0. Consequently, calculations cannot proceed, leading to an indeterminate result. The ultra-high enhancement factor observed above the critical angle is influenced by leakage caused by the refractive index of the material in the thin layer surpassing that of the incident medium. In any case, when the incident angle exceeds the critical angle,  $A_p$  approaches infinity, contributing to the increase in  $A_{pd}/A_p$ . This underscores the fundamental reason for obtaining an enhanced spectrum when an optically dense medium is incident on an optically sparse medium. This phenomenon becomes more pronounced when the refractive index of  $\text{SiO}_2$  varies with wavenumber as showed in Fig. 5.23.

In the second scenario, where the incident medium is optically sparse and the receiving medium is optically dense, it is noteworthy that there is no distinct critical angle, or it can be considered that the critical angle is infinitely close to  $90^\circ$ .

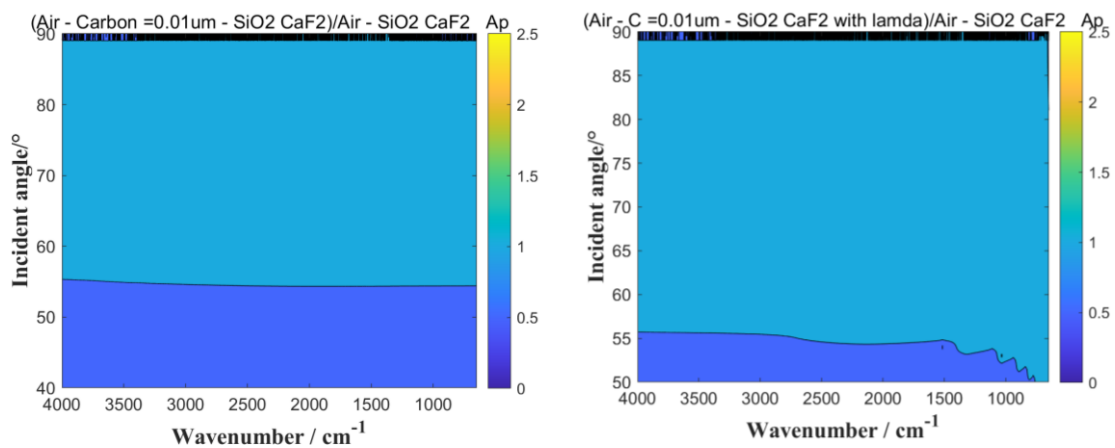


**Fig. 5.24**  $A_{pd}/A_p$  changing with wavenumber and incident angle ( $n_{Air} = 1$ , Carbon is sample 1 from Chapter1). The difference is  $n_{\text{SiO}_2\text{CaF}_2} = 1.4$ (Left);  $n_{\text{SiO}_2\text{CaF}_2}$  changing with wavenumber (Right).

As depicted in the Fig. 5.24, it is evident that there are some variations in  $A_{pd}/A_p$  near the Brewster angle. However, the overall change is relatively modest, and the enhancement likely remains within single-digit values. Therefore, in the context of surface enhancement, although there is a substantial enhancement near the Brewster Angle when altering the incident angle, a noteworthy aspect of this phenomenon is that, at the same incident angle near the Brewster Angle, both  $A_{pd}$  with a thin layer and  $A_p$  without a thin layer achieve a comparable degree of enhancement. Consequently, the final result of  $A_{pd}/A_p$  does not exhibit significant variation, implying that, in this scenario, the enhancing effect of adding thin layers on  $A_{pd}/A_p$  is not conspicuous.

Comparison of differences between enhancement between near Brewster Angle ( $\theta_B$ ) and near Critical Angle ( $\theta_C$ ) are showed in Table. 5.1.

**Table. 5.1** Differences enhancement between near Brewster Angle ( $\theta_B$ ) and near Critical Angle ( $\theta_C$ )

Property	Enhancement Near Brewster Angle ( $\theta_B$ )	Enhancement Near Critical Angle ( $\theta_C$ )
Linear IR (1D IR)	×	√
Nonlinear IR (2D IR)	√	√
From Dense to Parse	√	√
From Parse to Dense	√	×
Enhancement	$R_{Enhance} = -\frac{1}{r(\omega)} = \frac{S_r(\omega)}{S_t(\omega)}$	$R_{Enhance} = \frac{S_d(\omega)}{S(\omega)}$
Nature	The ratio of reflection to transmission spectrum	Increase the ratio of before and after the substance
Applicable scenarios	Enhancement effects of different spectra of the same substance	Enhancement effect of different substances at the same incident angle
Maximum position	$\theta$ is slightly higher than $\theta_B$	$\theta$ is slightly higher than $\theta_C$
Maximum reflection enhancement	√	×
Maximum surface enhancement	×	√



# Conclusion

Drawing upon Maxwell's equations, a series of theoretical propositions were formulated, and the ensuing calculations demonstrated consistency with experimental spectral data. In the context of ATR, calculations were conducted for scenarios where the refractive index of the mixture, either partially or entirely, surpassed the critical refractive index. This facilitated the computation of surface-enhanced, distorted, and perfect absorption spectra, driven by optical factors rather than intramolecular or intermolecular interactions.

Initiating the exploration from the distorted spectrum, Snell's law was employed to elucidate the origins of distortion. The complex refractive index was derived from the absorption spectrum using Fresnel's law calculations. Combining these calculations, the developmental process of the distorted spectrum was well-simulated. Kramers-Kronig (KK) transformation was utilized to obtain the correction map for the purely distorted spectrum. However, this method proved inapplicable for spectra blending absorption and refraction, leading to the implementation of Inverse Fast Fourier Transformation (IFFT) and Fast Fourier Transformation (FFT) to obtain mixed distorted spectrum correction maps by combining time and frequency domains.

Analysis of the corrected spectrum revealed a fallacy in perceiving the distorted spectrum as a red shift; instead, it exhibited a blue shift compared to the normal spectrum. The degree of peak blue shift was found to be proportional to the length of the twist. This groundwork laid the foundation for subsequent research and analysis, providing precise data and methods for researchers.

Despite the complexity of calculations and interpretations integrating numerous optical backgrounds, such endeavors can be challenging for researchers lacking relevant background knowledge. In this context, where ATR distorted spectra are commonplace in experimental analysis, deep learning emerges as a promising solution. Deep learning, particularly Neural Networks, mimics the human's neural network to continuously learn and approximate real values. In spectral classification and distortion spectrum correction, these methods, akin to language translation, demonstrated effective results through label classification and automatic learning, eliminating the need for extensive physics and optics knowledge. The integration of complex

calculations into simulated spectra, coupled with depth learning methods, ensures calculated results align closely with reality, facilitating the distinction and correction of relevant spectra through optimal learning models.

The practical application of these approaches involved simulations of distorted spectra using IFFT and FFT methods, followed by the superimposition of distorted baselines during experiments to obtain blended distorted spectra. Two distinct methods, Long Short-Term Memory (LSTM) and Transformer, were employed for spectral classification and correction, demonstrating close alignment with traditional methods but with increased speed and batch correction capabilities.

An acknowledged limitation in this work is the scarcity of experimental data for deep learning. Future aspirations include obtaining more extensive experimental data to enhance the accuracy and generalizability of conclusions within the realm of deep learning algorithms and spectral analysis.

At this juncture, our investigation into the realm of distorted spectra is essentially complete. However, a noteworthy revelation during our study is the frequent coexistence of distorted spectra with enhanced spectra. In the case of pure substances, the acquisition of corresponding surface-enhanced spectra is possible when the incident angle closely approaches the critical incident angle. Yet, the stringent conditions for obtaining this enhanced spectrum render it challenging to detect in experiments. (It is acknowledged that for single substances with varying shapes and sizes, corresponding differences in absorption spectrum values may arise, but this aspect is presently beyond the scope of our discussion). For mixtures, particularly solid-liquid combinations, the presence of a solid substance with a high refractive index allows for the acquisition of surface-enhanced spectra contingent upon factors such as quantity, shape, and thickness of the solid.

We delve into two scenarios to elucidate this phenomenon. Firstly, presuming the refractive index of the solid material surpasses the critical refractive index, and the thickness is known and extremely thin, we employ multi-layer Fresnel's law to calculate the corresponding surface enhancement spectrum. In this context, the solid material may encompass multiple layers, notably applicable to substances with a negative real-valued part of the complex refractive index, such as gold, platinum, and emerging semiconductors like graphene. The principle of surface-enhanced spectrum generation

is elucidated through configurations akin to Kretschmann and Otto, engendering surface plasmons. Secondly, when the solid material exists in particle form and is dispersed in a liquid, the simulation of corresponding surface enhancement spectra necessitates the creation of a model. Theoretical analysis, accounting for the thickness of the thin layer and incorporating conditions for surface plasmon generation, is combined with experimental results, exemplified by the enhanced spectrum of Pd for Rhodamine-6G. This integration of calculations with experiments not only validates the theoretical framework but also establishes a robust foundation for practical experimentation.

The exploration of perfect absorption spectra emerges as an enticing avenue, yet due to time constraints, our current research cannot delve deeper into this subject. Therefore, we harbor hopes of conducting more comprehensive investigations in this field in the future.

Next, the principle of 2D FT is elucidated, providing a foundation for understanding the mechanics of 2D IR spectroscopy. Subsequently, two pivotal methods within 2D IR spectroscopy are introduced. The first method, developed by Isao Noda, involves transforming multiple one-dimensional spectra and is reinterpreted here through the lens of the Hilbert transform. The second method involves spectra obtained via actual detection and 2D FT using nonlinear ultrafast laser techniques, with significant contributions from the research of Professor Peter Hamm and Professor Zanni. This section serves to establish a comprehensive understanding of the principles of 2DIR spectroscopy, which is crucial for the subsequent exploration of surface-enhanced spectroscopy applications within this domain.

Our research in ultrafast spectroscopy encompasses both the observation of distorted spectra in 2D IR spectroscopy, analogous to those seen in 1D IR spectroscopy, and the detection of surface-enhanced spectra akin to those observed in 1D spectroscopy. Additionally, our studies reveal a distinctive surface-enhanced spectrum near the Brewster angle, attributable to third-order nonlinear optical measurements in 2D IR spectroscopy. This research further includes a comprehensive analysis and comparison of the fundamental nature of these phenomena.

The synthesis of conclusions and phenomena from both two-dimensional and one-dimensional spectra not only facilitates the generation of corresponding simulated

spectra through theoretical calculations but also engenders more compelling experimental results. This integration further allows for the unification of 1D and 2D spectra. Importantly, the marriage of two-dimensional spectral calculations with deep learning algorithms, potentially linked to image recognition, holds promise for expanding the domain of spectral learning and research. This implies that our research can extend beyond applications in natural language learning (NLP) models to shine in the field of image analysis and generation.

# Acknowledgement

At the beginning, as the people who studied chemistry, I barely know anything about optical. It's PD Dr. Thomas Mayerhöfer, you're the people who opened the door of optical calculation for me. I have read almost all of your papers. And all of them are so enlightening. Because no matter what ideas I have, when I search relative literature, your paper always be included. Thank you so much with patient to answer my questions and provide me the opportunity to do experiment. I'm so grateful for all the help in research. You're the basement of my work.

Thanks for my college and my best friend Anja Lampe. Thank you for the help in life, in research. You're the best gift I have in Germany. In found of you, I can always be and be treated as myself, and only myself.

Thank you, professor Kazarian, it's my huge pleasure to communicate with you about the ATR spectrum, the paper and the invitation to the conferences of ICAVS.

Thank you, Dr. Ferri, not only you, but also the whole research group in PSI. Thanks for the trust, for the happy time with you all. Thanks all the help in research, methods and equipment. Also the time for all communication.

Thanks professor Zanni and the whole research group in University of Wisconsin-Madison. It's so funny to be there for 2D IR research as well as having fun.

Thanks for the correction from PD Dr. Thomas Mayerhöfer in Chapter 1 and Chapter 2.4; Thanks for the correction from AP Dr. Alexei A. Kananenka in Chapter 3; Thanks for the correction from PD Dr. Dieter Baurecht in Chapter 2.1; Thanks for the correction from professor Jianping Wang in Chapter 5.1.

And there're much more researchers give help and kindness when I communicate with them. It's exactly because all of your help, the way of climbing the mountain of science is not alone. And the discovery I had is just based on the baseline of all previous researchers. I'm full of acknowledgement for all researchers I communicated and gave me the help.

Thanks for the scholarship from CSC and the funding from DFG as well as funding from University of Bremen. It's from Bremen to link the whole world.

Thanks to professor Kiefer, thanks for the opportunity of research, for the freedom and support in my research, and of course for being so patient in correcting my poorly written paper. You're the best supervisor for me with patience, support, freedom and encouragement. I feel like the best part is I'm always so happy and confident to communicate with you, because it's always communicating equally and honestly, without any pressure. In addition, it's okay to admit that I don't know some parts, no need to pretend. As a person who never likes to submit to any form of authority and title, I am very grateful to you for your tolerance of my offense and recklessness; as a person who likes to be free and hates anyone trying to interfere, I am also very grateful to you for your respect, understanding and support. More importantly, you're always willing to try what you can when I need help.

Thanks for my father, for always support me no matter what I did. I know I'm your precious and proud. HAHAHAHAHA, sorry, my temper is not that nice.

Thanks my colleges, Frau Glade, Sabine, Bernd, Ulrike, Jan, Claudia, Petra, Malte, Marcus, Yu, Hasam, Felippo, Tom... Thank you all, and it's my pleasure to work with you.

Last but most important, thanks for myself. On the road of research, with dark, with frustrated, with excited, with recognition, with disappointed, all in all, I did good job, even I didn't, I'm still need to give a huge hug for myself, I'm so grateful for this brave, straightforward myself with courage, with hope, with patient to follow my curious to discovery something interesting. Which in the whole universe, there're too much unknown for me, I did proud for those tiny finding which didn't be known before, and I did except to follow the clue to find much more unknown in the future, even the whole world is still too mysterious, too unbeknown for me.

(PS: I know the grammar is horrible here, but I don't want to change not even one word. Because all of acknowledgement, with my sincerely, with my passion, are exactly what I want to say, even not perfect, even not good. Just like me, like everybody, like the world, we all growth small like dust. It's exactly those people who we are grateful to make us become unique ourselves)

# List of Symbols

Symbol	Meaning
$\nabla$	three-dimensional gradient operator, del
$\nabla \cdot$	divergence operator
$\nabla \times$	curl operator
$\vec{v}$	vector field
$\vec{E}$	electric field
$\vec{B}$	magnetic field
$\vec{H}$	magnetizing field
$\vec{D}$	displacement field
$\rho_v$	total electric charge density (total charge per unit volume)
$\vec{j}$	total electric current density (total current per unit area)
$\vec{i}, \vec{j}, \vec{k}$	direction vectors
$\epsilon$	electric permittivity
$t$	time
$\mu$	magnetic permeability
$\sigma$	electrical conductivity
$\epsilon_0$	vacuum permittivity $\epsilon_0 = 8.8541878176 \times 10^{-12} F/m$
$\epsilon_r$	relative permittivity
$\vec{P}$	polarization density
$\chi_e$	electric susceptibility of the medium
$\mu$	the permeability ( $H/m$ )
$\mu_0$	the vacuum permeability $\mu_0 = 1.2566370614 \times 10^{-6} H/m$
$\mu_r$	the relative permeability
$c$	the speed of light in vacuum $c = 2.99792458 \times 10^8 m/s$
$\vec{r}$	direction of the wave
$\vec{k}$	wave vector
$\vec{k}_0$	the wave vector of light in vacuum.
$\omega$	angular frequency ( $rad/s$ )
$f$	frequency ( $Hz$ )

---

$T$	period (s)
$\vec{k}_0$	wave vector of light in vacuum
$i$	$i^2 = -1$
$\hat{n}$	complex refractive index
$n$	real part of refractive index
$k$	imaginary part of refractive index
$r$	reflection
$t$	transmission
$\theta$	incident angle
$R$	reflectance spectra
$A$	absorbance spectra
$s$	$s$ -polarized
$p$	$p$ -polarized
$\theta_c$	critical angle
$d_p$	penetration depth
$\nu, f$	frequency
$n_c$	critical refractive index
$c_k$	the amplitude
$\varphi_k$	phase angle
$A_k^{\text{PSD}}(\nu)$	the phase -resolved modulation spectrum
$\phi_k^{\text{PSD}}$	phase angle with PSD
$F$	Fourier transform
$\mathcal{H}$	Hilbert transform
$L$	Laplace transform
$N$	the number of atoms per unit volume
$q$	the charge of an electron
$m$	mass
$m_e$	mass of electron
$\vec{p}$	the polarization
$\omega_p$	the plasma frequency
$\gamma, \gamma_j, \Gamma$	damping constant
$S_j$	oscillator strength

---



---

$v_j$	center frequency
$d$	thickness of the medium
$\varepsilon_\infty$	constant offset
$k_x$	wave vector in $x$ -direction
$e_{EF}$	enhancement factor
$I_{GEIRA}$	absorption peak intensity
$I_0$	absorption peak intensity of basis
$\widehat{W}$	the quantum mechanical operator
$\hat{\mu}$	the molecule's dipole
$\widehat{H}_0$	the principal component
$ n\rangle$	the molecular eigenstates
$ \psi(t)\rangle$	the state vector of the quantum system
$\widehat{H}(t)$	the Hamiltonian operator
$c_n$	the probability amplitude
$\rho$	density matrix (or density operator)
$p_s$	the associated eigenvalue
$ \psi_s\rangle$	the eigenstate corresponding to the density operator
$\hbar$	reduced Planck constant $\hbar = h/2\pi = 1.054571800 * 10^{-34} J \cdot s$
$\hat{A}$	the operator
$\widehat{W}_I(t)$	the perturbation Hamiltonian
$c_n$	the probability amplitude
$P(t)$	the macroscopic polarization
$R(t)$	the molecular response
$S$	signal
$E_{sig}$	the electric field energy of the signal
$\Gamma_f^{<t>}$	forget gate for $t$ step.
$\sigma$	sigmoid function.
$W_f$	the forget gate weight.
$x^{<t>}$	input data of $t$ step.
$a^{<t-1>}$	the hidden state from the previous cell.
$b_f$	the forget gate bias.
$\Gamma_u^{<t>}$	update gate for $t$ step.

---

---

$W_i$	the update gate weight (not $W_u$ ).
$W_y$	the prediction weight.
$b_y$	the prediction bias.
$b_i$	the update gate bias (not $b_u$ ).
$\hat{c}^{<t>}$	candidate value.
$\tanh$	the tanh function produces values between -1 and 1.
$W_c$	the candidate weight.
$b_o$	the candidate bias.
$c^{<t>}$	cell state for $t$ step.
$c^{<t-1>}$	cell state for $t-1$ step.
$\Gamma_o^{<t>}$	output gate for $t$ step.
$W_o$	the output gate weight.
$b_o$	the output gate bias.
$a^{<t>}$	the hidden state.
$y_{pred}^{<t>}$	prediction for $t$ step.
$m$	the diffraction order
$\Lambda$	the grating period

---

# List of Publications

1. Rui Cheng, Thomas G. Mayerhöfer, Johannes Kiefer\* “ Theoretical Calculation and Simulation of Peak Distortion of Absorption Spectra of Complex Mixtures.[J] ”.( Applied Spectroscopy (2024) in print).

## Manuscripts for publication underworking

1. Correction of distorted ATR spectra. **Rui Cheng**, Thomas Mayerhöfer, Anja Lampe, Johannes Kiefer (manuscript finished, under correction)
2. Long short-term memory (LSTM) and Transformer in Classification and Correction of ATR distorted spectrum. **Rui Cheng**, Johannes Kiefer (manuscript finished, under correction)
3. Computational comparison of enhanced spectra for single and multilayers in near-Brewster angle and near-critical angle reflective pump-probe geometries. **Rui Cheng**, Johannes Kiefer (manuscript finished, under correction)

## Conferences

1. “Distortion and correction of ATR-spectrum of high refractive index material”  
*04.2021 APACT21 - Advances In Process Analytics and Control Technologies*
2. “Distortion and correction of ATR-spectrum of high refractive index material”  
*08.2021 ICAVS11*  
*- 11th International Conference on Advanced Vibrational Spectroscopy*
3. “Long short-term memory(LSTM) and Transformer in Classification and Correction of ATR distorted spectrum”  
*04.2024 ICAVS12*  
*- 12th International Conference on Advanced Vibrational Spectroscopy*
4. “Computational comparison of enhanced spectra for single and multilayers in near-Brewster angle and near-critical angle reflective pump-probe geometries”  
*08.2023 ECONOS/ECW 2024*

# Reference

- (1) Milosevic, M. *Internal reflection and ATR spectroscopy*; John Wiley & Sons, 2012.
- (2) Kitadai, N.; Yokoyama, T.; Nakashima, S. In situ ATR-IR investigation of L-lysine adsorption on montmorillonite. *J Colloid Interface Sci* **2009**, *338* (2), 395-401.
- (3) Luo, J.; Amma, S.-i.; Chen, L.; Ngo, D.; Mauro, J. C.; Pantano, C. G.; Kim, S. H. Relative abundance of subsurface hydroxyl and molecular water species in silicate and aluminosilicate glasses. *Journal of Non-Crystalline Solids* **2019**, *510*, 179-185.
- (4) Raichlin, Y.; Avisar, D.; Gerber, L.; Katzir, A. Flattened infrared fiber-optic sensors for the analysis of micrograms of insoluble solid particles in solution or in a dry state. *Vibrational Spectroscopy* **2014**, *73*, 67-72.
- (5) Perez-Guaita, D.; Marzec, K. M.; Hudson, A.; Evans, C.; Chernenko, T.; Matthaus, C.; Miljkovic, M.; Diem, M.; Heraud, P.; Richards, J. S.; et al. Parasites under the Spotlight: Applications of Vibrational Spectroscopy to Malaria Research. *Chem Rev* **2018**, *118* (11), 5330-5358.
- (6) Aufort, J.; Lebon, M.; Gallet, X.; Segalen, L.; Gervais, C.; Brouder, C.; Balan, E. Macroscopic electrostatic effects in ATR-FTIR spectra of modern and archeological bones. *American Mineralogist* **2018**, *103* (2), 326-329.
- (7) Ramsay, M.; Beutier, C.; McGarvey, G. B.; Hore, D. K. Adsorption of heptane–toluene binary mixtures on a hydrophobic polymer surface. *The Journal of Chemical Physics* **2019**, *150* (1).
- (8) Prati, S.; Sciutto, G.; Bonacini, I.; Mazzeo, R. New frontiers in application of FTIR microscopy for characterization of cultural heritage materials. *Analytical Chemistry for Cultural Heritage* **2017**, 129-160.
- (9) Milosevic, M. On the nature of the evanescent wave. *Appl Spectrosc* **2013**, *67* (2), 126-131.
- (10) Berthomieu, C.; Hienerwadel, R. Fourier transform infrared (FTIR) spectroscopy. *Photosynthesis research* **2009**, *101* (2), 157-170.
- (11) Ghanbari-Siahkali, A.; Almdal, K.; Kingshott, P. Limitations of using Raman microscopy for the analysis of high-content-carbon-filled ethylene propylene diene monomer rubber. *Applied spectroscopy* **2003**, *57* (12), 1482-1486.
- (12) Mayerhofer, T. G.; Pahlow, S.; Popp, J. The Bouguer-Beer-Lambert Law: Shining Light on the Obscure. *Chemphyschem* **2020**, *21* (18), 2029-2046.
- (13) Thomasson, J.; Coin, C.; Kahraman, H.; Fredericks, P. Attenuated total reflectance infrared microspectroscopy of coal. *Fuel* **2000**, *79* (6), 685-691.
- (14) Delor, F.; Barrois-Oudin, N.; Duteurtre, X.; Cardinet, C.; Lemaire, J.; Lacoste, J. Oxidation of

- rubbers analysed by HATR/IR spectroscopy. *Polymer degradation and stability* **1998**, 62 (2), 395-401.
- (15) Do, T.-T.; Celina, M.; Fredericks, P. M. Attenuated total reflectance infrared microspectroscopy of aged carbon-filled rubbers. *Polymer Degradation and Stability* **2002**, 77 (3), 417-422.
- (16) Oh, Y.-J.; Cho, S. M.; Chung, C.-H. An In Situ ATR-FTIR Study on Palladium Displacement Reaction on Hydrogen-Terminated Silicon Surface. *Journal of The Electrochemical Society* **2005**, 152 (6).
- (17) Bürgi, T. ATR-IR spectroscopy at the metal-liquid interface: influence of film properties on anomalous band-shape. *Physical Chemistry Chemical Physics* **2001**, 3 (11), 2124-2130.
- (18) Lv, A.; Hu, C.; Nie, Y.; Qu, J. Catalytic ozonation of toxic pollutants over magnetic cobalt-doped Fe<sub>3</sub>O<sub>4</sub> suspensions. *Applied Catalysis B: Environmental* **2012**, 117, 246-252.
- (19) Diallo, A.; Beye, A.; Doyle, T. B.; Park, E.; Maaza, M. Green synthesis of Co<sub>3</sub>O<sub>4</sub> nanoparticles via *Aspalathus linearis*: physical properties. *Green Chemistry Letters and Reviews* **2015**, 8 (3-4), 30-36.
- (20) Fuchs, P. Chemical bath deposition of transparent conductive zinc oxide thin films for solar cell applications. ETH Zurich, 2017.
- (21) Miljkovic, M.; Bird, B.; Diem, M. Line shape distortion effects in infrared spectroscopy. *Analyst* **2012**, 137 (17), 3954-3964.
- (22) Tay, F. H.; Kazarian, S. G. Study of petroleum heat-exchanger deposits with ATR-FTIR spectroscopic imaging. *Energy & Fuels* **2009**, 23 (8), 4059-4067.
- (23) Datta, S.; Antoš, J.; Stoček, R. Smart numerical method for calculation of simple general infrared parameter identifying binary rubber blends. *Polymer Testing* **2017**, 57, 192-202.
- (24) Datta, S.; Harea, D.; Harea, E.; Stoček, R. An advanced method for calculation of infrared parameter to quantitatively identify rubber grade in a multi-component rubber blend. *Polymer Testing* **2019**, 73, 308-315.
- (25) Kiefer, J.; Grabow, J.; Kurland, H.-D.; Müller, F. A. Characterization of nanoparticles by solvent infrared spectroscopy. *Analytical chemistry* **2015**, 87 (24), 12313-12317.
- (26) Maxwell, J. C. *A treatise on electricity and magnetism*; Clarendon press, 1873.
- (27) Born, M.; Wolf, E. *Principles of optics: electromagnetic theory of propagation, interference and diffraction of light*; Elsevier, 2013.
- (28) Lewis, R. M.; Keller, J. B. *Asymptotic methods for partial differential equations: the reduced wave equation and Maxwell's equation*; Springer, 1964.
- (29) Gupta, S. D.; Ghosh, N.; Banerjee, A. *Wave optics: Basic concepts and contemporary trends*; CRC

Press, 2015.

- (30) Maxwell, J. C. VIII. A dynamical theory of the electromagnetic field. *Philosophical transactions of the Royal Society of London* **1865**, (155), 459-512.
- (31) Jones, D. S. *The theory of electromagnetism*; Elsevier, 2013.
- (32) Grant, I. S.; Phillips, W. R. *Electromagnetism*; John Wiley & Sons, 2013.
- (33) Mayerhöfer, T. G. Wave Optics in Infrared Spectroscopy: Theory, Simulation, and Modeling. *Elsevier* **2024**.
- (34) Griffiths, D. J. *Introduction to electrodynamics*; Cambridge University Press, 2023.
- (35) Shen, Y.-R. Principles of nonlinear optics. **1984**.
- (36) Boyd, R. W.; Gaeta, A. L.; Giese, E. Nonlinear optics. In *Springer Handbook of Atomic, Molecular, and Optical Physics*, Springer, 2008; pp 1097-1110.
- (37) Fowles, G. R. *Introduction to modern optics*; Courier Corporation, 1989.
- (38) Goodman, J. W. *Introduction to Fourier optics*; Roberts and Company publishers, 2005.
- (39) Huray, P. G. *Maxwell's equations*; John Wiley & Sons, 2009.
- (40) Griffiths, P. R.; Haseetha, J. A. d. Fourier Transform Infrared Spectrometry. *Vibrational Spectroscopy* **2007**, *43* (1), 78-85.
- (41) Harrick, N.; Beckmann, K. Internal reflection spectroscopy. In *Characterization of Solid Surfaces*, Springer, 1974; pp 215-245.
- (42) Averett, L. A.; Griffiths, P. R.; Nishikida, K. Effective path length in attenuated total reflection spectroscopy. *Analytical chemistry* **2008**, *80* (8), 3045-3049.
- (43) Harrick, N.; Du Pre, F. Effective thickness of bulk materials and of thin films for internal reflection spectroscopy. *Applied optics* **1966**, *5* (11), 1739-1743.
- (44) Bertie, J. E.; Eysel, H. H. Infrared intensities of liquids I: Determination of infrared optical and dielectric constants by FT-IR using the CIRCLE ATR cell. *Applied Spectroscopy* **1985**, *39* (3), 392-401.
- (45) Dale Keefe, C.; Wilcox, T.; Campbell, E. Measurement and applications of absolute infrared intensities. *Journal of Molecular Structure* **2012**, *1009*, 111-122.
- (46) Habuka, A.; Yamada, T.; Nakashima, S. Interactions of Glycerol, Diglycerol, and Water Studied Using Attenuated Total Reflection Infrared Spectroscopy. *Appl Spectrosc* **2020**, *74* (7), 767-779.
- (47) Myers, T. L.; Tonkyn, R. G.; Danby, T. O.; Taubman, M. S.; Bernacki, B. E.; Birnbaum, J. C.; Sharpe,

- S. W.; Johnson, T. Accurate measurement of the optical constants  $n$  and  $k$  for a series of 57 inorganic and organic liquids for optical modeling and detection. *Applied spectroscopy* **2018**, 72 (4), 535-550.
- (48) Sorensen, C. M.; Yon, J.; Liu, F.; Maughan, J.; Heinson, W. R.; Berg, M. J. Light scattering and absorption by fractal aggregates including soot. *Journal of Quantitative Spectroscopy and Radiative Transfer* **2018**, 217, 459-473.
- (49) Hardy, J.; Smith, S. Two-phonon infra-red lattice absorption in diamond. *Philosophical magazine* **1961**, 6 (69), 1163-1172.
- (50) Hadni, A. *Essentials of Modern Physics Applied to the Study of the Infrared: International Series of Monographs in Infrared Science and Technology*; Elsevier, 2016.
- (51) Amma, S.; Luo, J. W.; Pantano, C. G.; Kim, S. H. Specular reflectance (SR) and attenuated total reflectance (ATR) infrared (IR) spectroscopy of transparent flat glass surfaces: A case study for soda lime float glass. *Journal of Non-Crystalline Solids* **2015**, 428, 189-196.
- (52) Baurecht, D.; Fringeli, U. P. Quantitative modulated excitation Fourier transform infrared spectroscopy. *Review of scientific instruments* **2001**, 72 (10), 3782-3792.
- (53) Tolstov, G. P. *Fourier series*; Courier Corporation, 2012.
- (54) Zygmund, A. *Trigonometric series*; Cambridge university press, 2002.
- (55) Stein, E. M.; Shakarchi, R. *Fourier analysis: an introduction*; Princeton University Press, 2011.
- (56) Edwards, R. Trigonometric Series and Fourier Series. In *Fourier Series: A Modern Introduction Volume 1*, Springer, 1979; pp 1-13.
- (57) Bloomfield, P. *Fourier analysis of time series: an introduction*; John Wiley & Sons, 2004.
- (58) Moskowitz, M. A. *A course in complex analysis in one variable*; World Scientific, 2002.
- (59) Bürgi, T.; Baiker, A. In situ infrared spectroscopy of catalytic solid– liquid interfaces using phase-sensitive detection: Enantioselective hydrogenation of a pyrone over Pd/TiO<sub>2</sub>. *J. Phys. Chem. B* **2002**, 106 (41), 10649-10658.
- (60) Armen, G. B. Phase sensitive detection: the lock-in amplifier. *Department of Physics and Astronomy, The Uni-versity of Tennessee* **2008**.
- (61) Lucarini, V.; Saarinen, J. J.; Peiponen, K.-E.; Vartiainen, E. M. *Kramers-Kronig relations in optical materials research*; Springer Science & Business Media, 2005.
- (62) Kronig, R. d. L. On the theory of dispersion of x-rays. *Josa* **1926**, 12 (6), 547-557.
- (63) Kramers, H. A. *La diffusion de la lumiere par les atomes*; 1928.
- (64) Harrick, N. *Internal Reflection Spectroscopy*; Harrick Scientific Corporation; Ossining, New York,

1987. Original publication by John Wiley & Sons, New York **1967**.

- (65) Müller, P.; Hermans, I. Applications of modulation excitation spectroscopy in heterogeneous catalysis. *Industrial & Engineering Chemistry Research* **2017**, *56* (5), 1123-1136.
- (66) Bürgi, T. Attenuated total reflection infrared (ATR-IR) spectroscopy, modulation excitation spectroscopy (MES), and vibrational circular dichroism (VCD). In *Biointerface Characterization by Advanced IR Spectroscopy*, 2011; pp 115-144.
- (67) Urakawa, A.; Bürgi, T.; Baiker, A. Sensitivity enhancement and dynamic behavior analysis by modulation excitation spectroscopy: Principle and application in heterogeneous catalysis. *Chemical Engineering Science* **2008**, *63* (20), 4902-4909.
- (68) Andanson, J.-M.; Baiker, A. Exploring catalytic solid/liquid interfaces by in situ attenuated total reflection infrared spectroscopy. *Chem. Soc. Rev.* **2010**, *39* (12), 4571-4584.
- (69) Grunwaldt, J.-D.; Baiker, A. In situ spectroscopic investigation of heterogeneous catalysts and reaction media at high pressure. *Physical Chemistry Chemical Physics* **2005**, *7* (20), 3526-3539.
- (70) Muller, P.; Wolf, P.; Hermans, I. Insights into the complexity of heterogeneous liquid-phase catalysis: case study on the cyclization of citronellal. *ACS Catal.* **2016**, *6* (5), 2760-2769.
- (71) Ferri, D. Toward operando infrared spectroscopy of heterogeneous catalysts. *Heterogeneous Catalysts: Advanced Design, Characterization and Applications* **2021**, *1*, 311-338.
- (72) Urakawa, A.; Wirz, R.; Bürgi, T.; Baiker, A. ATR-IR flow-through cell for concentration modulation excitation spectroscopy: diffusion experiments and simulations. *J. Phys. Chem. B* **2003**, *107* (47), 13061-13068.
- (73) Greenaway, A. G.; Marberger, A.; Thetford, A.; Lezcano-Gonzalez, I.; Agote-Aran, M.; Nachtegaal, M.; Ferri, D.; Krocher, O.; Catlow, C. R. A.; Beale, A. M. Detection of key transient Cu intermediates in SSZ-13 during NH<sub>3</sub>-SCR deNO<sub>x</sub> by modulation excitation IR spectroscopy. *Chem Sci* **2020**, *11* (2), 447-455.
- (74) Nuguid, R. J. G.; Elsener, M.; Ferri, D.; Kröcher, O. Operando diffuse reflectance infrared detection of cyanide intermediate species during the reaction of formaldehyde with ammonia over V<sub>2</sub>O<sub>5</sub>/WO<sub>3</sub>-TiO<sub>2</sub>. *Applied Catalysis B: Environmental* **2021**, *298*.
- (75) Srinivasan, P. D.; Patil, B. S.; Zhu, H.; Bravo-Suárez, J. J. Application of modulation excitation-phase sensitive detection-DRIFTS for in situ/operando characterization of heterogeneous catalysts. *Reaction Chemistry & Engineering* **2019**, *4* (5), 862-883.
- (76) van Beek, W.; Urakawa, A.; Milanese, M. XRD-Raman and modulation excitation spectroscopy. *In-situ Characterization of Heterogeneous Catalysts* **2013**, 411-439.
- (77) Stötzel, J.; Lützenkirchen-Hecht, D.; Frahm, R.; Grunwaldt, J. D. Improving the sensitivity of QEXAFS using modulation excitation spectroscopy. *Journal of Physics: Conference Series* **2013**,



430.

- (78) Burgi, T. Attenuated total reflection infrared (ATR-IR) spectroscopy, modulation excitation spectroscopy (MES), and vibrational circular dichroism (VCD). *Biointerface Characterization by Advanced IR Spectroscopy* **2011**, 115-144.
- (79) Proakis, J. G. *Digital signal processing: principles, algorithms, and applications, 4/E*; Pearson Education India, 2007.
- (80) Gaspar, J.; Chen, S. F.; Gordillo, A.; Hepp, M.; Ferreyra, P.; Marqués, C. Digital lock in amplifier: study, design and development with a digital signal processor. *Microprocessors and Microsystems* **2004**, 28 (4), 157-162.
- (81) Scofield, J. H. Frequency-domain description of a lock-in amplifier. *American journal of physics* **1994**, 62 (2), 129-132.
- (82) Storer, D. M. Dynamic analysis of non-linear structures using higher order frequency response functions. The University of Manchester (United Kingdom), 1991.
- (83) Bochner, S.; Chandrasekharan, K. *Fourier transforms*; Princeton University Press, 1949.
- (84) Ifeachor, E. C.; Jervis, B. W. *Digital signal processing: a practical approach*; Pearson Education, 2002.
- (85) Oppenheim, A. V. *Discrete-time signal processing*; Pearson Education India, 1999.
- (86) Winograd, S. On computing the discrete Fourier transform. *Mathematics of computation* **1978**, 32 (141), 175-199.
- (87) Sundararajan, D. *The discrete Fourier transform: theory, algorithms and applications*; World Scientific, 2001.
- (88) Mersereau, R.; Speake, T. A unified treatment of Cooley-Tukey algorithms for the evaluation of the multidimensional DFT. *IEEE Transactions on Acoustics, Speech, and Signal Processing* **1981**, 29 (5), 1011-1018.
- (89) Nussbaumer, H. J.; Nussbaumer, H. J. *The fast Fourier transform*; Springer, 1982.
- (90) Boashash, B. Time-frequency concepts. Elsevier, 2003.
- (91) Haykin, S.; Van Veen, B. *Signals and systems*; John Wiley & Sons, 2007.
- (92) Kschischang, F. R. The hilbert transform. *University of Toronto* **2006**, 83, 277.
- (93) Feynman, R. P. The Feynman lectures on physics. *(No Title)* **1963**, 1, 46.
- (94) Lucarini, V.; Saarinen, J. J. *Kramers-Kronig Relations in Optical Materials Research*; 2005.

- (95) Phillip, H.; Taft, E. Kramers-Kronig analysis of reflectance data for diamond. *Physical Review* **1964**, *136* (5A), A1445.
- (96) Bardwell, J. A.; Dignam, M. J. Extensions of the Kramers-Kronig transformation that cover a wide range of practical spectroscopic applications. *The Journal of chemical physics* **1985**, *83* (11), 5468-5478.
- (97) Bertie, J. E.; Lan, Z. An accurate modified Kramers-Kronig transformation from reflectance to phase shift on attenuated total reflection. *The Journal of chemical physics* **1996**, *105* (19), 8502-8514.
- (98) Huang, J.; Urban, M. Evaluation and analysis of attenuated total reflectance FT-IR spectra using Kramers-Kronig transforms. *Applied Spectroscopy* **1992**, *46* (11), 1666-1672.
- (99) Ohta, K.; Ishida, H. Comparison among several numerical integration methods for Kramers-Kronig transformation. *Applied spectroscopy* **1988**, *42* (6), 952-957.
- (100) Liu, Y.; Lee, Y. J.; Cicerone, M. T. Broadband CARS spectral phase retrieval using a time-domain Kramers-Kronig transform. *Optics letters* **2009**, *34* (9), 1363-1365.
- (101) Urquidi-Macdonald, M.; Real, S.; Macdonald, D. D. Applications of Kramers-Kronig transforms in the analysis of electrochemical impedance data—III. Stability and linearity. *Electrochimica Acta* **1990**, *35* (10), 1559-1566.
- (102) Wyld, H. W.; Powell, G. *Mathematical methods for physics*; CRC Press, 2020.
- (103) Kuzmenko, A. Kramers-Kronig constrained variational analysis of optical spectra. *Review of scientific instruments* **2005**, *76* (8).
- (104) Grosse, P.; Offermann, V. Analysis of reflectance data using the Kramers-Kronig relations. *Applied Physics A* **1991**, *52*, 138-144.
- (105) Everall, N. J.; Chalmers, J. M.; Local, A.; Allen, S. Measurement of surface orientation in uniaxial poly (ethylene terephthalate) films using polarised specular reflectance fourier transform infrared microscopy. *Vibrational spectroscopy* **1996**, *10* (2), 253-259.
- (106) Bakry, M.; Klinkenbusch, L. Using the Kramers-Kronig transforms to retrieve the conductivity from the effective complex permittivity. *Advances in Radio Science* **2018**, *16*, 23-28.
- (107) Fano, W. G.; Boggi, S.; Razzitte, A. C. Causality study and numerical response of the magnetic permeability as a function of the frequency of ferrites using Kramers-Kronig relations. *Physica B: Condensed Matter* **2008**, *403* (4), 526-530.
- (108) Yamamoto, K.; Masui, A.; Ishida, H. Kramers-Kronig analysis of infrared reflection spectra with perpendicular polarization. *Applied optics* **1994**, *33* (27), 6285-6293.
- (109) Szabo, Z.; Park, G.-H.; Hedge, R.; Li, E.-P. A unique extraction of metamaterial parameters based

- on Kramers–Kronig relationship. *IEEE Transactions on Microwave Theory and Techniques* **2010**, *58* (10), 2646-2653.
- (110) Mayerhöfer, T. G.; Popp, J. Quantitative evaluation of infrared absorbance spectra–Lorentz profile versus Lorentz oscillator. *ChemPhysChem* **2019**, *20* (1), 31-36.
- (111) Mayerhofer, T. G.; Pipa, A. V.; Popp, J. Beer's Law-Why Integrated Absorbance Depends Linearly on Concentration. *Chemphyschem* **2019**, *20* (21), 2748-2753.
- (112) Bade, W. Drude-model calculation of dispersion forces. I. General theory. *The Journal of Chemical Physics* **1957**, *27* (6), 1280-1284.
- (113) Mayerhofer, T. G.; Popp, J. Quantitative Evaluation of Infrared Absorbance Spectra - Lorentz Profile versus Lorentz Oscillator. *Chemphyschem* **2019**, *20* (1), 31-36.
- (114) Tek, G.; Hamm, P. A Correction Scheme for Fano Line Shapes in Two-Dimensional Infrared Spectroscopy. *J Phys Chem Lett* **2020**, *11* (15), 6185-6190.
- (115) Kraack, J. P.; Hamm, P. Surface-Sensitive and Surface-Specific Ultrafast Two-Dimensional Vibrational Spectroscopy. *Chem Rev* **2017**, *117* (16), 10623-10664.
- (116) Bao, Q.; Feng, J.; Chen, F.; Mao, W.; Liu, Z.; Liu, K.; Liu, C. A new automatic baseline correction method based on iterative method. *J Magn Reson* **2012**, *218*, 35-43.
- (117) Müller, P.; Hermans, I. Applications of Modulation Excitation Spectroscopy in Heterogeneous Catalysis. *Industrial & Engineering Chemistry Research* **2017**, *56* (5), 1123-1136.
- (118) Portnoff, M. Time-frequency representation of digital signals and systems based on short-time Fourier analysis. *IEEE Transactions on Acoustics, Speech, and Signal Processing* **1980**, *28* (1), 55-69.
- (119) Griffin, D.; Lim, J. Signal estimation from modified short-time Fourier transform. *IEEE Transactions on acoustics, speech, and signal processing* **1984**, *32* (2), 236-243.
- (120) Owens, F.; Murphy, M. A short-time Fourier transform. *Signal Processing* **1988**, *14* (1), 3-10.
- (121) Pathak, R. S. *The wavelet transform*; Springer Science & Business Media, 2009.
- (122) Meyer, Y. *Wavelets and operators: volume 1*; Cambridge university press, 1992.
- (123) Chui, C. K. *An introduction to wavelets*; Elsevier, 2014.
- (124) Graps, A. An introduction to wavelets. *IEEE computational science and engineering* **1995**, *2* (2), 50-61.
- (125) Pinsky, M. A. *Introduction to Fourier analysis and wavelets*; American Mathematical Society, 2023.
- (126) Gabor, D. Theory of communication. Part 1: The analysis of information. *Journal of the Institution*

- of Electrical Engineers-part III: radio and communication engineering* **1946**, 93 (26), 429-441.
- (127) Lin, J.; Qu, L. Feature extraction based on Morlet wavelet and its application for mechanical fault diagnosis. *Journal of sound and vibration* **2000**, 234 (1), 135-148.
- (128) Bernardino, A.; Santos-Victor, J. A real-time gabor primal sketch for visual attention. In *Iberian Conference on Pattern Recognition and Image Analysis*, 2005; Springer: pp 335-342.
- (129) Sadowsky, J. Investigation of signal characteristics using the continuous wavelet transform. *johns hopkins apl technical digest* **1996**, 17 (3), 258-269.
- (130) Copiaco, A.; Ritz, C.; Fasciani, S.; Abdulaziz, N. Scalogram neural network activations with machine learning for domestic multi-channel audio classification. In *2019 IEEE International Symposium on Signal Processing and Information Technology (ISSPIT)*, 2019; IEEE: pp 1-6.
- (131) Shensa, M. J. The discrete wavelet transform: wedding the a trous and Mallat algorithms. *IEEE Transactions on signal processing* **1992**, 40 (10), 2464-2482.
- (132) LeCun, Y.; Bengio, Y.; Hinton, G. Deep learning. *nature* **2015**, 521 (7553), 436-444.
- (133) Krizhevsky, A.; Sutskever, I.; Hinton, G. E. Imagenet classification with deep convolutional neural networks. *Advances in neural information processing systems* **2012**, 25.
- (134) Saha, S. 15.10.2018. A Comprehensive Guide to Convolutional Neural Networks — the ELI5 way. <https://towardsdatascience.com/a-comprehensive-guide-to-convolutional-neural-networks-the-eli5-way-3bd2b1164a53>
- (135) LeCun, Y.; Jackel, L. D.; Bottou, L.; Cortes, C.; Denker, J. S.; Drucker, H.; Guyon, I.; Muller, U. A.; Sackinger, E.; Simard, P. Learning algorithms for classification: A comparison on handwritten digit recognition. *Neural networks: the statistical mechanics perspective* **1995**, 261 (276), 2.
- (136) He, K.; Gkioxari, G.; Dollár, P.; Girshick, R. Mask r-cnn. In *Proceedings of the IEEE international conference on computer vision*, 2017; pp 2961-2969.
- (137) Albawi, S.; Mohammed, T. A.; Al-Zawi, S. Understanding of a convolutional neural network. In *2017 international conference on engineering and technology (ICET)*, 2017; IEEE: pp 1-6.
- (138) He, K.; Zhang, X.; Ren, S.; Sun, J. Deep residual learning for image recognition. In *Proceedings of the IEEE conference on computer vision and pattern recognition*, 2016; pp 770-778.
- (139) Khoshdeli, M.; Cong, R.; Parvin, B. Detection of nuclei in H&E stained sections using convolutional neural networks. In *2017 IEEE EMBS International Conference on Biomedical & Health Informatics (BHI)*, 2017; IEEE: pp 105-108.
- (140) Agarap, A. F. Deep learning using rectified linear units (relu). *arXiv preprint arXiv:1803.08375* **2018**.
- (141) Lee, C.-Y.; Gallagher, P. W.; Tu, Z. Generalizing pooling functions in convolutional neural

- networks: Mixed, gated, and tree. In *Artificial intelligence and statistics*, 2016; PMLR: pp 464-472.
- (142) Hamker, F. H. Predictions of a model of spatial attention using sum-and max-pooling functions. *Neurocomputing* **2004**, *56*, 329-343.
- (143) Scherer, D.; Müller, A.; Behnke, S. Evaluation of pooling operations in convolutional architectures for object recognition. In *International conference on artificial neural networks*, 2010; Springer: pp 92-101.
- (144) Sun, M.; Song, Z.; Jiang, X.; Pan, J.; Pang, Y. Learning pooling for convolutional neural network. *Neurocomputing* **2017**, *224*, 96-104.
- (145) Farabet, C.; Couprie, C.; Najman, L.; LeCun, Y. Learning hierarchical features for scene labeling. *IEEE transactions on pattern analysis and machine intelligence* **2012**, *35* (8), 1915-1929.
- (146) Hochreiter, S.; Schmidhuber, J. Long short-term memory. *Neural Comput* **1997**, *9* (8), 1735-1780.
- (147) Sherstinsky, A. Fundamentals of Recurrent Neural Network (RNN) and Long Short-Term Memory (LSTM) network. *Physica D: Nonlinear Phenomena* **2020**, *404*.
- (148) Cho, K.; Van Merriënboer, B.; Gulcehre, C.; Bahdanau, D.; Bougares, F.; Schwenk, H.; Bengio, Y. Learning phrase representations using RNN encoder-decoder for statistical machine translation. *arXiv preprint arXiv:1406.1078* **2014**.
- (149) Hiji, S.; Bengio, Y. Hierarchical recurrent neural networks for long-term dependencies. *Advances in neural information processing systems* **1995**, *8*.
- (150) Sutskever, I. *Training recurrent neural networks*; University of Toronto Toronto, ON, Canada, 2013.
- (151) Sutskever, I.; Martens, J.; Hinton, G. E. Generating text with recurrent neural networks. In *Proceedings of the 28th international conference on machine learning (ICML-11)*, 2011; pp 1017-1024.
- (152) Schmidt, R. M. Recurrent neural networks (rnns): A gentle introduction and overview. *arXiv preprint arXiv:1912.05911* **2019**.
- (153) Salehinejad, H.; Sankar, S.; Barfett, J.; Colak, E.; Valaee, S. Recent advances in recurrent neural networks. *arXiv preprint arXiv:1801.01078* **2017**.
- (154) Lipton, Z. C.; Berkowitz, J.; Elkan, C. A critical review of recurrent neural networks for sequence learning. *arXiv preprint arXiv:1506.00019* **2015**.
- (155) Zhang, A.; Lipton, Z. C.; Li, M.; Smola, A. J. Dive into deep learning. *arXiv preprint arXiv:2106.11342* **2021**.
- (156) Mikolov, T.; Chen, K.; Corrado, G.; Dean, J. Efficient estimation of word representations in vector space. *arXiv preprint arXiv:1301.3781* **2013**.

- (157) Ramachandran, P.; Zoph, B.; Le, Q. V. Searching for activation functions. *arXiv preprint arXiv:1710.05941* **2017**.
- (158) Maas, A. L.; Hannun, A. Y.; Ng, A. Y. Rectifier nonlinearities improve neural network acoustic models. In *Proc. icml, 2013; Atlanta, GA: Vol. 30*, p 3.
- (159) De Boer, P.-T.; Kroese, D. P.; Mannor, S.; Rubinstein, R. Y. A tutorial on the cross-entropy method. *Annals of operations research* **2005**, *134*, 19-67.
- (160) Zhang, Z.; Sabuncu, M. Generalized cross entropy loss for training deep neural networks with noisy labels. *Advances in neural information processing systems* **2018**, *31*.
- (161) Medsker, L. R.; Jain, L. Recurrent neural networks. *Design and Applications* **2001**, *5* (64-67), 2.
- (162) Schuster, M.; Paliwal, K. K. Bidirectional recurrent neural networks. *IEEE transactions on Signal Processing* **1997**, *45* (11), 2673-2681.
- (163) Bahdanau, D.; Cho, K.; Bengio, Y. Neural machine translation by jointly learning to align and translate. *arXiv preprint arXiv:1409.0473* **2014**.
- (164) Hochreiter, S. The vanishing gradient problem during learning recurrent neural nets and problem solutions. *International Journal of Uncertainty, Fuzziness and Knowledge-Based Systems* **1998**, *6* (02), 107-116.
- (165) Philipp, G.; Song, D.; Carbonell, J. G. The exploding gradient problem demystified-definition, prevalence, impact, origin, tradeoffs, and solutions. *arXiv preprint arXiv:1712.05577* **2017**.
- (166) Bengio, Y.; Simard, P.; Frasconi, P. Learning long-term dependencies with gradient descent is difficult. *IEEE transactions on neural networks* **1994**, *5* (2), 157-166.
- (167) Pascanu, R.; Mikolov, T.; Bengio, Y. On the difficulty of training recurrent neural networks. In *International conference on machine learning, 2013; Pmlr: pp 1310-1318*.
- (168) Chung, J.; Gulcehre, C.; Cho, K.; Bengio, Y. Empirical evaluation of gated recurrent neural networks on sequence modeling. *arXiv preprint arXiv:1412.3555* **2014**.
- (169) Chung, J.; Gulcehre, C.; Cho, K.; Bengio, Y. Gated feedback recurrent neural networks. In *International conference on machine learning, 2015; PMLR: pp 2067-2075*.
- (170) Graves, A. Long short-term memory. *Supervised sequence labelling with recurrent neural networks* **2012**, 37-45.
- (171) Gers, F. A.; Schmidhuber, J.; Cummins, F. Learning to forget: Continual prediction with LSTM. *Neural computation* **2000**, *12* (10), 2451-2471.
- (172) Ranzato, M. A.; Chopra, S.; Auli, M.; Zaremba, W. Sequence level training with recurrent neural networks. *arXiv preprint arXiv:1511.06732* **2015**.

- (173) Sutskever, I.; Vinyals, O.; Le, Q. V. Sequence to sequence learning with neural networks. *Advances in neural information processing systems* **2014**, *27*.
- (174) Badrinarayanan, V.; Kendall, A.; Cipolla, R. Segnet: A deep convolutional encoder-decoder architecture for image segmentation. *IEEE transactions on pattern analysis and machine intelligence* **2017**, *39* (12), 2481-2495.
- (175) Cho, K.; Courville, A.; Bengio, Y. Describing multimedia content using attention-based encoder-decoder networks. *IEEE Transactions on Multimedia* **2015**, *17* (11), 1875-1886.
- (176) Gehring, J.; Auli, M.; Grangier, D.; Yarats, D.; Dauphin, Y. N. Convolutional sequence to sequence learning. In *International conference on machine learning*, 2017; PMLR: pp 1243-1252.
- (177) Niu, Z.; Zhong, G.; Yu, H. A review on the attention mechanism of deep learning. *Neurocomputing* **2021**, *452*, 48-62.
- (178) Luong, M.-T.; Pham, H.; Manning, C. D. Effective approaches to attention-based neural machine translation. *arXiv preprint arXiv:1508.04025* **2015**.
- (179) Shaw, P.; Uszkoreit, J.; Vaswani, A. Self-attention with relative position representations. *arXiv preprint arXiv:1803.02155* **2018**.
- (180) Vaswani, A.; Shazeer, N.; Parmar, N.; Uszkoreit, J.; Jones, L.; Gomez, A. N.; Kaiser, L.; Polosukhin, I. Attention Is All You Need. *Adv Neur In* **2017**, *30*.
- (181) Yang, B.; Tu, Z.; Wong, D. F.; Meng, F.; Chao, L. S.; Zhang, T. Modeling localness for self-attention networks. *arXiv preprint arXiv:1810.10182* **2018**.
- (182) Ba, J. L.; Kiros, J. R.; Hinton, G. E. Layer normalization. *arXiv preprint arXiv:1607.06450* **2016**.
- (183) Jacob, D.; Chang, M.-W.; Lee, K.; Toutanova, K. BERT: Pre-training of Deep Bidirectional Transformers for Language Understanding. *arXiv preprint arXiv:1810.04805* **2018**.
- (184) Beltagy, I.; Lo, K.; Cohan, A. SciBERT: A pretrained language model for scientific text. *arXiv preprint arXiv:1903.10676* **2019**.
- (185) Hartstein, A.; Kirtley, J.; Tsang, J. Enhancement of the infrared absorption from molecular monolayers with thin metal overlayers. *Physical Review Letters* **1980**, *45* (3), 201.
- (186) Hansen, W. N. Electric fields produced by the propagation of plane coherent electromagnetic radiation in a stratified medium. *JOSA* **1968**, *58* (3), 380-390.
- (187) Bassan, P.; Lee, J.; Sachdeva, A.; Pissardini, J.; Dorling, K. M.; Fletcher, J. S.; Henderson, A.; Gardner, P. The inherent problem of transfection-mode infrared spectroscopic microscopy and the ramifications for biomedical single point and imaging applications. *Analyst* **2013**, *138* (1), 144-157.
- (188) Maier, S. A. *Plasmonics: fundamentals and applications*; Springer, 2007.

- (189) Schmidt, F.-P.; Ditzbacher, H.; Hohenester, U.; Hohenau, A.; Hofer, F.; Krenn, J. R. Universal dispersion of surface plasmons in flat nanostructures. *Nat. Commun.* **2014**, *5* (1), 3604.
- (190) Enoch, S.; Bonod, N. *Plasmonics: from basics to advanced topics*; Springer, 2012.
- (191) Neubrech, F.; Huck, C.; Weber, K.; Pucci, A.; Giessen, H. Surface-enhanced infrared spectroscopy using resonant nanoantennas. *Chemical reviews* **2017**, *117* (7), 5110-5145.
- (192) Otto, A. Excitation of nonradiative surface plasma waves in silver by the method of frustrated total reflection. *Zeitschrift für Physik A Hadrons and nuclei* **1968**, *216* (4), 398-410.
- (193) Gomez, D. E.; Vernon, K. C.; Mulvaney, P.; Davis, T. J. Surface plasmon mediated strong exciton-photon coupling in semiconductor nanocrystals. *Nano Lett* **2010**, *10* (1), 274-278.
- (194) Torma, P.; Barnes, W. L. Strong coupling between surface plasmon polaritons and emitters: a review. *Rep Prog Phys* **2015**, *78* (1), 013901.
- (195) Zhizhin, G. N.; Vinogradov, E. A.; Moskalova, M. A.; Yakovlev, V. A. Applications of Surface Polaritons for Vibrational Spectroscopic Studies of Thin and Very Thin Films. *Applied Spectroscopy Reviews* **2006**, *18* (2), 171-263.
- (196) Kretschmann, E.; Heinz, R. Radiative decay of non radiative surface plasmons excited by light. *Zeitschrift für Naturforschung A* **1968**, *23.12*, 2135-2136.
- (197) Osawa, M. Surface-enhanced infrared absorption. In *Near-field optics and surface plasmon polaritons*, Springer, 2006; pp 163-187.
- (198) Nishikawa, Y.; Fujiwara, K.; Shima, T. A study on the qualitative and quantitative analysis of nanogram samples by transmission infrared spectroscopy with the use of silver island films. *Applied spectroscopy* **1991**, *45* (5), 747-751.
- (199) Orfanidis, S. J. *Electromagnetic waves and antennas.* **2002**.
- (200) Bibikova, O.; Haas, J.; Lopez-Lorente, A. I.; Popov, A.; Kinnunen, M.; Ryabchikov, Y.; Kabashin, A.; Meglinski, I.; Mizaikoff, B. Surface enhanced infrared absorption spectroscopy based on gold nanostars and spherical nanoparticles. *Anal Chim Acta* **2017**, *990*, 141-149.
- (201) Dai, W.; Wu, Y.-C.; Liu, F.-L. Unidirectional Excitation of Graphene Plasmon in Attenuated Total Reflection (ATR) Configuration. *Zeitschrift für Naturforschung A* **2016**, *71* (4), 373-379.
- (202) Pereira, C. F.; Viegas, I. M. A.; Souza Sobrinha, I. G.; Pereira, G.; Pereira, G. A. L.; Krebs, P.; Mizaikoff, B. Surface-enhanced infrared absorption spectroscopy using silver selenide quantum dots. *Journal of Materials Chemistry C* **2020**, *8* (30), 10448-10455.
- (203) Roy, D.; Fendler, J. Reflection and Absorption Techniques for Optical Characterization of Chemically Assembled Nanomaterials. *Advanced Materials* **2004**, *16* (6), 479-508.
- (204) Vincenti, M. A.; Ceglia, D. d.; Angelis, C. D.; Scalora, M. Surface-plasmon excitation of second-



- harmonic light: emission and absorption. *Journal of the Optical Society of America B* **2017**, *34* (3).
- (205) Yamamoto, K.; Ishida, H. Optical theory applied to infrared spectroscopy. *Vibrational spectroscopy* **8** (1), 1-36.
- (206) A, H.; Y, S.; W, S. Infrared absorption enhancement of monolayer species on thin evaporated Ag films by use of a Kretschmann configuration: Evidence for two types of enhanced surface electric fields. *Applied Physics A* **1984**, *35*, 135-140.
- (207) Barchiesi, D.; Andreas, O. Excitations of surface plasmon polaritons by attenuated total reflection, revisited. *La Rivista del Nuovo Cimento* **2013**, *36* (5), 173-209.
- (208) Bürgi, T.; Wirz, R.; Baiker, A. In situ attenuated total reflection infrared spectroscopy: A sensitive tool for the investigation of reduction– oxidation processes on heterogeneous Pd metal catalysts. *J. Phys. Chem. B* **2003**, *107* (28), 6774-6781.
- (209) Nong, J.; Tang, L.; Lan, G.; Luo, P.; Guo, C.; Yi, J.; Wei, W. Wideband tunable perfect absorption of graphene plasmons via attenuated total reflection in Otto prism configuration. *Nanophotonics* **2020**, *9* (3), 645-655.
- (210) Chen, Y. *Modeling of plasmon mediated single-photon devices*; Technical University of Denmark, 2010.
- (211) Rumpf, R. C. Electromagnetic analysis using finite-difference time-domain. *Lecture Notes in FDTD. USA* **2012**.
- (212) Toroglu, G.; Sevgi, L. Finite-difference time-domain (fdtd) matlab codes for first- and second-order em differential equations [testing ourselves]. *IEEE Antennas and Propagation Magazine* **2014**, *56* (2), 221-239.
- (213) Cao, T.; Wei, C. W.; Simpson, R. E.; Zhang, L.; Cryan, M. J. Broadband polarization-independent perfect absorber using a phase-change metamaterial at visible frequencies. *Sci Rep* **2014**, *4*, 3955.
- (214) Jin, J.-M. *The finite element method in electromagnetics*; John Wiley & Sons, 2015.
- (215) Sullivan, D. M. *Electromagnetic simulation using the FDTD method*; John Wiley & Sons, 2013.
- (216) Gedney, S. D. *Introduction to the finite-difference time-domain (FDTD) method for electromagnetics*; Morgan & Claypool Publishers, 2011.
- (217) Smajic, J.; Hafner, C.; Raguin, L.; Tavzarashvili, K.; Mishrikey, M. Comparison of numerical methods for the analysis of plasmonic structures. *Journal of Computational and Theoretical Nanoscience* **2009**, *6* (3), 763-774.
- (218) Yao, G.-Y.; Liu, Q.-L.; Zhao, Z.-Y. Studied localized surface plasmon resonance effects of Au nanoparticles on TiO<sub>2</sub> by FDTD simulations. *Catalysts* **2018**, *8* (6), 236.
- (219) Schlücker, S. Surface-Enhanced raman spectroscopy: Concepts and chemical applications. *Angew.*

*Chem. Int. Ed.* **2014**, *53* (19), 4756-4795.

- (220) Mayerhofer, T. G.; Popp, J. Electric field standing wave effects in internal reflection and ATR spectroscopy. *Spectrochim Acta A Mol Biomol Spectrosc* **2018**, *191*, 165-171.
- (221) Hakala, T. K.; Toppari, J. J.; Kuzyk, A.; Pettersson, M.; Tikkanen, H.; Kunttu, H.; Torma, P. Vacuum Rabi splitting and strong-coupling dynamics for surface-plasmon polaritons and rhodamine 6G molecules. *Phys Rev Lett* **2009**, *103* (5), 053602.
- (222) Hu, Y.; López-Lorente, Á. I.; Mizaikoff, B. Versatile Analytical Platform Based on Graphene-Enhanced Infrared Attenuated Total Reflection Spectroscopy. *ACS Photonics* **2018**, *5* (6), 2160-2167.
- (223) Alleyne, D.; Cawley, P. A two-dimensional Fourier transform method for the measurement of propagating multimode signals. *The Journal of the Acoustical society of America* **1991**, *89* (3), 1159-1168.
- (224) Ernst, R. R.; Bodenhausen, G.; Wokaun, A. *Principles of nuclear magnetic resonance in one and two dimensions*; Oxford university press, 1990.
- (225) Noda, I. Two-dimensional infrared spectroscopy. *J. Am. Chem. Soc.* **1989**, *111* (21), 8116-8118.
- (226) Noda, I.; Ozaki, Y. *Two-dimensional correlation spectroscopy: applications in vibrational and optical spectroscopy*; John Wiley & Sons, 2005.
- (227) Noda, I. Vibrational two-dimensional correlation spectroscopy (2DCOS) study of proteins. *Spectrochim Acta A Mol Biomol Spectrosc* **2017**, *187*, 119-129.
- (228) Noda, I. Determination of two-dimensional correlation spectra using the Hilbert transform. *Applied Spectroscopy* **2000**, *54* (7), 994-999.
- (229) Raffel, C.; Shazeer, N.; Roberts, A.; Lee, K.; Narang, S.; Matena, M.; Zhou, Y.; Li, W.; Liu, P. J. Exploring the limits of transfer learning with a unified text-to-text transformer. *Journal of machine learning research* **2020**, *21* (140), 1-67.
- (230) Wang, J. Ultrafast two-dimensional infrared spectroscopy for molecular structures and dynamics with expanding wavelength range and increasing sensitivities: from experimental and computational perspectives. *International Reviews in Physical Chemistry* **2017**, *36* (3), 377-431.
- (231) Ghosh, A.; Ostrander, J. S.; Zanni, M. T. Watching proteins wiggle: mapping structures with two-dimensional infrared spectroscopy. *Chemical reviews* **2017**, *117* (16), 10726-10759.
- (232) Cho, M. *Two-dimensional optical spectroscopy*; CRC press, 2009.
- (233) Zimdars, D.; Tokmakoff, A.; Chen, S.; Greenfield, S.; Fayer, M.; Smith, T.; Schwettman, H. Picosecond infrared vibrational photon echoes in a liquid and glass using a free electron laser. *Physical review letters* **1993**, *70* (18), 2718.

- (234) Jonas, D. M. Two-dimensional femtosecond spectroscopy. *Annu. Rev. Phys. Chem.* **2003**, *54* (1), 425-463.
- (235) Hybl, J. D.; Albrecht Ferro, A.; Jonas, D. M. Two-dimensional Fourier transform electronic spectroscopy. *The Journal of Chemical Physics* **2001**, *115* (14), 6606-6622.
- (236) Mukamel, S. Principles of nonlinear optical spectroscopy. (*No Title*) **1995**.
- (237) Hamm, P.; Martin, Z. Concepts and methods of 2D infrared spectroscopy. *Cambridge University Press* **2011**.
- (238) Zheng, J.; Kwak, K.; Fayer, M. Ultrafast 2D IR vibrational echo spectroscopy. *Accounts of Chemical Research* **2007**, *40* (1), 75-83.
- (239) Shim, S.-H.; Zanni, M. T. How to turn your pump-probe instrument into a multidimensional spectrometer: 2D IR and Vis spectroscopies via pulse shaping. *Physical Chemistry Chemical Physics* **2009**, *11* (5), 748-761.
- (240) Kraack, J. P. Ultrafast structural molecular dynamics investigated with 2D infrared spectroscopy methods. *Top Curr Chem (Cham)* **2017**, *375* (6), 86.
- (241) Petti, M. K.; Lomont, J. P.; Maj, M.; Zanni, M. T. Two-dimensional spectroscopy is being used to address core scientific questions in biology and materials science. *J. Phys. Chem. B* **2018**, *122* (6), 1771-1780.
- (242) Hunt, N. T. Transient 2D-IR spectroscopy of inorganic excited states. *Dalton Trans* **2014**, *43* (47), 17578-17589.
- (243) Zhang, T.; Kuznetsova, I.; Meier, T.; Li, X.; Mirin, R. P.; Thomas, P.; Cundiff, S. T. Polarization-dependent optical 2D Fourier transform spectroscopy of semiconductors. *Proc. Natl. Acad. Sci. USA* **2007**, *104* (36), 14227-14232.
- (244) Chen, H.; Bian, H.; Li, J.; Wen, X.; Zheng, J. Ultrafast multiple-mode multiple-dimensional vibrational spectroscopy. *International Reviews in Physical Chemistry* **2012**, *31* (4), 469-565.
- (245) Sun, A. The Limits in the Enhancement Factor in Near-Brewster Angle Reflection Pump-Probe Spectroscopy. University of Chinese Academy of Sciences, June 2020.
- (246) Khalil, M.; Demirdöven, N.; Tokmakoff, A. Coherent 2D IR spectroscopy: Molecular structure and dynamics in solution. *The Journal of Physical Chemistry A* **2003**, *107* (27), 5258-5279.
- (247) Kraack, J. P.; Lotti, D.; Hamm, P. 2D attenuated total reflectance infrared spectroscopy reveals ultrafast vibrational dynamics of organic monolayers at metal-liquid interfaces. *J Chem Phys* **2015**, *142* (21), 212413.
- (248) Kraack, J. P.; Kaech, A.; Hamm, P. Surface Enhancement in Ultrafast 2D ATR IR Spectroscopy at the Metal-Liquid Interface. *The Journal of Physical Chemistry C* **2016**, *120* (6), 3350-3359.

- (249) Bibikova, O.; Haas, J.; Lopez-Lorente, A. I.; Popov, A.; Kinnunen, M.; Meglinski, I.; Mizaikoff, B. Towards enhanced optical sensor performance: SEIRA and SERS with plasmonic nanostars. *Analyst* **2017**, *142* (6), 951-958.
- (250) Nishida, J.; Yan, C.; Fayer, M. D. Orientational Dynamics of a Functionalized Alkyl Planar Monolayer Probed by Polarization-Selective Angle-Resolved Infrared Pump-Probe Spectroscopy. *J. Am. Chem. Soc.* **2016**, *138* (42), 14057-14065.
- (251) Nishida, J.; Yan, C.; Fayer, M. D. Enhanced nonlinear spectroscopy for monolayers and thin films in near-Brewster's angle reflection pump-probe geometry. *The Journal of Chemical Physics* **2017**, *146* (9).
- (252) Osawa, M. Surface-enhanced infrared absorption. *Near-field optics and surface plasmon polaritons* **2006**, 163-187.
- (253) Hao, J.; Zhou, L.; Qiu, M. Nearly total absorption of light and heat generation by plasmonic metamaterials. *Physical Review B* **2011**, *83* (16).
- (254) Nishida, J.; Fayer, M. D. Theory of third-order spectroscopic methods to extract detailed molecular orientational dynamics for planar surfaces and other uniaxial systems. *The Journal of Chemical Physics* **2014**, *140* (14).
- (255) Sun, A.; Wang, J. Limits in enhancement factor in near-brewster angle reflection pump-probe two-dimensional infrared spectroscopy. *Chinese Journal of Chemical Physics* **2022**, *35* (1), 129-142.
- (256) Yan, C.; Yuan, R.; Pfalzgraff, W. C.; Nishida, J.; Wang, L.; Markland, T. E.; Fayer, M. D. Unraveling the dynamics and structure of functionalized self-assembled monolayers on gold using 2D IR spectroscopy and MD simulations. *Proc. Natl. Acad. Sci. USA* **2016**, *113* (18), 4929-4934.
- (257) Petti, M. K.; Ostrander, J. S.; Saraswat, V.; Birdsall, E. R.; Rich, K. L.; Lomont, J. P.; Arnold, M. S.; Zanni, M. T. Enhancing the signal strength of surface sensitive 2D IR spectroscopy. *The Journal of Chemical Physics* **2019**, *150* (2).

# Declaration of Originality

I hereby declare that the work presented in this document is my own and has been completed without any unauthorized assistance from third parties. I have used only the sources and aids specifically referenced and acknowledged within the work. Any passages or ideas derived from other sources have been appropriately cited and indicated as per academic standards.

**Title of the submitted work:**

Calculation, simulation, and experimental analysis of distorted and enhanced spectra from attenuated total reflection (ATR)

**Signature:** \_\_\_\_\_

**Date:** \_\_\_\_\_